High Energy Emissions from Astrophysical Objects

Anthony Paul SZABO B.Sc. (Hons.)

Thesis submitted for the degree of

Doctor of Philosophy

in

The University of Adelaide

(Faculty of Science)

October, 1992

Contents

This work contains no material which has been accepted for the award of any other degree or diploma in any university or other tertiary institution and, to the best of my knowledge and belief, contains no material previously published or written by another person, except where due reference has been made in the text.

I give consent to this copy of my thesis, when deposited in the University Library, being available for loan and photocopying.

SIGNED: ... . DATE: 22nd October 1992

Acknowledgements

Many people have helped and encouraged me during the course of the last three and a half years, and I take this opportunity to offer them my thanks. In addition, I would like to acknowledge the receipt of an Australian Postgraduate Research Award, without which none of this would have been possible.

Firstly, I would like to thank the following members of the High Energy Astrophysics Group for their help reading manuscripts and for advice on a number of topics: Roger Clay, Bruce Dawson, Phil Edwards and Greg Thornton. In addition, I would like to thank my fellow postgraduate students, Anthony Lee, Rishi Meyhanden, Mike Roberts, Gail Higginbottom, Gary Hill, Janice Reid, Andrew Smith, and Gavin Rowell, the *new wave* of the CRGGC, for their help and encouragement. I would like to thank Stephen Elton, for giving me his desk, desk lamp and other stuff when he submitted his thesis and headed for DSTO. I thank David Bird for his encouragement and for showing the way. I also thank the following general staff members of the Department of Physics and Maths Physics for their prompt an efficient help regarding a variety of matters: Deidre Simpson, Sharon Frencken, Janet Hobbs, Arlene Shaw, Brian Inwood, Mark Ferraretto, and Peter Berry–Smith.

I would like to take this opportunity to thank Prof. Maurice Shapiro and Prof. John Wefel, co-directors of the 8^{th} Course of the International School on Cosmic Ray Astrophysics, June 1992, and the Ettore Majorana Centre for Scientific Culture, Erice, Sicily, Italy, for enabling me to attend the school. I found it exceedingly beneficial and a good introduction into the field of high energy astrophysics.

My thanks are particularly given to my supervisor, Ray Protheroe, who has been both supporting and encouraging throughout my candidature. Despite a hectic schedule he has always made time to discuss aspects of this work and high energy astrophysics in general. In particular, I would like to thank him for the financial support which enabled me to attend both the Fifth Asian–Pacific Regional Astronomy Meeting held in Sydney, Australia, July 1990, and the 8^{th} Course of the International School on Cosmic Ray Astrophysics held in Erice, Italy, June 1992. He has always been prompt when reading drafts of my thesis and his constructive criticism has been much appreciated.

I would like to thank my immediate family for their interest, encouragement and support while I have been completing my Ph.D., in particular, my brother Jim for putting up with me while sharing a flat. I would also like to thank the Drysdale family for their encouragement.

And lastly, but by no means leastly, I would like to thank my wife Mary for being both understanding and supportive throughout my candidature, despite some trying and stressful circumstances.

Abstract

In this thesis, some of the consequences of accelerating protons to high energies via shock acceleration in diffuse matter and radiation fields are examined. In particular particle production in active galactic nuclei is investigated. In the central region (or nucleus) of an active galaxy protons primarily lose energy via proton–proton interactions with the accreting matter, and pair production and pion photoproduction on the radiation field. The decay of pions produced from proton–proton and pion photoproduction interactions results in a neutrino flux from the nuclei of active galaxies. While individual AGN are not observable with the proposed high energy neutrino telescopes, the diffuse neutrino background produced by all of the active galactic nuclei may be observable.

After a brief introduction to the field of high energy astrophysics in Chapter 1, cosmic ray physics relevant to particle production in active galactic nuclei is discussed in Chapter 2. Cosmic ray propagation is discussed in terms a transport equation similar to that suggested by Ginzburg and Syrovatskii (1964). Shock acceleration is introduced using the basic ideas of Fermi (1949) and is also discussed in the context of an infinite planar shock with a parallel magnetic field. The chapter is concluded with a description of how shock acceleration may be visualised in terms of a leaky box model.

High energy interactions (exclusive and inclusive) and decays (two and three body) are described in general terms in Chapter 3. In addition, some of the reference frames used in the modelling of high energy interactions are discussed along with a derivation of the mean path length for interaction of a particle in a relativistic gas. The techniques described in Chapter 3 are applied to pion photoproduction, pair production, proton–proton interactions and pion and muon decays in Chapter 4. Monte Carlo simulations of pion photoproduction and pair production are described along with a discussion of how proton–proton interactions may be modelled.

In Chapter 5, the techniques used for the observation of high energy neutrinos are discussed. Some of the proposed neutrino telescopes are described and their present status (or at least their status as of early in 1992) is reviewed. The method of calculating the neutrino signal in a neutrino telescope is described, and is applied to estimate

the neutrino signal from SN 1987A using the model of Harding *et al.* (1991) for particle acceleration in the supernova remnant.

A simple model of an active galactic nucleus involving accretion onto a super–massive black hole is used in Chapter 6 to investigate the consequences of high energy particle production within the central region. Particle acceleration is assumed to take place via the first order Fermi mechanism at a shock front which forms in the accretion flow, and be supported by pressure from high energy protons. Observations of the continuum radiation from active galactic nuclei are briefly reviewed and two "generic" photon spectra are developed. Particle production by pair production, pion photoproduction and proton–proton interactions is investigated both during and after acceleration of the protons. The question of neutron escape from the core region of the active galaxy is examined and the consequences are discussed. Calculation of the neutrino flux at Earth resulting from individual active galactic nuclei is described along with the cosmological integration to find the contribution to the neutrino background. The prospects for observing both individual active galaxies and the diffuse background with the proposed neutrino telescopes are discussed. The results are compared to recent work by Stecker *et al.* (1992), Biermann (1992) and Sikora and Begelman (1992).

Chapter 7 summarises the work presented in this thesis and briefly discusses some of the other consequences of particle acceleration in active galaxies. The application of this work to other astrophysical objects is also briefly discussed.

Chapter 1

High Energy Astrophysics—An Overview

1.1 Introduction

The term high energy astrophysics encompasses several fields of physics, including cosmic ray astrophysics, γ–ray astrophysics and high energy neutrino astrophysics. Of these, cosmic ray astrophysics is the best established with an eighty year history of experimental and theoretical advances. Gamma ray astrophysics has a shorter history, and progress really accelerated with the launch of satellite borne γ–ray telescopes, the most recent of which is the Compton Gamma Ray Observatory (GRO) launched in 1991. In contrast, high energy neutrino astrophysics is a relatively new field. While a number of small detectors capable of being used as neutrino telescopes have already been built, a large neutrino detector is required to make meaningful observations of astrophysical sources. There are several promising proposals for high energy neutrino telescopes and some of these may begin operating within the next few years.

The idea that active galactic nuclei (AGN) may be a source of high energy neutrinos and γ–rays was first suggested more than a decade ago. Since this time there has been steady theoretical progress. Early work was focussed on neutrino and γ–ray production from the decay of pions produced in proton–proton interactions. However, it was soon realised that proton interactions with the radiation field may also be an important loss mechanism in AGN. In fact proton–photon interactions are found to limit the maximum energy achievable by shock acceleration in AGN. Initially the neutrino flux

from individual AGN was emphasised. However, despite the high luminosities of these galaxies, individual AGN (with the possible exception of some nearby AGN with jets) are not thought to be observable with the proposed high energy neutrino telescopes. However, in recent times much of the focus has shifted to the diffuse neutrino flux produced by the sum of all AGN.

In this thesis, some of the consequences of proton acceleration at a shock front in diffuse matter are discussed. In particular with relation to high energy particle production in the central region of active galaxies. First order Fermi acceleration at a plane shock, along with a simple leaky box model of shock acceleration, are discussed in Chapter 2. For AGN pion photoproduction ($p\gamma \rightarrow \pi X$, where X represents all of the other particles produced), pair production ($p\gamma \rightarrow pe^-e^+$) and proton–proton interactions ($pp \rightarrow \pi X$) are found to be the dominant loss mechanisms. Each of these interactions along with pion and muon decay are examined in detail in Chapter 4. Pion photoproduction has been modelled exclusively near threshold using the fits to the differential cross section of Genzel, Joos and Pfeil (1973). At higher energies, pion photoproduction has been modelled inclusively using the concept of scaling and the data of Moffeit *et al.* (1972). For pair production, the interactions have been modelled assuming negligible proton recoil in the proton rest frame, and using the formulae for the differential cross sections given by Motz, Olsen and Koch (1969). Proton–proton interactions have been modelled using the fits to the inclusive data of Hillas (1979).

A simple model of AGN involving accretion onto a supermassive black hole (described in Chapter 6) has been used to calculate the flux of neutrinos expected from individual AGN. In the model proton acceleration takes place via shock acceleration. The leaky box model of shock acceleration discussed in Chapter 2 has been used to calculate the spectrum of neutrinos produced during and after acceleration. Neutrons produced from charge exchange interactions ($p \rightarrow n$) are not confined by the magnetic field in AGN and so may escape from the central region. For the present work, the approximation that all of the neutrons escape from the central region of the AGN has been used. However, a more detailed analysis of neutron escape and the possible AGN origin of high energy ($> 10^{15}$ eV) cosmic rays has been discussed by Protheroe and Szabo (1992). The procedure for scaling the resulting neutrino spectra for individual AGN is described. The contribution to the diffuse neutrino background from AGN has

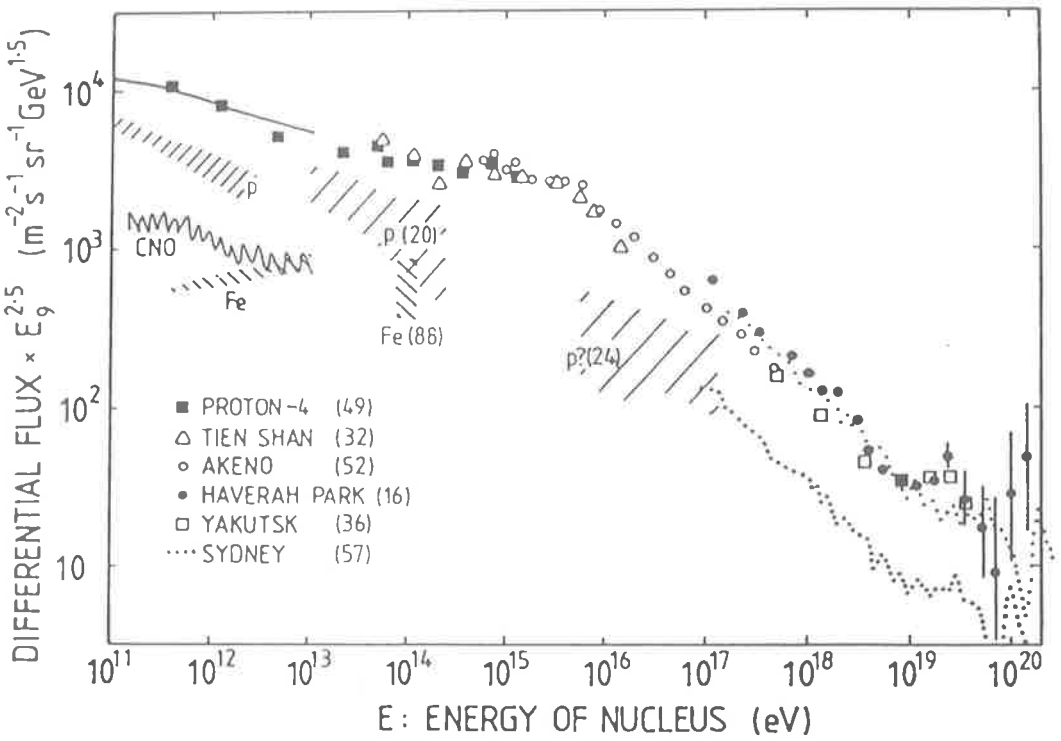

Figure 1.1: A plot of the cosmic ray energy spectrum measured by a few selected experiments. The spectrum has been multiplied by a factor of $E_9^{2.75}$, where E_9 is the energy of the nucleus in GeV, to flatten the spectrum and accentuate the "knee" at 10^{15}–10^{16} eV, and the "ankle" at 10^{19} eV. The shaded bands refer to particular nuclear species or groups. From Hillas (1984).

also been calculated by using the observed X–ray luminosity function and performing a cosmological integration over all AGN. The prospects for observing both the individual AGN and the diffuse AGN background with the proposed high energy neutrino telescopes are discussed.

In the rest of this chapter, a brief overview of cosmic ray, γ–ray and high energy neutrino astrophysics is given. Emphasis is placed on neutrino astrophysics and what the observation of high energy neutrinos may be able to tell us.

1.2 Cosmic Ray and γ–Ray Astrophysics

The observed spectrum of cosmic rays is shown in Figure 1.1. The spectrum[1] is dominated by two features, the "knee" at 10^{15}–10^{16} eV, and the "ankle" at approximately 10^{19} eV. Below the "knee", the spectrum may be understood in terms of the acceleration of particles at shock fronts in galactic supernova remnants, along with diffusion in the galactic magnetic field and modulation of the cosmic ray flux due to the solar wind. However, above the "knee" the origin of cosmic rays is less well understood. For energies greater then 10^{19} eV the cosmic ray spectrum is thought to be extra–galactic in nature as even heavy particles, such as iron nuclei, might not be confined by the galactic magnetic field. The production of cosmic rays with energy above the "knee" by jets in AGN has been the focus of several recent papers (Biermann and Strittmatter 1987, Ip and Axford 1991, Rachen and Biermann 1992). Between the "knee" and the "ankle" the origin of the cosmic rays is even more unclear. If the cosmic rays in this energy range are primarily heavy particles then they could be galactic in origin, produced by young supernovae and galactic compact objects. Alternatively, most of the cosmic rays with energy above 10^{15} eV could be extra–galactic. For example, Protheroe and Szabo (1992) have calculated the flux of cosmic rays expected from AGN, and have shown that AGN may be a source of the observed cosmic rays above the "knee". Clearly, the situation would be clarified if the sources of high energy particles could be observed directly. Some aspects of cosmic ray astrophysics, including first and second order Fermi acceleration, are discussed in Chapter 2. For reviews of cosmic ray astrophysics

[1]Notice that the spectrum has been multiplied by a factor of $E^{2.5}$ to reduce the dynamic range of the plot

	Area (m^2)	Design Function
KOLAR	25-40	Atmospheric Neutrinos
CWI	174	Atmospheric Neutrinos
BAKSAN	260	Neutrino Telescope
HOMESTAKE	120	Muon Telescope
IMB	400	PDK
HPW	102	PDK
KAMIOKANDE I, II	160	PDK
NUSEX	12	PDK
FREJUS	74	PDK
LSD	~50	Super Nova Neutrinos
SOUDAN I	10	PDK
SOUDAN II	128	PDK
MACRO	1100	Monopoles
LVD		Super Nova Neutrinos
SNO	180	Solar Neutrinos
SuperK	~900	PDK, Solar neutrinos

Table 1.1: A table showing the neutrino telescopes which have been built or are in the process of being built, and the purpose for which they have been designed. PDK detectors refer to proton decay experiments. Also shown is the approximate detector area. From Sobel (1991).

see Hillas (1975), Longair (1981), Hillas (1984), Gaisser (1990) and Berezinskiĭ *et al.* (1990).

In contrast to cosmic rays, γ–rays are not scattered by the galactic and extra–galactic magnetic fields. Therefore, γ–rays travel directly to the Earth and may be identified with specific sources. At high energies, γ–rays are primarily produced by the decay of neutral pions which are produced in hadronic interactions. Hence, γ–ray emissions may be used as a tracer of high energy protons and nuclei. Unfortunately, if the source is shrouded by diffuse matter (such as an accretion flow) or by low energy radiation, then the γ–rays may be reprocessed before they reach the Earth. Gamma rays may suffer several interactions before escaping from the source, making it difficult to reconstruct the details of the primary cosmic rays. A natural by–product of the hadronic interactions producing γ–rays are high energy neutrinos produced by charged pion decay. High energy neutrinos are also tracers of high energy cosmic rays. However, because they interact weakly with matter, neutrinos have the additional benefit that most of them are not reprocessed between production and arrival at Earth. Thus, neutrinos may be one of the only means of directly 'observing' cosmic ray acceleration to ultra high energies. Many of the early estimates of the neutrino fluxes from astrophysical objects were made by scaling from the observed γ–ray flux. However, a lack of knowledge regarding the reprocessing of the γ–ray flux can can lead to large uncertainties in these types of calculations. For reviews of γ–ray astrophysics see Stecker (1971), Trombka and Fichtel (1983), Hillier (1984) and Weekes (1988).

1.3 High Energy Neutrino Astrophysics

While the construction of neutrino detectors began in the early 1960s with experiments to measure the flux of atmospheric neutrinos (Achar *et al.* 1965, Reines *et al.* 1965), it is only in the last two or three decades that people have seriously thought about building high energy neutrino telescopes. As yet, no telescopes designed specifically for high energy neutrino astronomy have been built. However, a number of detectors which can detect neutrinos have been built for other purposes, e.g. as proton decay experiments. In Table 1.1 a list of these detectors and the purpose for which they were designed is shown. It was from some of these detectors that our first taste of neutrino

astronomy was obtained. In 1987 a supernova in the large magellenic cloud, SN 1987A, was observed by neutrino detectors (see Arnett *et al.* 1989 for a review of SN 1987A and the neutrino observations). While the number of neutrinos observed was small, only 20 events over approximately 12 seconds in IMB and Kamiokande II, with possibly a further 5 events from Baksan, this was sufficient to confirm conventional wisdom regarding stellar collapse. The neutrino observations of SN 1987A also provided limits on the neutrino lifetime and magnetic moment, and gave a limit to the neutrino mass similar to that obtained in terrestrial experiments (Halzen, Learned and Stanev 1989). This has given us an insight into what may be achievable with a telescope designed specifically for neutrino astronomy.

In the late 1970s, the first high energy neutrino telescope (DUMAND) was proposed. The proposal was for a detector composed of a large array of photomultiplier tubes which were to be placed in the deep ocean off the coast of Hawaii. Subsequently, there have been a number of other proposals for neutrino telescopes, including BAIKAL, GRANDE, AMANDA, the SINGAO neutrino telescope and RAMAND. In Chapter 5 each of these proposals plus the high resolution Fly's Eye (HiRes) are reviewed. The status of the experiments as of early 1992 is also given. For a recent review of neutrino telescopes see Sobel (1991).

1.3.1 Possible Sources of High Energy Neutrinos

As discussed earlier, high energy neutrinos are produced as a result of the same hadronic interactions which produce γ–rays. Therefore, the necessary ingredients for a high energy neutrino source are a population of high energy protons or nuclei and some matter or radiation on which the energetic particles can interact. This has prompted some authors (see e.g. Halzen, Learned and Stanev 1989 and Gaisser 1990) to describe a high energy neutrino source as a giant particle/nuclear physics experiment in which a beam (high energy protons and nuclei) interacts with a target (diffuse matter and radiation) yielding pions which decay to neutrinos.

Where might such a cosmic accelerator exist? One possibility is a galactic binary system in which one of the stars is a compact object, such as a neutron star or a black hole. Particles accelerated near the compact object (by whatever mechanism) could interact with the binary companion producing γ–rays and neutrinos. However,

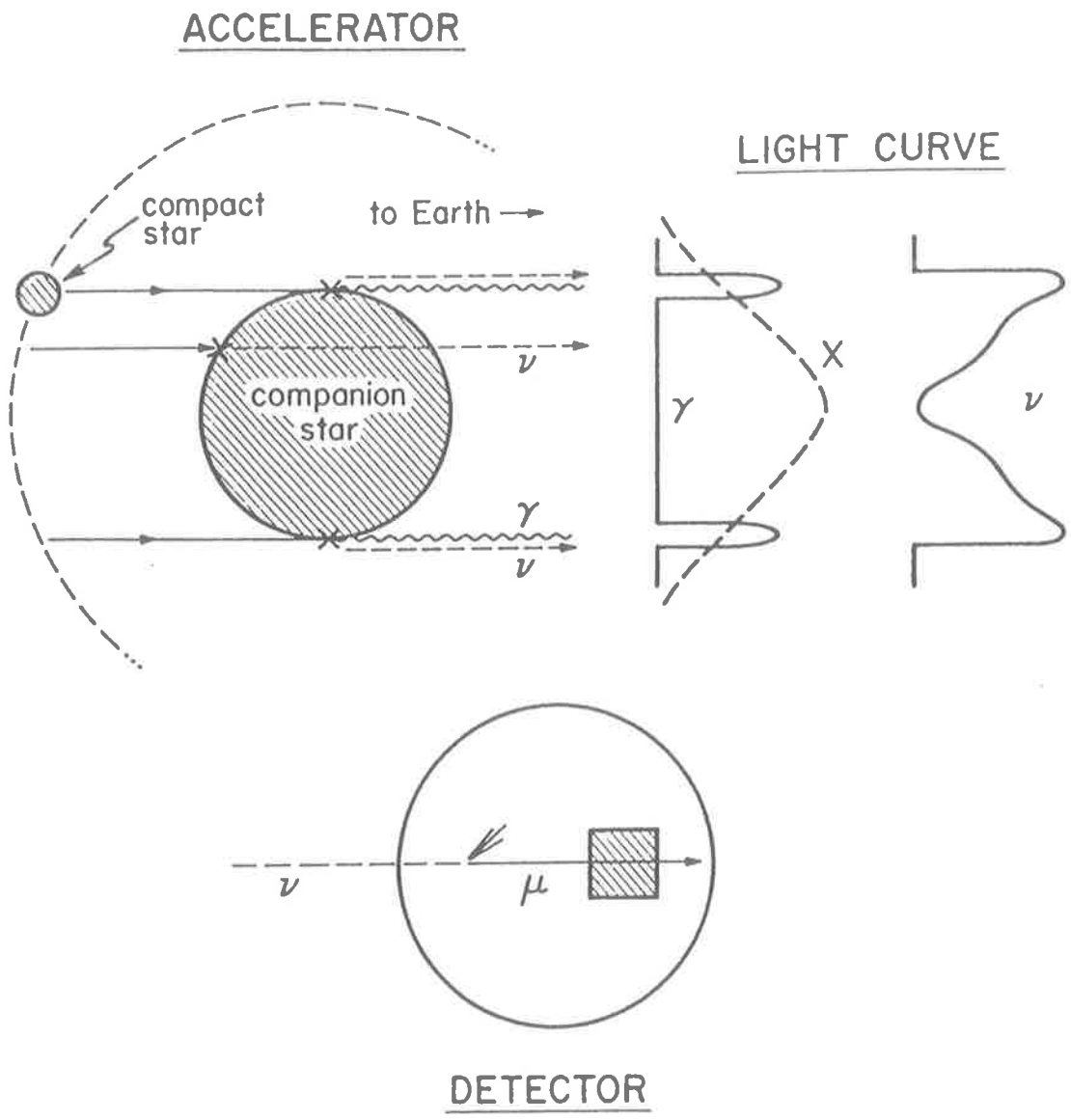

Figure 1.2: A schematic diagram illustrating the mechanism for the production of high energy γ–rays and neutrinos in galactic binary star system. Only protons interacting in the limb of the companion star will produce γ–rays observable at Earth. Also shown are the γ–ray, X–ray and neutrino light curves, and a schematic diagram illustrating the interaction of a neutrino within the Earth and the passage of the produced muon through a detector. From Halzen, Learned and Stanev (1989).

only γ–rays produced in the limb of the star would be seen at Earth. The scenario is shown schematically in Figure 1.2. It is possible to imagine a number of scenarios in which a galactic compact object is in an environment conducive to neutrino production. Clearly, they are variations on the theme described above.

In the late 1970s it was suggested that active galactic nuclei may be sources of γ–rays and neutrinos (see e.g. Berezinskiĭ and Zatsepin 1977 and Eichler 1979). It was quickly realised that complementary γ–ray and neutrino observations of AGN may be able to give us important information about the acceleration of high energy particles (Shapiro and Silberberg 1983, Silberberg and Shapiro 1983) and may even be able to differentiate between models of AGN (Berezinsky and Ginzburg 1981). Since then there has been steady theoretical progress. A review of most of the theoretical contributions may be found in Chapter 6. See also Stanev (1992) for a recent review of the current theoretical status of high energy neutrino astrophysics with emphasis on neutrino emission from AGN.

Recently, Stecker *et al.* (1991a,b) have calculated the contribution to the diffuse neutrino background from AGN. They used a simple model for the AGN and shock acceleration, and only considered pion photoproduction interactions. Fits to the X–ray luminosity function were used to integrate over the contribution to the total neutrino flux from all AGN. Several authors have subsequently pointed out that the predictions of Stecker *et al.* are inconsistent with their results and the observed energy density of the diffuse X–ray background (see e.g. Berezinsky 1991,1992; Szabo and Protheroe 1992a; Biermann 1992; and Berezinsky and Learned 1992), resulting from a typographical error in the published X–ray luminosity function. See Chapter 6 for more details. In a revised calculation using a more appropriate X–ray luminosity function, Stecker *et al.* (1992) found the diffuse neutrino flux from AGN to be reduced by a factor of ~ 40 compared to their original prediction.

In Chapter 6 an independent calculation of the flux of neutrinos from individual AGN, along with the diffuse flux of neutrinos produced by the sum of all AGN is described. A model based on the supermassive black hole model of Protheroe and Kazanas (1983), together with the developments of Kazanas and Ellison (1986) has been adopted for AGN. In this model proton acceleration takes place via the first order Fermi mechanism at a shock in the accretion flow. All relevant loss mechanisms

have been considered, and the dominant loss processes are found to be synchrotron radiation and proton–proton, pion photoproduction and pair production interactions. Proton advection onto the black hole is found to be important at low energies. Two generic radiation spectra based on the observed AGN continuum emissions have been developed. Interactions of the high energy protons with the radiation and matter in the AGN are modelled exactly. Particle production both during and after acceleration has been considered, and the question of neutron escape from the central region of the AGN has been examined. Particle production by neutrons which have escaped from the central region of the active galaxy has also been included. Scaling of the results to calculate the flux of neutrinos from individual AGN is described, along with the the cosmological integration which has been used to calculate the contribution to the diffuse neutrino background from AGN. The results are compared to those of Stecker *et al.* (1992). Biermann (1992) and Sikora and Begelman (1992) have also made independent calculations of the diffuse flux of neutrinos from AGN, and comparisons with their results are made. The prospects for observing the diffuse emissions from AGN by the proposed neutrino telescopes is discussed.

While such calculations of the neutrino flux from astrophysical objects are at best order of magnitude estimates, they none the less indicate the scale on which neutrino telescopes have to be built to have a good chance of observing sources. From the calculations presented in this thesis it can be seen that AGN are a good candidates for observation with the proposed neutrino telescopes.

Chapter 2

Cosmic Ray Physics

2.1 Introduction

In this Chapter some aspects of cosmic ray propagation and acceleration are discussed. Much of the discussion is based on the transport equations. A simple homogeneous or leaky box model of cosmic ray propagation within the galaxy is also briefly discussed. The Fermi mechanism for accelerating particles to high energies is introduced using the scenario originally envisaged by Fermi (1949), namely scattering from gas clouds in the galaxy. Shock acceleration is a very promising mechanism for the acceleration of cosmic rays, and so first order Fermi acceleration at a plane shock front is discussed. The Chapter is concluded by examining a simple idealised picture of shock acceleration in which the accelerator is visualised as a leaky box, and only energy gains due to acceleration are considered. This idealisation of shock acceleration will be used in Chapter 6 to model particle acceleration in AGN.

2.2 Cosmic Ray Propagation

The propagation of a cosmic rays through the interstellar medium (ISM) or the intergalactic medium (IGM) may be described by the transport equations (Ginzburg and Syrovatskii, 1964)

$$\frac{\partial \mathcal{N}_i}{\partial t} = \nabla \cdot (D_i \nabla \mathcal{N}_i - \vec{u}\mathcal{N}_i) + \frac{\partial}{\partial E}[b_i \mathcal{N}_i] + Q_i - p_i \mathcal{N}_i + \sum_{k \geq i} \int P_i^k(E', E)\mathcal{N}_k(E', \vec{r}, t)dE'. \quad (2.1)$$

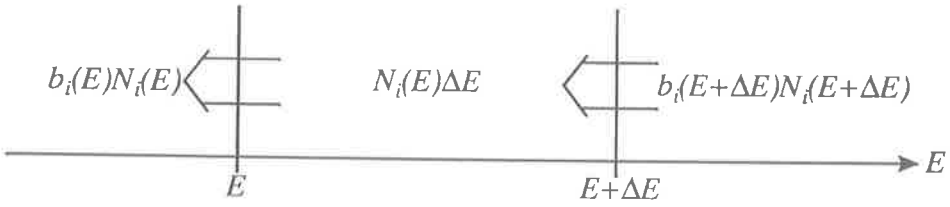

Figure 2.1: A schematic diagram of energy interval E to $E+\Delta E$, in which the number density of cosmic rays is $\mathcal{N}_i(E)\Delta E$. For energy losses, cosmic rays enter the interval from above at a rate, $b_i(E+\Delta E)\mathcal{N}_i(E+\Delta E)$. Similarly, cosmic rays leave the interval at a rate, $b_i(E)\mathcal{N}_i(E)$. In each case, only the dependence of $\mathcal{N}_i$ on energy is shown explicitly.

Here $\mathcal{N}_i = \mathcal{N}_i(E, \vec{r}, t)$ is the differential number density of cosmic rays (number of cosmic rays cm^{-3} eV^{-1}) of type i with energy E at position $\vec{r}$ at time t. The physical significance of each of the terms in Equation 2.1 is now discussed.

The first term on the right hand side (RHS) of Equation 2.1, accounts for diffusion of cosmic rays and also for any bulk motion of the medium, such as convection of the ISM or IGM. If the particle current density is defined as, $\vec{J} = \vec{u}\mathcal{N}_i - D_i \nabla \mathcal{N}_i$ (number of particles cm^{-2} s^{-1} eV^{-1}), where $\vec{u}$ is the convection velocity of the medium and D_i is the diffusion coefficient, then conservation of particles gives,

$$\begin{aligned} \frac{\partial \mathcal{N}_i}{\partial t} &= -\nabla \cdot \vec{J} \\ &= \nabla \cdot (D_i \mathcal{N}_i - \vec{u}\mathcal{N}_i). \end{aligned} \tag{2.2}$$

The second term describes any energy gains or losses made by the cosmic rays, where $b_i = dE/dt$ is the mean energy loss rate. This can be seen from a derivation similar to that given by Longair (1981). Consider the flux of cosmic rays entering and leaving an energy interval $E \rightarrow E + \Delta E$, as shown in Figure 2.1. In the case of energy losses, the rate at which particles enter the interval is $b_i(E + \Delta E)\mathcal{N}_i(E + \Delta E, \vec{r}, t)$. Similarly, the rate at which cosmic rays leave the energy interval is $b_i(E)\mathcal{N}_i(E, \vec{r}, t)$. Hence, the net rate of change of the number of particles in the interval is

$$\begin{aligned} \frac{\partial}{\partial t}(\mathcal{N}_i(E, \vec{r}, t)\Delta E) &= b_i(E + \Delta E)\mathcal{N}_i(E + \Delta E, \vec{r}, t) - b_i(E)\mathcal{N}_i(E, \vec{r}, t) \\ &= \left(b_i(E) + \frac{\partial b_i}{\partial E}\Delta E + \cdots\right)\left(\mathcal{N}_i(E, \vec{r}, t) + \frac{\partial \mathcal{N}_i}{\partial E}\Delta E + \cdots\right) \\ &\qquad - b_i(E)\mathcal{N}_i(E, \vec{r}, t) \\ &\simeq \mathcal{N}_i(E, \vec{r}, t)\frac{\partial b_i}{\partial E}\Delta E + b_i(E)\frac{\partial \mathcal{N}_i}{\partial E}\Delta E \\ &\simeq \frac{\partial}{\partial E}[b_i(E)\mathcal{N}_i(E, \vec{r}, t)]\Delta E, \end{aligned} \tag{2.3}$$

where only the first two terms of a Taylor expansion for both $b_i(E + \Delta E)$ and $\mathcal{N}_i(E + \Delta E, \vec{r}, t)$ have been retained. Thus, $\frac{\partial \mathcal{N}_i}{\partial t} \simeq \frac{\partial}{\partial E}[b_i(E)\mathcal{N}_i(E, \vec{r}, t)]$.

The source term, $Q_i = Q_i(E, \vec{r}, t)$ (number of particles cm^{-3} eV $^{-1}$ s^{-1}), gives the rate at which particles are injected into the ISM or the IGM. Cosmic rays may also suffer catastrophic losses due to processes such as radioactive decay and processes in which a large portion of the energy of the particle is lost per interaction. These losses are accounted for by the term $p_i\mathcal{N}_i$, where p_i is the rate at which catastrophic losses

occur. For example, if the catastrophic losses occur with time scale $T_i = \overline{\lambda}/\overline{v}$, where $\overline{\lambda}$ is the mean path length for the interaction and $\overline{v}$ is the mean velocity of the particle, then $p_i = T_i^{-1} = \overline{v}/\overline{\lambda}$.

The final term in Equation 2.1, gives the rate at which cosmic rays are produced by catastrophic losses such as spallation. The function $P_i^k(E', E)$ is the rate at which a cosmic ray of energy E' (type k) interacts to produce a particle of energy E (type i). The summation is over contributions from all cosmic rays which can interact to produce a particle of type i.

Solution of the system of equations represented by Equation 2.1 is not straightforward and examples of how the transport equation may be solved for a variety of boundary conditions can be found in Ginzburg and Syrovatskii (1964), Berezinskiĭ *et al.* (1990) and Gaisser (1990). However, for most applications not all of the terms in the transport equation need to be included. For example, in the homogeneous or leaky box model, cosmic rays are assumed to be uniformly distributed throughout the galaxy. In addition, if there is no convection, then the first term on the RHS in Equation 2.1 can be replaced by $\mathcal{N}/T_{\rm esc}$, where $T_{\rm esc}$ is the time scale on which cosmic rays escape from the galaxy. In the absence of catastrophic losses or spallation, Equation 2.1 becomes,

$$\frac{\partial \mathcal{N}}{\partial t} = -\frac{\mathcal{N}(E,t)}{T_{\rm esc}} + \frac{\partial}{\partial E}[b\mathcal{N}] + Q. \tag{2.4}$$

For a δ–function source and no acceleration or energy losses the solution of Equation 2.4 results in an exponential age distribution of cosmic rays. This somewhat unrealistic model is often used for cosmic ray propagation because of its simplicity, and because the low energy abundances of cosmic rays may be approximately understood in terms of a leaky box model.

2.3 Shock Acceleration of Cosmic Rays

The mechanism by which cosmic rays are accelerated to high energies with a power law spectrum is one of the most important unresolved issues in cosmic ray physics. In recent times much emphasis has been placed on first order Fermi acceleration at shocks, because it naturally gives rise to a power law particle spectrum. In supernova remnants for example, shock acceleration is thought to produce the low energy (less than $\sim 10^{15}$–10^{16} eV) cosmic rays (see e.g. Gaisser 1990 and Berezinskiĭ *et al.* 1990).

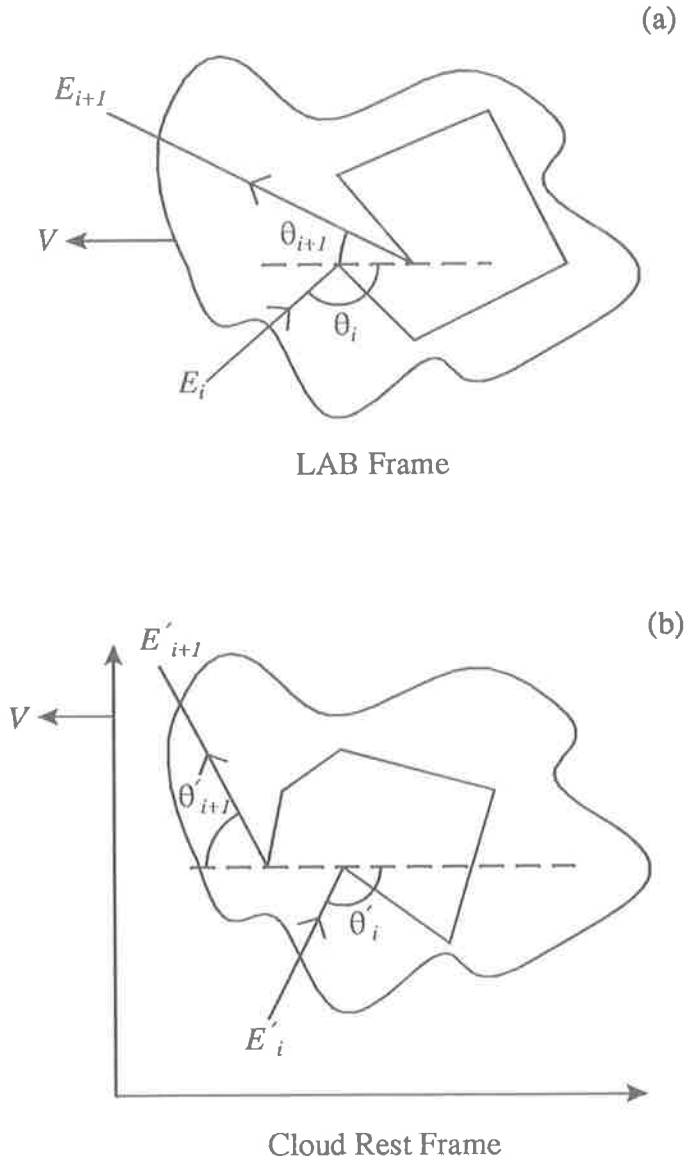

Figure 2.2: A schematic diagram of a "collisionless" interaction between a cosmic ray of energy E_i and a gas cloud moving with speed V, (a) the interaction viewed from the LAB frame and (b) the interaction when viewed from the rest frame of the cloud. Adapted from Gaisser (1990).

An introduction to particle acceleration by the Fermi mechanism is given below. Simple discussions of particle acceleration may be found in Longair (1981) and Gaisser (1990).

2.3.1 Fermi Acceleration

In 1949, Fermi suggested a mechanism by which cosmic rays could be accelerated by "collisionless" interactions with clouds of gas within our galaxy. While this is not shock acceleration as such, it serves as a useful illustration of how particle acceleration can occur via scattering from magnetic fields, which are frozen into the plasma of the gas cloud.

Consider a cosmic ray of energy E_i, which interacts with a gas cloud moving with speed V (to the left) as shown in Figure 2.2. The interaction must be collisionless in the sense that the energy of the particle is unchanged during the collision when viewed from the rest frame of the cloud. Fermi envisaged this occurring in two ways. If the magnetic field lines are bent in a semi circle (see Figure 2.3a), then a cosmic ray which is spiraling about the field lines will have its mean direction changed by an amount roughly corresponding to the angle through which the field is bent. Alternatively, if a cosmic ray moves into a region where the magnetic field strength is increasing (see Figure 2.3b), it may be reflected due to conservation of the particle's magnetic moment (the magnetic mirror effect). Hence, in the rest frame of the cloud the energy of the cosmic ray after the interaction is $E'_{i+1} = E'_i$, where $E'_i \simeq \gamma E_i(1 - \beta \cos\theta_i)$ is the energy of the cosmic ray before the interaction. The incident angle of the cosmic ray, θ_i, is defined in Figure 2.2, and $\beta = V/c$, $\gamma = (1 - \beta^2)^{-1/2}$ is the boost of the cloud. Thus, the energy of the cosmic ray when it emerges from the cloud is

$$E_{i+1} \simeq \gamma^2 E_i[1 - \beta \cos\theta_i + \beta \cos\theta'_{i+1} - \beta^2 \cos\theta_i \cos\theta'_{i+1}], \tag{2.5}$$

where θ'_{i+1} is the angle at which the particle leaves the cloud, measured in the cloud's rest frame. In his original work, Fermi calculated the energy gained or lost in head on or following collisions, respectively. He attributed the net gain to head on collisions being more probable than following interactions. However, the version of Gaisser (1990) is followed below.

The probability of an interaction occurring is proportional to the relative velocity between the cloud and the cosmic ray, $(c - V\cos\theta_i)$. Hence, the mean interaction angle

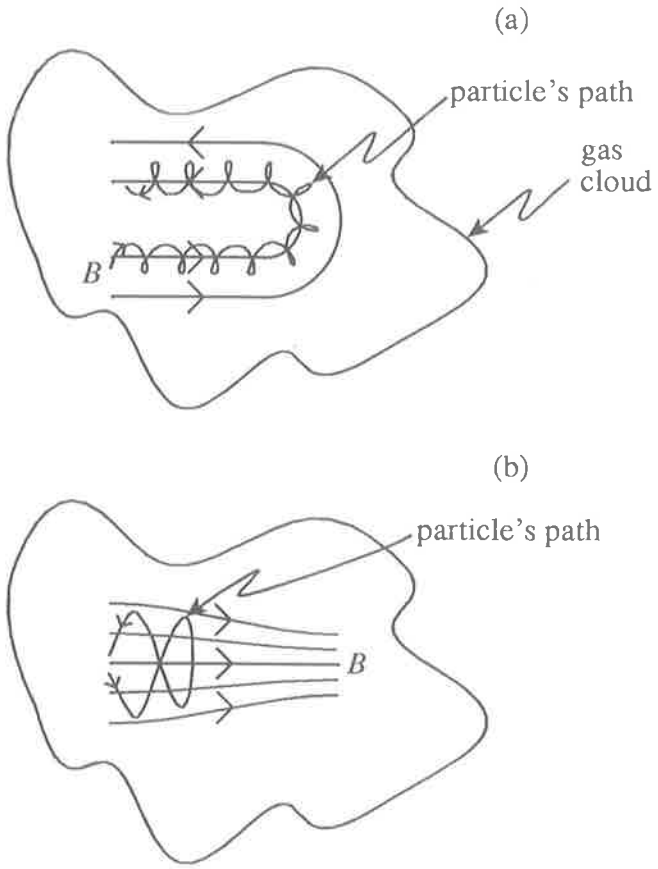

Figure 2.3: The schematic diagram of the magnetic field configurations within the cloud envisaged by Fermi (1949) which could lead to a "collisionless" interaction between the cosmic ray and the cloud.

is

$$\begin{aligned}\langle \cos\theta_i \rangle &= \int_{-1}^{1} \frac{(c - V\cos\theta_i)}{2c} \cos\theta_i d\cos\theta_i \\ &= -\frac{V}{3c}. \end{aligned} \tag{2.6}$$

The average fractional energy gained per collision is

$$\begin{aligned}\xi &= \left\langle \frac{E_{i+1} - E_i}{E_i} \right\rangle \\ &\simeq \gamma^2[1 - \beta\langle\cos\theta_i\rangle + \beta\langle\cos\theta'_{i+1}\rangle - \beta^2\langle\cos\theta_i\rangle\langle\cos\theta'_{i+1}\rangle] - 1 \\ &\simeq \frac{4\beta^2}{3(1-\beta^2)}, \end{aligned} \tag{2.7}$$

where the direction of the cosmic ray in the cloud is assumed to have been isotropised due to multiple scatterings, and so $\langle\cos\theta'_{i+1}\rangle = 0$.

If $T_{\rm cycle}$ is the time scale on which interaction with the clouds occur, and the cosmic ray is injected with energy E_o, then its energy as a function of particle age is,

$$E(t) = E_o(1+\xi)^{t/T_{\rm cycle}}. \tag{2.8}$$

If cosmic rays suffer catastrophic losses on an energy independent time scale T, due to particle escape from the galaxy or spallation for example, then they will have an exponential particle age distribution, $p(t) = T^{-1}\exp[-t/T]$. This can be seen by substituting $b = 0$ and $Q = \delta(t)$ into Equation 2.4 and solving for $\mathcal{N}(t)$. The probability of a cosmic ray having an energy in the range $E \rightarrow E+dE$ is the same as the probability of the cosmic ray having an age in the range $t \rightarrow t + dt$, and hence $p(E)dE = p(t)dt$. Therefore the spectrum of cosmic rays produced is,

$$p(E) = \frac{T_{\rm cycle}}{\ln(1+\xi)T} \frac{E_o^{T_{\rm cycle}/\ln(1+\xi)T}}{E^{1+(T_{\rm cycle}/\ln(1+\xi)T)}}. \tag{2.9}$$

From Equation 2.9 it can be seen that the Fermi mechanism naturally gives rise to a power law particle spectrum with index $-(1+(T_{\rm cycle}/\ln(1+\xi)T))$. This is an example of second order Fermi

acceleration, as the the mean energy gained per interaction is proportional to the square of the cloud's velocity. An example of first order Fermi acceleration is described below.

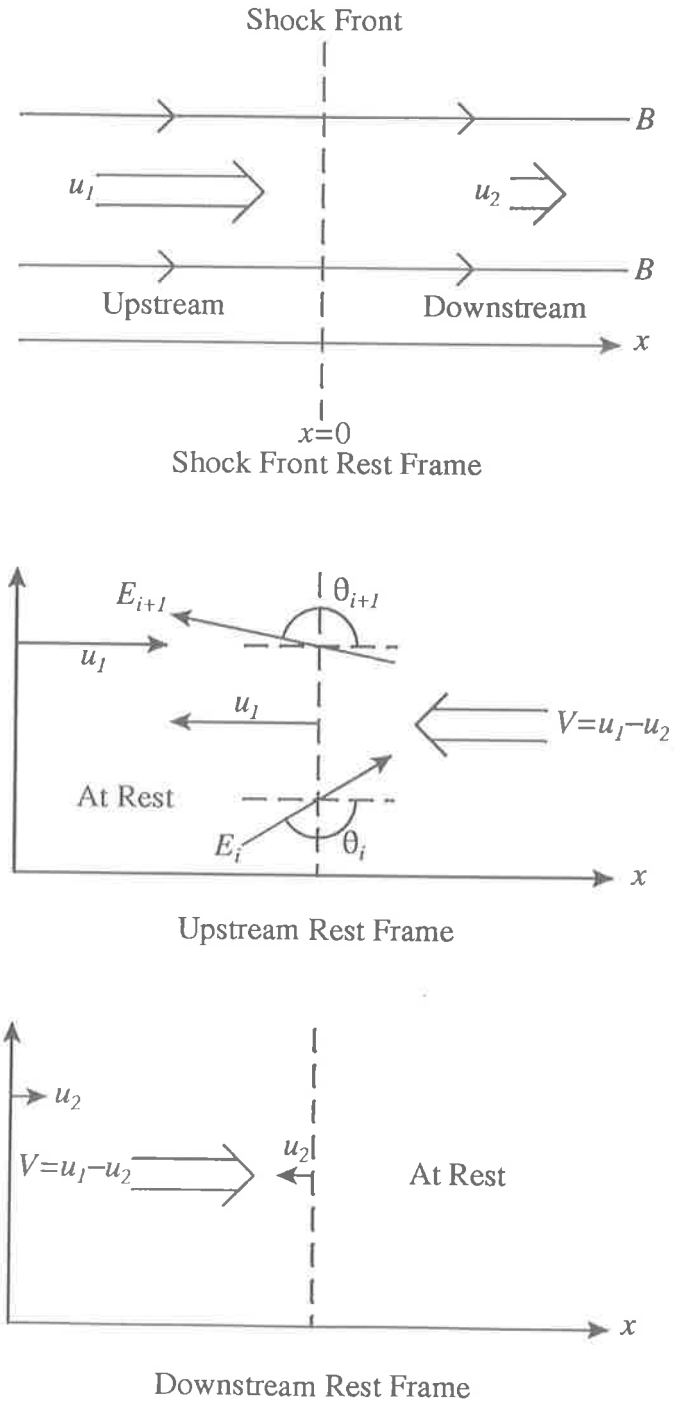

Figure 2.4: A schematic diagram of a shock in a plasma flow viewed from the shock front rest frame, the upstream rest frame and the downstream rest frame. The shock front is situated at $x = 0$ with upstream and downstream flow velocities u_1 and u_2 in the shock rest frame. The upstream and downstream rest frames are analagous to the LAB and cloud rest frames shown in Figure 2.2.

2.3.2 Shock Acceleration at a Parallel Shock Front

Acceleration of the cosmic ray would be much more efficient if the particle experienced an energy gain on each interaction. This is possible in the convergent fluid flows which occur near a shock front. The mechanism of cosmic ray acceleration at a parallel shock front was examined almost simultaneously by Krymsky (1977), Axford, Leer and Skadron (1977), Bell (1978a,b) and Blandford and Ostriker (1978). In the following, the microscopic approach of Bell (1978a) is used to derive the spectrum of cosmic rays produced by shock acceleration, rather than the statistical approach adopted by the other authors.

Consider an plane shock front situated at $x = 0$ in an fluid flow as shown in Figure 2.4. Assume that the magnetic field is perpendicular to the shock front, and let the upstream and downstream flow velocities be u_1 and u_2, respectively. Notice that while the field is perpendicular to the shock, it is parallel to the plasma flows, upstream and downstream, and hence this is referred to as a parallel shock in the literature. Let the cosmic rays have diffusion coefficients D_1 and D_2 in the upstream and downstream regions respectively. The ingredients required to calculate the spectrum of cosmic rays are the probability of escape from the shock and the number of acceleration cycles (upstream→downstream→upstream) required to accelerate from E_o to energy E. Derivation of these quantities is described below.

Cosmic rays upstream of the shock front are all convected back to the shock, whereas particles downstream tend to be convected away from the shock front and so have probability η of escaping to $x = \infty$. The probability of escape is calculated, by comparing the rate at which cosmic rays are convected to $x = \infty$ to the rate at which they are injected into the downstream region. If only convection and diffusion in the downstream region is considered then the transport equation becomes,

$$\frac{d\mathcal{N}}{dt} = \frac{\partial}{\partial x}\left(D_2\frac{\partial \mathcal{N}}{\partial x} - u_2\mathcal{N}\right), \tag{2.10}$$

which has only one physical solution, $\mathcal{N}(E, x, t) =$ constant, for static equilibrium (Bell, 1978a). Hence, the rate at which cosmic rays are convected to $x = \infty$ is $u_2\mathcal{N}(E, 0, t)$, where $\mathcal{N}(E, 0, t)$ is the differential number density of particles at the shock. The rate at which ultra relativistic cosmic rays cross the shock, assuming an isotropic particle

distribution, is

$$\int_0^1 \frac{\cos\theta_i \mathcal{N}(E,0,t)c}{2} d\cos\theta_i = \frac{c\mathcal{N}(E,0,t)}{4}. \tag{2.11}$$

Thus, the probability of escape is, $\eta = 4u_2/c$.

Consider the reference frame in which the fluid upstream from the shock is at rest. In this frame, the downstream fluid is moving towards the left with velocity $u_1 - u_2$, (see Figure 2.4). When viewed in the downstream rest frame the cosmic ray's energy remains constant during scattering. Thus, the energy of the cosmic ray after the $(i+1)^{\text{th}}$ cycle is

$$E_{i+1} = E_i \frac{1+\beta\cos\theta_i}{1+\beta\cos\theta_{i+1}}, \tag{2.12}$$

where $\beta = (u_1 - u_2)/c$ and θ_i and θ_{i+1} are defined as in Figure 2.4 [1]. Hence, if particles are injected with energy E_o, after n cycles they will have energy,

$$E_n = E_o \prod_{i=1}^{n-1} \left(\frac{1+\beta\cos\theta_i}{1+\beta\cos\theta_{i+1}} \right). \tag{2.13}$$

Therefore,

$$\begin{aligned} \ln\left[\frac{E_n}{E_o}\right] &= \sum_{i=1}^{n-1} \ln\left[\frac{1+\beta\cos\theta_i}{1+\beta\cos\theta_{i+1}}\right] \\ &\simeq n \ln\left\langle \frac{1+\beta\cos\theta_i}{1+\beta\cos\theta_{i+1}} \right\rangle, \end{aligned} \tag{2.14}$$

where the average of the fractional energy gained per interaction has been taken. The average value of θ_i is found by assuming an isotropic particle distribution and integrating over the probability that a cosmic ray crosses the shock front with θ_i in the range $\theta_i \rightarrow \theta_i + \Delta\theta_i$. Thus, $\langle\cos\theta_i\rangle = 2/3$ and $\langle\cos\theta_{i+1}\rangle = -2/3$, and so

$$\begin{aligned} \ln\left[\frac{E_n}{E_o}\right] &\simeq n \ln\left[\frac{1+\frac{2}{3}\beta}{1-\frac{2}{3}\beta}\right] \\ &\simeq n\left[\left(\frac{2\beta}{3} + \frac{4\beta^2}{18} + \cdots\right) - \left(-\frac{2\beta}{3} + \frac{4\beta^2}{18} - \cdots\right)\right] \\ &\simeq \frac{4}{3} n \frac{u_1 - u_2}{c}, \end{aligned} \tag{2.15}$$

where a Taylor series expansion for $\ln(1+x)$ has been used and only the two highest order terms have been retained. The mean fractional energy gain per interaction may be calculated by substituting the mean values of θ_i and θ_{i+1} into Equation 2.12, giving

$$\begin{aligned} \xi &= \frac{\beta(\langle\cos\theta_i\rangle - \langle\cos\theta_{i+1}\rangle)}{1+\beta\langle\cos\theta_{i+1}\rangle} \\ &\simeq \frac{4}{3}\beta, \end{aligned} \tag{2.16}$$

[1] note that the angles are not defined in the same way as in Section 2.3.1

for $\beta \ll 1$. Shock acceleration is an example of a first order Fermi mechanism as the mean energy gained per cycle is proportional to velocity of the plasma in the upstream rest frame (c.f. the second order Fermi mechanism described in Section 2.3.1).

The probability of the cosmic ray completing n acceleration cycles is $P_n = (1 - \eta)^n$, where Equation 2.15 can be used to express n as a function of energy. The integral cosmic ray spectrum (the number of particles with energy greater than E_n) is proportional to P_n. Hence, the differential spectrum of cosmic rays produced is

$$\mathcal{N}(E_n, t) \propto \left(\frac{E_n}{E_o}\right)^{-(2u_2+u_1)/(u_1-u_2)}. \tag{2.17}$$

Once again a power law cosmic ray spectrum is a natural consequence of the Fermi mechanism. However, in this case the spectral index is set by the parameters of the shock. For example, for a shock in which the flow velocities are much greater than the speed of sound in the plasma (the Mach number is large) $u_1 = 4u_2$. This is described as a strong shock, and in this case the spectral index is -2.

To calculate the rate at which cosmic rays are accelerated, the time scale for one acceleration cycle, T_{cycle}, is required. Consider first the upstream region. In the steady state, the transport equation becomes

$$\frac{\partial}{\partial E}\left(D_1 \frac{\partial \mathcal{N}}{\partial x} - u_1 \mathcal{N}\right) = 0, \tag{2.18}$$

and hence the number density as a function of x is

$$\mathcal{N}(x) = \mathcal{N}(0) \exp\left[\frac{u_1 x}{D_1}\right] \qquad \text{for } x < 0, \tag{2.19}$$

where $\mathcal{N}(0)$ is the number density at the shock and only the dependence on x is shown explicitly. Thus, the total number of cosmic rays in the upstream region per unit area or shock front is,

$$\int_{-\infty}^{0} \mathcal{N}(0) \exp\left[\frac{u_1 x}{D_1}\right] dx = \frac{D_1 \mathcal{N}(0)}{u_1}. \tag{2.20}$$

From Equation 2.11, it can be seen that the rate per unit area at which cosmic rays cross the shock is $c\mathcal{N}(0)/4$. Hence, the mean residence time in the upstream region is $(D_1\mathcal{N}(0)/u_1)/(c\mathcal{N}(0)/4) = 4D_1/(cu_1)$. An analysis of the downstream region results in a mean residence time with the same form (Drury, 1983), and therefore

$$T_{\text{cycle}} = \frac{4}{c}\left(\frac{D_1}{u_1} + \frac{D_2}{u_2}\right). \tag{2.21}$$

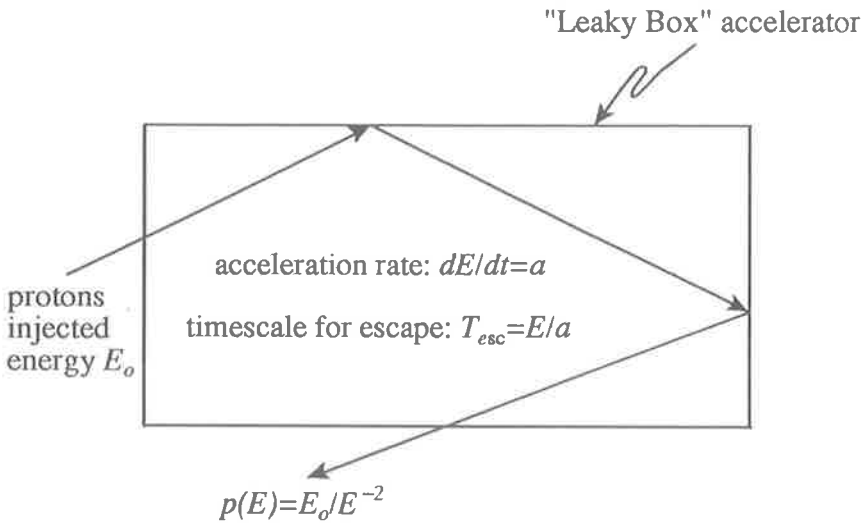

Figure 2.5: A schematic diagram of the simple idealised picture of shock acceleration discussed in the text. Protons are injected into the leaky box with energy E_o. While within the box they accelerate at a constant rate, $dE/dt = a$, with a time scale for escape, $T_{\rm esc} = E/a$. Protons escaping the accelerator have an E^{-2} distribution, typical of shock acceleration at a strong parallel shock.

Hence, the acceleration rate is

$$\begin{aligned} \frac{dE}{dt} &\simeq \frac{\xi E}{T_{\rm cycle}} \\ &\simeq \frac{E(u_1 - u_2)}{3}\left(\frac{D_1}{u_1} + \frac{D_2}{u_2}\right)^{-1}. \end{aligned} \tag{2.22}$$

In the discussion above, a very simple version of shock acceleration is described. For this derivation, it has been assumed that the cosmic rays do not effect the upstream or downstream flows or the shock (the test particle approximation), that the shock is a plane with parallel magnetic fields, and that all of the flow velocities are non–relativistic. In practice, any or all of these assumptions may not be appropriate and effects such as energy loss may also need to be included. Recent comprehensive reviews dealing with these and other issues have been written by Drury (1983), Blandford and Eichler (1987) and Jones and Ellison (1991).

2.3.3 A Simple Idealised Picture of Shock Acceleration

Consider a plane shock which is strong ($u_1 = 4u_2$), and for which $D_1 \simeq D_2 \simeq br_g c/3 = D$, where $b \geq 1$ is the ratio of the cosmic ray's mean free path length to its gyroradius, $r_g \simeq E/(ZeBc)$. The acceleration rate (using Equation 2.22) becomes

$$\begin{aligned} \frac{dE}{dt} &\simeq \frac{Eu_1^2}{20D} \\ &\simeq \frac{3}{20}\frac{ZeBcu_1^2}{b}, \end{aligned} \tag{2.23}$$

where Ze is the charge of the cosmic ray and B is the magnetic field at the shock. As the diffusion coefficient is proportional to the cosmic ray's energy, dE/dt is independent of energy and shock acceleration occurs at a constant rate, $dE/dt = a$. Hence, one could imagine the accelerator as being a region in which particles gain energy at a constant rate. If one also assumes that there is no additional diffusion or convection, and that there are no loss processes aside from escape from the acceleration region, then the accelerator may be visualised as a leaky box (see Figure 2.5). If there is a source $Q(E) = \mathcal{N}_o\delta(E - E_o)$ injecting cosmic rays with energy E_o at a rate of $\mathcal{N}_o$ particles s^{-1}, then the transport equation becomes

$$\frac{\partial \mathcal{N}}{\partial t} = -\frac{\partial}{\partial E}[a\mathcal{N}] - \frac{\mathcal{N}}{T_{\rm esc}} + \mathcal{N}_o\delta(E - E_o), \tag{2.24}$$

where $T_{\rm esc}$ is the time scale for escape. Clearly, for equilibrium, particles must be lost at the same rate as they are produced and so

$$T_{\rm acc} = T_{\rm esc} = \frac{E}{\frac{dE}{dt}} = \frac{E}{a}, \tag{2.25}$$

where $T_{\rm acc} = T_{\rm cycle}/\xi$ is the acceleration time scale. For static equilibrium $d\mathcal{N}/dt = 0$, and hence Equation 2.24 gives the spectrum of cosmic rays in the accelerator as

$$\mathcal{N}(E) = \frac{\mathcal{N}_o E_o}{E}. \tag{2.26}$$

Therefore, the probability that a cosmic ray reaches energy E is $P(E) = \mathcal{N}(E)/\mathcal{N}_o = E_o/E$. However, all particles eventually escape and so the integral spectrum of escaping cosmic rays is $\mathcal{N}_{\rm esc}(> E) = \mathcal{N}(E) = \mathcal{N}_o E_o/E$. The differential spectrum of cosmic rays escaping the accelerator is

$$\frac{d\mathcal{N}_{\rm esc}}{dE} = \frac{\mathcal{N}_o E_o}{E^2}, \tag{2.27}$$

or alternatively cosmic rays leave the accelerator with an energy distribution $p(E) = E_o E^{-2}$.

This simple picture of shock acceleration will be used in Chapter 6 to model particle acceleration in active galactic nuclei.

Chapter 3

The Description of High Energy Processes

3.1 Introduction

In this chapter a brief description of high energy processes is given. The discussion is purposefully kept as general as possible so that formulae and results can easily be applied to a variety of interactions and decays. Specific examples of high energy interactions and decays relevant to particle acceleration in active galactic nuclei will be discussed in Chapter 4. It is intended that this Chapter should be used as a reference for the discussion in Chapter 4.

When modelling interactions and decays it is often advantageous to work in either the centre of momentum frame of the particles or the rest frame of a particle. In Section 3.2, each of these frames are defined and the boost required from the laboratory frame is derived.

Two body decays are examined in detail. The spectrum of particles which result from the decay of a given spectrum of primaries is derived. Two body decays are very similar to exclusive interactions which produce two particles, and these similarities are highlighted. Multi–particle decays and exclusive interactions are discussed qualitatively.

For interactions in which the final state is too complicated to describe exclusively, an inclusive description is often used. In this case, only the details of one type of produced particle are measured, and so the final state of the interaction is *not* exclusively defined.

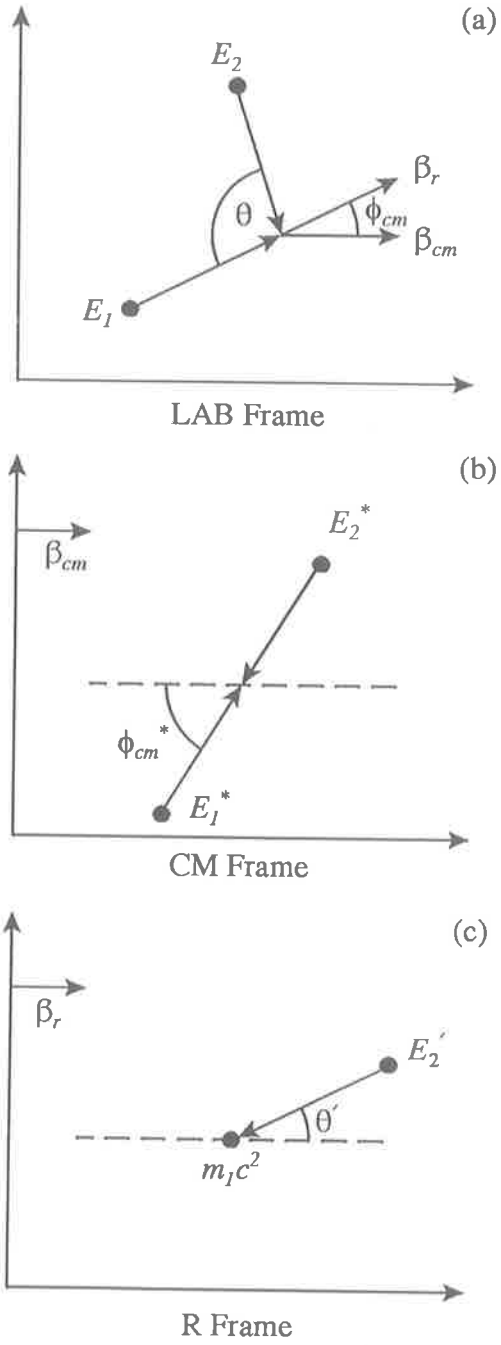

Figure 3.1: A schematic diagram of an interaction when viewed from (a) the laboratory (LAB) frame, (b) the centre of momentum (CM) frame, and (c) the rest (R) frame of particle 1. The boost required to get from the LAB frame to the CM frame (β_{cm}), and the R frame (β_r), are also shown. Starred ($\star$) quantities are measured in the CM frame, and primed ($'$) quantities are measured in the R frame.

The concept of scaling is particularly useful when modelling interactions inclusively. It enables the inclusive distributions of products to be reconstructed at any energy where scaling is valid, without requiring data for all energies. Some of the variables commonly used when describing inclusive interactions are also reviewed.

The chapter is concluded by a derivation of the mean path length for interaction when a particle traverses a relativistic gas.

3.2 Some Useful Reference Frames

The position of an event in space–time may be described by a 4–vector $r_\mu = (ct, \vec{r})$, (see e.g. Bowler 1986). The quantity $g_{\mu\nu} r_\mu r_\nu = c^2t^2 - \vec{r}\cdot\vec{r}$ is an invariant, and any quantities which transform in the same manner as $\vec{r}$ and t also have an analogous invariant quantity. Here, $g_{\mu\nu}$ is a metric tensor defined such that $g_{00} = 1$, $g_{11} = g_{22} = g_{33} = -1$, and $g_{\mu\nu} = 0$ for $\mu \neq \nu$.

Consider a particle with energy E and momentum $\vec{p} = (p_x, p_y, p_z)$. The momentum and energy transformations from the laboratory (LAB) frame to a primed frame moving with velocity βc along the x axis are (see e.g. French 1968),

$$\begin{aligned} p'_x &= \gamma(p_x - \beta E/c) \\ p'_y &= p_y \\ p'_z &= p_z \\ E'/c &= \gamma(E/c - \beta p_x), \end{aligned} \tag{3.1}$$

where $\gamma = (1-\beta^2)^{-1/2}$ is the Lorentz gamma. The quantities $\vec{p}$ and E/c transform like $\vec{r}$ and ct, and the 4-momentum of the particle can be defined as $p_\mu = (E/c, \vec{p})$. In this case, the invariant $g_{\mu\nu} p_\mu p_\nu = E^2/c^2 - \vec{p}\cdot\vec{p} = m^2$ may be interpreted as a statement of the invariance of the rest mass of the particle, m. Similarly, the total energy and momentum of a system of particles also transform like $\vec{r}$ and ct. The invariant in this case, when multiplied by a factor of c^2, is the square of the total centre of momentum (CM) frame energy, $s = c^2(E_{\rm tot}^2/c^2 - |\vec{p}_{\rm tot}|^2)$. This invariant is used extensively to relate quantities in different reference frames when modelling interactions and decays. Hence, s in terms of quantities measured in the LAB frame, the CM frame and the rest frame of a particle are derived below.

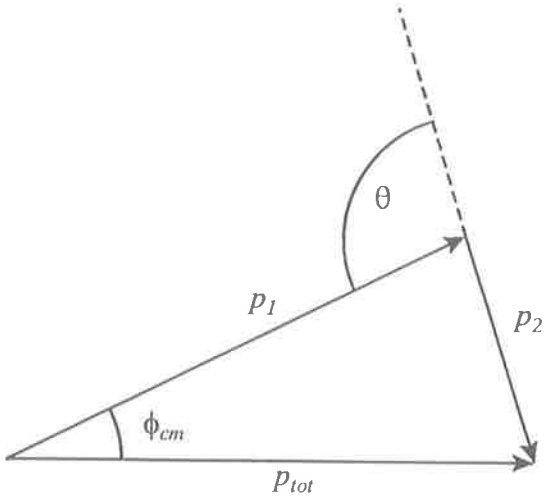

Figure 3.2: A schematic diagram illustrating the quantities used to derive the boost required to go from the LAB frame to the CM frame.

Consider two particles of energy E_1 and E_2 and rest mass m_1 and m_2 which interact in the LAB frame, as shown in Figure 3.1. The square of the total CM energy in terms of quantities measured in the LAB frame is

$$s = m_1^2c^4 + m_2^2c^4 + 2(E_1E_2 - c^2|\vec{p}_1||\vec{p}_2|\cos\theta), \tag{3.2}$$

where $\vec{p}_1$ and $\vec{p}_2$ are the momenta of particles 1 and 2, and θ is the angle between $\vec{p}_1$ and $\vec{p}_2$ as shown in Figure 3.1.

The CM frame is the reference frame in which the total momentum of the particles which interact or decay is zero. It is obtained from the LAB frame by applying a boost β_{cm} at an angle ϕ_{cm} relative to the momentum of particle 1, as shown in Figure 3.1. The boost expressed in terms of the total energy of the interacting particles, $E_{tot} = \gamma_{cm}\sqrt{s} = \sqrt{|\vec{p}_{tot}|^2 + s}$, is

$$\begin{aligned} \beta_{cm} &= \sqrt{1 - \frac{1}{\gamma_{cm}^2}} \\ &= \frac{c|\vec{p}_{tot}|}{E_{tot}}. \end{aligned} \tag{3.3}$$

The magnitude of the total momentum of the interaction in the LAB frame $|\vec{p}_{tot}|$ is given by (see Figure 3.2)

$$|\vec{p}_{tot}|^2 = |\vec{p}_1|^2 + |\vec{p}_2|^2 + 2|\vec{p}_1||\vec{p}_2|\cos\theta. \tag{3.4}$$

The angle ϕ_{cm} can also be found by using Figure 3.2, and is given by

$$\sin\phi_{cm} = \frac{|\vec{p}_2|\sin\theta}{(|\vec{p}_1|^2 + |\vec{p}_2|^2 + 2|\vec{p}_1||\vec{p}_2|\cos\theta)^{1/2}}. \tag{3.5}$$

The momentum and energy of particle 1 in the CM frame are given by [1]

$$|\vec{p}_1^{\star}|\cos\phi_{cm}^{\star} = \gamma_{cm}(|\vec{p}_1|\cos\phi_{cm} - \beta_{cm}E_1/c) \tag{3.6}$$

$$E_1^{\star} = \gamma_{cm}(E_1 - \beta_{cm}c|\vec{p}_1|\cos\phi_{cm}), \tag{3.7}$$

where $\gamma_{cm} = (1-\beta_{cm}^2)^{-1/2}$ is the Lorentz γ, and the angle $\phi_{cm}^{\star}$ is given by the aberration formula (see e.g. Rindler 1969),

$$\sin\phi_{cm}^{\star} = \frac{\sin\phi_{cm}}{\gamma_{cm}(1 - \beta_{cm}\cos\phi_{cm})}. \tag{3.8}$$

[1] Throughout this thesis starred ($\star$) quantities are measured in the centre of momentum frame and primed ($\prime$) quantities are measured in the rest frame of a particle, unless indicated otherwise.

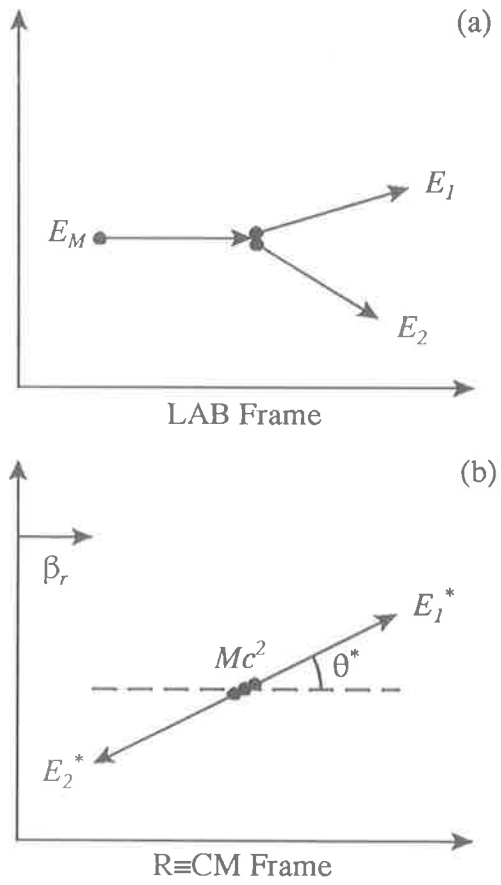

Figure 3.3: A schematic diagram of the decay of a particle with energy E_M and rest mass M, viewed from (a) the LAB frame, and (b) the R frame of M. In this case the R frame is equivalent to the CM frame.

In the centre of momentum frame, the total momentum of the system is zero by definition, and hence the square of the total CM frame energy is simply

$$s = (E_1^\star + E_2^\star)^2. \tag{3.9}$$

The CM frame will be used in Chapter 4 to model pion photoproduction and proton–proton interactions.

The rest frame of a particle is often used, particularly when considering particle decay. The rest frame of particle 1 is obtained from the LAB frame by applying a boost $\beta_r = c|\vec{p}_1|/E_1$ in the same direction as $\vec{p}_1$, as shown in Figure 3.1. The square of the total CM frame energy in terms of quantities measured in the R frame is

$$s = m_1^2c^4 + m_2^2c^4 + 2m_1c^2E_2', \tag{3.10}$$

where $E_2' = \gamma_r(E_2 - \beta_r|\vec{p}_2|c\cos\theta)$. In Chapter 4, the R frame will be used when modelling ordinary pair production, and the decay of pions and muons.

3.3 Two and Three Body Decays

Consider a particle of rest mass M and energy E_M which decays into two particles with rest masses m_1 and m_2 respectively, as shown in Figure 3.3. In the R frame of the primary particle, which is equivalent to the CM frame in this case, the energies of secondary particles are uniquely defined by the total CM frame energy $\sqrt{s} = Mc^2$. The CM frame energy of particle 2 can be expressed in terms of $E_1^\star$ using conservation of momentum, $|\vec{p}_2^\star| = |\vec{p}_1^\star| = \sqrt{E_1^{\star 2} - m_1^2c^4}$, and is given by

$$E_2^{\star 2} = m_2^2c^4 + E_1^{\star 2} - m_1^2c^4. \tag{3.11}$$

Substitution into Equation 3.9 and using $s = M^2c^4$ gives (see e.g. Stecker 1971),

$$E_1^\star = \frac{M^2c^4 - m_2^2c^4 + m_1^2c^4}{2Mc^2}, \tag{3.12}$$

with a similar equation for the energy of particle 2 given by interchanging indices.

By transforming the CM frame energy of particle 1 to the LAB frame, it can be seen that E_1 is only a function of $\cos\theta^\star$ as $E_1^\star$ is a constant for a given Mc^2,

$$E_1 = \gamma_r(E_1^\star + \beta_r c|\vec{p}_1^\star|\cos\theta^\star), \tag{3.13}$$

and hence

$$dE_1 = \gamma_r \beta_r c|\vec{p}_1^{\star}| d\cos\theta^{\star},$$

where $\gamma_r = E_M/Mc^2$. Hence, the probability of finding a particle with energy in the range $E_1 \rightarrow E_1 + dE_1$ in the LAB frame, $p(E_1)dE_1$, is equal to the probability of finding a particle in the interval $\cos\theta^{\star} \rightarrow \cos\theta^{\star} + d\cos\theta^{\star}$ in the CM frame, $p(\cos\theta^{\star})d\cos\theta^{\star}$. Thus,

$$\begin{aligned} p(E_1, E_M)dE_1 &= p(\cos\theta^{\star})d\cos\theta^{\star} \\ &= p(\cos\theta^{\star})\frac{d\cos\theta^{\star}}{dE_1}dE_1 \\ &= \frac{p(\cos\theta^{\star})}{\gamma_r\beta_r c|\vec{p}_1^{\star}|}dE_1. \end{aligned} \tag{3.14}$$

for $\gamma_r(E_1^{\star} - \beta_r c|\vec{p}_1^{\star}|) \leq E_1 \leq \gamma_r(E_1^{\star} + \beta_r c|\vec{p}_1^{\star}|)$, where the energy bounds correspond to $\cos\theta^{\star} = -1$ and $\cos\theta^{\star} = 1$. Hence, if the angular distribution of particle 1 in the CM frame is known, then the corresponding energy distribution in the LAB frame can be calculated. For example, if particle 1 is emitted isotropically in the CM frame then $p(\cos\theta^{\star}) = 1/2$, and

$$p(E_1, E_M) = \frac{1}{2\gamma_r\beta_r c|\vec{p}_1^{\star}|}. \tag{3.15}$$

This distribution is appropriate for the decay of particles such as pions which have no spin. Notice that $p(E_1)$ is independent of E_1 and therefore secondaries with energy bounded by $\gamma_r(E_1^{\star} \pm \beta_r c|\vec{p}_1^{\star}|)$ are produced with equal probability.

Consider the decay of primary particles which have a spectrum $\mathcal{Q}_M(E_M)$. The spectrum of secondary particles produced can be calculated by considering primaries with energy in the range $E_M \rightarrow E_M + dE_M$. The number of secondaries produced with energy in the range $E_1 \rightarrow E_1 + dE_1$ by primaries in this energy range is $p(E_1)dE_1\mathcal{Q}_M(E_M)dE_M$. Thus, the total spectrum is given by

$$\mathcal{Q}_1(E_1) = \int_{E_M^{min}}^{E_M^{max}} p(E_1, E_M)\mathcal{Q}_M(E_M)dE_M \tag{3.16}$$

where E_M^{min} and E_M^{max} are found as follows. Consider a secondary particle with energy E_1. The lowest energy primary which could have produced this secondary must satisfy the equation, $E_1 = \gamma_r(E_M)(E_1^{\star} + \beta_r(E_M)c|\vec{p}_1^{\star}|)$. Therefore, E_M^{min} is given by solving the equation

$$\begin{aligned} E_1 &= \gamma_r(E_M^{min})(E_1^{\star} + \beta_r(E_M^{min})c|\vec{p}_1^{\star}|) \\ &= \gamma_r(E_M^{min})E_1^{\star} + c|\vec{p}_1^{\star}|\sqrt{\gamma_r^2(E_M^{min}) - 1}. \end{aligned} \tag{3.17}$$

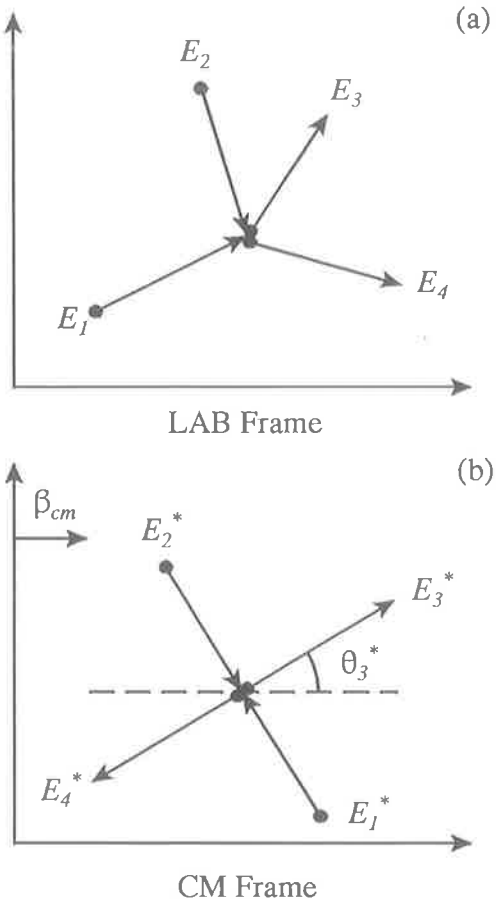

Figure 3.4: A schematic diagram of an interaction between particles with energies E_1 and E_2, producing particles with energies E_3 and E_4, viewed from (a) the LAB frame, and (b) the CM frame.

Squaring Equation 3.17 and rearranging gives a quadratic in $\gamma_r(E_M^{min})$,

$$\gamma_r^2(E_M^{min})m_1^2c^4 - 2E_1E_1^\star\gamma_r(E_M^{min}) + E_1^2 + E_1^{\star 2} - m_1^2c^4 = 0. \tag{3.18}$$

The same equation results when considering the maximum energy, and has solutions

$$\frac{\overset{max}{E_M^{min}}}{Mc^2} = \frac{-E_1E_1^\star \pm \sqrt{E_1^2E_1^{\star 2} - m_1^2c^4(E_1^2 + E_1^{\star 2} - m_1^2c^4)}}{m_1^2c^4}. \tag{3.19}$$

For example, in the case where secondary 1 is massless (e.g. a photon), the minimum bound is given by solving Equation 3.18 with $m_1c^2 = 0$, giving

$$\frac{E_M^{min}}{Mc^2} = \frac{E_1^2 + E_1^{\star 2}}{2E_1E_1^\star}. \tag{3.20}$$

As the energy of the primary becomes large the minimum energy of the secondary tends to zero, and hence $E_M^{max} = \infty$. The above description of two body decay will be used in Chapter 4 to model charged and neutral pion decay.

For three body decays the situation is some what more complicated. In general the energies of the secondary particles are no longer uniquely defined in the CM frame by the rest mass of the primary particle. However, if the distribution of the secondary particles in the CM frame is known, then it is possible to Lorentz transform the distribution to the LAB frame. For a description of how this can be done for the decay of muons see Gaisser (1990).

3.4 The Exclusive Description of Interactions

Consider an interaction between particles 1 and 2 which produces particles 3 and 4, as shown in Figure 3.4. The energies of the secondary particles are uniquely defined in terms of the total energy available for the interaction, $\sqrt{s}$. Hence, the final state of the interaction may be defined exclusively in terms of the distribution of the particles directions in the CM frame. Clearly, the situation is directly analogous to two body decays described above. The distribution of particle directions in the CM frame can be defined in terms of differential cross section for the interaction $d\sigma/d\Omega_3^\star$,

$$p(\Omega_3^\star, s) = \frac{1}{\sigma_{12}(s)}\frac{d\sigma}{d\Omega_3^\star}(\Omega_3^\star, s), \tag{3.21}$$

where $\sigma_{12}(s)$ is the total cross section for the interaction given by integrating the differential cross section over solid angle $\Omega_3^\star$,

$$\sigma_{12}(s) = \int \frac{d\sigma}{d\Omega_3^\star}(\Omega_3^\star, s) d\Omega_3^\star. \tag{3.22}$$

Here $p(\Omega_3^\star)d\Omega_3^\star$ is the probability of particle 3 having a direction in the solid angle $\Omega_3^\star \rightarrow \Omega_3^\star + d\Omega_3^\star$. The energy of the produced particles in the CM frame is given by Equation 3.12 substituting $\sqrt{s}$ for Mc^2.

For example, if the interaction is cylindrically symmetric (e.g. the differential cross section may be symmetric about a beam direction), then $d\Omega_3^\star = d\phi_3^\star d\cos\theta_3^\star = 2\pi d\cos\theta_3^\star$. Hence, the total cross section becomes

$$\sigma_{12}(s) = 2\pi \int \frac{d\sigma}{d\Omega_3^\star}(\Omega_3^\star, s) d\cos\theta_3^\star, \tag{3.23}$$

and the particle distribution,

$$\begin{aligned} p(\theta_3^\star, s) &= \frac{2\pi}{\sigma_{12}(s)} \frac{d\sigma}{d\Omega_3^\star}(\Omega_3^\star, s) \\ &= \frac{1}{\sigma_{12}(s)} \frac{d\sigma}{d\cos\theta_3^\star}(\cos\theta_3^\star, s), \end{aligned} \tag{3.24}$$

is a function of $\cos\theta_3^\star$ and s only. By analogy with two body decay the distribution in energy of particle 3 in the LAB frame is given by,

$$p(E_3) = \frac{1}{\gamma_{cm}\beta_{cm}c|\vec{p}_3^\star|} \frac{2\pi}{\sigma_{12}(s)} \frac{d\sigma}{d\Omega_3^\star}(\Omega_3^\star, s) \tag{3.25}$$

with $E_3^{min}{}^{max} = \gamma_{cm}(E_3^\star \pm \beta_{cm}c|\vec{p}_3^\star|)$. Pion photoproduction interactions are cylindrically symmetric and the example above will be used in Chapter 4 to model pion photoproduction near threshold.

It is possible to exclusively define the final state of an interaction with more than two particles. However, in practice it is often infeasible because the interaction becomes too complicated. Hence, other approaches are often used unless simplifying approximations can be made. For example, consider the interaction $1 + 2 \rightarrow 1 + 3 + 4$, where particle 1 experiences negligible recoil in its rest frame. In this case, the interaction has been effectively reduced to the two body decay $2 \rightarrow 3 + 4$. For a practical example of such an interaction see Chapter 4, where this approach is used to model ordinary pair production interactions.

3.5 The Inclusive Description of Interactions

If the final state of an interactions has more than three particles, it is often not feasible to exclusively define the interaction. However, useful information about the interaction may still be derived by adopting an inclusive description of the interaction, where only the momenta of one or more types of particles are measured. For example, consider an interaction between a beam of particles of type 1 and a target of particles of type 2 producing particles of type 3, which are measured by a detector. The reaction is signified by $1 + 2 \rightarrow 3 + X$, where X represents everything else which is produced. The distribution of particles of type 3 can be defined in terms of an inclusive differential cross section, $d\sigma/d\vec{p}_3$, in a manner directly analogous to exclusive interactions. However, because $d\sigma/d\vec{p}_3$ is defined so that only the details of particles of type 3 are measured, there is a summation over multiparticle final states. Hence, integrating over the inclusive differential cross section gives

$$\int \frac{d\sigma}{d\vec{p}_3}(\vec{p}_3, s)d\vec{p}_3 = \langle n_3(s)\rangle \sigma_{12}(s), \tag{3.26}$$

where $\langle n_3(s)\rangle$ is the mean number of particles of type 3 produced in the interaction, and $\sigma_{12}(s)$ is the total cross section for the interaction.

To make use of the inclusive description of an interaction, the inclusive differential cross section is required at all energies of interest. Fortunately it is not necessary to have data at all energies because of the concept of scaling. Scaling was developed as an approximate means of describing the accelerator data. In one form of scaling attributed to Feynman (1969), the invariant cross section $E_3 d\sigma/d\vec{p}_3 = E_3^\star d\sigma/d\vec{p}_3^\star$ becomes dependent only on the transverse component of momentum $p_\perp = p_\perp^\star$, and the Feynman x variable $x = p_l^\star/p_{max}^\star \simeq 2p_l^\star/\sqrt{s}$ at high energies, i.e.

$$E_3\frac{d\sigma}{d\vec{p}_3}(p_l^\star, p_\perp^2, s) \overset{s\rightarrow\infty}{\rightarrow} E_3\frac{d\sigma}{d\vec{p}_3}(x, p_\perp^2), \tag{3.27}$$

where $p_l^\star$ is the longitudinal component of momentum measured in the CM frame. Feynman scaling means that, at sufficiently high energies, the shape of invariant cross section does not change. Hence, for energies where scaling is valid, the invariant cross section is only needed at one energy to be able to generate the inclusive differential cross section at all energies. Clearly, scaling will not be a good approximation to the low energy data. It is also thought that at very high energies, scaling will not be valid because of jet events.

Another variable which is used to present data is the LAB frame rapidity y of the particle defined as,

$$y = \frac{1}{2} \ln \left[\frac{E + p_l}{E - p_l} \right] \tag{3.28}$$

where E and p_l are the LAB frame values of the particles energy and longitudinal component of momentum respectively. When the invariant cross section is expressed in terms of y, it may be roughly be divided into three regions. At low values of y, particles are are associated with the target particle and so this is called the target fragmentation region. Similarly, at high values of y produced particles are in the beam fragmentation region. In between these extremes is the central or plateau region. When scaling energies have been achieved, the effect of increasing the total energy of the interaction is to lengthen the central region so that it forms a "plateau" between the beam and target fragmentation regions. The shape of the distribution in the beam and target fragmentation regions stays constant with $\sqrt{s}$. Similarly, beam and target fragmentations regions as well as a central region can also be defined when the invariant cross section is expessed in terms of the Feynman x variable.

In Chapter 4, pion photoproduction interactions which occur at energies above the resonance region are modelled inclusively. For reviews of inclusive interactions see Frazer *et al.* (1972), Gaisser (1974), and Bøggild and Ferbel (1974), and more recently Collins and Martin (1984) and Halzen (1990). A recent discussion of particle physics and accelerator data relevant to cosmic ray physics may be found in Gaisser (1990).

3.6 Mean Free Path Length

A derivation of the mean path length for interaction in a relativistic gas following Gould (1971) is given below. Consider a particle (of type 1) which is traversing a gas made up of particles of type 2. The mean path length for interaction is found by comparing the rate at which interactions occur in the LAB frame with the particle's velocity ($v \simeq c$ for relativistic particles). In the rest frame of particle 1 the interaction rate is

$$\frac{dN'}{dt'} = c \int \sigma_{12} dn_2', \tag{3.29}$$

where σ_{12} is the total cross for the interaction, and n_2' is the number density of the gas in the rest frame of particle 1. The number density of gas particle 1 sees in the

LAB frame can be found by using the invariant cdn_2/E_2 (see e.g. Blumenthal and Gould 1970), giving $dn_2' = E_2' dn_2/E_2$). Using the time dilation formula $t = \gamma_r t'$, the interaction rate in the LAB frame is

$$\begin{aligned}
\frac{dN}{dt} &= \gamma_r{}^{-1} c \int \sigma dn_2' \\
&= \gamma_r{}^{-1} c \int \sigma \frac{E_2'}{E_2} dn_2 \\
&= \gamma_r{}^{-1} c \int \sigma \frac{\gamma_r (E_2 - |\vec{p}_2| c\beta_r \cos\theta)}{E_2} dn_2,
\end{aligned} \tag{3.30}$$

where $E_2' = \gamma_r(E_2 - |\vec{p}_2|c\beta_r \cos\theta)$ is the energy of particle 2 in the rest frame of particle 1. In general the number density will be a function of both particle energy and direction, $dn_2 = n(E_2, \Omega) dE_2 d\Omega$. However, if the gas is isotropic then $d\Omega = d\phi d\cos\theta = 2\pi d\cos\theta$ and the number density becomes

$$\begin{aligned}
dn_2 &= n(E_2) dE_2 p(\Omega) d\Omega \\
&= n(E_2) dE_2 p(\cos\theta) d\cos\theta \\
&= n(E_2) dE_2 \frac{d\cos\theta}{2},
\end{aligned} \tag{3.31}$$

where $n(E_2)dE_2$ is the number of particles with energy in the range $E_2 \rightarrow E_2 + dE_2$, and $p(\cos\theta)d\cos\theta$ is the probability of of a particle having a direction in the range $\cos\theta \rightarrow \cos\theta + d\cos\theta$. In this case, the mean path length for interaction $\overline{\lambda}$ is given by

$$\begin{aligned}
\overline{\lambda}^{-1}(E_1) &= \frac{1}{c}\frac{dN}{dt} \\
&= \int n(E_2) \int \frac{\sigma}{2} \frac{(E_2 - |\vec{p}_2| c\beta_r \cos\theta)}{E_2} d\cos\theta dE_2.
\end{aligned} \tag{3.32}$$

For example, if particle 1 is traversing a uniform soft photon field then the mean path length for interaction is given by

$$\overline{\lambda}^{-1}(E_1) = \int n(\varepsilon) \int \frac{\sigma(s)(1 - \beta_r \cos\theta)}{2} d\cos\theta d\varepsilon, \tag{3.33}$$

where $\sigma(s)$ is the total cross section, $E_2 = |\vec{p}_2|c = \varepsilon$ is the photon energy, and s given by equation 3.2,

$$s = m_1^2 c^4 + 2\varepsilon(E_1 - c|\vec{p}_1|\cos\theta). \tag{3.34}$$

The mean path length can be expressed as an integral over s by rearranging equation 3.34 (see e.g. Gould and Schréder 1967, and Protheroe 1986),

$$\cos\theta = \frac{E_1}{|\vec{p}_1|c} - \frac{s - m_1^2 c^4}{2\varepsilon|\vec{p}_1|c}, \tag{3.35}$$

and hence

$$d\cos\theta = \frac{-ds}{2\varepsilon|\vec{p}_1|c}. \tag{3.36}$$

Using $\beta_r = |\vec{p}_1|c/E_1$ Equation 3.33 becomes,

$$\begin{aligned} \overline{\lambda}^{-1}(E_1) &= \int n(\varepsilon) \int \frac{\sigma(s)}{2} \frac{(s - m_1^2c^4)}{2\varepsilon E_1} \frac{(-ds)}{2\varepsilon|\vec{p}_1|c} d\varepsilon \\ &= -\int \frac{n(\varepsilon)}{8\varepsilon^2 E_1|\vec{p}_1|c} \int \sigma(s)(s - m_1^2c^4) ds d\varepsilon. \end{aligned} \tag{3.37}$$

The advantage of expressing the mean path length in this way is that the integration over s only depends on E_1 and ε through the integration bounds and so need only be calculated once. The mean path length for protons traversing both black body and power law radiation fields is calculated in Chapter 4.

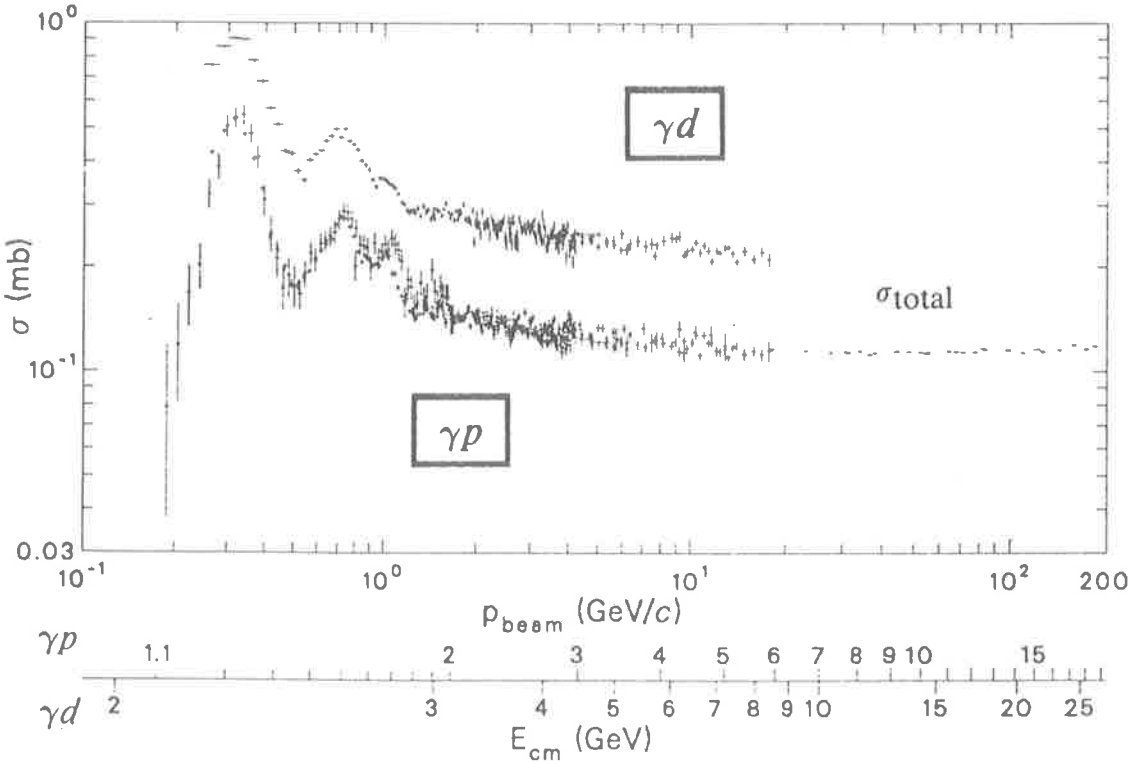

Figure 4.1: The total cross section for pion photoproduction (lower data points, marked γp). Also shown is the total cross section for photoproduction on deuterons. Threshold for pion photoproduction is $E_{CM} \simeq 1.08$ GeV. From Particle Data Group (1988).

Chapter 4

Modelling High Energy Interactions and Decays

4.1 Introduction

The generalisations of Chapter 3 are now used to describe how a number of high energy interactions and decays may be modelled.

The production of pions when a photon interacts with a proton, is called pion photoproduction. I have calculate the mean path length of protons for pion photoproduction in both power law and black body photon fields. The spectrum of photons which interact with the proton has been calculated, and the method of sampling the photon's initial energy and direction is also discussed. At low energies, the exclusive data of Genzel, Joos and Pfeil (1973) has been used to model the interaction. The sampling of the pion's energy and direction in the CM frame, and the subsequent transformation to the LAB frame are discussed in detail. At higher energies, the inclusive data of Moffeit *et al.* (1972) and Feynman scaling have been used to model the interaction. As a test of the modelling algorithm, I have calculated the mean inelasticity for pion photoproduction using a Monte Carlo simulation, and compare this to the mean inelasticity calculated by Stecker (1968) and Begelman, Rudak and Sikora (1990).

Pair production in the field of a proton is modelled assuming that the proton does not experience any recoil in its rest frame. I have used the cross sections given in a review of pair production by Motz, Olsen and Koch (1969). Once again, the mean path length for interaction in both a power law and a blackbody photon field has been

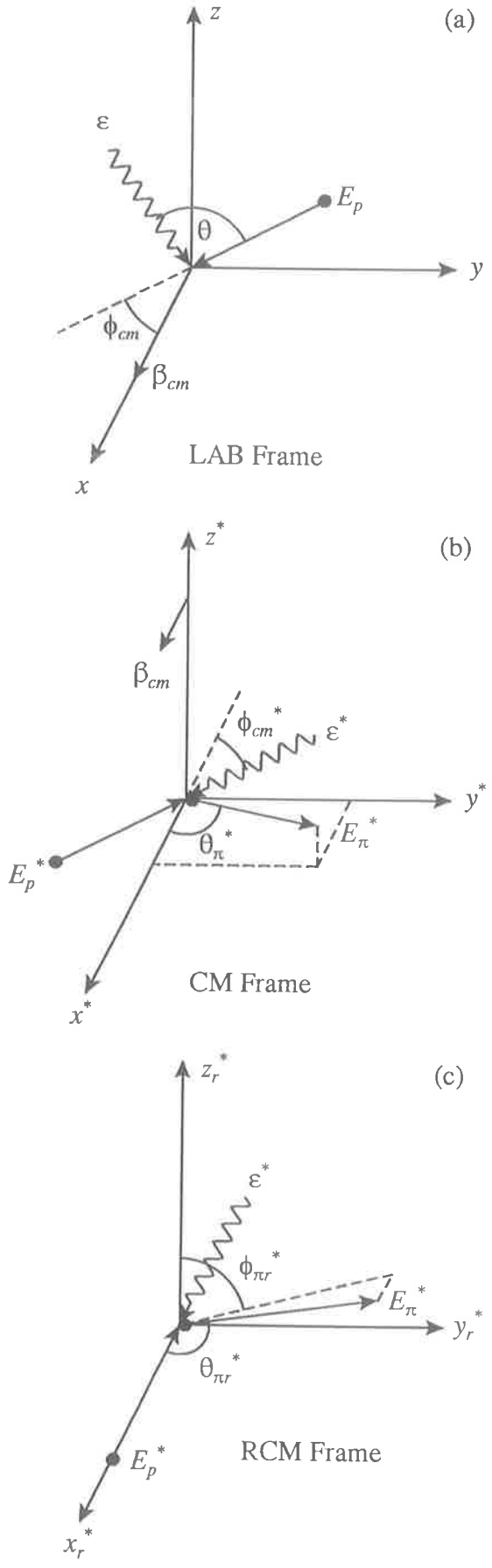

Figure 4.2: A schematic diagram of a pion photoproduction interaction, when viewed from (a) the laboratory (LAB) frame, (b) the centre of momentum (CM) frame, and (c) the rotated centre of momentum (RCM) frame.

calculated. Sampling of the initial and final states of the interaction are discussed in detail. The mean inelasticity for the interaction has been calculated and compared to the numerical calculation of Chodorowski and Zdziarski (1990).

The modelling of proton–proton interactions is discussed using the particle distributions derived by Hillas (1979). Neutral and charged pion decays are also discussed. In each case, I calculate the spectrum of particles produced when a power law spectrum of pions decay. Finally, a description of muon decay is given using the approximation that the muon is unpolarised.

4.2 Pion Photoproduction

The total cross section for pion photoproduction, $\sigma^{\pi}_{\gamma p}(s)$, is shown in Figure 4.1. At low energies ($\sqrt{s} < 2$ GeV) the cross section is characterised by a resonance region due to the channels $p\gamma \rightarrow \Delta^+ \rightarrow p\pi^o$ and $p\gamma \rightarrow \Delta^+ \rightarrow n\pi^+$. At higher energies ($\sqrt{s} >$ a few GeV) the cross section becomes approximately constant with a value of $\sigma^{\pi}_{\gamma p}(s) \simeq 116\ \mu\text{b} = 1.16 \times 10^{-32}\ \text{m}^2$. It has recently been suggested that at high energies ($\sqrt{s} > 100$ GeV) the total cross section rises due to the dominance of jet events (Drees and Halzen, 1988). However, for the astrophysical applications discussed in this thesis most of the pion photoproduction events occur near threshold. Hence, I have made the approximation that the total cross section is constant for energies above the resonance region. The energy threshold seen in Figure 4.1, corresponds to the production of a proton and pion at rest. This occurs for a total CM frame energy of $E_{CM} = \sqrt{s_{min}} = m_\pi c^2 + m_p c^2 \simeq 1.08$ GeV, where m_π and m_p are the mass of the pion and proton respectively.

Consider a proton of energy E_p which interacts with a photon of energy ε, as shown in Figure 4.2(a). The square of the total CM frame energy for the interaction is (c.f. Equation 3.2),

$$s = m_p^2 c^4 + 2\varepsilon(E_p - c|\vec{p}_p|\cos\theta), \tag{4.1}$$

where θ is the angle between the proton and the photon as shown in Figure 4.2(a). The lowest energy photon, ε^{π}_{th}, which can interact with the proton is given by equating s_{min} with s for a head on collision, i.e. $m_\pi^2 c^4 + m_p^2 c^4 + 2m_p c^2 m_\pi c^2 = m_p^2 c^4 + 2\varepsilon^{\pi}_{th}(E_p + |\vec{p}_p|c)$,

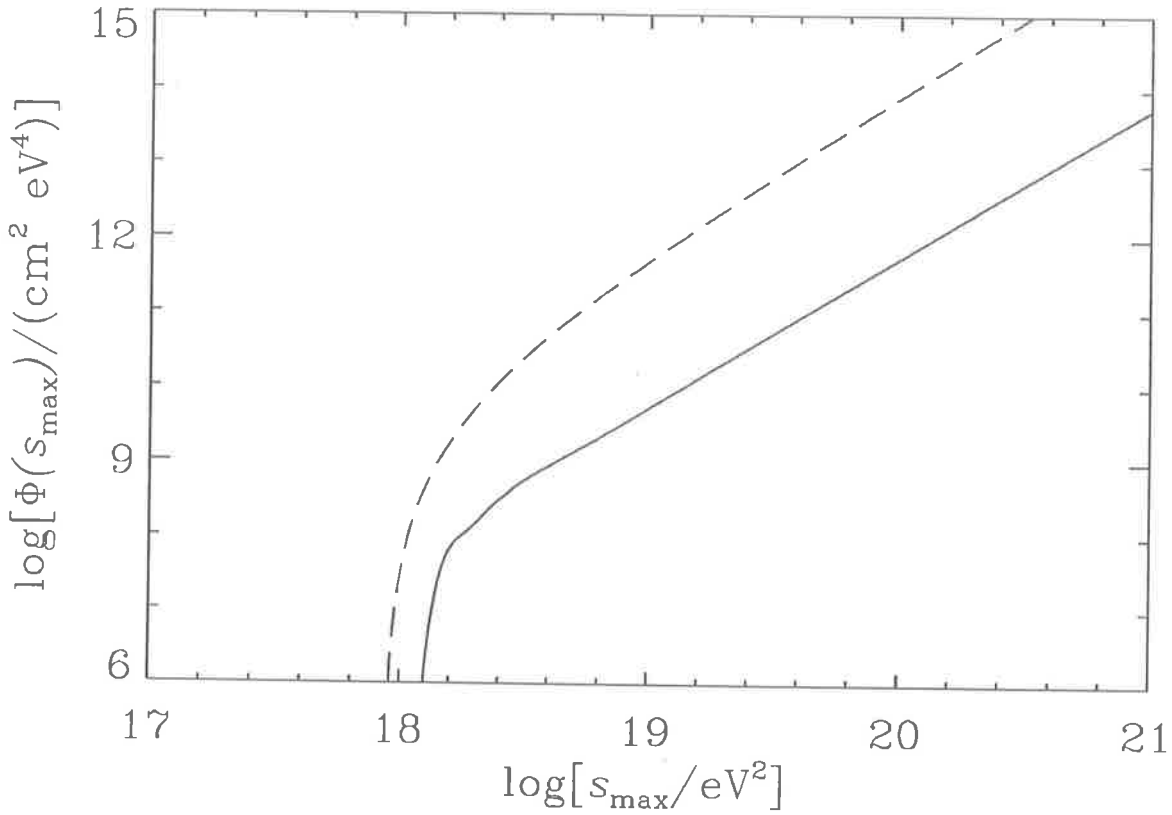

Figure 4.3: A plot of the function $\Phi(s_{max}) = \int_{s_{min}}^{s_{max}} \sigma(s)(s - m_p^2c^4)ds$. Curves are for pion photoproduction (solid) and pair production (dashed). Using $\Phi(s_{max})$ and Equation 4.5, it is straightforward to calculate the mean path length for interaction in an arbitrary photon field.

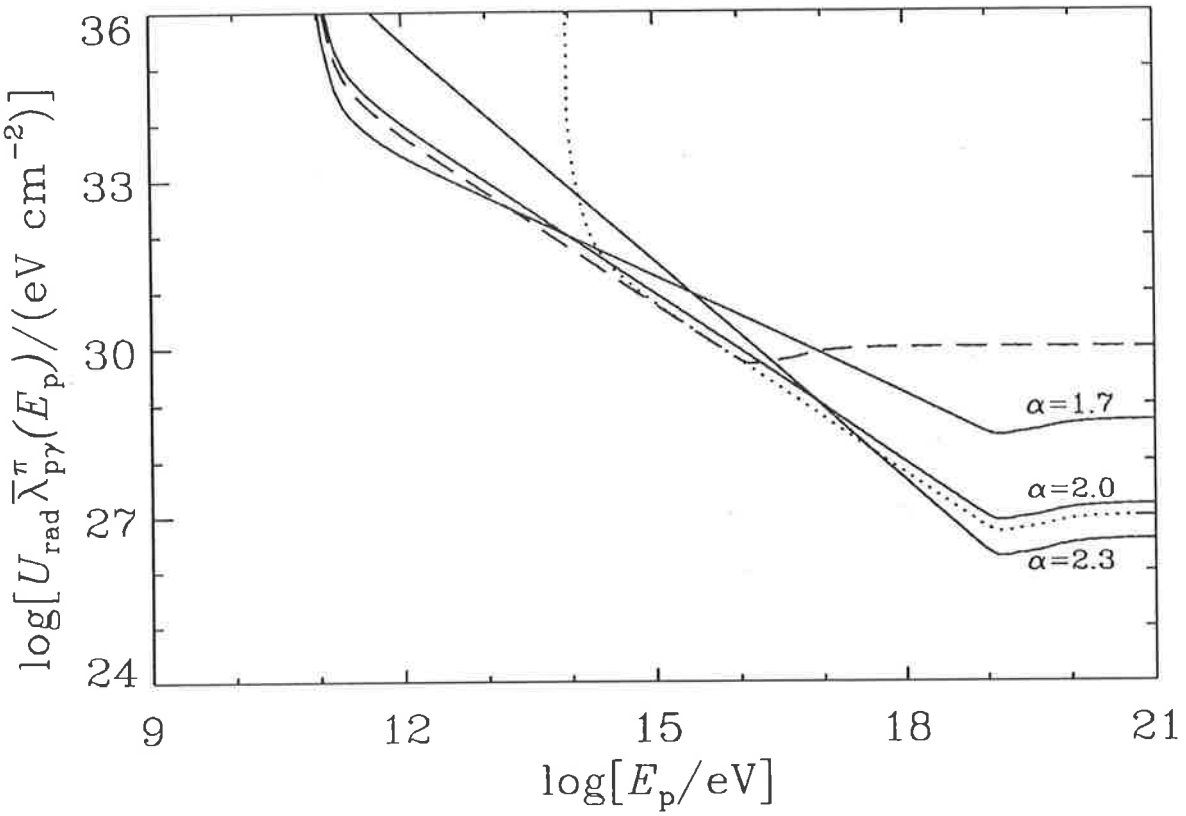

Figure 4.4: A plot of the mean path length for pion photoproduction, $\overline{\lambda}^{\pi}_{\gamma p}(E_p)$, as a function of proton energy. The solid curves are for a power law photon field with spectral indices α =1.7, 2.0 and 2.3, as indicated. All three curves have $\varepsilon_{min} = 10^{-2}$ eV and $\varepsilon_{max} = 10^6$ eV. To illustrate how ε_{min} and ε_{max} affect $\overline{\lambda}^{\pi}_{\gamma p}(E_p)$, I have plotted the mean path length for $\varepsilon_{min} = 10$ eV (dotted curve) and $\varepsilon_{max} = 10^3$ eV (dashed curve). Both the dashed and dotted curves have $\alpha = 2.0$. In each case, the mean path length has been scaled by the radiation energy density U_{rad}.

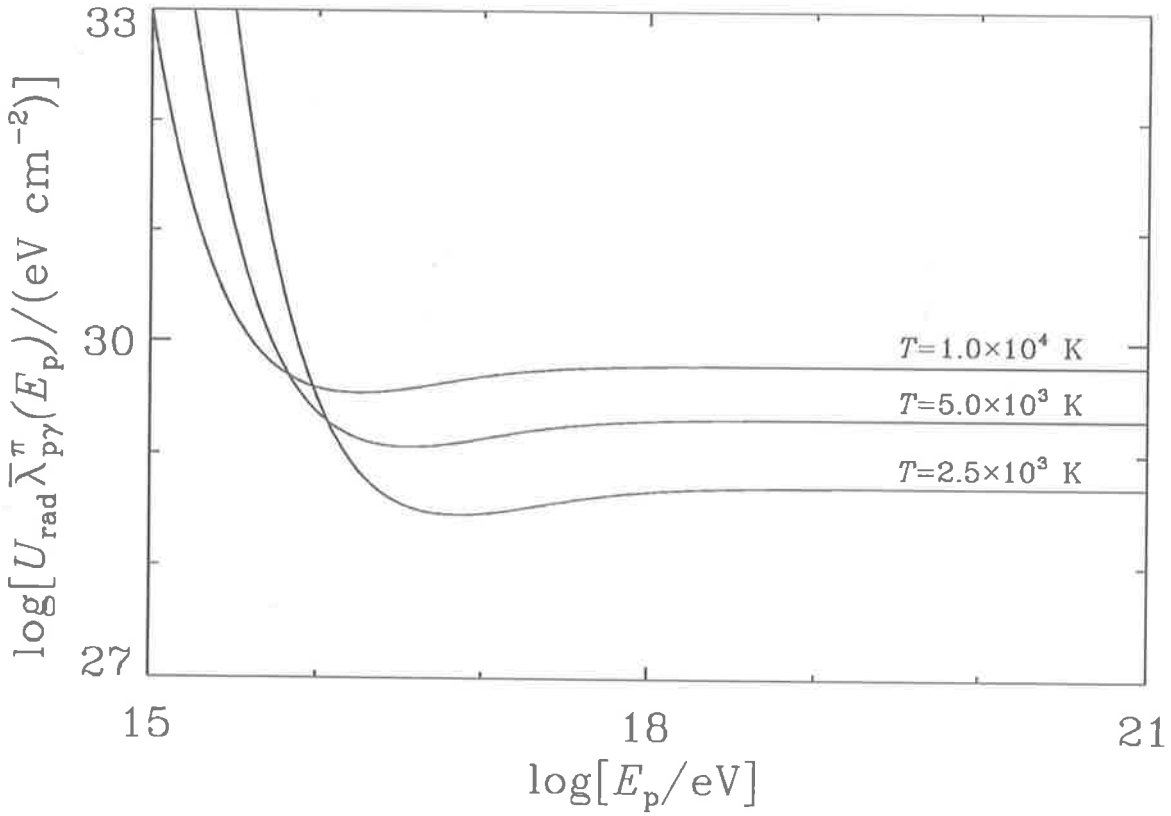

Figure 4.5: A plot of the mean path length for pion photoproduction as a function of proton energy, in a blackbody photon field. Curves are for blackbody temperatures, $T = 2.5\times10^3$, 5.0×10^3, and 1.0×10^4 K, as indicated. Once again the mean path length has been scaled by the radiation energy density U_{rad}.

and so

$$\varepsilon_{th}^{\pi} = \frac{m_\pi c^2(m_\pi c^2 + 2m_p c^2)}{2(E_p + |\vec{p}_p|c)}. \tag{4.2}$$

If the proton is traversing a photon field with differential number density, $dn/d\varepsilon = n(\varepsilon)$ (photons cm^{-3} eV^{-1}), then the mean path length for interaction is given by (c.f. Equation 3.33),

$$[\overline{\lambda}_{\gamma p}^{\pi}(E_p)]^{-1} = \int_{\varepsilon_{th}^{\pi}}^{\infty} n(\varepsilon) \int_{\cos\theta_{min}}^{\cos\theta_{max}} \frac{(1 - \beta_p \cos\theta)}{2} \sigma_{\gamma p}^{\pi}(s)\, d\cos\theta d\varepsilon. \tag{4.3}$$

The lower integration bound corresponds to a head on collision and so $\cos\theta_{min} = -1$. However, the upper bound is governed by the threshold for pion photoproduction and so is given by rearranging Equation 4.1 with $s = s_{min}$,

$$\begin{aligned} \cos\theta_{max} &= \frac{E_p}{|\vec{p}_p|c} - \frac{s_{min} - m_p^2 c^4}{2\varepsilon|\vec{p}_p|c} \\ &= \frac{E_p}{|\vec{p}_p|c} - \frac{m_\pi^2 c^4 + 2m_p c^2 m_\pi c^2}{2\varepsilon|\vec{p}_p|c}. \end{aligned} \tag{4.4}$$

As in Section 3.6, one can rewrite Equation 4.3 in terms of an integral over s, giving

$$\begin{aligned} [\overline{\lambda}_{\gamma p}^{\pi}(E_p)]^{-1} &= \int_{\varepsilon_{th}^{\pi}}^{\infty} \frac{n(\varepsilon)}{8\varepsilon^2 E_p|\vec{p}_p|c} \int_{s_{min}}^{s_{max}} \sigma_{\gamma p}^{\pi}(s)(s - m_p^2 c^4) ds d\varepsilon \\ &= \int_{\varepsilon_{th}^{\pi}}^{\infty} \frac{n(\varepsilon)}{8\varepsilon^2 E_p|\vec{p}_p|c} \Phi_\pi(s_{max}) d\varepsilon, \end{aligned} \tag{4.5}$$

where $s_{max} = m_p^2 c^4 + 2\varepsilon(E_p + |\vec{p}_p|c)$ is the square of the total CM frame energy for a head on collision. The function $\Phi_\pi(s_{max})$ is shown in Figure 4.3, allowing the mean path length for interaction for protons in a variety of photon fields to be calculated. For example, consider an $\varepsilon^{-\alpha}$ power law photon spectrum with ε in the range $\varepsilon_{min} \leq \varepsilon \leq \varepsilon_{max}$. The mean path lengths for spectral indices of α =1.7, 2.0 and 2.3, and with $\varepsilon_{min} = 10^{-2}$ eV and $\varepsilon_{max} = 10^6$ eV are shown in Figure 4.4. Here $\overline{\lambda}_{\gamma p}^{\pi}(E_p)$ has been multiplied by the energy density of the radiation field U_{rad}, to enable the result to easily be scaled for an arbitrary radiation density. In each case, one can see that while $\varepsilon_{min} \leq \varepsilon_{th}^{\pi} \leq \varepsilon_{max}$, $\overline{\lambda}_{\gamma p}^{\pi} \propto E_p^{-\alpha+1}$. This occurs because the integrand of Equation 4.5 is dominated by contributions from energies near threshold. For higher proton energies where $\varepsilon_{th}^{\pi} < \varepsilon_{min}$, the mean path length for interaction is approximately constant. This is because the entire photon spectrum is available to the proton, and because $\Phi_\pi(s_{max}) \propto E_p^2$, cancelling out the factor of $\sim E_p^{-2}$ in Equation 4.5. The effect of changing ε_{min} and ε_{max} may be seen from the dotted and dashed curves in Figure 4.4.

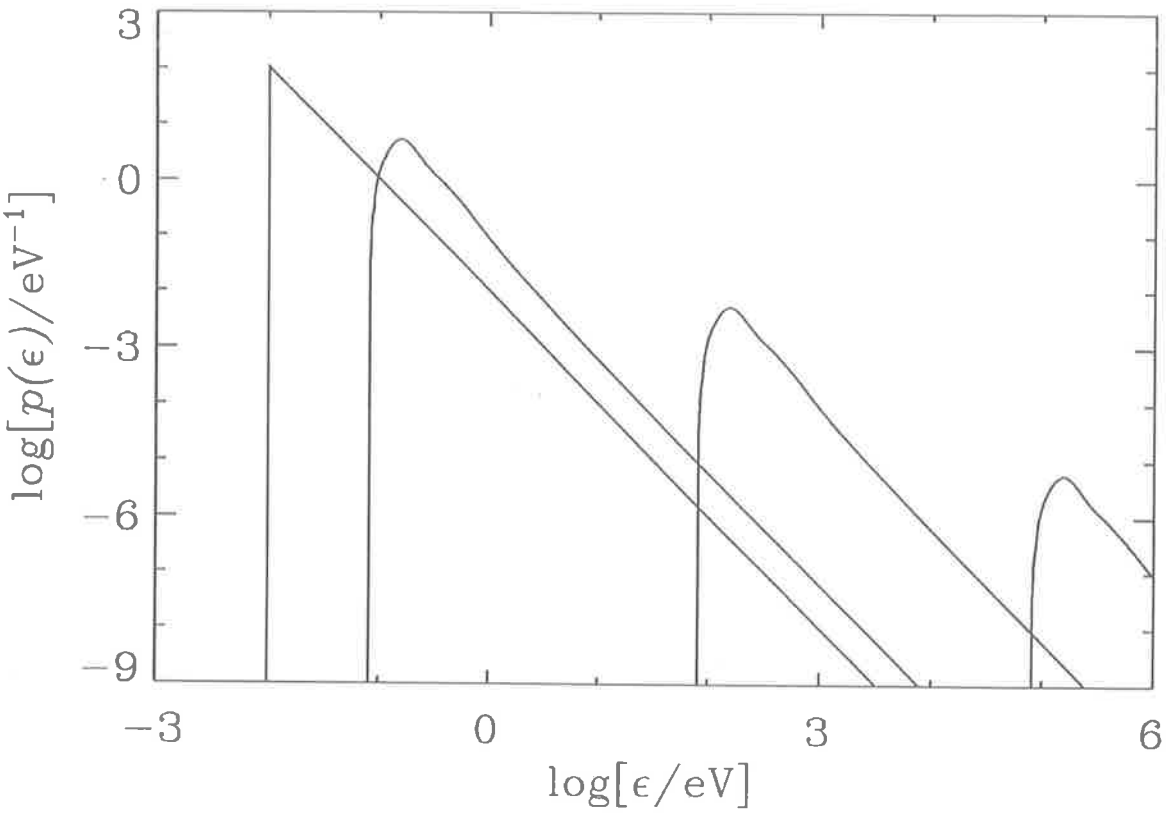

Figure 4.6: The energy distribution of photons which interact with the proton via pion photoproduction, $p(\varepsilon)$. Curves, from right to left, are for $E_p = 10^{12}$, 10^{15}, 10^{18} and 10^{21} eV. In each case, there is a power law ambient photon field with spectral index $\alpha = 2.0$, which has cutoffs $\varepsilon_{min} = 10^{-2}$ eV and $\varepsilon_{max} = 10^{6}$ eV.

Another useful example, is the mean path length for interaction on a black body photon field of temperature T. Figure 4.5 shows $U_{rad}\overline{\lambda}^{\pi}_{\gamma p}(E_p)$ for $T = 2.5\times10^3$, 5.0×10^3 and 1.0×10^4 K. All three curves exhibit similar features to those seen for the power law case. While the photon threshold energy is greater than $\sim kT$, $\overline{\lambda}^{\pi}_{\gamma p}(E_p)$ is dominated by photons with energy near ε^{π}_{th}. Whereas, for $\varepsilon^{\pi}_{th} \ll kT$, the mean path length for interaction is approximately constant as most of the photons in the distribution are available to interact with the proton.

While traversing the photon field, protons will interact with photons whose energy distribution will differ from that of the underlying field. This can be seen by considering the contribution to the mean path length for interaction from photons with energy in the range $\varepsilon \rightarrow \varepsilon + d\varepsilon$ (see Equation 4.5). Normalising these contributions to 1 gives the energy distribution of photons which interact as,

$$p(\varepsilon) = \overline{\lambda}^{\pi}_{\gamma p}(E_p)\frac{n(\varepsilon)}{8\varepsilon^2 E_p|\vec{p}_p|c}\Phi_{\pi}(s_{max}), \tag{4.6}$$

for $\varepsilon^{\pi}_{th} \leq \varepsilon \leq \infty$. An alternative way of arriving at Equation 4.6, is to consider the rate of interaction with photons whose energy is in the range $\varepsilon \rightarrow \varepsilon + d\varepsilon$ and to compare this to the total rate of interaction, $dN/dt = c/\overline{\lambda}^{\pi}_{\gamma p}(E_p)$.

Photon energy distributions for a power law photon field ($\alpha = 2.0, \varepsilon_{min} = 10^{-2}$ eV and $\varepsilon_{max} = 10^6$ eV) are shown in Figure 4.6, for $E_p = 10^{12}$, 10^{15}, 10^{18} and 10^{21} eV. For the three lowest E_p values, the effect of the resonance region in the total cross section is clearly evident. For the $E_p = 10^{21}$ eV case, $\varepsilon^{\pi}_{th} < \varepsilon_{min}$ and so the entire photon spectrum is available to the proton. The spectrum of photons which interact is now the same as the underlying photon field and most of the interactions occur with $\varepsilon \sim \varepsilon_{min}$. For each of the proton energies, one can see that most of the interactions occur near threshold. For both power law and blackbody photon fields, I use the rejection method described in Appendix A to sample a value of ε from Equation 4.6.

The distribution of the square of the CM frame energies for the interaction, found using a similar argument to that above is,

$$p(s) = \Phi^{-1}_{\pi}(s_{max})\sigma^{\pi}_{\gamma p}(s)(s - m_p^2c^4), \tag{4.7}$$

for $s_{min} \leq s \leq s_{max}$. It is interesting to note that most of the interactions occur with $s \simeq s_{max}$. This arises because head on collisions are more likely to occur than following collisions, and so the proton 'sees' more photons coming towards it than going in the

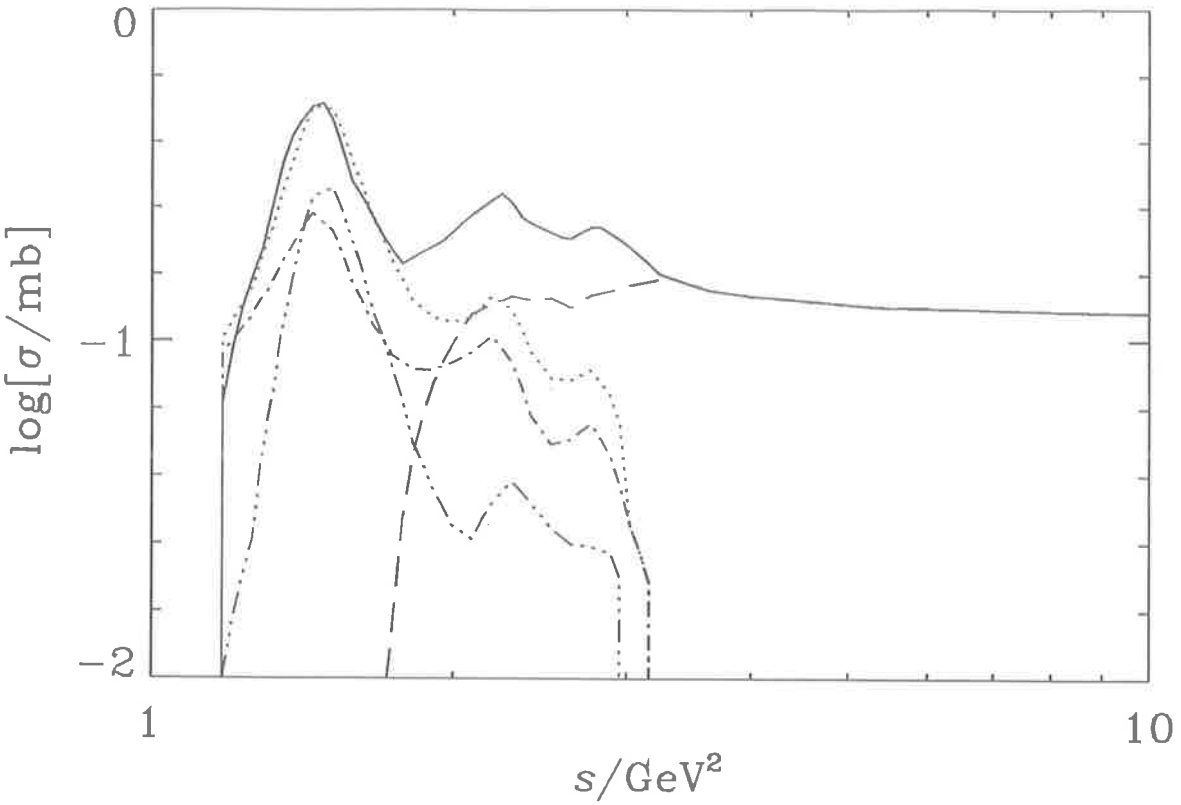

Figure 4.7: A plot of the total cross section, $\sigma(s)$, versus the square of the total CM frame energy, s. The solid line shows my digitisation of the data for the total cross section for pion photoproduction. Also shown, are the total cross sections for the exclusive channels $\gamma p \to \pi^o p$ (dash dot dot dot curve) and $\gamma p \to \pi^+ n$ (dash dot curve). The remaining two curves show $\sigma_{\pi^o}(s) + \sigma_{\pi^+}(s)$ (dotted curve) and $\sigma_X(s)$ (dashed curve), defined in the text.

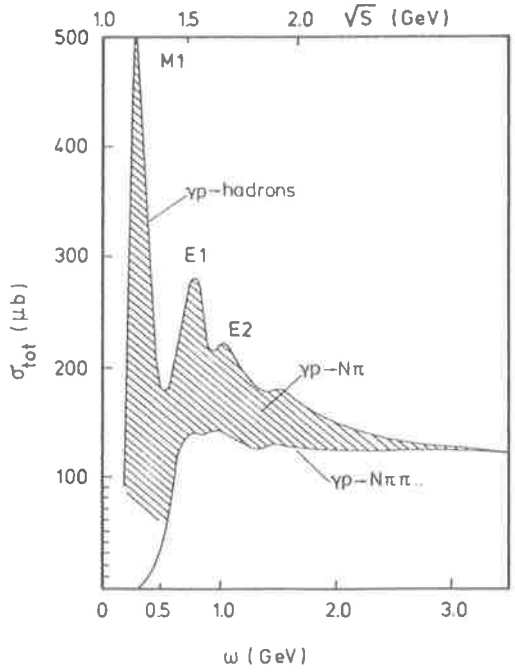

Figure 4.8: A decomposition of the total cross section near threshold, into components due to the channels $\gamma p \to N\pi\pi\ldots$ and $\gamma p \to N\pi$. From Drechsel and Tiator (1992).

same direction. One can see from Equation 4.7 that $p(s) \propto s$ for $s \gg s_{min}$, as $\sigma^{\pi}_{\gamma p}(s)$ becomes constant. Hence, I use the rejection method with the function$f(s) \propto \sigma^{\pi}_{\gamma p}(s)s$ to sample $p(s)$ quite efficiently.

Genzel, Joos and Pfeil (1973) have compiled the data for the exclusive channels $p\gamma \rightarrow p\pi^o$ and $p\gamma \rightarrow n\pi^+$. They have made fits to the differential cross section for these reactions, and I have integrated over these fits to calculate the cross section for each channel. Both of these cross sections, signified by σ_{π^o} and σ_{π^+} respectively, along with a digitisation of the total cross section are shown in Figure 4.7. By subtracting $\sigma_{\pi^o}(s)$ and $\sigma_{\pi^+}(s)$ from $\sigma^{\pi}_{\gamma p}(s)$, one can see that the resonance region is due mainly to these exclusive channels. The portion which remains, $\sigma_X(s) = \sigma^{\pi}_{\gamma p}(s) - \sigma_{\pi^o}(s) - \sigma_{\pi^+}(s)$, is due to multiple pion final states. The separation of the exclusive contributions to the total cross section is in qualitative agreement with a similar decomposition found in a very recent review by Drechsel and Tiator (1992), shown in Figure 4.8.

Insufficient data exists to model the multi pion final states exclusively. Hence, I have used the inclusive data of Moffeit *et al.* (1972) to model these events. At a given value of s, I decide which whether an exclusive or an inclusive interaction takes place, based on the ratio of the cross sections. For example, if one samples a random deviate ξ and $\xi < \sigma_{\pi^o}(s)/\sigma^{\pi}_{\gamma p}(s)$, then the interaction $p\gamma \rightarrow p\pi^o$ is modelled. Similarly, if $\sigma_{\pi^o}(s) \leq \xi\sigma^{\pi}_{\gamma p}(s) < (\sigma_{\pi^o}(s) + \sigma_{\pi^+}(s))$ then the interaction $p\gamma \rightarrow \pi^+ n$ is modelled. Otherwise, the interaction is modelled inclusively. Both the data and the means of modelling the interactions will be discussed in detail in the following sections.

4.2.1 Exclusive Pion Photoproduction

The compilation of Genzel, Joos and Pfeil (1973) contains data for photon beam energies (ε') less than 1.5 GeV. They have made fits to the differential cross sections for the channels $p\gamma \rightarrow p\pi^o$ and $p\gamma \rightarrow n\pi^+$ of the form,

$$\gamma p \rightarrow \pi^o p \quad : \quad \frac{d\sigma_{\pi^o}}{d\Omega^\star}(\varepsilon', \cos\theta^\star_{\pi r}) = \sum_{n=0}^{8} a_n(\varepsilon') \cos^n \theta^\star_{\pi r} \tag{4.8}$$

$$\gamma p \rightarrow \pi^+ n \quad : \quad \frac{d\sigma_{\pi^+}}{d\Omega^\star}(\varepsilon', \cos\theta^\star_{\pi r}) = \frac{1}{(1 - \beta^\star_\pi \cos\theta^\star_{\pi r})^2} \sum_{n=0}^{8} a_n(\varepsilon') \cos^n \theta^\star_{\pi r}, \tag{4.9}$$

where $\theta^\star_{\pi r}$ is the angle between the beam direction and the produced pion's direction (see Figure 4.2(c)) and $\beta^\star_\pi$ is the velocity of the pion in the CM frame. The coefficients

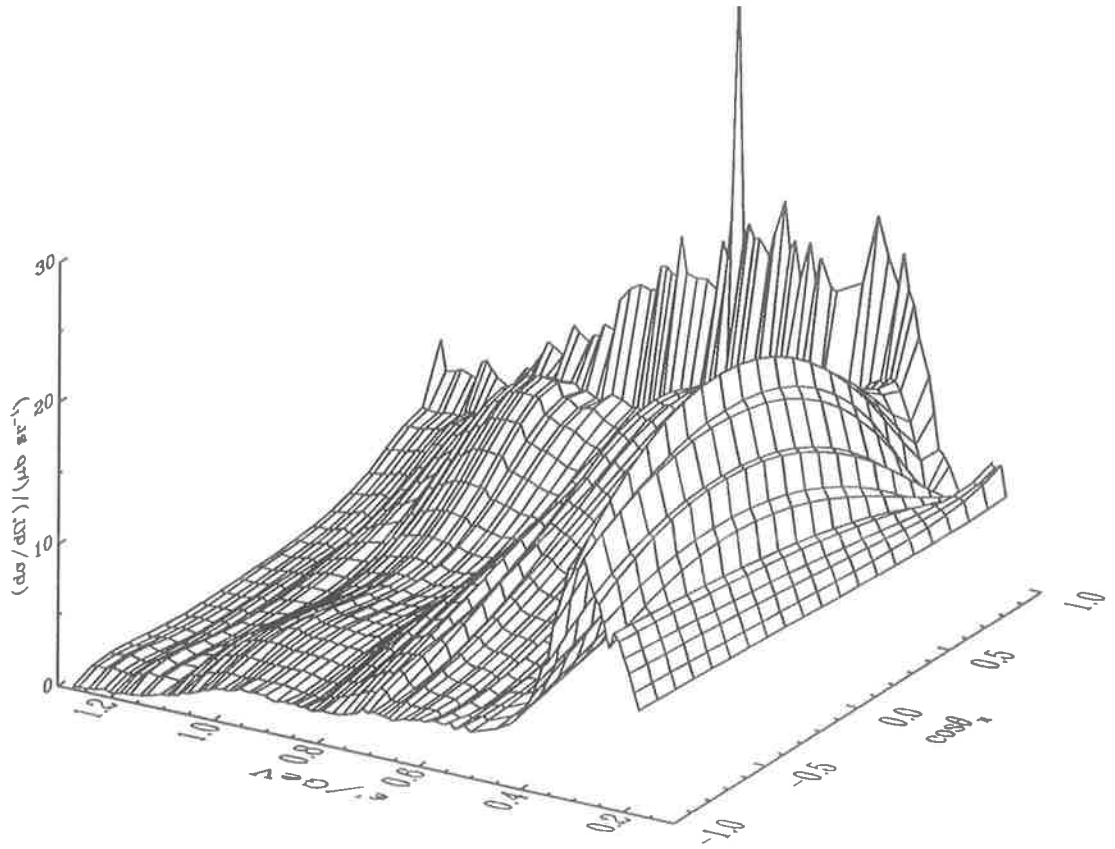

Figure 4.9: A plot of the fits to the differential cross section, $\frac{d\sigma}{d\Omega^*}$, for the exclusive pion photoproduction channel $\gamma p \rightarrow \pi^o p$, given by Genzel, Joos and Pfeil (1971). The fits are in terms of the photon beam energy, ε', and the angle at which the pion is produced in the CM frame, relative to the beam direction, $\cos\theta_\pi = \cos\theta^*_{\pi r}$. The large spike at $\varepsilon' = 0.69$ GeV, is assumed to be caused by a typographical error and the fit for this energy is not included in the simulation.

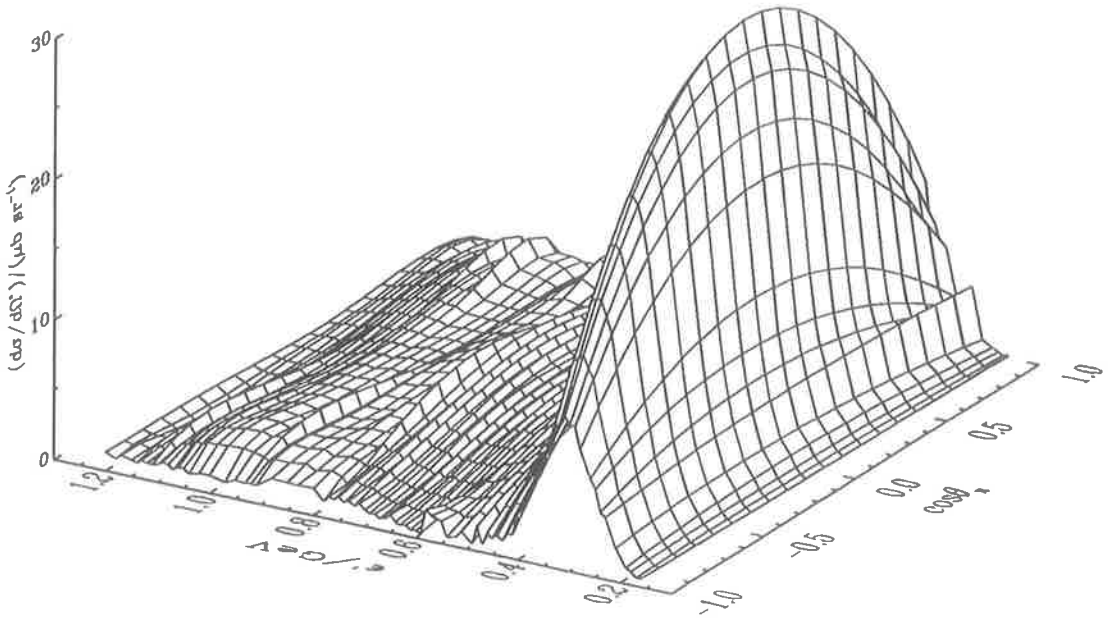

Figure 4.10: The fits to the differential cross section for the exclusive pion photoproduction channel $\gamma p \rightarrow \pi^+ n$ given by Genzel, Joos and Pfeil (1971). Variables are defined as in Figure 4.9.

$a_n(\varepsilon')$ are given in Appendix B, as a function of the photon's energy in the proton rest frame, ε'. The fits give the direction of the pion relative to the direction of the photon in the CM frame. For astrophysical applications one usually has a high energy proton interacting with low energy photons, and so it is more meaningful to define directions relative to the proton's direction. However, to simplify the sampling procedure for the pion's direction I define a rotated centre of momentum (RCM) frame[1] in which the photon's direction is aligned with the x–axis , as shown in Figure 4.2(c). The fits to the differential cross sections are shown in Figures 4.9 and 4.10, as a function of both ε' and $\cos\theta^\star_{\pi r}$. One can see that for $\varepsilon' = 0.69$ GeV there is a large spike in Figure 4.9, which is not consistent with the rest of the plot. Hence, I have ignored the fit for this beam energy and conjecture that there may have been a typographical error in the published coefficients. To calculate values for the differential cross section at all s and $\theta^\star_{\pi r}$ values, a linear interpolation in both variables is used. For example, consider the interaction $\gamma p \rightarrow \pi^o p$ which has fits to the differential cross section for values of the square of the total CM frame energy given by, s_i for $i = 1$ to n. If $s_i < s < s_{i+1}$ and $\cos\theta^\star_j < \cos\theta^\star_{\pi r} < \cos\theta^\star_{j+1}$, where $\theta^\star_j$ and $\theta^\star_{j+1}$ are the angles at which the differential cross section has been digitised, then a linear interpolation in the variable $\cos\theta^\star_{\pi r}$ is used to find $\frac{d\sigma_{\pi^o}}{d\Omega^\star}(\varepsilon'(s_i), \cos\theta^\star_{\pi r})$ and $\frac{d\sigma_{\pi^o}}{d\Omega^\star}(\varepsilon'(s_{i+1}), \cos\theta^\star_{\pi r})$. A linear interpolation in s is then used to find $\frac{d\sigma_{\pi^o}}{d\Omega^\star}(\varepsilon'(s), \cos\theta^\star_{\pi r})$.

The CM frame energies of the nucleon and pion produced in the interaction, are only dependent on the total CM frame energy, $\sqrt{s}$. Hence, by analogy with two body decay (see Section 3.3), the CM frame energy of the pion is

$$E^\star_\pi = \frac{s - m_p^2c^4 + m_\pi^2c^4}{2\sqrt{s}}. \tag{4.10}$$

Conservation of momentum gives the CM energy of the produced nucleon as

$$E^\star_N = \sqrt{E^{\star 2}_\pi - m_\pi^2c^4 + m_p^2c^4}. \tag{4.11}$$

The direction of the pion in the RCM frame is given by sampling angles $\theta^\star_{\pi r}$ and $\phi^\star_{\pi r}$, defined in Figure 4.2(c). I assume that pions are produced symmetrically about the beam direction, and hence $\theta^\star_{\pi r}$ and $\phi^\star_{\pi r}$ are sampled from the distributions

$$p(\cos\theta^\star_{\pi r}) = \frac{2\pi}{\sigma_i(s)}\frac{d\sigma_i}{d\Omega^\star}(\cos\theta^\star_{\pi r}), \qquad \text{for } -1 \leq \cos\theta^\star_{\pi r} \leq 1, \tag{4.12}$$

[1]quantities measured in the RCM are denoted by the sub–script r

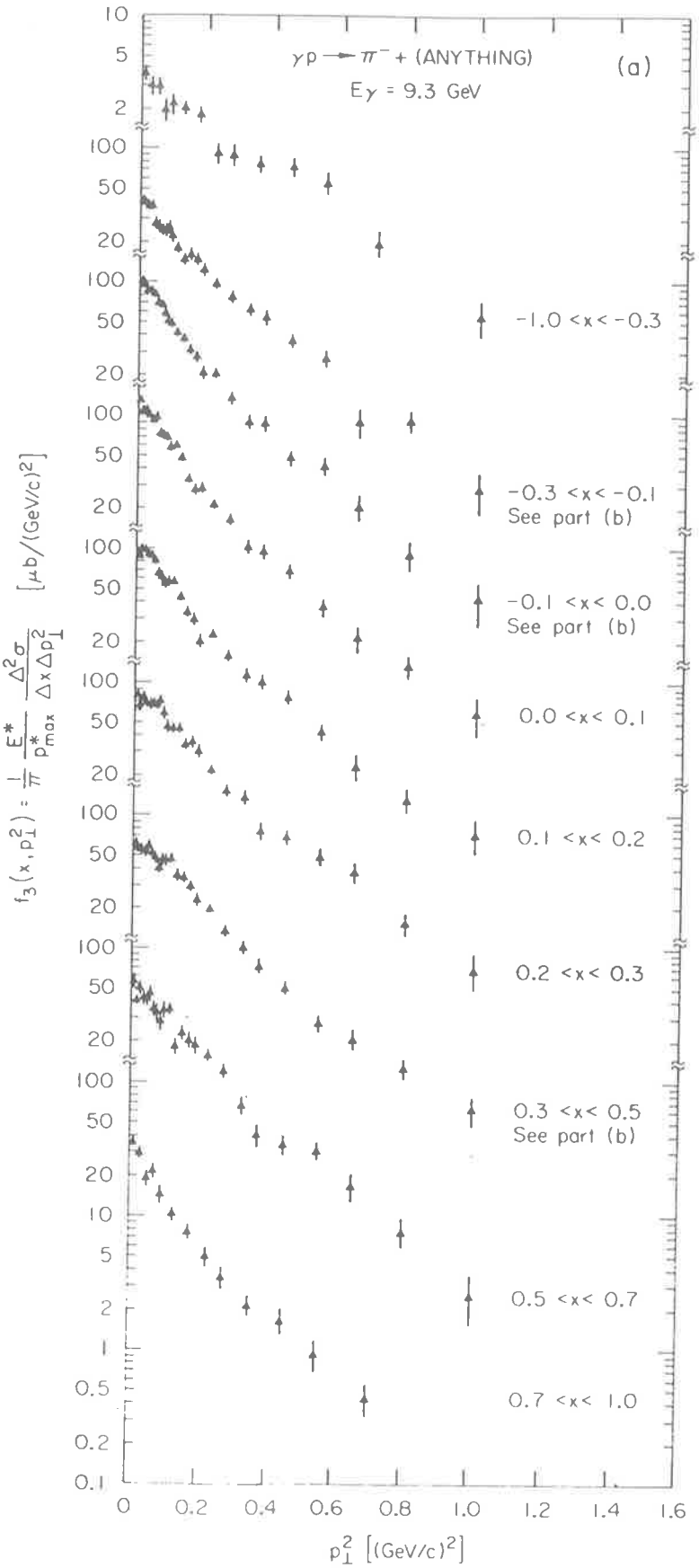

Figure 4.11: A plot of the tranverse momentum distributions, $f_3(x, p_\perp^2)$, for the inclusive interaction $\gamma p \to \pi^- X$, integrated over the intervals in Feynmann x shown. Data are for a beam energy of 9.3 GeV. From Moffeit *et al.* (1972).

and

$$p(\phi^{\star}_{\pi r}) = \frac{1}{2\pi}, \qquad \text{for } 0 \leq \phi^{\star}_{\pi r} \leq 2\pi, \tag{4.13}$$

where the subscript i refers to either of the two exclusive channels. The rejection technique (as described in Appendix A) is used to sample $\cos\theta^{\star}_{\pi r}$, and the formula $\phi^{\star}_{\pi r} = 2\pi\xi$ is used to sample $\phi^{\star}_{\pi r}$.

To transform from the RCM frame to the CM frame, I apply a rotation through angle $\phi^{\star}_{cm}$ about the $z^{\star}_{r}$ axis, as shown in Figure 4.2(b). The angle at which the pion is emitted, relative to the $x^{\star}$–axis in the CM frame is

$$\cos\theta^{\star}_{\pi} = -[\cos\theta^{\star}_{\pi r}\cos\phi^{\star}_{cm} + \sin\theta^{\star}_{\pi r}\sin\phi^{\star}_{\pi r}\sin\phi^{\star}_{cm}], \tag{4.14}$$

where $\phi^{\star}_{cm}$ is given by the aberration formula, i.e. Equation 3.8. Hence, the energy of the pion in the LAB frame is

$$E_{\pi} = \gamma_{cm}(E^{\star}_{\pi} + \beta_{cm}c|\vec{p}^{\star}_{\pi}|\cos\theta^{\star}_{\pi}). \tag{4.15}$$

Similarly, the energy of the nucleon is

$$E_{N} = \gamma_{cm}(E^{\star}_{N} - \beta_{cm}c|\vec{p}^{\star}_{N}|\cos\theta^{\star}_{\pi}), \tag{4.16}$$

where $\vec{p}^{\star}_{N}$ is the nucleon's momentum in the CM frame.

4.2.2 Inclusive Pion Photoproduction

At high energies (for beam energies greater than 1.5 GeV) one must resort to inclusive data to model pion photoproduction. The concept of scaling makes the inclusive modelling of interaction feasible, as one only needs the invariant cross section at one energy to be able to construct the inclusive differential cross section at any energy for which scaling is valid. Moffeit *et al.* (1972) have measured the inclusive cross section for the reaction $p\gamma \rightarrow \pi^{-}X$, for beam energies of $\varepsilon' = 2.8, 4.7$ and 9.3 GeV. While scaling does not hold at these energies (Moffeit *et al.* 1972), the 9.3 GeV data is the highest beam energy available for which the transverse momentum distributions have been measured. Thus, the 9.3 GeV data have been used as the best approximation to the invariant cross section.

The transverse momentum data for a beam energy of 9.3 GeV are shown in Figure 4.11, and the structure function for all three energies used by Moffeit *et al.* is shown in

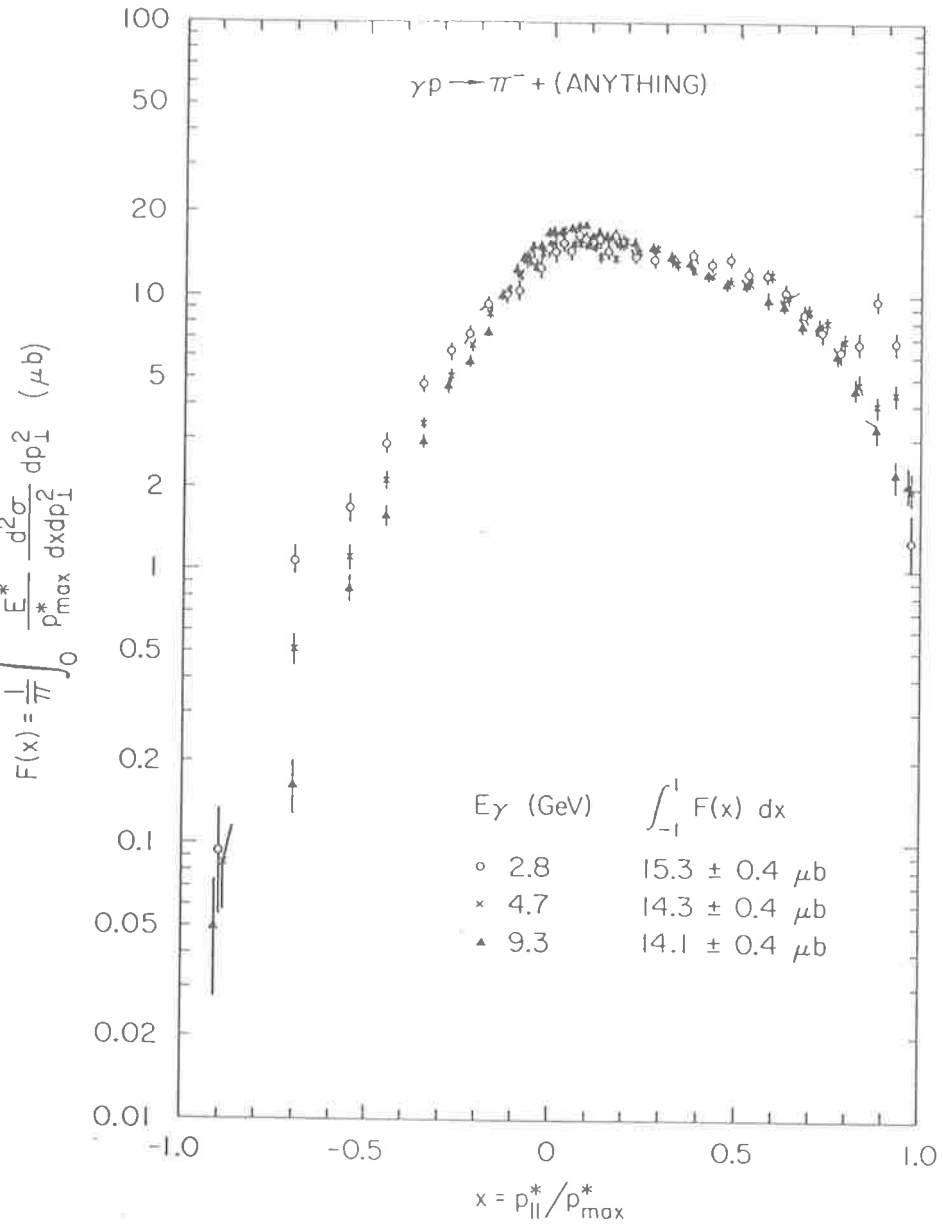

Figure 4.12: A plot of the structure function, $F(x)$, for the inclusive interaction $\gamma p \rightarrow \pi^- X$. Data are for beam energies of 2.8, 4.7 and 9.3 GeV. From Moffeit *et al.* (1972).

4.12. Longitudinal and transverse components of momentum are defined with respect to the beam direction, and hence, once again, the pion's direction is sampled in the rotated centre of momentum (RCM) frame, defined in Section 4.2.1. However, for clarity I will adopt the same terminology as used by Moffeit *et al.* when discussing the data. Notice also that Moffeit *et al.* have obtained their data by having γ–rays interact with a stationary proton target. Hence, the beam fragmentation region will correspond to the photon fragmentation region.

To construct the inclusive differential cross section, $d^3\sigma/d^3p$, I assume that the function

$$\begin{aligned} f_3(x,p_\perp^2) &= \int_{\Delta x} E_\pi^\star \frac{d^3\sigma}{d^3p^\star} dx \\ &\simeq \frac{1}{\pi} \frac{E_\pi^\star}{p_{max}^\star} \frac{\Delta^2\sigma}{\Delta x \Delta p_\perp^2} \end{aligned} \tag{4.17}$$

is separable into functions of x and $p_\perp^2$, i.e $f_3(x,p_\perp^2) = f(x)p(p_\perp^2)$, where $p(p_\perp^2)$ is normalised such that $\int_0^\infty p(p_\perp^2)dp_\perp^2 = 1$. Moffeit *et al.* have examined the data to see if it can be factorised in this way. They have done this by averaging the structure function over intervals in the square of the transverse component of the pion's momentum, $p_\perp^2$, by calculating

$$F(x,\langle p_\perp^2\rangle) = \frac{1}{\pi}\int_a^b \frac{E_\pi^\star}{p_{max}^\star}\frac{d^2\sigma}{dx dp_\perp^2} dp_\perp^2 \tag{4.18}$$

for $a \leq p_\perp^2 \leq b$. Their results are shown in Figure 4.13. As the shape of the structure function changes from interval to interval, Moffeit *et al.* have concluded that $f_3(x,p_\perp^2)$ cannot be factorised into functions of x and $p_\perp^2$. However, the variation in shape is relatively small, and so for astrophysical applications one can make the approximation that $f_3(x,p_\perp^2)$ can be factorised.

From Figure 4.11, one can see that the dependence on $p_\perp^2$ is approximately exponential. Hence, distributions of the form,

$$p(p_\perp^2) \simeq \langle p_\perp^2(x)\rangle^{-1} \exp\left[\frac{-p_\perp^2}{\langle p_\perp^2(x)\rangle}\right], \tag{4.19}$$

have been fitted to the data, where $\langle p_\perp^2(x)\rangle$ is the mean transverse momentum squared for the distribution. The values of $\langle p_\perp^2(x)\rangle$ obtained from the fits are given in Table 4.1.

I integrate $f_3(x,p_\perp^2)$ over $p_\perp^2$ to calculate the structure function $F(x)$

$$F(x) = \int_0^\infty f_3(x,p_\perp^2)dp_\perp^2$$

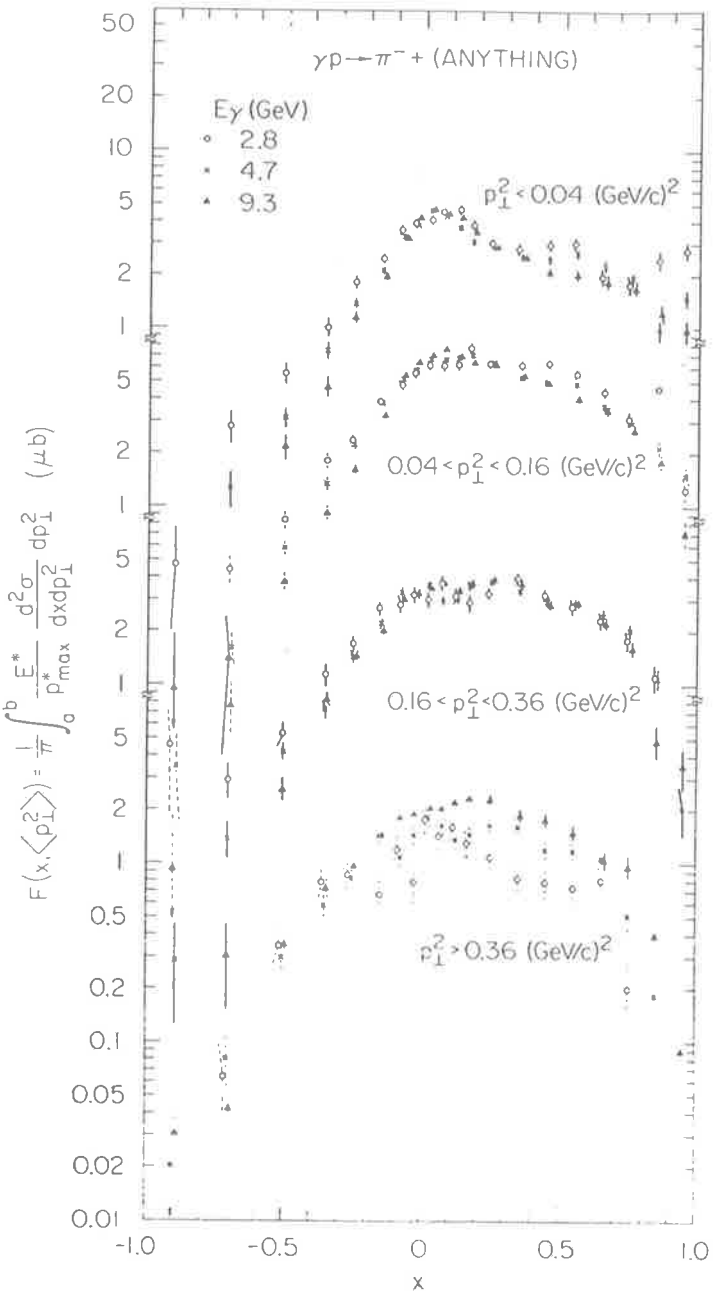

Figure 4.13: A plot of the data for the structure function integrated over various intervals in transverse momentum. The shape of $F(x, \langle p_\perp^2 \rangle)$ is not uniform from interval to interval. Hence, the data cannot be factorized into independent functions of x and $p_\perp^2$. From Moffeit *et al.* (1972).

Interval	$\langle p_\perp^2 \rangle$ (GeV$^2/c^2$)
$-1.0 < x < -0.3$	0.225
$-0.3 < x < -0.1$	0.161
$-0.1 < x < 0.0$	0.129
$0.0 < x < 0.1$	0.128
$0.1 < x < 0.2$	0.161
$0.2 < x < 0.3$	0.155
$0.3 < x < 0.5$	0.181
$0.5 < x < 0.7$	0.218
$0.7 < x < 1.0$	0.109

Table 4.1: A table of the mean transverse momentum, $\langle p_\perp^2 \rangle$, obtained from fits to the data of Moffeit *et al.* (1972).

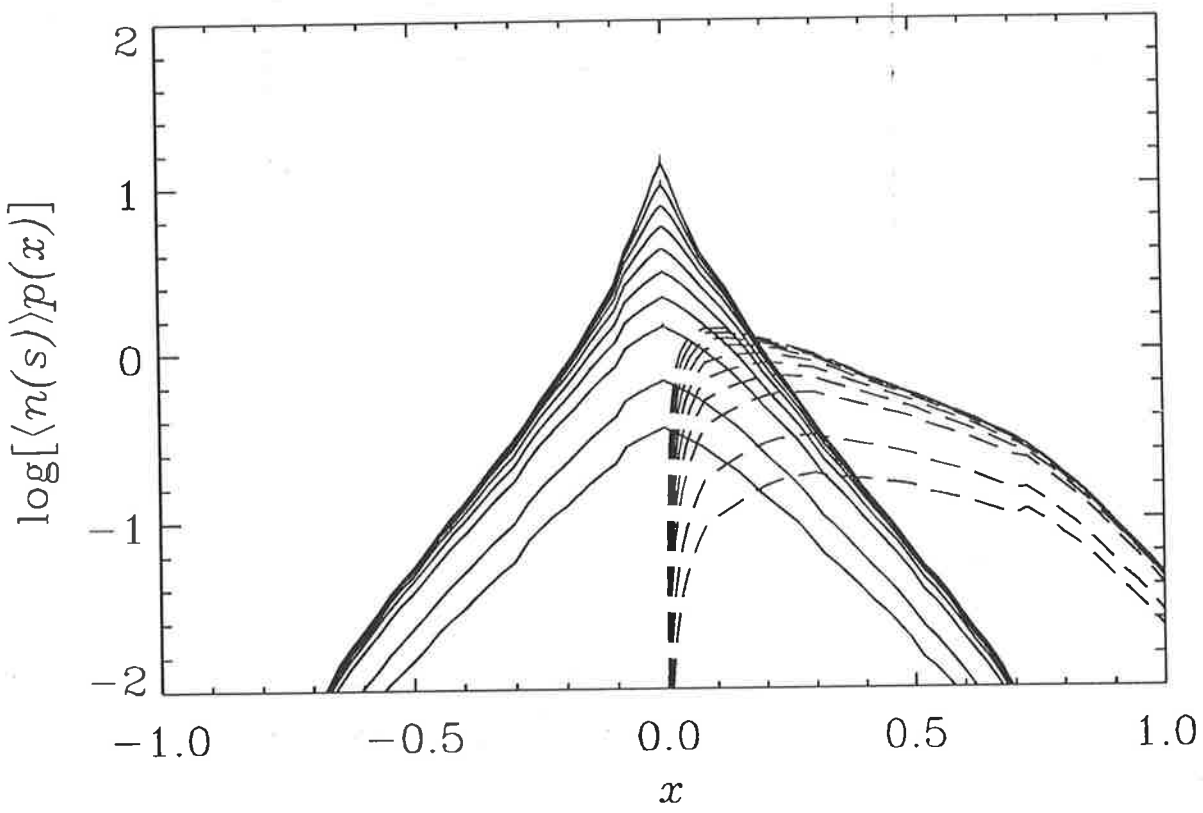

Figure 4.14: Plots of the central region (solid curves) and leading particle (dashed curves) distributions. The curves have been normalised so that the area under each curve corresponds to the mean number of pions in that component, i.e. plots are normalised to the mean multiplicity, $\langle n(s) \rangle$. Curves are for $s = 10^{18.25}$ (lowest curve), $10^{18.5}$,...,$10^{20.5}$ (highest curve) eV^2.

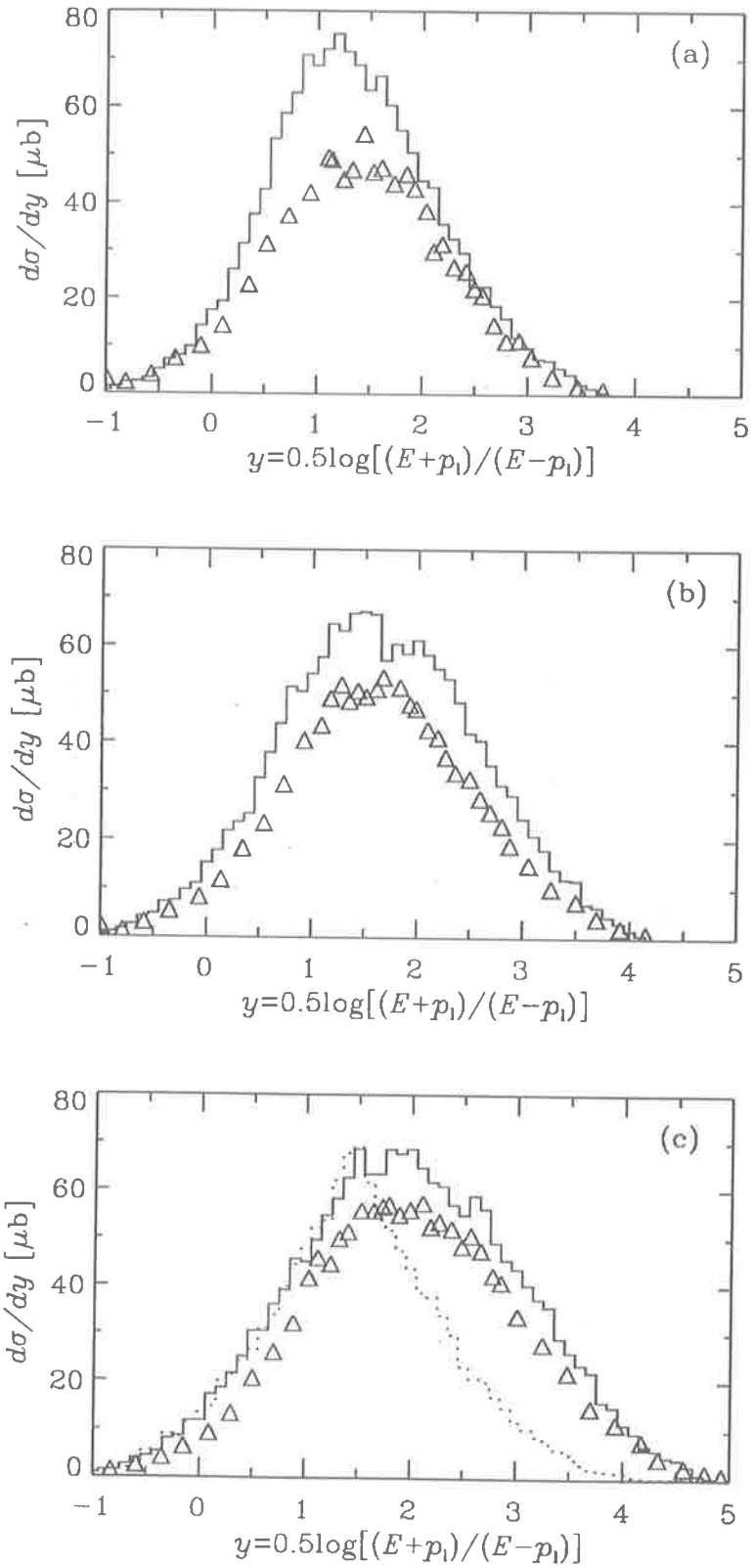

Figure 4.15: Plots of the rapidity distributions for the interaction $\gamma p \to \pi^- X$, for beam energies of (a) 2.3 GeV, (b) 4.7 GeV and (c) 9.3 GeV. In each case, the histograms are the results from the Monte Carlo simulation described in the text. Data points are from Moffeit *et al.* (1972). In plot (c), I also show the distribution of π^os produced (dotted histogram), with a beam energy of 9.3 GeV.

$$= f(x), \tag{4.20}$$

where the normalization of $p(p_\perp^2)$ has been used. Hence, with the data for the structure function (see Figure 4.12) one has all of the ingredients required to construct the inclusive differential cross sections. Rearranging Equation 4.17 gives,

$$\begin{aligned} \frac{d^3\sigma}{d^3p^\star} &\simeq \frac{f(x)p(p_\perp^2)}{E_\pi^\star} \\ &= \frac{F(x)\exp\left[\frac{-p_\perp^2}{\langle p_\perp^2(x)\rangle}\right]}{E_\pi^\star\langle p_\perp^2(x)\rangle}. \end{aligned} \tag{4.21}$$

To calculate the pion distribution in x, the inclusive differential cross section is integrated over $p_\perp^2$, giving

$$\begin{aligned} p(x) &= \frac{1}{\langle n(s)\rangle\sigma_X(s)}\int_0^\infty \frac{d^3\sigma}{d^3p^\star}dp_\perp^2 \\ &= \frac{\pi}{\langle n(s)\rangle\sigma_X(s)}\int_0^\infty \frac{F(x)\exp\left[-p_\perp^2/\langle p_\perp^2(x)\rangle\right]}{E_\pi^\star\langle p_\perp^2(x)\rangle}dp_\perp^2, \end{aligned} \tag{4.22}$$

where $\langle n(s)\rangle$ is the mean multiplicity for the interaction.

In reality, the structure functions shown in Figure 4.12 will consist of two components, from leading and central region pions. To separate these components, I have assumed that the distribution of central region pions is symmetric about $x = 0$, i.e. no leading pions are produced with $x < 0$. The resultant central region and leading particle distributions are shown in Figure 4.14. As the square of the total CM frame energy increases, the distribution of central region pions becomes sharply peaked near $x = 0$. However, the leading pion distribution becomes independent of s, as s increases. This is consistent with the production of a leading particle which decays to produce the leading pions. To simplify the simulation of inclusive interactions, $p(x)$ has only been calculated for ten values of the square of the total CM frame energy, $s_i = 10^{18.25}, 10^{18.5}, \ldots, 10^{20.5}$. I have also assumed that for $s_i \leq s \leq s_{i+1}$, the distribution is independent of s, and so p(x) remains unchanged over the interval $[s_i, s_{i+1}]$.

To decide if the pion to be sampled comes from the central or leading particle distributions, the mean number of pions (or the mean multiplicity) contained in each has been calculated. Hence, if one samples a random deviate $\xi < \langle n_{\text{leading}}(s)\rangle/\langle n(s)\rangle$, where $\langle n_{\text{leading}}(s)\rangle$ is the mean multiplicity of the leading pions, then the pion comes from the leading particle region. In this case, a value of x for the pion is sampled

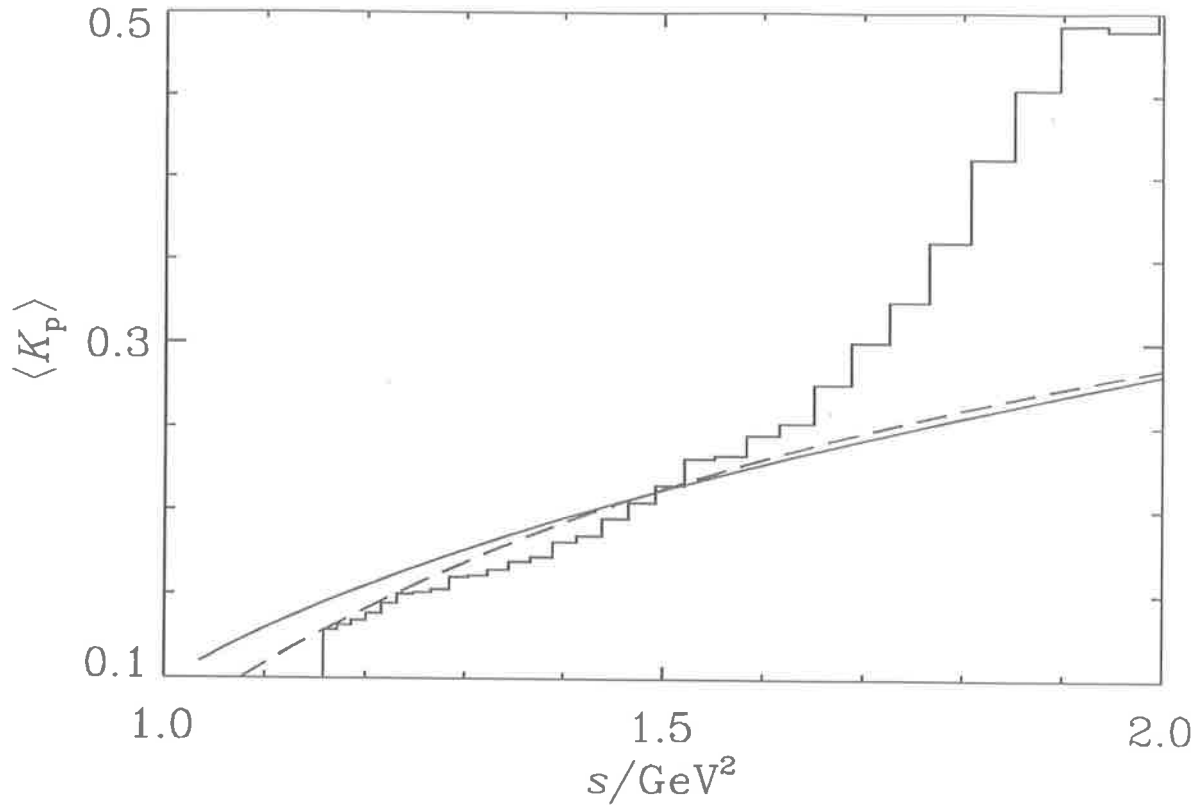

Figure 4.16: A plot of the mean inelasticity for pion photoproduction, $\langle K_p \rangle$, versus the square of the total CM frame energy, s. The histogram shows the results from the Monte Carlo simulation described in the text. Also shown, are the mean multiplicities calculated by Stecker (1968) (dashed curve) and Begelman, Rudak and Sikora (1990) (solid curve).

from the leading distributions using the rejection technique described in Appendix A. Similarly, if $\xi > \langle n_{\rm leading}(s)\rangle/\langle n(s)\rangle$ then I sample a value of x from the central region distributions. In each case, a transverse momentum for the pion is sampled from the function $g(p_\perp^2)$ for an appropriate value of $\langle p_\perp^2(x)\rangle$, using the rejection method.

The maximum energy that the leading nucleon can have in an inclusive pion photoproduction interaction is $E_p^{max} \simeq \sqrt{s}/2$. Thus, pions are selected in the method described above, until the energy which remains for the proton is less than E_p^{max}. Pions which are produced in the photon fragmentation region are assumed to be π^+ and π^- produced in equal numbers. This is based on a simple argument in which the leading particles are assumed to be produced by the decay of a ρ meson. The decay channel $\rho^\circ \rightarrow \pi^+\pi^-$ has a branching ration of 100% (Particle Data Group 1990). In the central region, all three charge types of pions are assumed to be produced in the same ratio. A simple consideration of the interaction at the quark level, gives the ratio of protons to neutrons in the proton fragmentation region as 3:2.

As a simple test of the sampling algorithm for inclusive interactions, one can calculate the rapidity distribution, $d\sigma/dy$, of the produced pions and compare this to the data of Moffeit *et al.* (1972). I have used a Monte Carlo simulation to model a large number of inclusive interactions, and bin the pions in rapidity,

$$y = \frac{1}{2}\ln\left[\frac{E_\pi + p_l}{E_\pi - p_l}\right], \tag{4.23}$$

where E_π and p_l are the LAB frame values of the pion's energy and longitudinal momentum respectively. The results are plotted for beam energies of 2.8, 4.7 and 9.3 GeV, in Figure 4.15. Also plotted, are the results from Moffeit *et al.* As expected, the 9.3 GeV data are best reproduced, although the results become worse for lower beam energies. This is not surprising, as scaling is only hypothesised to work at high energies (as $s \rightarrow \infty$). Clearly, scaling is not a good approximation at these low energies. However, for the purpose of an astrophysical calculation the modelling algorithm described above is adequate.

4.2.3 Mean Inelasticity for Pion Photoproduction

The mean inelasticity for pion photoproduction, $\langle K_N(s)\rangle$, gives a measure of the mean fractional energy lost by the nucleon during the interaction. I have calculated $\langle K_N(s)\rangle$

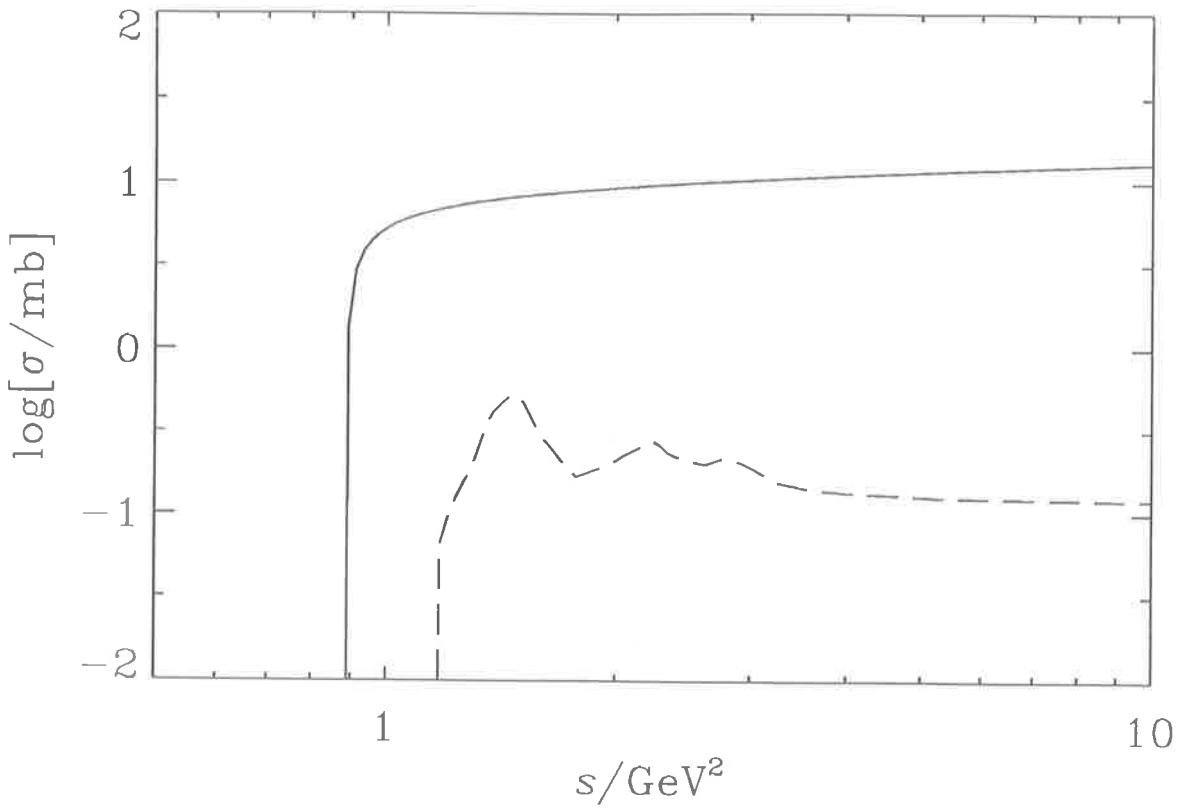

Figure 4.17: The total cross section for pair production, based on the parameterisation of Maximon (1969) (solid curve). Also shown for comparison, is my digitisation of the total cross section for pion photoproduction (dashed curve).

as a function of the square of the total CM frame energy, using a Monte Carlo simulation. The results are shown in Figure 4.16. For comparison, the mean inelasticity calculated by Stecker (1968) for the single pion channels,

$$\langle K_p(s) \rangle = \frac{1}{2}\left(1 + \frac{m_\pi^2 c^4 - m_p^2 c^4}{s}\right), \tag{4.24}$$

and Begelman, Rudak and Sikora (1990)

$$\langle K_p(x) \rangle = \begin{cases} 9.78 \times 10^{-3} x^{0.4756} & \text{for } x < 3913 \\ 0.5 & \text{otherwise} \end{cases}, \tag{4.25}$$

are also shown, where x is the photon's energy in the proton rest frame in units of electron rest masses. Near threshold there is reasonable agreement between my calculations and those of Stecker (1968) and Begelman, Rudak and Sikora (1990). However, at energies above $\sqrt{s} \sim 1.3$ GeV the results diverge. In my calculations multiple pion final states are included whereas in the other calculations they are not, and this may account for the departure. Also, as pointed out earlier scaling is not appropriate at low energies and this may cause inaccuracies in the calculation of the mean inelasticity. Fortunately, as most of the interactions take place near threshold for the astrophysical applications of interest in this thesis, the effects of uncertainties in the inclusive interactions should be minimal.

4.3 Pair Production

The total cross section for pair production in the field of a proton is shown in Figure 4.17, and is based on the parameterisation of Maximon (1969). Threshold for the interaction is $\sqrt{s_{min}} = m_p c^2 + 2m_e c^2 \simeq 0.939$ GeV, and this corresponds to a beam energy of $2m_e c^2$ =1.02 MeV in the proton rest (PR) frame. Prior to the interaction, the situation is identical to that for pion photoproduction, as can be seen from Figure 4.2(a), and hence the square of the total CM energy is given by Equation 4.1.

The lowest energy photon which can interact with a proton of energy E_p via pair production is

$$\varepsilon_{th}^{e} = \frac{2m_e c^2(m_e c^2 + m_p c^2)}{E_p + |\vec{p}_p| c}, \tag{4.26}$$

where a similar argument as for the calculation of ε_{th}^{π} in Section 4.2 has been used. The mean path length for pair production in a photon field with number density $n(\varepsilon)$ is

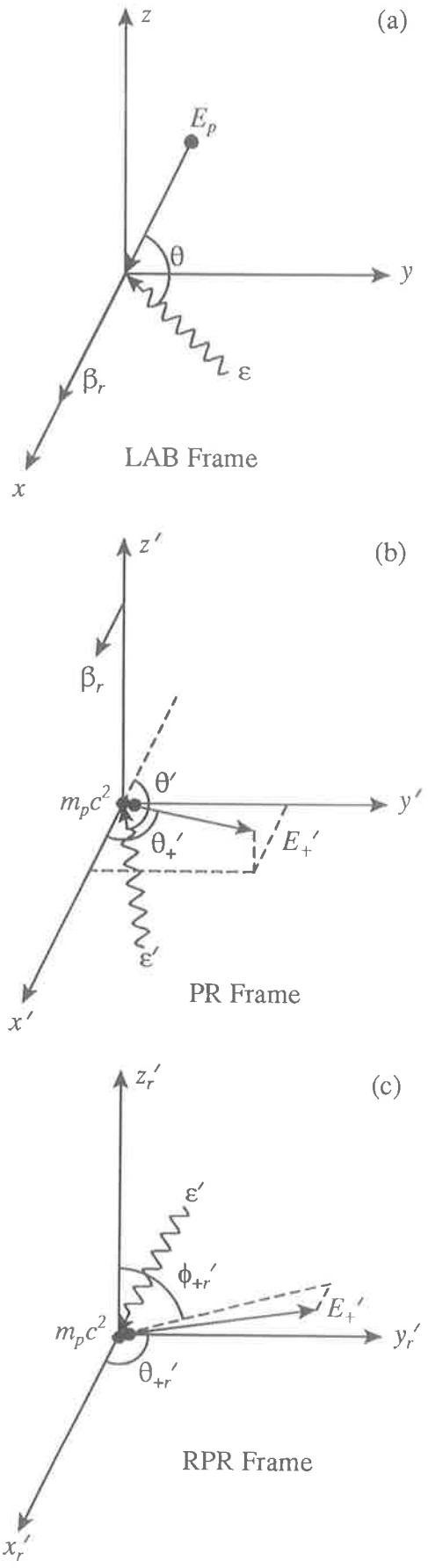

Figure 4.18: A schematic diagram of a pair production interaction, when viewed from (a) the laboratory (LAB) frame, (b) the proton rest (PR) frame and (c) the rotated proton rest (RPR) frame.

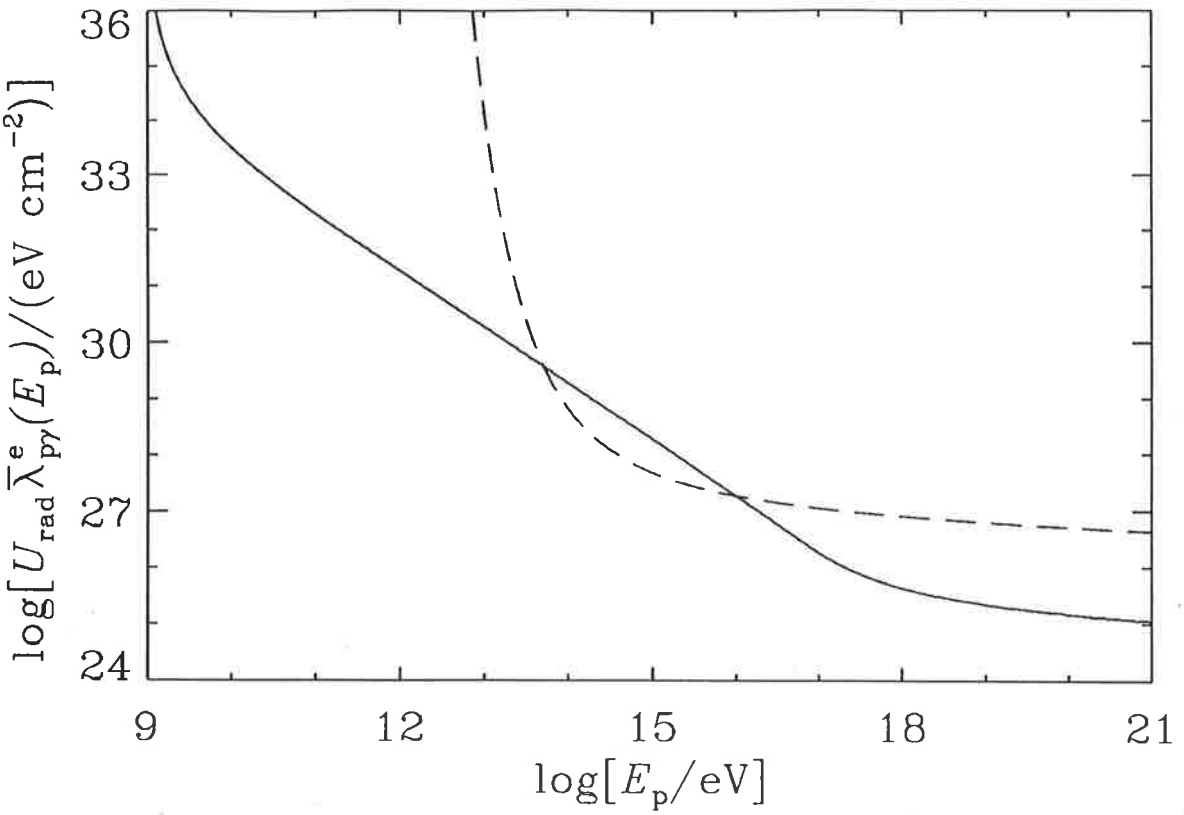

Figure 4.19: A plot of the mean path length for pair production, $\overline{\lambda}^{e}_{\gamma p}(E_p)$, as a function of proton energy, E_p. The solid curve is for a power law photon field ($\alpha = 2.0$, $\varepsilon_{min} = 10^{-2}$ eV, $\varepsilon_{max} = 10^{6}$ eV) and the dashed curve is for a black body photon field ($T = 5.0 \times 10^{4}$ K). Both of the curves have been scaled by the radiation energy density U_{rad}.

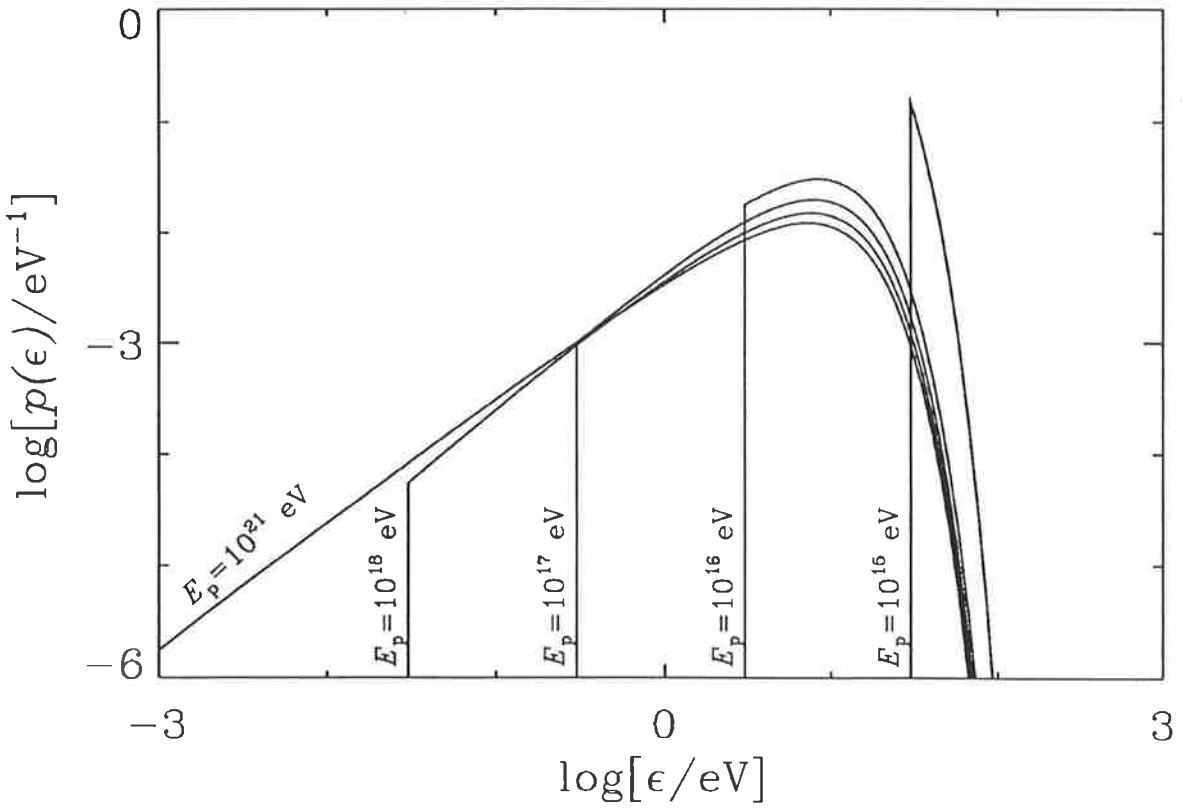

Figure 4.20: A plot of the energy distribution of the photons which interact, $p(\varepsilon)$, with a proton of energy, E_p. The proton energy for each of the curves is indicated.

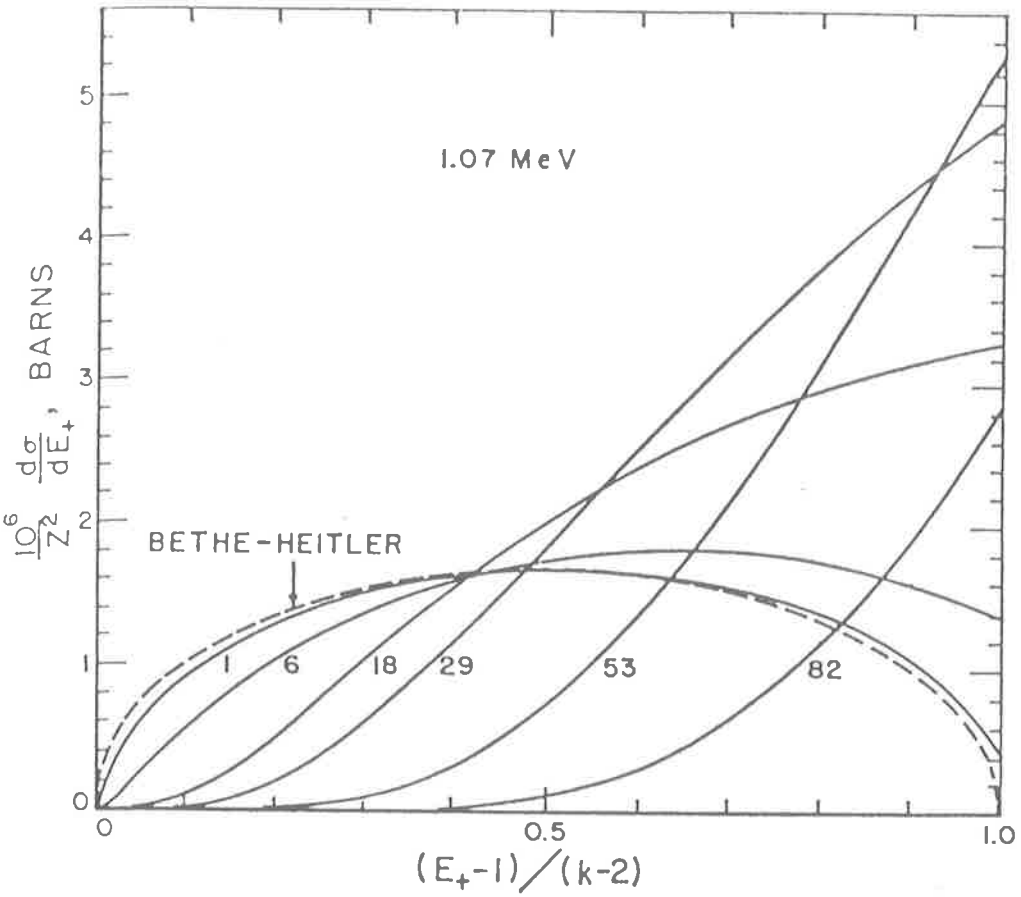

Figure 4.21: The single differential cross section for pair production, $d\sigma/dE_+$. Here, E_+ and k are the energies of the positron and the photon in the proton rest frame. All energies are in units of the electron rest mass energy. Curves are shown for a photon energy of 1.07 MeV. The dashed line shows the cross section resulting when the Bethe–Heitler formula (Formula 3D–1000 from Motz, Olsen and Koch 1969.) is used. Solid curves show the exact cross sections, and are labelled with the atomic number of the nucleus. For protons the exact differential cross section is well represented by the Bethe–Heitler formula. From Motz, Olsen and Koch 1969.

given by,

$$[\overline{\lambda}^{e}_{\gamma p}(E_p)]^{-1} = \int_{\varepsilon^{e}_{th}}^{\infty} \frac{n(\varepsilon)}{8\varepsilon^2 E_p |\vec{p}_p| c} \int_{s_{min}}^{s_{max}} \sigma^{e}_{\gamma p}(s)(s - m_p^2 c^4) ds d\varepsilon$$
$$= \int_{\varepsilon^{e}_{th}}^{\infty} \frac{n(\varepsilon)}{8\varepsilon^2 E_p |\vec{p}_p| c} \Phi_e(s_{max}) d\varepsilon, \quad (4.27)$$

where once again s_{max} is the square of the CM frame energy for a head on collision. The function $\Phi_e(s_{max})$ is plotted in Figure 4.3 and one can see that while the threshold energies are similar, $\Phi_e \sim 100\Phi_\pi$. This reflects the ratio of the total cross sections, as can be seen from Figure 4.17. As for pion photoproduction, I calculate the mean path length for interaction on both power law and black body photon fields. These are shown in Figure 4.19, and they behave in a similar manner as the mean path length for pion photoproduction, described in Section 4.2.

The energy distribution of photons which interact with the proton is,

$$p(\varepsilon) = \overline{\lambda}^{e}_{\gamma p}(E_p) \frac{n(\varepsilon)}{8\varepsilon^2 E_p |\vec{p}_p| c} \Phi_e(s_{max}), \quad (4.28)$$

for $\varepsilon^{e}_{th} \leq \varepsilon \leq \infty$. I have calculated $p(\varepsilon)$ for a blackbody photon field of temperature $T = 5.0 \times 10^4$ K, which I plot in Figure 4.20 for $E_p = 10^{15}$–10^{21} eV. When the photon threshold energy is greater than $\sim kT$ (for $E_p = 10^{15}$ eV) most of the interactions occur near threshold. However, when $\varepsilon^{e}_{th} \ll kT$ (for $E_p = 10^{16}$–10^{21} eV) most of the interactions are with photons with energy $\varepsilon \sim kT$. I have developed routines for sampling photon energies from Equation 4.28, for both power law and black body photon fields. In each case, the rejection method described in Appendix A is used. The distribution of total CM frame energies for the interaction is,

$$p(s) = \Phi_e^{-1}(s_{max}) \sigma^{e}_{\gamma p}(s)(s - m_p^2 c^4), \quad (4.29)$$

for $s_{min} \leq s \leq s_{max}$. As for pion photoproduction, the rejection method is used to sample values of s from this distribution.

Pair production interactions have been modelled exclusively, making the approximation that the proton experiences negligible recoil in the PR frame. Motz, Olsen and Koch (1969) have compiled formulae for the cross sections for pair production, and I have used Equations 3D-1000 and 3D-2000 for the differential cross sections $d\sigma/dE'_+$ and $d^2\sigma/dE'_+ d\Omega'_{+r}$ respectively. Here E'_+ is the energy of the positron in the PR frame, and Ω'_{+r} is the solid angle containing the positron's momentum measured with respect

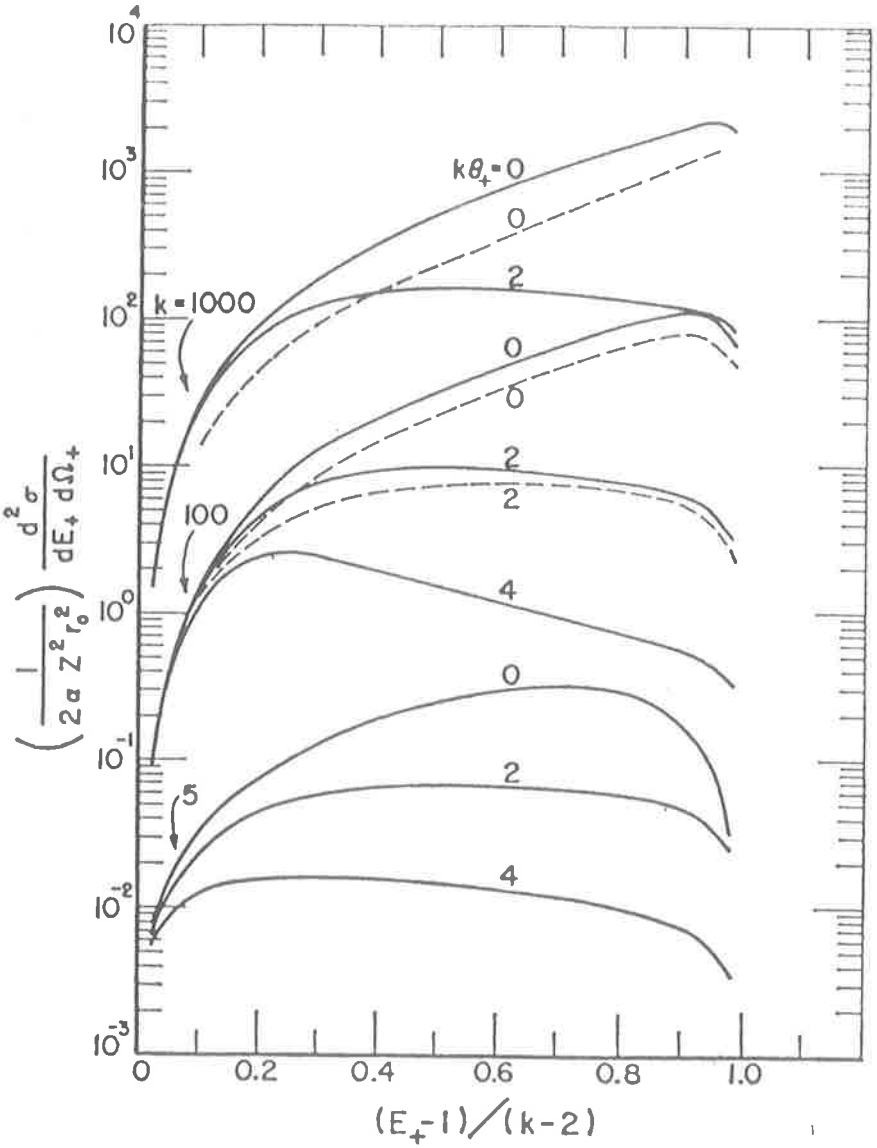

Figure 4.22: The double differential cross section for pair production, $d^2\sigma/dE_+d\Omega_+$. Here, E_+ and k are the energies of the positron and the photon in the proton rest frame, in units of the electron rest mass energy. The positron solid angle Ω_+ is also measure in the proton rest frame. Solid curves are for $k = 5$, 100 and 1000, using the Born approximation (Formula 3D–2000 from Motz, Olsen and Koch 1969). The dashed lines are calculated using the exact formula for an atomic number of 82. From Motz, Olsen and Koch 1969.

to the photon's direction. The differential cross sections are plotted in Figures 4.21 and 4.22. As the differential cross sections are expressed in the proton rest frame with directions given with respect to the photon direction, I model the interaction in the rotated proton rest (RPR) frame (c.f. the RCM frame used for the pion photoproduction), shown in Figure 4.18(c). The energy of the produced electron and positron are then transformed to the LAB frame. The reference frames used to model pair production are all shown in Figure 4.18.

Positrons are produced in the PR frame with an energy distribution (c.f. Section 3.4)

$$p(E'_+) = \frac{1}{\sigma^e_{\gamma p}(s)} \frac{d\sigma}{dE'_+}(\varepsilon', E'_+) \qquad \text{for } m_e c^2 \leq E'_+ \leq (\varepsilon' - m_e c^2), \tag{4.30}$$

where $\varepsilon' = (s - m_p^2 c^4)/2m_p c^2$, and the assumption of negligible nuclear recoil has been made to calculate the electron's energy and momentum, i.e. $\vec{p}'_- = \vec{\varepsilon}' - \vec{p}'_+$ and $E'_- = \varepsilon' - E'_+$. Once again, the rejection method has been used to sample a positron energy from this distribution. A direction for the positron is selected in the RPR frame by sampling angles θ'_{+r} and ϕ'_{+r}, defined in Figure 4.18(c), from the distributions,

$$p(\cos\theta'_{+r}) = \frac{2\pi}{\sigma^e_{\gamma p}(s)} \frac{d^2\sigma}{dE'_+ d\Omega'_+}(\cos\theta'_{+r}, E'_+, \varepsilon') \qquad \text{for } -1 \leq \cos\theta'_{+r} \leq 1, \tag{4.31}$$

and

$$p(\phi'_{+r}) = \frac{1}{2\pi} \qquad \text{for } 0 \leq \phi'_{+r} \leq 2\pi. \tag{4.32}$$

using the rejection technique for $\cos\theta'_{+r}$, and using the inverse function method for ϕ'_{+r} (see Appendix A). As I have assumed that the proton does not recoil in the PR frame, once the energy and direction of the positron have been sampled, one can solve for the energy of the electron. Conservation of transverse and longitudinal components of momentum, relative to the photon's direction in the RPR frame gives the equations,

$$|\vec{p}'_{+r}| \sin\theta'_{+r} = |\vec{p}'_{-r}| \sin\theta'_{-r} \tag{4.33}$$

$$\varepsilon' = |\vec{p}'_{+r}| \cos\theta'_{+r} + |\vec{p}'_{-r}| \cos\theta'_{-r}, \tag{4.34}$$

where $\vec{p}'_{-r}$ is the electron's momentum in the RPR frame, and θ'_{-r} is the angle between $\vec{p}'_{-r}$ and the x'_r axis. These Equations are solved for θ'_{-r} and $|\vec{p}'_{-r}|$ resulting in

$$\tan\theta'_{-r} = \frac{|\vec{p}'_{+r}| \sin\theta'_{+r}}{\varepsilon' - |\vec{p}'_{+r}| \cos\theta'_{+r}} \tag{4.35}$$

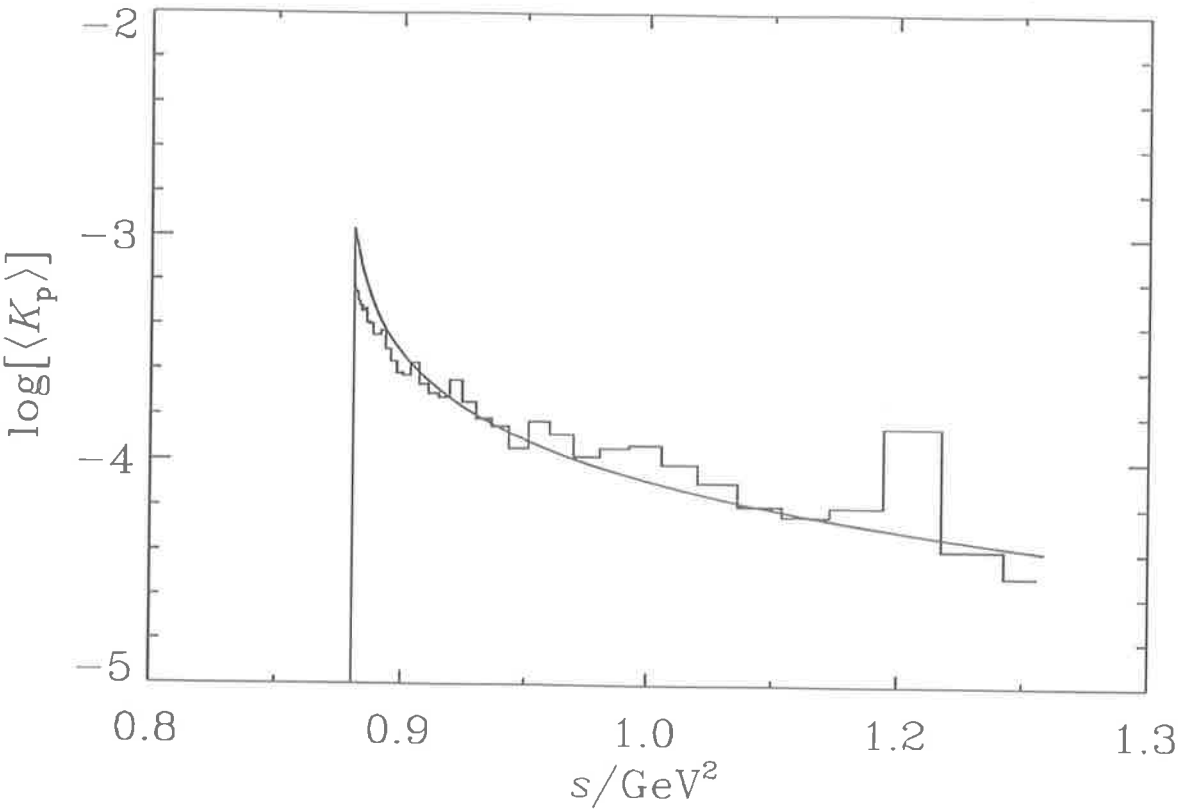

Figure 4.23: A plot of the mean inelasticity for pair production, $\langle K_p \rangle$, versus the square of the total CM frame energy s. The histogram shows the results from the Monte Carlo simulation described in the text. For comparison, fits to the numerical calculations of Chodorowski and Zdziarski (1990) are also shown (solid curve).

and

$$|\vec{p}'_{-r}| = |\vec{p}'_{+r}|\frac{\sin\theta'_{+r}}{\sin\theta'_{-r}} \tag{4.36}$$

In the RPR frame, the transverse components of the electron and positron's momentum are equal and opposite, and hence $\phi'_{-r} = \pi + \phi'_{+r}$.

To transform from the RPR frame to the LAB frame, I first transform to the PR frame by applying a rotation through angle θ' about the z'_r axis. Thus, the angle between the positron's momentum and the x' axis (aligned with the boost β_r) is

$$\cos\theta'_+ = -[cos\theta'_{+r}\cos\theta' + \sin\theta'_{+r}\sin\theta'\sin\phi'_{+r}], \tag{4.37}$$

where θ' is given by the aberration formula (see Equation 3.8),

$$\sin\theta' = \frac{\sin\theta}{\gamma_r(1-\beta_r\cos\theta)}. \tag{4.38}$$

A similar equation can be found for the electron. Hence, the energy of the positron in the LAB frame is

$$E_+ = \gamma_r(E'_+ + |\vec{p}'_+|c\beta_r\cos\theta'_+), \tag{4.39}$$

with a similar expression for the electron. Conservation of energy gives the final energy of the proton as,

$$E = E_p + \varepsilon - E_+ - E_-. \tag{4.40}$$

4.3.1 Mean Inelasticity for Pair Production

As for pion photoproduction, I have calculated the mean inelasticity for pair production using a Monte Carlo Simulation. The results are shown in Figure 4.23. Also shown is the mean inelasticity calculated numerically by Chodorowski and Zdziarski (1990), represented by the analytical fit

$$\langle K_p(x)\rangle = 4\frac{m_e}{m_p}x^{-1}[1 + 0.3957\ln(x-1) + 0.1\ln^2(x-1) + 0.0078\ln^3(x-1)], \tag{4.41}$$

where $x = \varepsilon'/m_ec^2$ is the ratio of the photon's energy in the PR frame and the electron's rest mass. For $\sqrt{s}$ greater than $\sim$ 0.95 GeV, the curve and the histogram are in agreement. However, at threshold there is a departure of a factor of $\sim$ 2. As the results of Chodorowski and Zdziarski (1990) have not yet been published, it has not been possible to account for this apparent discrepancy.

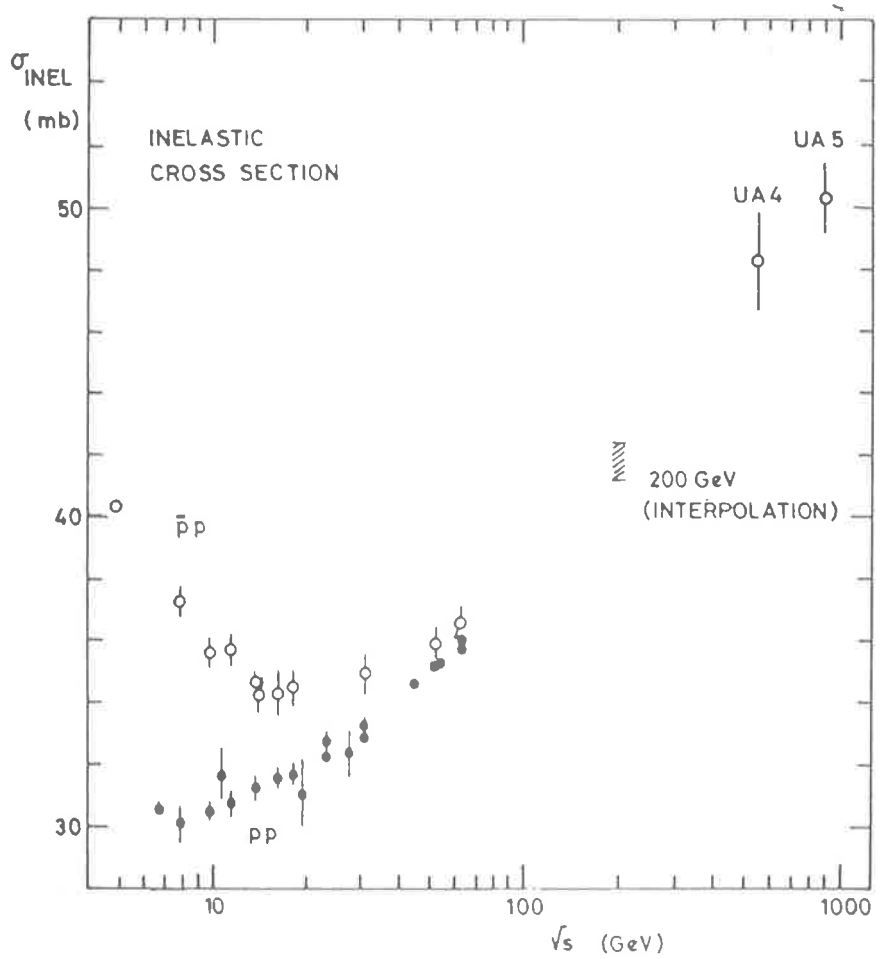

Figure 4.24: A plot of the inelastic cross section for proton–proton interactions, as a function of the total CM frame energy. The solid circles are pp data, while the open circles are $p\overline{p}$ data. From Alner *et al.* (1986).

4.4 Proton–Proton Interactions

In contrast to pion photoproduction and pair production, proton–proton (pp) interactions are straightforward to model. Consider a proton of energy E_p traversing diffuse matter consisting of relatively low energy protons. In this case, the mean path length for interaction is given by $[\overline{\lambda}_{pp}(E_p)]^{-1} = n_p \sigma_{pp}(s)$, where n_p is the number density of the diffuse protons, and $\sigma_{pp}(s)$ is the total inelastic cross section as a function of $s = m_p^2 c^4 + 2E_p m_p c^2$. The total cross section is shown in Figure 4.24.

Hillas (1979) has made fits to the data and assumed radial scaling to produce the differential spectrum of particles, dn/dx, resulting from a pp interaction,

$$x\frac{dn}{dx} = F_{pp\to c}(x) H_c(E), \tag{4.42}$$

where x is the ratio of produced particle's energy to the beam energy E'_p. The functions $F_{pp\to c}(x)$ and $H_c(E)$ are given below for pions,

$$\begin{aligned} F_{pp\to\pi^+}(x) = F_{pp\to\pi^-}(x) = F_{pp\to\pi^\circ}(x) &= 1.22(1-x)^{3.5} + 0.98\exp(-18x) \\ H_{\pi^+}(E) = H_{\pi^-}(E) = H_{\pi^\circ}(E) &= \left[1 + \frac{0.4}{E - 0.14}\right]^{-1} \end{aligned} \tag{4.43}$$

Thus, to calculate the total spectrum of particles, it is simply a matter of convolving the spectrum of protons which interact with the spectrum of particles produced per interaction, given above.

4.5 Pion Decay

Neutral pions decay into two γ–rays ($\pi^o \to 2\gamma$) with a branching ratio of 98.798% (Particle Data Group, 1990). Clearly, the CM frame energy of the γ–rays is half of the rest energy of the pion,

$$E^\star_\gamma = \frac{m_\pi c^2}{2}. \tag{4.44}$$

The pion is spinless and hence the γ–rays will be produced isotropically in the CM frame. Thus, the distribution of γ–ray energies in the LAB frame is (c.f. Equation 3.15),

$$\begin{aligned} p(E_\gamma) &= \frac{2}{2\gamma_r \beta_r E^\star_\gamma} \\ &= \frac{2}{|\vec{p}_\pi| c}, \end{aligned} \tag{4.45}$$

for $\gamma_r E^\star_\gamma(1-\beta_r c) \leq E_\gamma \leq \gamma_r E^\star_\gamma(1+\beta_r c)$, since $c|\vec{p}_\pi| = E_\pi \beta_r = \gamma_r m_\pi c^2 \beta_r$. Here β_r and γ_r are the boost and Lorentz gamma required to get to the pion rest frame. The factor of 2 in the numerator arises because 2 γ–rays are produced, each contributing the same spectrum to the total.

Consider a spectrum of pions, $\mathcal{Q}_\pi(E_\pi)$, which decay. The spectrum of γ–rays produced is,

$$\begin{aligned}\mathcal{Q}_\gamma(E_\gamma) &= \int_{E_\pi^{min}}^{E_\pi^{max}} p(E_\gamma)\mathcal{Q}_\pi(E_\pi)dE_\pi \\ &= \int_{E_\gamma+\frac{m_\pi^2 c^4}{4E_\gamma}}^{\infty} \frac{2}{|\vec{p}_\pi|c}\mathcal{Q}_\pi(E_\pi)dE_\pi, \end{aligned} \tag{4.46}$$

where the integration bounds are found as described in Section 3.3. For example, consider a power law spectrum of pions $\mathcal{Q}_\pi(E_\pi) = \mathcal{Q}_o E_\pi^{-\alpha}$, for $E_\pi^{min} \leq E_\pi \leq E_\pi^{max}$ and $\alpha \geq 0$. The spectrum of γ–rays produced is

$$\mathcal{Q}_\gamma(E_\gamma) \simeq \begin{cases} \frac{2\mathcal{Q}_o}{\alpha}[E_\gamma^{-\alpha} - (E_\pi^{max})^{-\alpha}] & \text{for } E_\gamma > E_\pi^{min} \\ \frac{2\mathcal{Q}_o}{\alpha}[(E_\pi^{min})^{-\alpha} - (E_\pi^{max})^{-\alpha}] & \text{for } E_\gamma \leq E_\pi^{min} \end{cases}, \tag{4.47}$$

for $E_\gamma \gg m_\pi^2 c^4$ and $E_\pi^{min} \gg m_\pi^2 c^4$. Thus, for energies greater than E_π^{min} the spectrum of γ–rays mirrors the spectrum of primaries, i.e. $\mathcal{Q}_\pi(E_\gamma) \propto E_\gamma^{-\alpha}$ for $E_\pi^{min} < E_\gamma < E_\pi^{max}$.

Charged pions decay into a muon and muon neutrino ($\pi^\pm \rightarrow \mu^\pm + \nu_\mu(\overline{\nu}_\mu)$) with a branching ratio of 100% (Particle Data Group, 1990). The decay is very similar to π^o decay. However, in this case only one of the products is massless, and therefore the particle distributions are not the same. The CM frame energies of the products are (see Equation 3.12),

$$E^\star_\mu = \frac{m_\pi^2 c^4 + m_\mu^2 c^4}{2m_\pi c^2} \tag{4.48}$$

$$E^\star_\nu = \frac{m_\pi^2 c^4 - m_\mu^2 c^4}{2m_\pi c^2}. \tag{4.49}$$

Hence, the distributions of particle energies produced in the LAB frame are (see Section 3.3),

$$p(E_\mu) = \frac{1}{2\gamma_{cm}\beta_{cm}|\vec{p}^\star_\mu|c} \tag{4.50}$$

$$p(E_\nu) = \frac{1}{2\gamma_{cm}\beta_{cm}E^\star_\nu}. \tag{4.51}$$

The spectra of particles which result when pions with energy spectrum $\mathcal{Q}_\pi(E_\pi)$ decay are

$$\mathcal{Q}_\mu(E_\mu) = \int_{E_\pi^{min}}^{E_\pi^{max}} \frac{m_\pi c^2}{2|\vec{p}^\star_\pi||\vec{p}^\star_\mu|c^2}\mathcal{Q}_\pi(E_\pi)dE_\pi \tag{4.52}$$

$$\mathcal{Q}_\nu(E_\nu) = \int_{\frac{E_\nu^{\star 2}+E_\nu^2}{2E_\nu^\star E_\nu}}^{\infty} \frac{m_\pi c^2}{2|\vec{p}_\pi^{\star}|cE_\nu^\star} \mathcal{Q}_\pi(E_\pi) dE_\pi \tag{4.53}$$

using $\gamma_{cm}\beta_{cm} = |\vec{p}_\pi|c/m_\pi c^2$. For the muon spectrum, the integration bounds, $E_\pi^{\min}$ and $E_\pi^{\max}$, are given by Equation 3.19. If the pion spectrum is a power law, such as given above for π^o decay, then the spectra of muons and neutrinos are power laws with the same index.

4.6 Muon Decay

Muons decay via the channels

$$\begin{aligned} \mu^+ &\rightarrow e^+ + \nu_e + \overline{\nu}_\mu \\ \mu^- &\rightarrow e^- + \overline{\nu}_e + \nu_\mu, \end{aligned}$$

with a branching ratio of 100% (Particle Data Group 1990). Zatsepin and Kuz'min (1962) have calculated the distribution of particles produced in the muon rest frame, using the approximation that the muon is unpolarised. The spectrum of neutrinos, $\mathcal{Q}_{\nu_e}(E_{\nu_e})$ and $\mathcal{Q}_{\nu_\mu}(E_{\nu_\mu})$, produced when muons with a spectrum, $\mathcal{Q}_\mu(E_\mu)$, decay is

$$\mathcal{Q}_{\nu_e}(E_{\nu_e}) = \int_{E_\mu^{min}}^{E_\mu^{max}} \frac{1}{2} \left[p(E_{\nu_e}) + p(E_{\overline{\nu}_e})\right] \mathcal{Q}_\mu(E_\mu) dE_\mu \tag{4.54}$$

$$\mathcal{Q}_{\nu_\mu}(E_{\nu_\mu}) = \int_{E_\mu^{min}}^{E_\mu^{max}} \frac{1}{2} \left[p(E_{\nu_\mu}) + p(E_{\overline{\nu}_\mu})\right] \mathcal{Q}_\mu(E_\mu) dE_\mu \tag{4.55}$$

where $p(E_{\nu_e}) = p(E_{\nu_\mu})$ are the spectra of electron neutrinos and muon neutrinos produced in the muon rest frame, by the decay of a μ^+ (see Zatsepin and Kuz'min 1962). Similarly, $p(E_{\overline{\nu}_e}) = p(E_{\overline{\nu}_\mu})$, are the spectra of electron and muon anti-neutrinos produced. In Equations 4.54 and 4.55, I have assumed that the muon spectrum consists equal numbers of μ^+s and μ^-s. Similarly and the spectrum of electrons produced is

$$\mathcal{Q}_e(E_e) = \int_{E_\mu^{min}}^{E_\mu^{max}} \frac{1}{2} \left[p(E_{e^-}) + p(E_{e^+})\right] \mathcal{Q}_\mu(E_\mu) dE_\mu, \tag{4.56}$$

where $p(E_{e^-}) = p(E_{\overline{\nu}_\mu})$ and $p(E_{e^+}) = p(E_{\nu_\mu})$.

4.7 Summary

In this Chapter, the modelling of pion photoproduction, pair production and proton–proton interactions was discussed in detail. Pion photoproduction was modelled exclusively near threshold using the fits to the data given by Genzel, Joos and Pfeil (1973),

and was modelled inclusively above the resonance region using the data of Meffeit *et al.* (1972). Pair production was modelled exclusively using the formulae for the differential cross sections given by Motz, Olsen and Koch (1969). The fits of Hillas (1979) were used to model *pp* interactions. The techniques developed in this chapter for modelling these interactions will be used in Chapter 6 to calculate the spectrum of pions produced in the nucleus of an active galaxy. Once the pion spectra have been obtained, they will be decayed using the formulae described in Sections 4.5 and 4.6 to calculate the spectrum of muon neutrinos and anti–neutrinos produced in active galactic nuclei.

Chapter 5

Observation of Astrophysical Neutrinos

5.1 Introduction

Neutrinos interact weakly with matter, making the design of neutrino telescopes challenging. The cross section for interaction between a neutrino, ν, and a nucleon, N, which produces a charged lepton is (Gaisser 1990)

$$\sigma_{\nu \mathrm{N}} \simeq 5.0 \times 10^{-39} \left(\frac{E_\nu}{\mathrm{GeV}} \right) \quad \mathrm{cm}^2. \tag{5.1}$$

Hence, unless the sources of neutrinos are very strong, neutrino telescopes must be very large. Neutrino interactions with matter occur via the channels (see e.g. Berezinskiĭ *et al.* 1990),

$$\nu_{\mathrm{e}}(\overline{\nu}_e) + N \rightarrow e^-(e^+) + X \tag{5.2}$$

$$\nu_\mu(\overline{\nu}_\mu) + N \rightarrow \mu^-(\mu^+) + X \tag{5.3}$$

where X represents all other particles which are produced. For example, electron antineutrinos can interact with protons via inverse neutron decay, $\overline{\nu}_e + p \rightarrow e^+ + n$. Electron antineutrinos may also interact with electrons via the Glashow resonance

$$\overline{\nu}_{\mathrm{e}} + e^- \rightarrow W^- \rightarrow \mathrm{hadrons}, \tag{5.4}$$

where the resonance energy of the antineutrino is 6.3×10^6 GeV (see e.g. Berezinskiĭ *et al.* 1990). Electrons produced in νN interactions lose energy quickly in matter via

an electromagnetic cascade, and therefore neutrino telescopes are generally designed as high energy muon detectors. Alternatively, some of the telescopes are designed to detect the electromagnetic cascades initiated by the electrons or the hadrons produced by W^- decay.

In this Chapter, the techniques used for detecting the products of neutrino interactions with matter are discussed. Over the past decade, there have been a number of proposals for neutrino telescopes, and some of these are reviewed. Their status, as of early 1992 is also discussed. The Chapter is concluded with a discussion of how the signal in a neutrino telescope may be calculated. As an example, the neutrino signal from SN 1987A is calculated.

5.1.1 High Energy Muon Detectors

At high energies, relativistic beaming means that the direction of the produced muon is well correlated with the direction of the original neutrino. The average angle between the muon's direction and the neutrino's direction is approximately (see e.g. Berezinskiĭ *et al.* 1990)

$$\overline{\theta} \simeq 2.6 \left(\frac{E_\mu}{100 \text{ GeV}} \right)^{-0.5} \quad \text{degrees.} \tag{5.5}$$

Hence, for neutrinos with energy greater than $\sim$ 700 GeV on average the direction of the muon will be within 1° of the neutrino's direction. Thus, to detect high energy neutrinos (with energies greater than $\sim$ 1 TeV) a muon detector only needs to have an angular resolution of approximately 1°.

A high energy muon will radiate Čerenkov light if its velocity is greater than the velocity of light in the medium. The Čerenkov emissions may be detected by using a large array of photomultiplier tubes in a transparent medium such as water or ice. The use of ice as a detector medium has the advantage of providing a solid base and framework within which to work, greatly simplifying the engineering of the detector (see e.g. Barwick *et al.* 1991b, 1992). In such an array, the direction of the muon may be reconstructed using the relative timing of the photomultipliers triggered by the muon's passage.

The main source of noise in muon detectors comes from the large flux of muons, produced when cosmic rays interact with the atmosphere. A one TeV muon has a range of about 2 kilometres in water and about 450 metres in rock (Berezinskiĭ *et al.* 1990).

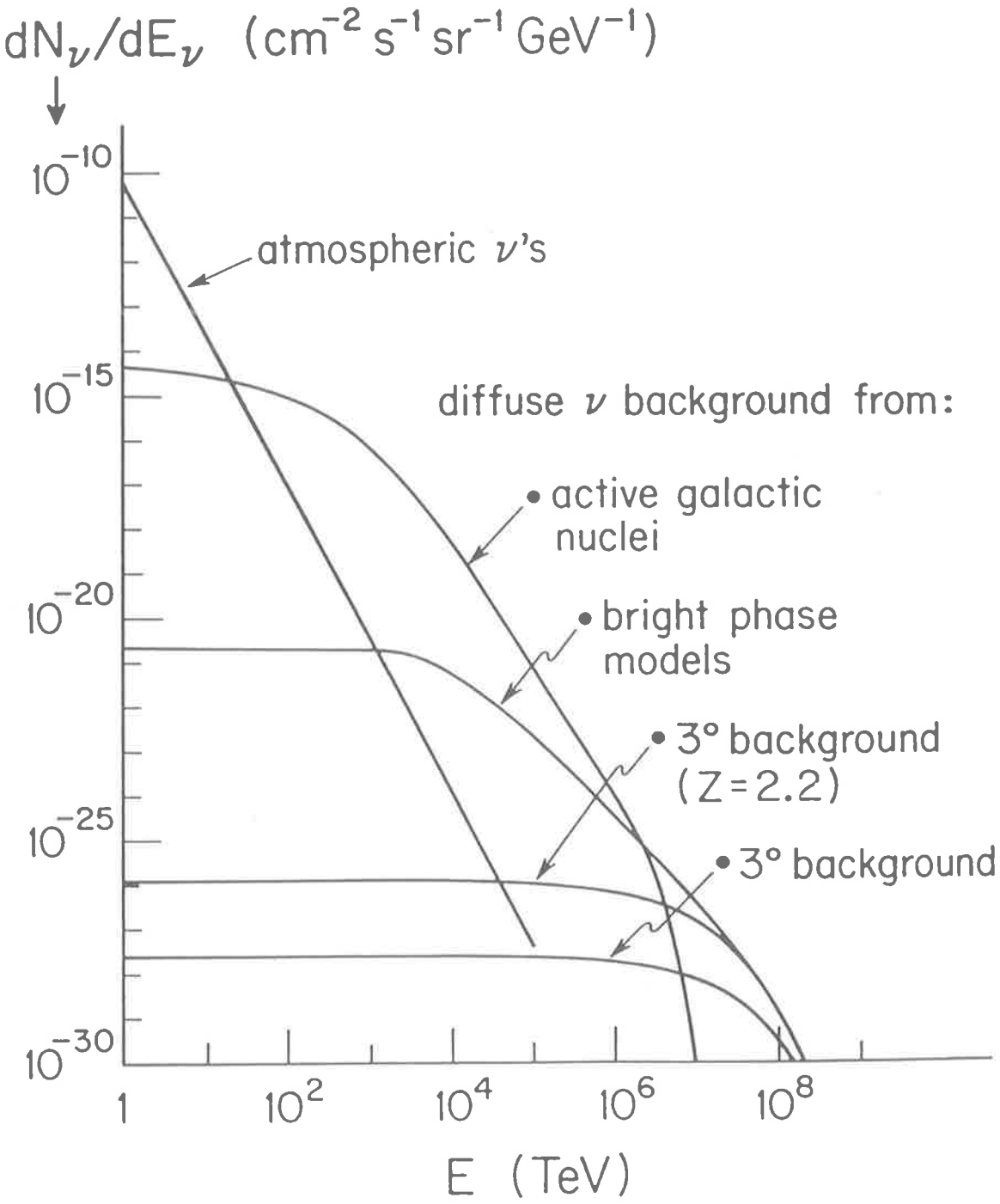

Figure 5.1: The flux of high energy neutrinos, from the decay of charged pions produced in air showers (curve labelled "atmospheric ν's"). Also shown are other astrophysical sources of diffuse neutrino background radiation. Note that the flux from active galactic nuclei is the original incorrect version from Stecker *et al.* (1991a,b), and is a factor of ~ 17 too high (Szabo and Protheroe 1992a). From Barwick *et al.* (1991b).

Hence, one method of reducing the noise from muons produced in the atmosphere is to shield the detector by placing it at a depth of several kilometres. One disadvantage of this approach is that it is difficult and expensive to build a detector at such a great depth. Another solution is to discriminate against the predominantly downward going atmospheric muons in a surface detector by looking for upward going muons. Upward going muons result from neutrinos which pass through the Earth and interact below the telescope. A disadvantage of this approach, is that the field of view of the telescope is greatly reduced.

Another source of noise comes from the neutrinos produced from the decay of the charged pions present in cosmic ray air showers. The differential flux of "atmospheric" neutrinos is shown in Figure 5.1 along with other astrophysical sources of diffuse neutrino radiation. Note that in this diagram the diffuse neutrino background from AGN is the original incorrect version from Stecker *et al.* (1991a,b), and should be scaled down by a factor of $3^{2.6} \sim 17$ (Szabo and Protheroe 1992a). The signal decreases with energy, and hence it is advantageous to have a high muon energy threshold as this can improve signal to noise in the detector.

Another means of detecting high energy muons is by using the ionisation they induce during their passage through the detector. Directional information is obtained from the timing of the passage of the muon through several layers of detectors.

5.1.2 Electromagnetic Cascade Detectors

Muons, electrons and hadrons produced in νN interactions can initiate electromagnetic cascades, which may be detected by several different techniques. Showers initiated in ice by high energy muons produce microwave Čerenkov radiation. An array of microwave antennas could be used to detect the radiation (see e.g. Boldyrev *et al.* 1991). In contrast, the passage of a ultra high energy shower in the atmosphere may be observed by N_2 flourescence (see e.g. Cassiday (1989) and Boyer (1991)). Another interesting idea is that the cascades could be detected acoustically (Bowen 1979); ionisation losses from the cascade heat the medium, initiating a pressure wave which could be detected by an array of pressure tranducers. All three of the above methods of detecting high energy electromagnetic cascades suffer from having very high energy thresholds.

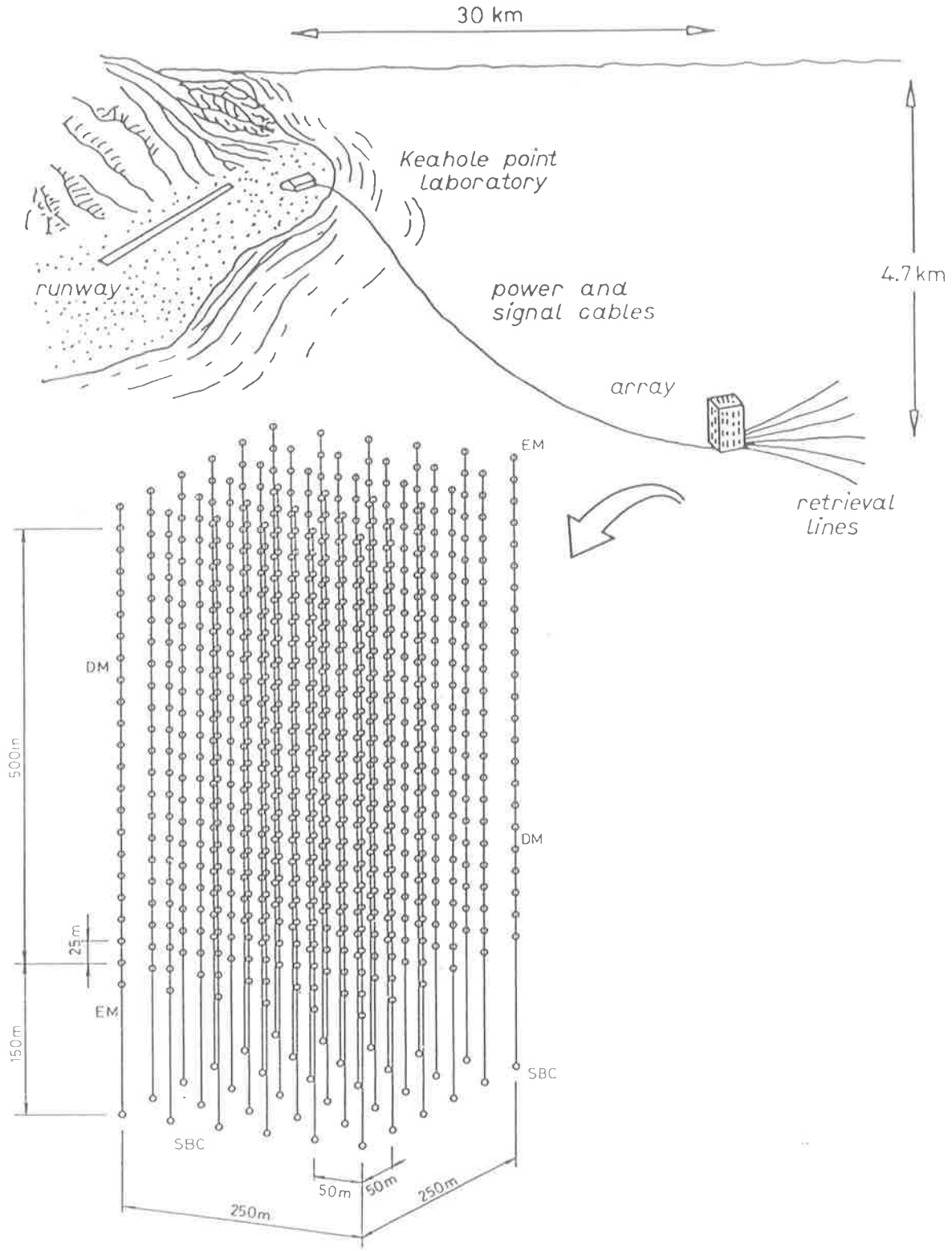

Figure 5.2: A schematic diagram of the location of the DUMAND telescope off the coast of Hawaii. An expanded view of the original array is shown, with the 756 detector modules indicated by the open circles labelled DM. The modules marked EM are environmental modules, whereas the ones marked SBC are string control modules. The present phase of the experiment, DUMAND II, will have an effective area of 20,000 m^2, and should be large enough to perform meaningful astrophysical observations. Adapted from Grieder (1986).

5.2 Neutrino Telescopes

In Sections 5.2.1–5.2.7, some of the proposed neutrino telescopes are reviewed. Only those telescopes designed specifically for high energy neutrino astronomy are reviewed, with the exception of the HiRes Fly's Eye, which is included because of its high energy threshold and its large detection area. The status of the experiments prior to early 1992 is also reviewed.

5.2.1 DUMAND

The Deep Underwater Muon And Neutrino Detector (DUMAND), is a proposed neutrino telescope consisting of an array of 756 detector modules, in a volume of (250 $\times$ 250 $\times$ 500) m^3 (Grieder 1986). The telescope is a water Čerenkov detector, and is to be placed approximately 4.7 km beneath the ocean surface approximately 30 km off the coast of Hawaii, as illustrated in Figure 5.2. The benefits of placing the detector at a great depth in the ocean are that the water acts as cosmic ray shielding, as a dark room, and as a uniform detector medium. The detector also has approximately 100% sky coverage, and the potential for virtually unlimited expansion, unlike underground detectors. The disadvantages come primarily from the technical difficulty of designing and building a large telescope which will operate at a depth of $\sim$ 5 km. As a result, much new technology has been developed specifically for the DUMAND detector.

The idea for a large neutrino telescope in the deep ocean arose in the early 1970's, and the DUMAND proposal was submitted to the U. S. Department of Energy in 1983. At present the first phase of the telescope construction, the deployment of a short prototype string of detector modules, has been successfully completed (Stenger 1990). The second phase, deployment of an octagonal array of detector strings, has received endorsement by the U. S. High Energy Physics Advisory Panel. *DUMAND II*, as the second phase has been dubbed, consists of 216 photomultipliers, has a hardware energy threshold of $\sim$ 25 GeV and will have an effective area of 20,000 m^2 (Learned and Stanev 1991). An angular resolution of 1° is predicted and this means that DUMAND II will have comparable sensitivity to the GRANDE proposal described in Section 5.2.4.

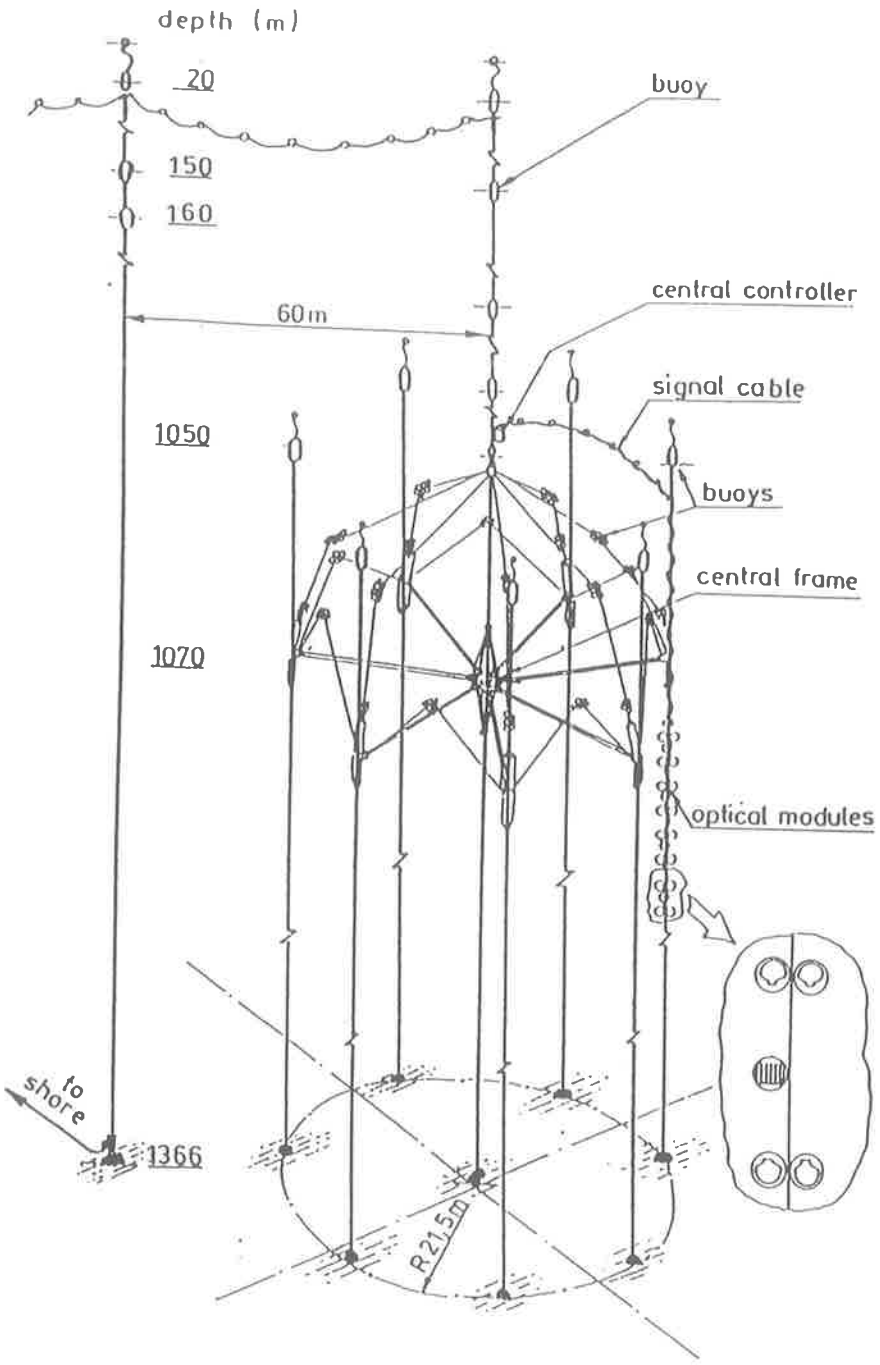

Figure 5.3: A schematic diagram of the NT–200 phase of the BAIKAL experiment. The eight string design is shown, and only one of the signal cables has been included for simplicity. One of the detector modules is shown in expanded view, illustrating the combination of upward and downward facing photomultipliers used in each module. From Belolaptikov *et al.* (1991a).

5.2.2 BAIKAL

The BAIKAL experiment is a muon detector similar to the DUMAND proposal to be placed in Lake Baikal in Siberia (Belolaptikov *et al.* 1991a, Belolaptikov *et al.* 1991b). The ultimate goal of the BAIKAL experiment (Belolaptikov *et al.* 1990) is to build a full scale detector with a volume of 10^7 m^3 (c.f. $\sim 3\times10^7$ m^3 for the original DUMAND proposal). The detector will be placed at a depth of 1350 m, approximately 4 km from the shore near the mouth of the Angara river. The telescope is based on the water Čerenkov principle. However, it is not completely shielded from atmospheric cosmic ray muons because it is not deep enough, and so can only look for neutrinos which interact in the rock below the detector. Lake Baikal has a stable surface of ice for two months in late winter which makes construction of the telescope technically easier than the DUMAND project. However, there are still many technical difficulties, and a photomultiplier has been designed specifically for the BAIKAL experiment. The benefits of using lake Baikal as the site for a neutrino detector are many. For example, high water transparency, a lower optical background than the ocean, a steep smooth lake bed, and the absence of strong currents.

The project began in 1980 with a site and feasibility study. A short stationary string of detector modules was successfully deployed in 1984 (Belolaptikov *et al.* 1990), and yielded stringent limits on the flux of heavy magnetic monopoles. At present, planning and construction are underway for a second phase detector called *NT–200.* It was originally planned to have six strings of eight detector modules, however Monte Carlo calculations have shown that an array of eight strings is preferable, as there is a marked improvement in event quality. The detector array is shown schematically in Figure 5.3. NT–200 will have an effective area of 2000–4000 m^2, depending on the muon's energy (c.f. 20,000 m^2 for DUMAND II), an average angular resolution of $\sim 1°$, and an aperture of 60°–70°. During 1991/1992 it is hoped that two strings of NT–200 can be deployed and that the second phase of the BAIKAL experiment will be completed by 1993. However, it is difficult to imagine the construction of the Lake Baikal detector being completed, given the present economic circumstances in Russia.

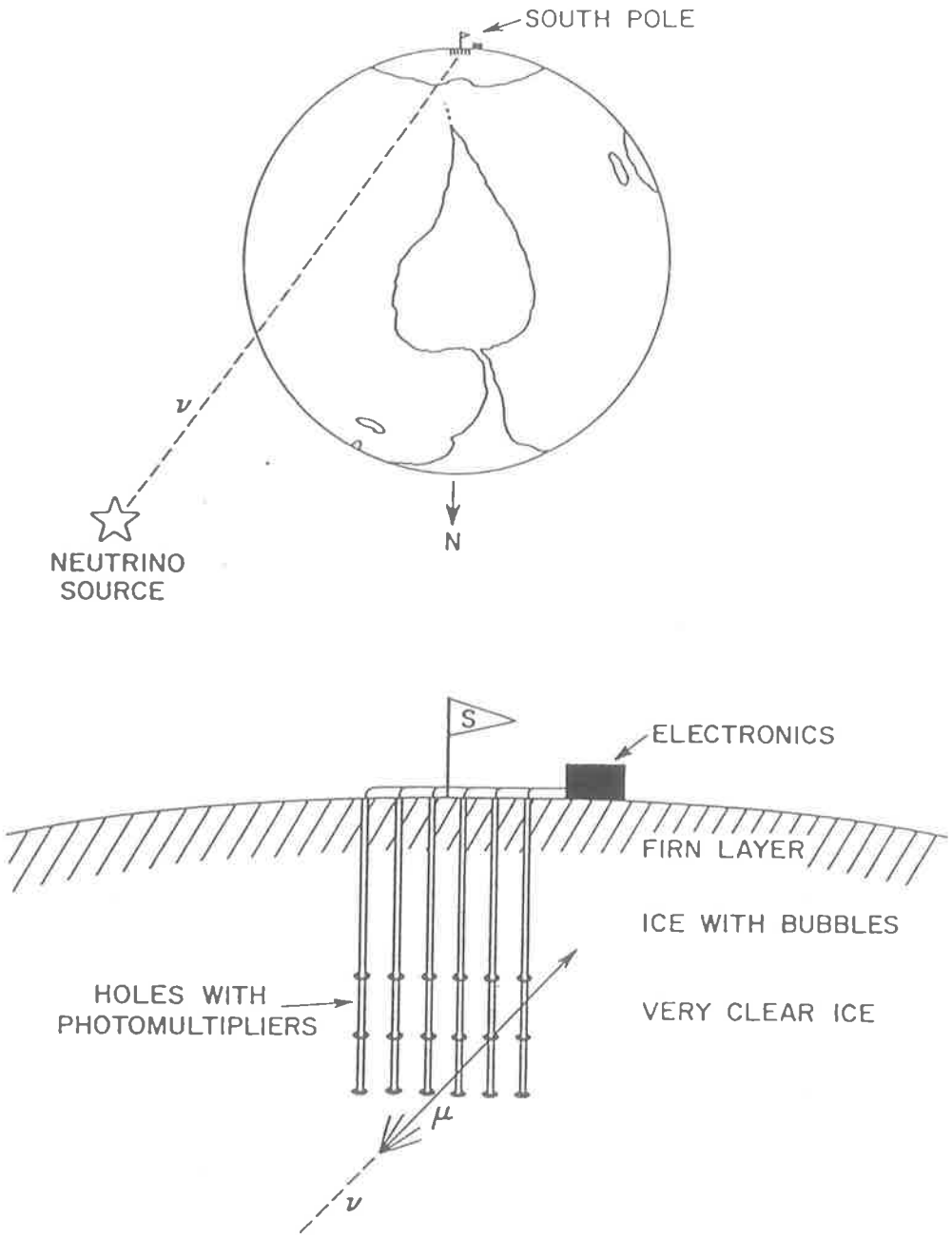

Figure 5.4: A schematic diagram of AMANDA. The top diagram illustrates how a Southern Pole telescope could be used to observe a northern sky source. The bottom diagram shows the passage of a neutrino induced muon through the detector array placed in the deep very clear ice of Antarctica. From Halzen, Learned and Stanev (1989).

5.2.3 AMANDA

A very promising and cost effective proposal for a neutrino telescope is the Antarctic Muon And Neutrino Detector Array (AMANDA), shown schematically in Figure 5.4. This detector is based on the same general principle as DUMAND. However, the deep ice of Antarctica is proposed as a detector medium (Barwick *et al.* 1991a). The array will be placed at a depth of approximately one kilometre, where it is hoped that the ice will be largely bubble free and therefore suitable for the Čerenkov technique. Construction of a neutrino telescope in polar ice has many advantages (Barwick *et al.* 1991a; Barwick *et al.* 1991b, 1992). For example, AMANDA will have virtually unlimited potential for expansion and will use a stable and sterile detector medium. Antarctic ice has a much lower concentration of β emitters than the ocean and no bioluminescence. As a southern hemisphere telescope, it will also be able to observe northern hemisphere sources continuously. This is advantageous as most of the high energy γ–ray telescopes are in the northern hemisphere. Therefore, *simultaneously* neutrino and γ–ray observations of sources in the northern sky could be made (Barwick *et al.* 1991a). The main disadvantage, is that the Antarctic is an inhospitable environment in which to build and operate a detector.

The maximum attenuation length in polar ice has been measured in Greenland (Lowder *et al.* 1991) and found to be greater than 18 metres. This is comparable to that for ice produced under pressure in the laboratory. An *in situ* measurement of the maximum attenuation length in Antarctic ice will be made in the 1991–1992 Antarctic campaign (Barwick *et al.* 1991a) by placing a string of detector modules at a depth of 500–1000 m. The results will influence the direction in which the design of the subsequent telescope will proceed.

5.2.4 GRANDE

In contrast to the DUMAND proposal, the Gamma–Ray And Neutrino DEtector (GRANDE) will be built on the Earth's surface and will discriminate against cosmic rays muons (Haines 1989, Sobel 1990). GRANDE consists of two semi independent detectors (an air shower array and a neutrino telescope) which operate on the water Čerenkov principle. The telescope, shown schematically in Figure 5.5, will be built

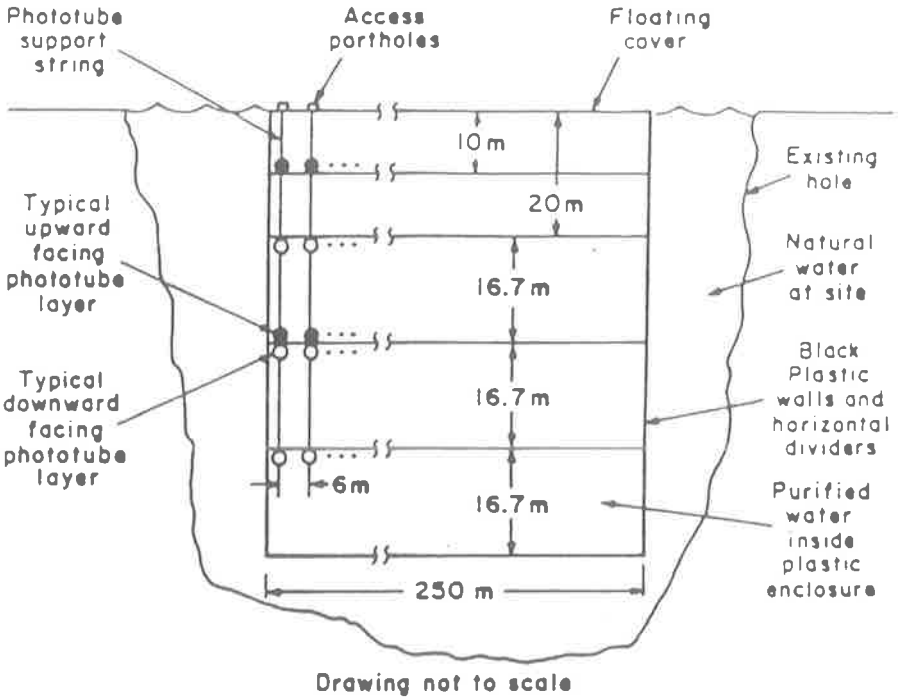

Figure 5.5: A schematic diagram of the GRANDE γ–ray and neutrino detector. The muon detector consists of three optically isolated planes of downward facing photomultiplier tubes, signified by the open circles. The proposed telescope will have an area of approximately 62,500 m^2. From Haines (1989).

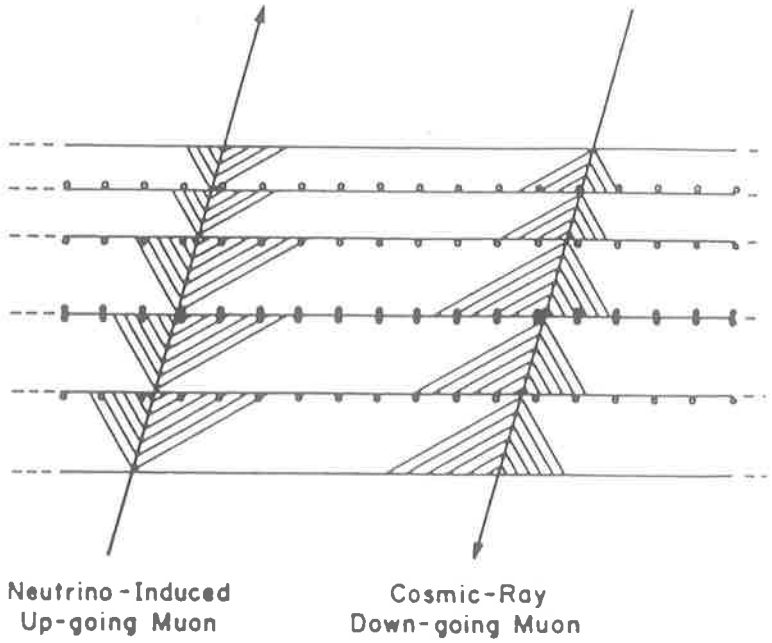

Figure 5.6: A schematic diagram, showing the passage of an neutrino induced muon through the GRANDE detector. The passage of a typical cosmic ray muon is also shown for comparison. From Haines (1989).

in a covered lake and will have a surface area of (250 m×250 m)= 62,500 m^2. The neutrino detector consists of three optically–isolated downward–facing planes of photomultipliers. When a neutrino interacts in the rock beneath the detector and produces a muon which moves upward through the telescope, the Čerenkov light is detected by the downward facing photomultiplier tubes as depicted in Figure 5.6. The direction of the muon is calculated from the relative timing of detection by the photomultiplier tubes. An average angular resolution of 0.8° is predicted.

One of the main disadvantages of the GRANDE proposal is that it has a field of view which is much less than 100%. The main benefit gained from building a surface detector is that no new technology is required. The telescope could, in principle at least, be built immediately (Haines 1989).

5.2.5 SINGAO Neutrino Telescope

The Southern Italy Neutrino and Gamma Astronomy Observatory (SINGAO),has proposed the construction of a surface neutrino telescope of area greater than 10^4 m^2 (De Palma *et al.* 1990, Pistilli 1991, Auriemma 1991). The detector will consist of high angular resolution tracking modules, each of which will have an area of (40 m×40 m)= 1,600 m^2. The tracking modules consist of nine planes of resistive plate counters separated by 50 cm layers of concrete as shown in Figure 5.7. An angular resolution of approximately 10^{-2} radians ($\sim 0.6°$) is expected for muons with energy $E_\mu \geq 1.5$ GeV traversing greater than 5 metres of concrete. As for the Čerenkov detectors, the SINGAO neutrino telescope will use the time of flight of the muon's path to reconstruct its direction, and so discriminate against atmospheric muons. Resistive plate counters are a reasonably cost effective means of making large area muon detectors, and because the detector is on the surface there is great potential for expansion.

The telescope will be located approximately 350 km south of Rome, at a height of approximately 1200 m in the Southern Appennins. At the present, a telescope of volume (4 m×4 m×11 m)= 776 m^3 has been built (Pistilli 1991), which will take data used to develop a detailed proposal for the full scale neutrino telescope. Depending on funding, construction could begin in 1992 and be completed in five years.

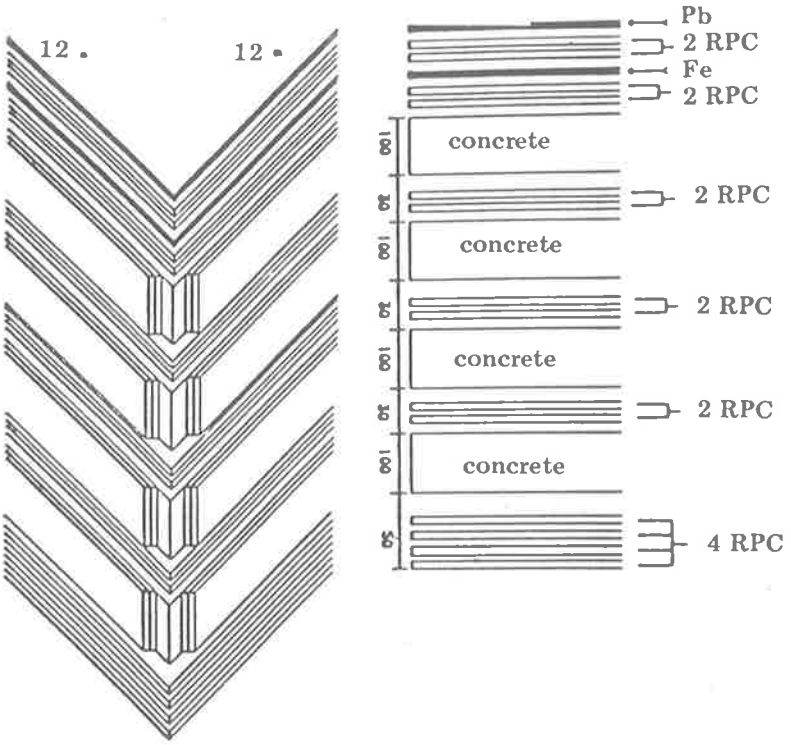

Figure 5.7: A cut away section of the prototype mini SINGAO layout. The proposed SINGAO neutrino telescope will consist of a number of similar tracking modules. Each module consists of several layers of Resistive Plate Counters (RPCs), interspersed with layers of concrete. In this case, muons are tracked by the ionization they produce as they pass through a detector module. From De Palma *et al.* (1990).

5.2.6 HiRes Eye

The High Resolution (HiRes) Fly's Eye, is a second generation cosmic ray telescope which observes the N_2 fluorescence generated by the passage of a cosmic ray air shower through the atmosphere. HiRes consists of three individual "eyes", separated by approximately 15 kilometres, which simultaneously observe the night sky in $1° \times 1°$ segments. Passage of an air shower is mapped with time, and the direction of the primary particle is reconstructed from observation of the shower by at least two of the "eyes". An electron neutrino which interacts in the atmosphere produces an electron or a W^- which initiates an electromagnetic cascade observable by HiRes. Deeply penetrating or upward moving showers, are used as the signature of neutrino event in HiRes. Unfortunately, a very large electron neutrino flux is required at ultra high energies to be observed by HiRes (Cassiday *et al.* 1989, Boyer 1991).

5.2.7 RAMAND

The Radiowave Antarctic Muon And Neutrino Detector (RAMAND), is a proposed detector which will observe the microwave Čerenkov emissions from upward going electromagnetic showers. These showers are initiated by ultra high energy ($E_\mu \geq 10^{15}$ eV) neutrino induced muons (Boldyrev *et al.* 1991). The cold ice (approximately $-50°$) of an antarctic glacier near the Soviet Vostok base is the proposed detector medium. The ice here is almost completely transparent to microwaves, with an attenuation length of several kilometres. The RAMAND proposal consists of a hexagonal array of 1260 microwave antennas separated by approximately 100 metres. The detector will have an effective area of approximately 10 km^2 for muons. The antennas will be put in 15 metre deep drill holes, as shown in Figure 5.8, to help reduce noise from temperature variations and man made sources of microwaves. A detector of this type has the advantage that it is easily expandable, and that at ultra high energies the atmospheric background is greatly reduced. However, once again the main disadvantage comes from the difficulty of building and operating a detector in Antarctica.

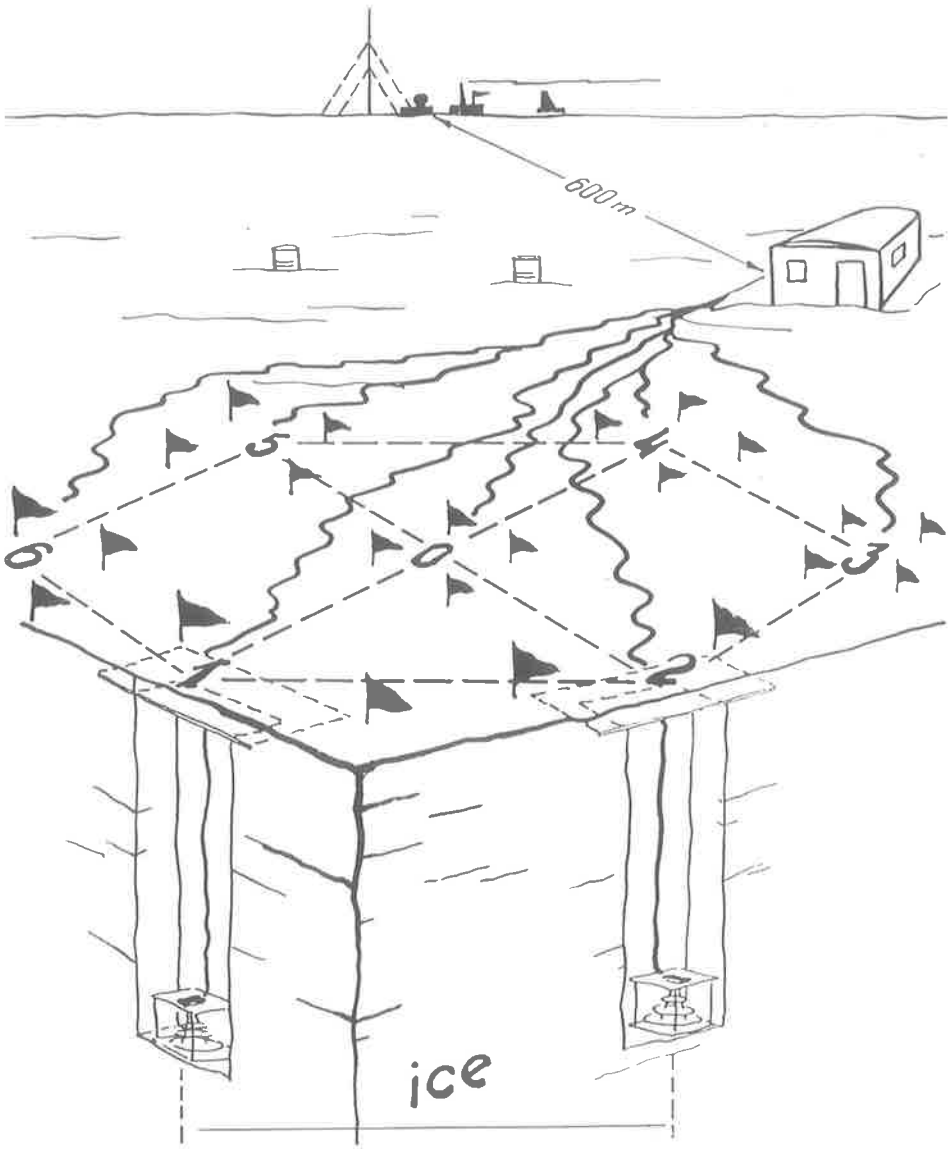

Figure 5.8: A schematic diagram of the prototype neutrino detector GIDRA–7. The full scale RAMAND telescope will consist of a hexagonal grid of 1260 microwave antennas which will be placed near the Soviet Vostok base in Antarctica. The antennas are placed at the bottom of 15 metre deep drill holes to shield them from temperature variations and man made microwave noise. From Boldyrev *et al.* (1991).

5.3 Calculation of the Signal in a Neutrino Telescope

Consider a neutrino telescope with cross sectional area A. An upward going muon may be detected if it is produced within the volume $AR_\mu(E_\mu)$ below the telescope, where $R_\mu(E_\mu)$ is the range of a muon with energy E_μ in rock. If the number density of nucleons in the rock is $n_{\rm N}$, then the mean interaction time for a neutrino of energy E_ν is $(\sigma_{\nu{\rm N}}(E_\nu)n_{\rm N}c)^{-1}$, where $\sigma_{\nu{\rm N}}(E_\nu)$ is the νN total cross section. If the neutrinos have a differential flux dF_ν/dE_ν (cm^{-2} s^{-1} eV^{-1}), then the rate at which neutrino induced muons with energy in the range $E_\mu \rightarrow E_\mu + dE_\mu$ pass through the detector is

$$\frac{dS_\mu}{dE_\mu}dE_\mu \simeq (AR_\mu(E_\mu))(\sigma_{\nu{\rm N}}(E_\nu)n_{\rm N}c)\frac{1}{c}\frac{dF_\nu}{dE_\nu}dE_\nu. \tag{5.6}$$

Above $\sim 10^{15}$ eV the mean inelasticity for νN interactions is $(E_\nu - E_\mu)/E_\nu \sim 0.2$ (Quigg, Reno and Walker, 1986), and so the approximation $E_\mu \sim E_\nu$ is adequate for most calculations. The total muon signal in the telescope is

$$S_\mu \simeq \int AR_\mu(E_\mu)\sigma_{\nu{\rm N}}(E_\nu)n_{\rm N}\frac{dF_\nu}{dE_\nu}dE_\nu. \tag{5.7}$$

This is a somewhat simplified treatment of the problem as neutrinos are attenuated within the Earth. A correct treatment would take into account the apparent motion of the neutrino source in the sky. However, for an order of magnitude estimate of the signal produced by a given neutrino flux, the above discussion is adequate.

Gaisser and Stanev (1984,1985) have folded all of the details of the interaction and the rock surrounding the detector, into a function $P(E_\nu, E_\mu > E)$. This function is the probability that a neutrino of energy E_ν interacts and produces an upward going muon of energy E_μ greater than E which passes through the detector. Subsequent calculations of the νN total cross section have shown that at 10^{19} eV the cross section may be an order of magnitude larger than traditionally estimated (Quigg, Reno and Walker 1986). Gaisser and Grillo (1987) have recalculated $P(E_\nu, E_\mu)$ to reflect this increased total cross section, and this is shown in Figure 5.9 for $E_\mu > 2$ GeV. The signal per unit detector area is then simply given by,

$$\frac{S_\mu(E_\mu > 2\,{\rm GeV})}{A} = \int P(E_\nu, E_\mu > 2\ {\rm GeV})\frac{dF_\nu}{dE_\nu}dE_\nu. \tag{5.8}$$

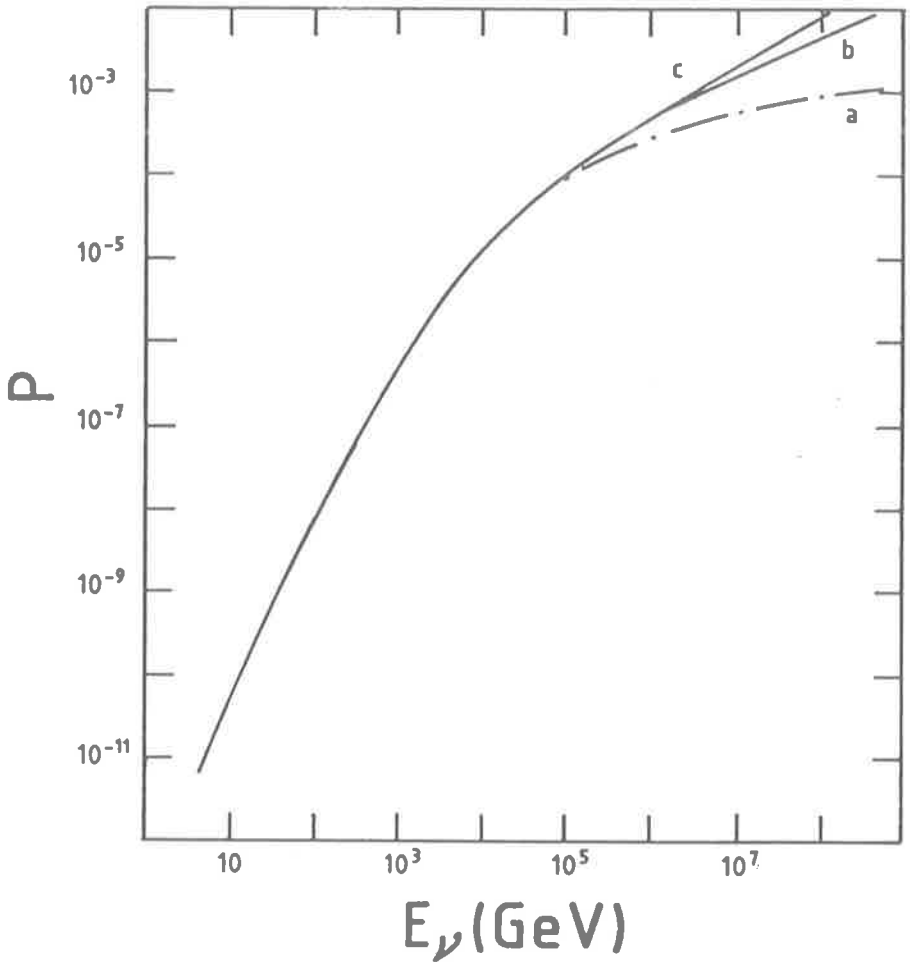

Figure 5.9: The probability P that a neutrino of energy E_ν will interact and produce a muon of energy $E_\mu > 2$ GeV which passes through the detector. To estimate the signal in a detector, it is simply a matter of multiplying P by the differential neutrino flux dF_ν/dE_ν and the detector's area, A. Curves a–c result from assuming three different structure functions for the calculation. From Gaisser and Grillo (1987).

However, at high energies the effective area of the detector may be larger than its physical area because the range of the muons increase with energy, and this effect must also be taken into account in a full calculation of the muon signal in a neutrino telesope. From Figure 5.9 it can be seen that for $10 \leq E_\nu \leq 10^3$ GeV, $P(E_\nu, E_\mu > 2\,\mathrm{GeV})$ is approximately proportional to E_ν^2. Above 1 TeV, the function flattens off. Hence, if there is an E_ν^{-2} power law neutrino flux the main contribution to the signal will come from neutrinos with energies less than $\sim$ 1 TeV. It should also be noticed that while an increased cross section means that the interaction rate will increase, it also means that high energy neutrinos are more strongly attenuated within the Earth. In fact, for energies greater then 10^{15} eV, the Earth is opaque to neutrinos (Reno and Quigg 1988).

5.3.1 The Predicted Neutrino Signal from SN 1987A

As an example of how to estimate the signal from an astrophysical source, I have calculated the signal expected from SN 1987A using the model for particle production in the remnant described by Harding, Mastichiadis and Protheroe (1990) and Harding *et al.* (1991). The basic idea is that a pulsar within the remnant drives a magneto hydrodynamic wind which piles up inside the ejecta, forming a shock. Cosmic rays are shock accelerated, and mix with the ejecta due to Rayleigh–Taylor instabilities. Hadronic interactions within the ejecta produce π^os, which decay to γ–rays. Charged pions are also produced, and they decay to give muons and neutrinos. The muons also decay to produce neutrinos.

The pion flux has been calculated as a function of supernova age (Harding *et al.* 1991) and I have decayed these to derive the neutrino flux. Equation 5.8 is used to calculate the resultant muon signal in a neutrino telescope as a function of supernova age. The results are shown in Figure 5.10 for a detector with an area of 1000 m^2. One can see from Figure 5.10 that even if the supernova remnant has a luminosity of 10^{40} erg s^{-1} only $\sim$ 0.07 events are expected in a 10^4 m^2 detector, such as DUMAND or GRANDE. Clearly this is much too low to be observable.

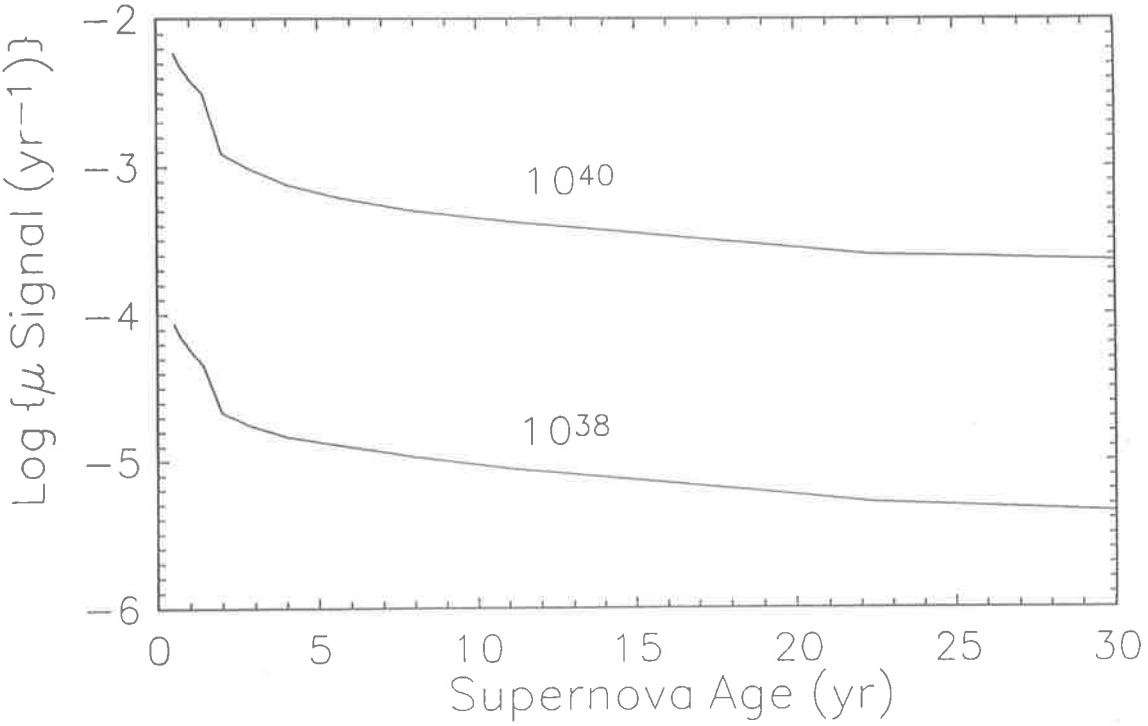

Figure 5.10: The muon signal ($E_\mu > 2$ GeV) expected in a neutrino telescope (area of 1000 m^2) from SN 1987A as a fuction of supernova age. Curves are labelled with the proton luminosity in units of erg s^{-1}. From Harding *et al.* (1991).

5.4 Summary

Most of the proposed neutrino telescopes rely on the Čerenkov technique to detect neutrino induced muons. The main problem with this technique is that there is a large flux of cosmic ray muons produced in the atmosphere which acts as a background for the signal. There are two approaches generally used to overcome this noise, either shielding the detector by putting it at great depth, e.g. DUMAND, or by looking for upward going events in a surface detector, e.g. BAIKAL, AMANDA, GRANDE and the SINGAO neutrino telescope. Alternatively, the electromagnetic showers initiated by high energy muons, electrons and hadrons may be used to detect neutrinos, e.g. HiRes and RAMAND.

Chapter 6

High Energy Emissions from Active Galactic Nuclei

6.1 Introduction

The term active galaxy is used to describe a wide variety of galaxies which exhibit energetic behaviour. They include objects such as quasars (quasi–stellar objects), Seyfert galaxies, radio galaxies, blazars and BL lacertae objects. The high energy phenomena exhibited by these galaxies takes many forms. However, high luminosities relative to normal galaxies is a common feature. For example, the first quasars discovered, 3C 273, has a luminosity of $\sim 10^{47}$ erg s^{-1}, which may be compared with the radio luminosity of the galactic centre, $L \sim 10^{39}$ erg s^{-1} (Blandford, Netzer and Woltjer, 1990). In many cases, active galaxies also exhibit large scale structure in the form of radio lobes or jets which appear to originate in the nucleus of the galaxy. Most of the galaxy's luminosity may also come from the nucleus. The term active galactic nuclei (AGN) is used to describe the central region of active galaxies. Despite the wide variety of energetic phenomena exhibited by AGN, some authors have suggested that active galactic nuclei may all be due to the same basic mechanism, accretion onto a massive compact object. In this case, the classes of AGN may result from evolution or environmental effects.

The best evidence for high energy particle production in active galaxies comes from observations of jets. The radio emissions from the jets are assumed to be produced by synchrotron emission from high energy electrons. The jets appear to originate in the nucleus of active galaxies and so there must be a mechanism, either within the AGN

or in the jet, which is capable of producing large numbers of energetic particles. One means of accelerating particles to high energies is via the first order Fermi mechanism. In AGN, electrons lose energy on a time scale much shorter than the light crossing time of the source, and hence they must be continuously accelerated throughout the source to account for the coherent emissions observed from AGN. In practice this is difficult to achieve and this problem is referred to as the "Compton catastrophe" (see e.g. Kazanas and Ellison 1986). However, protons can be accelerated to high energies and they can inject high energy electrons via the decay of charged pions produced in hadronic interactions. A natural consequence of proton acceleration is the production of γ–rays and neutrinos from the decay of the pions produced when protons interact. Recently, the Compton Gamma Ray Observatory (GRO) has observed at least fourteen active galaxies at energies greater then 30 MeV. However, all of the active galaxies observed by GRO have jets, and so it is likely that the energetic protons required for γ–ray production at these energies are also associated with the jets. This is not inconsistent with proton acceleration within the AGN as the central region is likely to be optically thick to γ–rays because of the high radiation and matter densities present. However, if high energy protons are produced in AGN then an accompanying flux of neutrinos is expected.

The observation of neutrinos from AGN can provide us with useful information about AGN models and the acceleration of protons to ultra high energies. For example, the ratio of the γ–ray to neutrino flux can be used to constrain models for the supermassive compact objects thought to exist within AGN. Also, as most of the high energy neutrinos escape from the AGN (unless their path lies through a star) they preserve the spectrum they were produced with and this may be able to provide information about shock acceleration and the conditions within the AGN.

In this chapter, I shall describe the calculation of the flux of neutrinos expected from AGN. A simple model of the source is used, but all of the interactions are modelled accurately using the techniques described in Chapter 4. While individual AGN will probably not be observable by the proposed neutrino telescopes, the diffuse neutrino background due to unresolved AGN may be observable. Thus, in addition to calculating the neutrino flux from individual AGN, one may integrate over all AGN to obtain the diffuse neutrino flux.

Previous theoretical work concerned with modelling high energy emissions from AGN are reviewed in Section 6.2. In Section 6.3 the observations of AGN (in infrared, ultraviolet/optical and X–ray bands) relevant to modelling the continuum emissions from active galaxies are reviewed. A model of AGN involving shock acceleration in the accretion flow onto a supermassive black hole, along with two average AGN continuum spectra based on the observations are described in Section 6.4. The average AGN continua have been used to calculate the rate at which protons lose energy, and the loss rates for the dominant loss processes have been used to calculate the maximum proton energy achievable in the AGN. The question of neutron escape from the central region of AGN is addressed by calculating the optical depth of the source to neutron induced pion photoproduction.

In Section 6.8, I describe the calculation of the spectrum of particles produced in AGN per proton injected into the accelerator (thought of as the region in which shock acceleration takes place). This has been done by calculating the spectra of particles produced during acceleration, the spectra of particles produced after acceleration, and the spectra particles produced by neutrons which have escaped from the central region of the AGN. The total pion spectra have been decayed to find the spectra of neutrinos, γ–rays and primary electrons produced in AGN. The scaling of the total muon neutrino spectrum to calculate the flux of neutrinos produced by individual AGN is described in Section 6.9. As examples, the flux of neutrinos seen at Earth from the quasar 3C 273 and the nearby active galaxy NGC 4151 has been calculated. The neutrino fluxes from these objects are compared to those of Stecker *et al.* (1991a,b). The cosmological integration over all AGN using the X–ray luminosity function to calculate the diffuse neutrino background is described in Section 6.10. The results are compared to those of Stecker 1992, Biermann (1992) and Sikora and Begelman (1992). The Chapter is concluded by discussing the prospects for observing the neutrinos from individual AGN and the diffuse neutrino background with the proposed high energy neutrino telescopes, reviewed in Chapter 5.

6.2 Previous Work

Eichler (1979) was one of the first to suggest that AGN may be a source of high energy neutrinos. This was based on a simple model in which the relativistic electrons responsible for the non–thermal emissions in AGN are assumed to be accompanied by comparable amounts of energy in the form of relativistic protons. Proton–proton and pion photoproduction interactions would then be responsible for neutrino production via pion decay, with $\sim 50\%$ of the initial proton's energy being radiated as neutrinos. Gamma rays produced would not necessarily escape from the AGN because of the large matter and radiation densities, and so Eichler contended that neutrino observation are the only means of probing the processes occurring within the AGN. Individual AGN, the galactic centre and the neutrino background due to AGN were identified as potential sources for observation with a DUMAND type detector.

The use of neutrino radiation from active galaxies to distinguish between models for the nucleus was suggested by Berezinsky and Ginzburg (1981). They compared the γ–ray and neutrino luminosities predicted by superstar and supermassive black hole models of AGN, and found that in the former case the ratio of the γ–ray and neutrino fluxes is tightly constrained. The supermassive black hole model of AGN is favoured if there is a low flux of γ–rays relative to the neutrino flux. Berezinsky and Ginzburg assumed a power law primary spectrum to calculate the flux of neutrinos from the decay of charged pions produced by proton–proton interactions. The resultant flux for a "typical" active galaxy would be observable by a neutrino detector such as DUMAND.

Protheroe and Kazanas (1983) suggested a model for the production of relativistic particles and γ–rays in quasars, in which protons are shock accelerated in an accretion flow onto a supermassive black hole. They argued that once a shock formed in the accretion flow then it would be supported by the pressure from high energy protons accelerated at the shock. Another appealing feature of the model is that it avoids the "Compton catastrophe", as high energy electrons are injected into the quasar via the decay of charged pions produced when protons interact. Gamma rays would also be produced from neutral pion decay, and the model predicted a correlation between the radio and γ–ray emissions in good agreement with the observations of the quasar 3C 273. Using the model they predicted a neutrino flux of $\sim 1.4 \times 10^{-10}(1+2\alpha)$ neutrinos

(of all types) cm^{-2} s^{-1} above 1 TeV for 3C 273, where α is the ratio of the magnetic energy density to the radiation energy density for the quasar.

The model of Protheroe and Kazanas (1983) has been developed by Kazanas and Ellison (1986) to include the acceleration details given by Ellison and Eichler (1984). They use the model to find the mass–luminosity relationship for AGN and found that it is consistent with observations. Kazanas and Ellison pointed out that the model naturally gives rise to a population of energetic electrons via proton–proton interactions, which in turn may produce the observed continuum emissions from AGN. They also predicted emissions of high energy neutrinos from AGN with roughly the same luminosity as contained in photons.

Both electron and proton acceleration at a shock front in an AGN has been examined by Biermann and Strittmatter (1987). They considered synchrotron and pion photoproduction losses for protons, and synchrotron and Compton losses for electrons. By comparing the total loss rate to the acceleration rate, they have calculated the maximum energy achievable during acceleration. The maximum proton energy was found to be governed by proton–photon interactions. Biermann and Strittmatter estimated the time scale for variability predicted by the model, and found that this was consistent with observations. They also predicted that a significant fraction of the luminosity may be emitted in the form of high energy neutrons. Substantial fluxes of neutrinos and γ–rays were also predicted.

Proton–photon interactions, rather than the size of the acceleration region, were found to limit the maximum energy achievable by first order Fermi acceleration in AGN by Sikora *et al.* (1987). They compared time scales for proton–proton interactions, pion photoproduction and pair production assuming an ε^{-2} power law photon spectrum. Sikora *et al.* found that interactions with photons dominate at high energies. Direct acceleration of electrons was found to be inefficient due to synchrotron and Compton losses. However, high energy electrons suitable for initiating synchrotron/Compton cascades may be injected via proton–photon interactions.

Using the loss rates and the acceleration rate derived by Sikora *et al.* (1987), Sikora, Begelman and Rudak (1989) examined the question of neutron production in AGN. They found that the acceleration of protons to relativistic energies, naturally leads to a flux of relativistic neutrons which escape from the central region of the AGN.

The neutrons decay well outside the central region and Sikora, Begelman and Rudak examined the consequences of the injection of relativistic protons into this environment. They found that protons could drive a wind as the energy contained in high energy particles exceeds the gravitational binding energy at these radii. The protons could also confine the narrow and broad emission line clouds within the AGN. Gamma–ray production is a natural consequence of neutron escape because of the neutral pions produced in proton–proton interactions.

A phenomenological model of pion photoproduction was used by Mannheim and Biermann (1989) to calculate the mean energy of pions produced in the interaction. They also considered a total cross section for pion photoproduction which rises at high centre of momentum frame energies ($\sqrt{s} \geq 100$ GeV) due to jet events. The effect of this increased cross section was examined for the case in which an E_p^{-2} proton spectrum interacts with a power law or a δ–function photon spectrum. They also discussed the effect of a higher pion photoproduction cross section in the context of particle production in AGN. Mannheim and Biermann pointed out that the observation of neutrino *spectra* from AGN could be used to provide constraints on the cross section.

The flux of neutrons which escape from AGN has been estimated by Kirk and Mastichiadis (1989). They assumed an ε^{-2} photon spectrum and an E_p^{-2} proton spectrum to calculate the rate at which neutrons are produced within the source. The optical depth of the source due to neutron induced pion photoproduction was calculated using the Monte Carlo method. They have used the optical depth to estimate the flux of neutrons escaping from the source.This neutron flux was found to be able to produce both a cosmic–ray driven wind, and high energy γ–ray emissions. However, Kirk and Mastichiadis pointed out that the best constraints on the model may come from observations of the boron abundance. The model predicts enhanced abundances of boron produced by the spallation of heavier elements by the neutrons which have escaped from the central region of the AGN. Observation of a boron line would provide good supporting evidence for the model.

The flux of escaping neutrons calculated by Kirk and Mastichiadis (1989) has been used by Mastichiadis and Protheroe (1990) to calculate the flux of γ–rays expected from AGN. They calculate contributions to the spectrum both from neutrons which interact as they escape from the central region of the AGN, and from proton–proton

interactions which occur after the neutrons decay. Synchrotron emissions from high energy electrons and positrons produced from the decay $\pi^{\pm} \rightarrow \mu^{\pm} \rightarrow e^{\pm}$ have also been included. Using the model Mastichiadis and Protheroe predicted γ–ray fluxes from AGN close to present–day detector sensitivities. They pointed out that another consequence of relativistic neutron escape from AGN is the production of cosmic–rays.

Begelman, Rudak and Sikora (1990) have completed a fully analytical calculation of the neutrino, neutron and primary γ–ray spectra produced by an AGN. They considered a model in which protons are accelerated at a constant rate via a mechanism such as first order Fermi acceleration, in a two component photon field with a black body spectrum superimposed on a power law. They have modelled the proton–proton, pion photoproduction and pair production interactions which occur using simple δ–function final particle distributions. Solutions for several power law photon spectra were presented, and Begelman, Rudak and Sikora predict that the nearest AGN may be observable by DUMAND type detectors. Also discussed is the spectrum of neutrons which escape from the AGN. They emphasised that one consequence of high energy neutrino production may be to accelerate the evolution of stars in the inner region of the active galaxy due to neutrino heating.

Recently, Stecker *et al.* (1991a,b) have calculated the flux of diffuse neutrinos from unresolved AGN. The calculation was based on a simple model of AGN in which particles are accelerated to relativistic energies at an accretion shock. They assumed that equal energy densities are contained in UV and power law X-ray components of the observed AGN continuum and that pion photoproduction via the channel $p\gamma \rightarrow \Delta^{+} \rightarrow n\pi^{+}$ on UV photons is the dominant loss mechanism. Interactions and pion decay have been treated by using δ–function particle distributions. Using this model they have made predictions for the neutrino flux from NGC 4151 and 3C 273. However, individual sources are found to be masked by the contribution to the diffuse neutrino background from AGN. The X–ray luminosity function of Morisawa and Takahara (1989) has been used to integrate over the neutrino spectra from all active galaxies and they found that the resultant event rates in existing and proposed neutrino telescopes should be observable.

This positive prediction attracted much attention amongst the high energy astrophysics community. Unfortunately, a typographical error in the published X–ray lumi-

nosity function has meant that the predicted neutrino flux was a factor of $3^{2.6}$ too high (Szabo and Protheroe 1992a). The results of Stecker *et al.* (1991a,b) were also shown to be in conflict with the observed X–ray background by Berezinsky (1991, 1992) and Berezinsky and Learned (1992). Biermann (1992) has scaled the observed X–ray background to estimate the diffuse neutrino background from AGN, and has found that the results are approximately 30 times lower than those predicted by Stecker *et al.* (1991a,b). In a revised calculation, Stecker *et al.* (1992) have used a more appropriate luminosity function and predict a neutrino flux ~ 40 times lower than originally published. They have also made estimates of the flux of neutrinos expected from the jets of some of the AGN recently observed by the EGRET experiment on GRO. For one of these objects, 3C 279, the neutrino flux during flaring was found to be observable by DUMAND II. In addition they have argued that high fluxes of neutrinos in the central region of AGN may be able to disrupt the evolution of stars in this region, and may be responsible for the broad line emissions observed in AGN.

Using the model of Begelman, Rudak and Sikora (1990) and by scaling the observed diffuse X–ray background, Sikora and Begelman (1992) have calculated the contribution to the diffuse neutrino background from AGN. The results are comparable to those of Stecker *et al.* (1992). In addition the acceleration and the subsequent dissociation of helium has been shown to be a significant source of high energy neutrons in AGN.

Preliminary results of the calculation presented in this chapter may be found in Szabo and Protheroe (1991, 1992a, 1992b). In addition, an analysis of neutron escape from the central region of AGN which predicts an AGN component of the observed cosmic rays above the "knee" may be found in Protheroe and Szabo (1992).

6.3 Relevant Observations of AGN

Active galactic nuclei have been observed in all available energy bands, from radio to γ–ray. In the following sections the observations in each energy band, with the exception of the radio band, are briefly reviewed. The radio observations are not included because most AGN exhibit a low energy turn over in the infrared, and also because the radio emissions are thought to be produced at large radii. Hence, the energy density contained in the radio frequencies is negligible in the central region of

active galaxies. Some AGN have strong radio emission but these are thought to be associated with jets. No attempt has been made to review all observations. Instead, only observations directly used for modelling the AGN continuum have been included. This section is concluded with a description of two model AGN continua which have been used to represent the photon spectrum in the central region of AGN. For reviews of the observations of active galactic nuclei see Hazard and Mitton (1979), Wiita (1985) and Blandford, Netzer and Woltjer (1990).

6.3.1 Infrared

The nature of the infrared (IR) emissions from active galactic nuclei has been the subject of much debate. Some authors have argued that the infrared emissions are primarily non–thermal in nature, whereas others have argued that the IR emissions are primarily thermal. In reality, most AGN will almost certainly have both thermal and non–thermal components in the infrared.

Edelson and Malkan (1986) have measured spectral energy distributions from 0.1–100μm for 29 active galaxies, all of which are Seyfert 1 or Seyfert 2 galaxies. They have fitted a power law to the spectra, and for Seyfert 1 galaxies they have found a mean spectral index of $\alpha = 1.36 \pm 0.21$, where $\varepsilon dn/d\varepsilon \propto \varepsilon^{-\alpha}$and $dn/d\varepsilon$ is the differential photon density. Edelson and Malkan have interpreted the non–thermal spectra as being caused by synchrotron radiation. All of the spectra turn over at wavelengths shorter than 300μm, and this has been interpreted as the wavelength at which the source becomes synchrotron self absorbed. In Seyfert 2 galaxies, absorption of ultraviolet photons by dust and the subsequent re–radiation means that the infrared has a significant thermal component. In this case, Edelson and Malkan found that a power law does not represent the data very well.

In a group of 37 hard X–ray selected emission line active galaxies (mostly Seyfert 1 galaxies), Ward *et al.* (1987) have observationally identified 3 classes of AGN. These are (A) those in which from $\sim$ 1–100μm the IR is relatively flat or rising into the blue/optical region, (B) those in which the IR is relatively flat and the spectra decline for wavelengths shorter than $\sim$ 1μm, and (C) those which are distinguished by a steep rise in the far IR. Carleton *et al.* (1987) have identified these three classes as follows. Class (A) Objects are strong in the UV and hence are assumed to be minimally

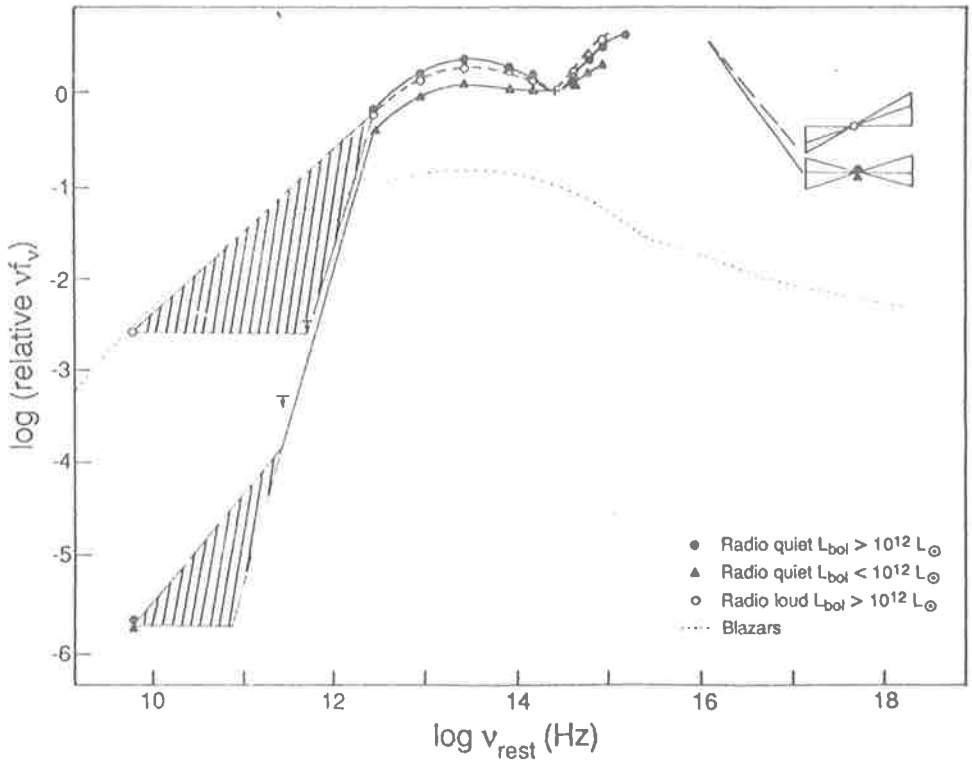

Figure 6.1: The average spectrum of bright quasars in the Palomar–Green survey of stellar objects. Data points are for radio–loud (open circles) and radio–quiet (filled circles and triangles) quasars. The dotted line is the mean continuum energy distribution for blazars. From Saunders *et al.* (1989).

reddened by dust (a "bare" AGN). For class (B) objects, much of the UV/optical has been absorbed by dust and re–emitted in the infrared. The final class represents AGN in which the continuum is dominated by the underlying galaxy. Carleton *et al.* have suggested that all Seyfert 1 nuclei have the same underlying non–thermal spectrum fitted by a power law of slope $\alpha = 1.02 \pm 0.10$, which has been modified by dust resulting in the range of IR continua observed. This hypothesis is supported by a correlation between the hard X–ray and the underlying power law in the infrared, which suggests these components may be produced in same region.

In contrast, Saunders *et al.* (1989) have found that for quasars in the Palomar bright quasar survey, there is no evidence for a significant non–thermal component in the infrared. They have compiled observations of more than one hundred of the brightest quasars in the Palomar–Green (PG) survey of stellar objects. Using these results Saunders *et al.* have compiled an average spectrum for bright PG quasars. This spectrum is shown in Figure 6.1. Clearly, the infrared ($\nu \sim 2\times10^{12}$–3×10^{14} Hz) cannot be well approximated by a single power law. They attribute the IR to re–radiation of central region emissions from a warped accretion disk.

In a less model dependent manner, Chini, Kreysa and Biermann (1989) have found that for radio–quiet quasars the infrared is due to dust emission on the kiloparsec scale. They also found that a synchrotron self absorbed model of the IR emissions does not fit the data for the majority of sources in their sample.

6.3.2 UV/Optical

Most AGN exhibit an excess in the optical or UV region of the continuum. In the literature, this excess is referred to as either the "big blue bump" or the "UV bump". This bump has been interpreted as thermal emission from the inner region of an accretion disk (Malkan and Sargent 1982). Edelson and Malkan (1986) have fitted black body spectra to the far UV region of the spectrum, and have found that all of the spectra in their sample are consistent with a temperature of $T = (26 \pm 4) \times 10^3$ K. On the other hand, in a sample of 109 PG quasars, Saunders *et al.* (1989) have found that the "UV bump" is consistent with an accretion disk with temperature in the range $10^4 \leq T \leq 10^5$ K. In reality, the UV bump will not consist of a single temperature thermal spectrum but will be broadened due to emission from different parts of the

accretion flow.

6.3.3 X–ray

In contrast to the infrared observations, there is general agreement that the X–rays are produced by a non–thermal mechanism. This is based on the good fits obtained using a power law photon spectrum and also on the rapid variability exhibited by AGN in the X–ray band. The variability on time scales of $\sim$ a few hours also means that the X–rays are produced at small radii within the central region of the AGN.

In a sample of 33 quasars, Wilkes and Elvis (1987) found that for radio loud quasars the 0.1–3.5 keV X–ray band has a mean power law spectral index of $\alpha = 1.0$ ($\varepsilon dn/d\varepsilon \propto \varepsilon^{-\alpha}$). Whereas, for radio quiet quasars they found a mean index of $\alpha = 0.5$. In each case, there was a large scatter in the power law indices with values in the range ($-0.2 < \alpha < 1.8$). Wilkes and Elvis have suggested a three component model for the X–ray spectrum above $\sim$ 0.1 keV. The first component is a power law with spectral index $\alpha = 0.5$. This component dominates above $\sim$ 0.5 keV in radio loud quasars and it dominates above a few keV for all other quasars. At energies below $\sim$ 0.3 they have identified a component with a power law index which ranges from 2.0 to 3.0, which may be the tail of the "UV bump". In addition, for radio quiet quasars they have suggested that an $\alpha = 1.0$ component which dominates for photon energies in the range $0.5 \leq \varepsilon \leq 3.5$ keV. Wilkes and Elvis argued that this latter component may simply be an extension of the $\alpha = 1.0$ power law observed in the infrared region of some quasars.

At higher energies (in the 2–20 keV band) Turner and Pounds (1989) have found that a power law spectrum with a mean index of $\alpha = 0.7 \pm 0.17$ fits the data of a group of 48 hard X-ray selected Seyfert galaxies. This is consistent with earlier measurements of the X–ray spectrum in the 2–50 keV and 12–165 keV bands (Rothschild *et al.* 1983). At these energies AGN may make a significant contribution to the diffuse X–ray background which also has a spectral index of $\alpha \simeq 0.7$. However, the diffuse X–ray spectrum is observed to steepen at a energies above a few MeV. Hence, if AGN do significantly contribute to the observed AGN background, then either there is a corresponding break in the AGN spectrum or the average AGN spectrum cuts off at these energies.

6.3.4 A Generic AGN Continuum Spectrum

From the above overview of the observations it can be seen that many of the AGN continua display remarkably similar features. For example, most of them have a power law component which may extend from infrared to X–ray energies. Superimposed on top of this power law is a bump in the UV and optical bands. Hence, for the purpose of modelling AGN it is possible to define a generic photon spectrum which embodies the features found in the average AGN continuum. Clearly, this is an over simplification as the various classes of AGN (quasars, Seyfert galaxies, etc.) display a wide variety of properties in their continuum emissions. Even within a particular class of AGN there is often considerable variation from object to object. However, I have constructed two AGN continuum spectra which reflect the main features observed. The first is similar to the AGN spectrum used by Stecker *et al.* (1991a,b, 1992), whereas the second has a power law component similar to that used by Kirk and Mastichiadis (1989) and Mastichiadis and Protheroe (1990), superimposed with a thermal spectrum in the UV. These continua have been used to model the spectrum of photons found in the central region of AGN. The use of two possible photon spectra also enables one to gauge how the wide variety of observed AGN continua might affect the results.

Palomar–Green Continuum (Spectrum a)

The first generic continuum is based on the average continuum obtained by Saunders *et al.* (1989), shown in Figure 6.1. They have averaged over 109 of the brightest quasars found in the Palomar–Green survey of stellar objects, and hence I shall refer to this AGN spectrum as the PG continuum or spectrum (a).

As discussed in Section 6.3.1, Saunders *et al.* identified the infrared emissions from AGN as being thermal re–emission from dust in a warped accretion disk on scales of 1–1000 pc. Similarly, Chini, Kreysa and Biermann (1989) attribute the far infrared emissions to re–emission from dust on the one kiloparsec scale. Hence, the energy density of infrared photons within the central region of the active galaxy (within $\sim 10^{-2}$ pc) will be small relative to the energy density contained in the other energy bands which are produced at small radii. For simplicity I have assumed that there are no infrared photons within the central region of the AGN.

Saunders *et al.* have fitted thermal spectra to the UV bump, and they have found

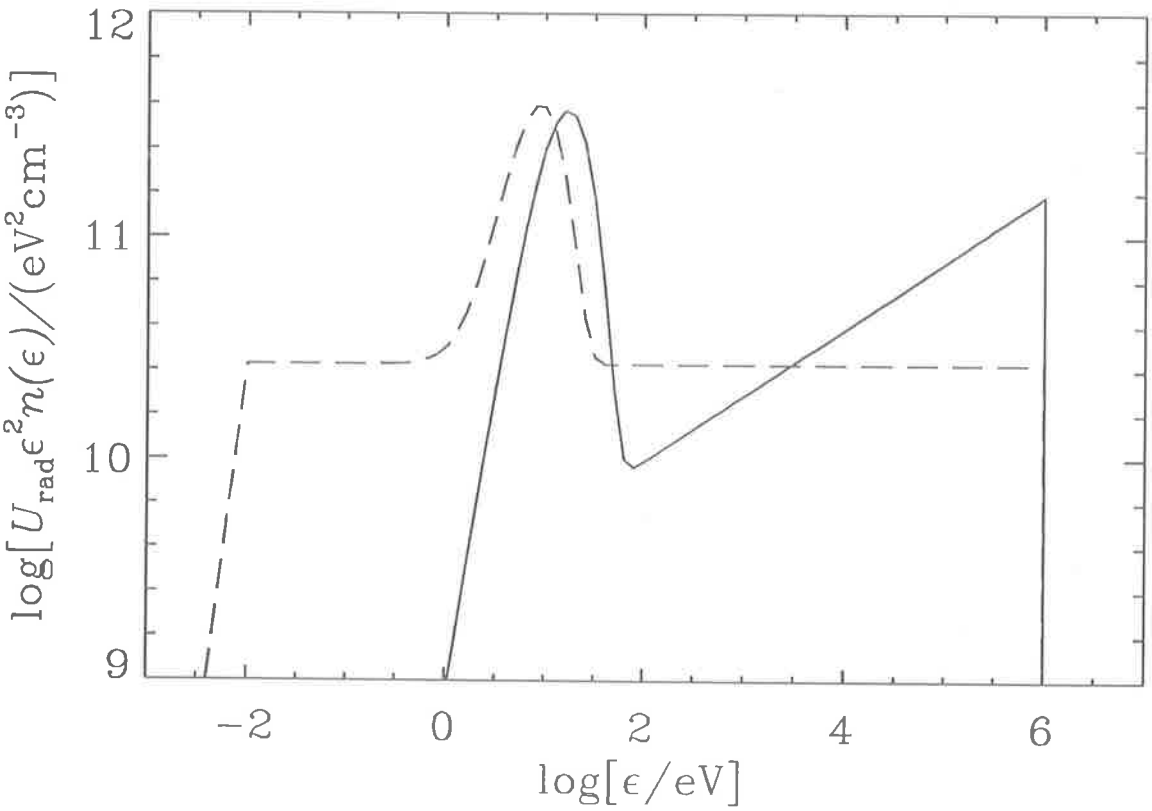

Figure 6.2: A plot of the two average photon spectra used to model the AGN continuum. The Palomar–Green continuum (spectrum (a), solid curve) consists of an $\varepsilon^{-1.7}$ power law for photon energies in the range $10 \leq \varepsilon \leq 10^6$ eV, superimposed with a thermal spectrum of temperature $T = 5 \times 10^4$ K. The flat AGN continuum (spectrum (b), dashed curve) has an ε^{-2} power law for photon energies in the range $10^{-2} \leq \varepsilon \leq 10^6$ eV. Below 10^{-2} eV there is an $\varepsilon^{1.5}$ spectrum, appropriate for a synchrotron self–absorbed source. In this case, the thermal spectrum has a temperature of 2.6×10^4K. For both spectrum (a) and (b) equal energy densities are contained in both the thermal and power law components. The plots have been multiplied by ε^2 to reduce the dynamic range, and have been normalised to the total radiation energy density U_{rad}.

that blackbody temperatures in the range $10^4 \leq T \leq 10^5$ K fit the observations. From Figure 6.1 it can seen that the UV bump is quite broad and is not well represented by a single blackbody. However, while the thermal emission will come from various parts of the inner accretion disk and a range of black body temperatures is expected, the averaging procedure also tends to broaden the bump. For simplicity I have assumed that all of the AGN will have a UV bump which can be represented by a single black body spectrum with a temperature of 5×10^4 K.

If the X–ray background comes primarily from unresolved AGN, then on average the X–ray spectrum of AGN would be expected to mirror the background with a spectral index of $\alpha = 0.7$. As discussed in Section 6.3.3 the diffuse X–ray background steepens at energies of a few MeV, and hence on average the X–ray spectrum of AGN will either steepen or cut off at this energy. However, as shall be discussed in Sections 6.5.2 and 6.5.3 the high energy photons have no effect on the results, and so I have nominally chosen $\varepsilon_{\max} = 1$ MeV as a high energy cut off. At low energies, I have assumed that the power law component has a low energy cut off at a frequency above above the infrared, nominally at an energy of 10 eV. The results are not sensitive to the exact value of the low energy cut off as in this region most of the photons come from the thermal distribution.

Some variations of the strength of the UV bump relative to the X–ray band have been observed (see e.g. Wiita 1985). However, for simplicity I have assumed that equal energy densities are contained in both the thermal and power law components. The resulting average Palomar–Green continuum spectrum is shown in Figure 6.2.

Flat AGN Continuum (Spectrum b)

The flat AGN continuum is based on the class of bare AGN identified by Carleton *et al.* (1987). In this case, the infrared is principally non–thermal in nature and may simply be an extension of the power law observed at X–ray energies. For this class of objects, Carleton *et al.* have found a mean spectral index of $\alpha = 1.02 \pm 0.1$. X–rays are thought to be produced at small radii in the AGN. Hence, if the infrared photons are produced by the same mechanism, as indicated by a single infrared to X–ray power law component, then the infrared emissions will also come from small radii. Therefore, in contrast to the PG continuum described above, comparable energy

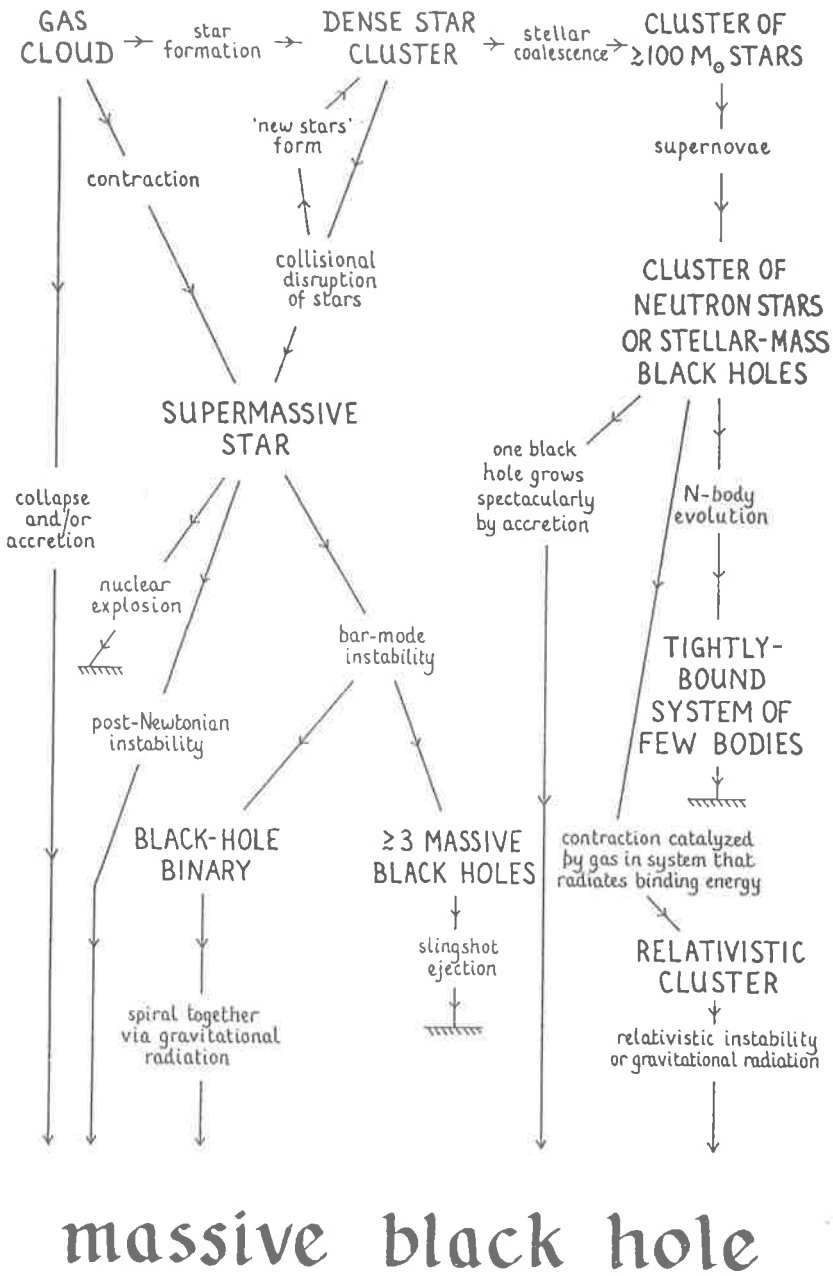

Figure 6.3: A schematic diagram illustrating that the bottom line for many of the exotic models for active galactic nuclei is evolution into a massive black hole. From Rees (1984).

densities will be contained in the infrared and X–ray bands within the central region of the AGN. I have assumed a spectral index of $\alpha = 1.0$ for the infrared to X–ray power law component which extends from $\varepsilon_{\rm min} = 10^{-2}$ eV, in rough agreement with the turn over fitted by Edelson and Malkan (1986), to $\varepsilon_{\rm max} = 1$ MeV. The low energy turn over is assumed to occur when the AGN becomes synchrotron self–absorbed, and hence for $\varepsilon < \varepsilon_{\rm min}$ a spectrum with a spectral index of $\alpha = -2.5$, appropriate for an optically thick self–absorbed source (see e.g. Rybicki and Lightman 1979), has been used.

In addition, a thermal spectrum with a temperature of 26,000 K has been superimposed on the power law component, based on the spectra fitted by Edelson and Malkan (1986). As for the Palomar–Green continuum I have assumed that there is equal energy density contained in both the thermal and power law components. The flat AGN spectrum has been added to Figure 6.2.

6.4 A Supermassive Black Hole Model of AGN

There has been much debate regarding the mechanism and the type of object responsible for the large energy outputs in active galactic nuclei. However, accretion onto a supermassive black hole is now generally thought to be the power source in AGN. For reviews of black hole models of AGN see Rees (1984) and Begelman, Blandford and Rees (1984). A general discussion of AGN models can also be found in Blandford, Netzer and Woltjer (1990).

A supermassive black hole is an attractive model for the nucleus of an active galaxy because it is the logical evolutionary end point for many of the other more exotic models. This is shown schematically in Figure 6.3, from which it can be seen that the evolutionary bottom line is a massive black hole. The supermassive black hole model is also appealing because it is one of the simplest models. The "no–hair" theorems of general relativity say that the end point of gravitational collapse is a black hole characterised by its mass and spin, and is described exactly by the Kerr metric (Rees 1984). Hence, for the purpose of modelling the high energy emissions from AGN, it does not matter by which evolutionary route the black hole was formed in Figure 6.3. If a supermassive black hole does exist in the nucleus of an AGN, then it is natural to think that matter will accrete onto it. Accretion is an efficient means of converting

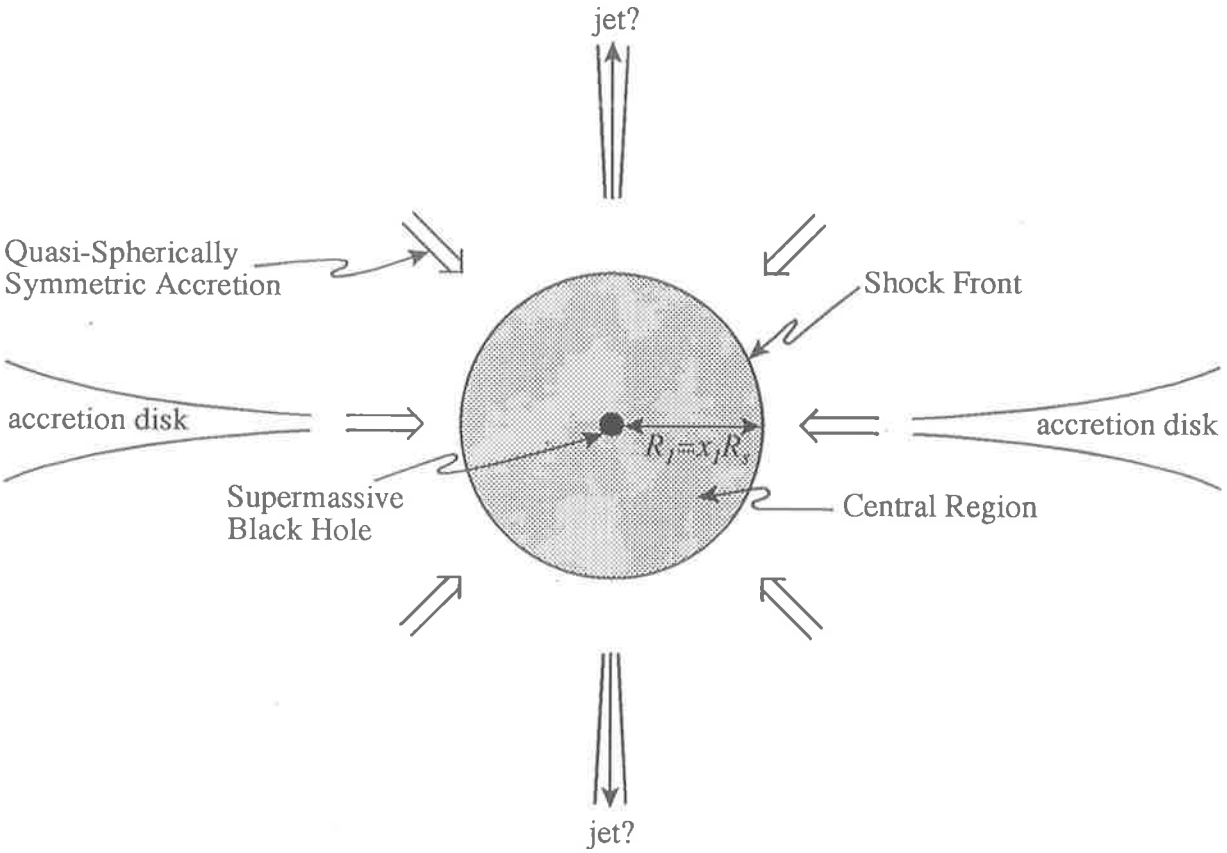

Figure 6.4: A schematic diagram of the supermassive black hole model. At large radii matter accretes via an accretion disk. However, as the matter approaches the black hole the accretion becomes quasi spherically symmetric. A shock forms at a radius R_1 in the accretion flow, and the volume contained by the shock is assumed to correspond to the central region of the AGN. The possibility of jets within the model is also indicated.

gravitational potential energy into kinetic energy, and hence it is an attractive feature in a model of AGN as it is able to supply the large amounts of energy required. Accretion has also been seen to work in galactic X–ray binaries, and hence may be considered a proven mechanism.

Protheroe and Kazanas (1983) have developed a model for active galactic nuclei in which protons are accelerated by first order Fermi acceleration at a shock in a spherical accretion flow onto a supermassive black hole. They argued that such a shock may be supported by the pressure from high energy protons which have been accelerated by the shock front. This model has been further developed by Kazanas and Ellison (1986) to include the steady–state, non–linear shock acceleration solutions of Eichler (1984) and Ellison and Eichler (1984). One of the uncertainties in this model is the question of how the shock forms in the accretion flow in the first place. Kazanas and Ellison suggested that some other agent such as conservation of angular momentum, plasma instabilities or the magnetic field might initially shock the accretion flow. Once the shock has formed, proton acceleration takes place and the pressure provided by the population of relativistic protons will increase until the shock front is self supporting.

For this work the basic model of Protheroe and Kazanas (1983) has been adopted, along with the subsequent extensions of Kazanas and Ellison (1986). A schematic representation of the model is shown in Figure 6.4. Matter accreting onto a supermassive black hole of mass, $M \simeq 10^9 \mathrm{M}_\odot$, will probably form an accretion disk due to the angular momentum of the accreting material. At small radii the accretion disk may become geometrically thick (see e.g. Rees 1984, Begelman, Blandford and Rees 1984 and Blandford, Netzer and Woltjer 1990), and so the accretion may become quasi–spherical. A shock is assumed to form at a dimensionless radius $x_1 = R_1/R_s$, where $R_s = 2GM/c^2$ is the Schwarzschild radius of the black hole. The central region of the AGN, where the continuum emissions come from, is assumed to correspond to the volume enclosed by the shock.

The mass–luminosity relationship obtained by Kazanas and Ellison (1986) may be approximated as

$$M \simeq 10^{-38} x_1 \left(\frac{L_c}{\mathrm{erg\ s^{-1}}} \right) \quad \mathrm{M}_\odot, \tag{6.1}$$

where L_c is the infrared to X–ray continuum luminosity of the AGN. Using Equation 6.1, I follow Kazanas and Ellison in deriving some useful parameters for the model

expressing quantities in terms of x_1 and L_c where possible. The Schwarzschild radius becomes,

$$R_s \simeq 2.95 \times 10^{-33} x_1 \left(\frac{L_c}{\text{erg s}^{-1}} \right) \quad \text{cm.} \tag{6.2}$$

Approximately 50% of the total luminosity, L_{tot}, goes into neutrinos (Eichler 1979), and hence $L_c \simeq 0.5 L_{\text{tot}}$. The total luminosity of an AGN is approximately given by the product of the accretion rate (number of particles accreted s^{-1}), the kinetic energy of each particle and the efficiency of the source $Q = Q(x_1)$. If one assumes that the accreting matter consists entirely of protons, then the mass accretion rate is

$$\begin{aligned} \dot{M} &\simeq \frac{4 L_c}{u_1^2 Q(x_1)} \\ &\simeq 7.1 \times 10^{-47} \left(\frac{L_c}{\text{erg s}^{-1}} \right) \frac{x_1}{Q(x_1)} \quad \text{M}_\odot \text{ yr}^{-1}, \end{aligned} \tag{6.3}$$

where the kinetic energy of the particles at the shock has been used for this estimate. The efficiency, $Q(x_1)$, may be found as a function of x_1 using Equations (10) and (17) of Kazanas and Ellison (1986) and by assuming that the temperature of the accreting plasma is $T = 10^8$ K, giving

$$Q(x_1) \simeq 1 - 0.1 x_1^{0.31}. \tag{6.4}$$

The free fall velocity of the accreting material can be calculated by a simple conservation of energy argument. The total energy of a particle of mass m, at a radius r from the black hole is $GMm/r + mu^2/2$, and this must be equal to the potential energy of the particle at $r = \infty$ where the particle is at rest. Re–arranging the resulting formula gives $u(r) = (2GM/r)^{1/2} = x^{-1/2} c$, where $x = r/R_s$ is the dimensionless radial distance from the black hole. The density of the accretion flow upstream from the shock front, may be estimated by equating the mass accretion rate, with the flux of matter across a surface at radius R in the accretion flow, which gives

$$\begin{aligned} n(r) &= \frac{\dot{M}}{4\pi r^2 u(r) m_p} \\ &\simeq 1.3 \times 10^8 \frac{x_1^{0.5}}{Q(x_1)} \left(\frac{L_c}{\text{erg s}^{-1}} \right)^{0.5} \left(\frac{r}{\text{cm}} \right)^{-1.5} \quad \text{cm}^{-3}, \end{aligned} \tag{6.5}$$

where m_p is the rest mass of a proton.

If the central region of the AGN is optically thick to radiation then the radiation density in the nucleus may be estimated using the relationship $F = \pi B_s$, where F is

the flux at the surface of the central region and B_s is the brightness (see e.g. Rybicki and Lightman, 1979). Hence, the radiation density in the central region of the AGN is

$$\begin{aligned} U_{rad} &= \frac{4\pi B_s}{c} \\ &= \frac{L_c}{\pi R_1^2 c} \\ &\simeq 7.6 \times 10^{65} x_1^{-4} \left(\frac{L_c}{\text{erg s}^{-1}}\right)^{-1} \quad \text{eV cm}^{-3}. \end{aligned} \tag{6.6}$$

To estimate the magnetic field strength at the shock, B, one can make the approximation that there is equipartition between the radiation energy density and the magnetic energy density, i.e. $B^2/8\pi = U_{rad}$ in cgs units, which gives

$$\begin{aligned} B &= \left(\frac{8L_c}{R_1^2 c}\right)^{1/2} \\ &= 5.5 \times 10^{27} x_1^{-2} \left(\frac{L_c}{\text{erg s}^{-1}}\right)^{-0.5} \quad \text{gauss}. \end{aligned} \tag{6.7}$$

The diffusion coefficient in the vicinity of the shock front may be expressed in terms of the minimum or Bohm diffusion coefficient $r_g c/3$, giving

$$D \simeq 6.0 \times 10^{-21} b x_1^2 \left(\frac{E_p}{\text{eV}}\right) \left(\frac{L_c}{\text{erg s}^{-1}}\right)^{0.5} \quad \text{cm}^2\ \text{s}^{-1}, \tag{6.8}$$

where $r_g = E_p/eBc$ is the gyroradius of the proton for $E \gg m_p c^2$, and $b \geq 1$. Assuming that the shock in the accretion flow is strong ($u_1 = 4u_2$) the rate at which protons gain energy via shock acceleration is (see Section 2.3.2)

$$\begin{aligned} \left.\frac{dE_p}{dt}\right|_{\text{acc}} &\simeq \frac{E_p u_1^2}{20D} \\ &\simeq 7.5 \times 10^{39} b^{-1} x_1^{-3} \left(\frac{L_c}{\text{erg s}^{-1}}\right)^{-0.5} \quad \text{eV s}^{-1}, \end{aligned} \tag{6.9}$$

Therefore, the time scale $T_{\text{acc}}(E_p) = E_p/(dE_p/dt)$ required to accelerate protons to energy E_p is given by

$$(U_{rad} T_{\text{acc}}(E_p))^{-1} \simeq 9.8 \times 10^{-27} b^{-1} x_1 \left(\frac{E_p}{eV}\right)^{-1} \left(\frac{L_c}{\text{erg s}^{-1}}\right)^{0.5} \quad \text{s}^{-1}\ (\text{eV cm}^{-3})^{-1}, \tag{6.10}$$

where the acceleration rate $T_{\text{acc}}{}^{-1}(E_p)$ has been scaled by the radiation energy density in order to compare the acceleration rate with the loss rates to be calculated below. In the absence of energy losses, the maximum energy proton which may be produced by shock acceleration is governed by the size of the central region. Once the mean

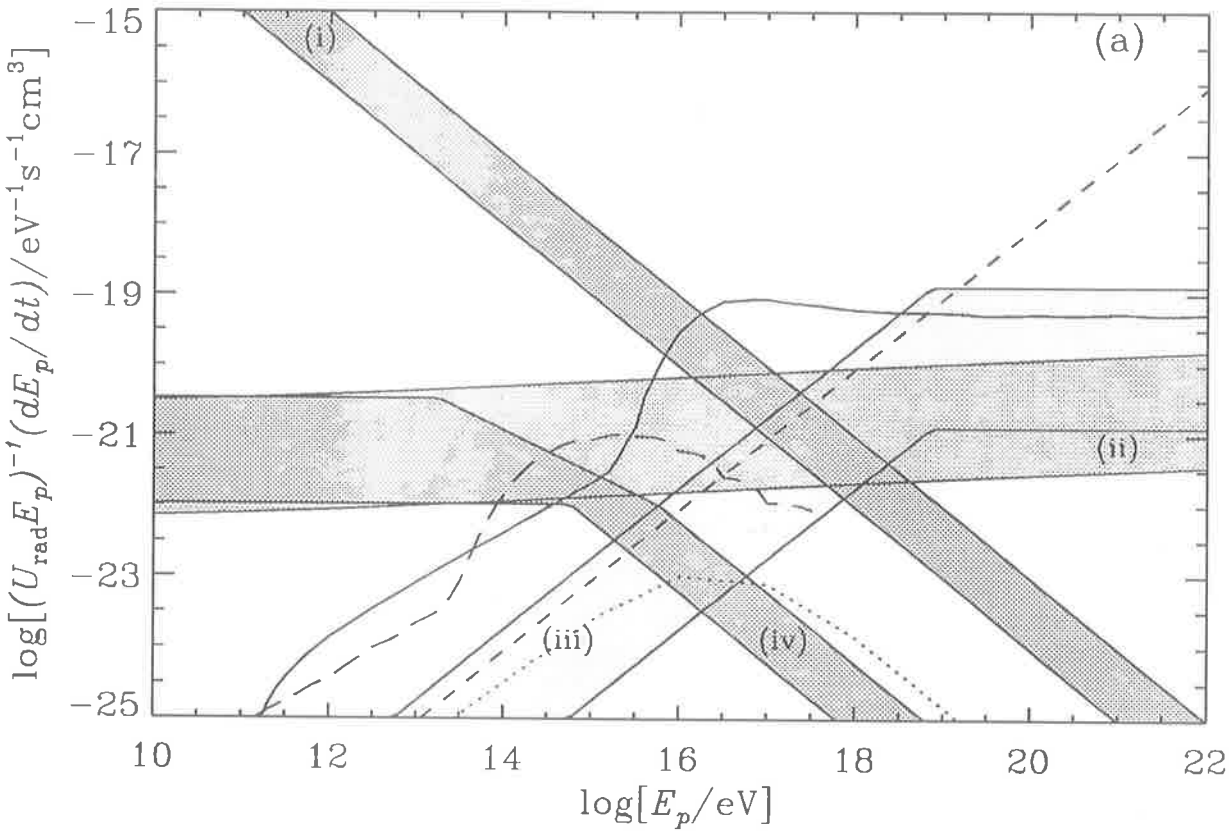

Figure 6.5: (a) A plot of the mean loss rates and the acceleration rate for $b^{-1}L_c^{0.5} = 10^{21}$ (erg s^{-1})$^{0.5}$, using the Palomar–Green AGN continuum. The shaded bands are defined as follows: (i) the acceleration rate, (ii) the loss rate due to proton–proton interactions, (iii) the loss rate due to diffusion away from the central region, and (iv) the loss rate due to advection onto the black hole. For bands (i)–(iii) and for low energies in band (iv), the lower bound is for $x_1 = 10$ and the upper bound is for $x_1 = 100$. Also shown are the loss rates for pion photoproduction (solid curve), pair production (long dashed curve), synchrotron radiation (short dashed curve) and Compton scattering (dotted curve). The curves have all been scaled by the total radiation energy density U_{rad} to aid comparison.

path length of the proton for scattering on the magnetic field exceeds the radius of the central region diffusive shock acceleration will cease. Hence, the maximum proton energy produced in the AGN is

$$E_p^{max} \simeq 7.4 \times 10^{-3} b^{-1} \left(\frac{L_c}{\text{erg s}^{-1}} \right)^{0.5} \quad \text{eV}. \tag{6.11}$$

Equation 6.10 only applies for plane shock fronts, and clearly in an accretion flow onto a black hole the shock will be spherical. However, so long as the typical length scale for acceleration D/u_1 (see e.g. Berezinskiĭ *et al.* 1990) is much less than R_1 the plane shock approximation will be appropriate. Hence, for proton energies less than

$$E_p = 1.5 \times 10^{-2} x_1^{0.5} \left(\frac{L_c}{\text{erg s}^{-1}} \right)^{0.5} \quad \text{eV} \tag{6.12}$$

the acceleration rate will not be significantly affected by the approximation that the shock front is a plane.

What values of x_1 are appropriate for AGN. Comparing the mass–luminosity relationship for AGN (Equation 6.1) with the observations, Kazanas and Ellison (1986) have found that values in the $5 \leq x_1 \leq 150$ are consistent with the optical observations. However, for diffusive shock acceleration to take place the Alfven velocity of the plasma $u_A = B/\sqrt{4\pi m_p n(R_1)} \simeq 4.21 \times 10^{10} x_1^{-0.25} (Q(x_1))^{0.5}$ cm s^{-1} must be less than the flow velocity of the plasma, u_1. If $u_A > u_1$ then the magnetic irregularities which scatter the proton as it accelerates, travel faster than the plasma flow and diffusive acceleration will not take place. This provides a lower bound for the dimensionless shock radius, and from a re–examination of Figure 5 of Kazanas and Ellison (1986) values in the range $10 \leq x_1 \leq 100$ has been used in this thesis.

6.5 Loss Processes in AGN

In the central region of an AGN protons lose energy via pion photoproduction, pair production, proton–proton interactions, synchrotron radiation and Compton scattering. In addition, protons may be catastrophically lost due to escape from the central region or by being advected onto the black hole. Fortunately, in practice not all of these loss mechanisms are important in AGN. To determine which of the energy loss processes are important, and at which energies they dominate, I have calculated the

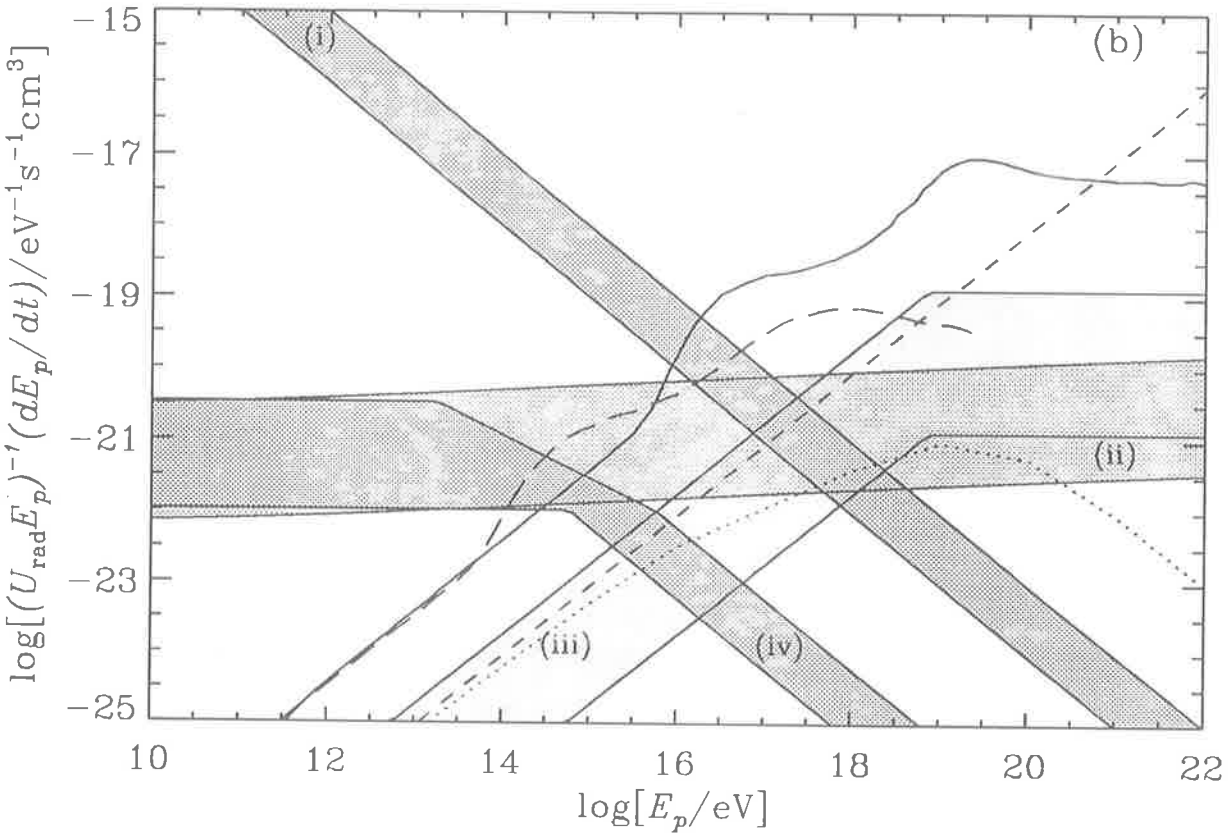

Figure 6.5: (b) A plot of the mean loss rates and the acceleration rate for $b^{-1}L_c^{0.5} = 10^{21}$ (erg s^{-1})$^{0.5}$, using the flat AGN continuum. The shaded bands are defined as follows: (i) the acceleration rate, (ii) the loss rate due to proton–proton interactions, (iii) the loss rate due to diffusion away from the central region, and (iv) the loss rate due to advection onto the black hole. For bands (i)–(iii) and for low energies in band (iv), the lower bound is for $x_1 = 10$ and the upper bound is for $x_1 = 100$. Also shown are the loss rates for pion photoproduction (solid curve), pair production (long dashed curve), synchrotron radiation (short dashed curve) and Compton scattering (dotted curve). The curves have all been scaled by the total radiation energy density U_{rad} to aid comparison.

mean energy loss rate, [1]

$$\frac{dE_p}{dt} \simeq -\frac{\Delta E_p}{T(E_p)}, \tag{6.13}$$

for each process, where ΔE_p is the mean energy lost per interaction and $T(E_p)$ is the mean time scale on which the loss process occurs. For interactions, $\Delta E_p = E_p \langle K(E_p) \rangle$ and $T(E_p) = \overline{\lambda}(E_p)/c$, where $\langle K(E_p) \rangle$ is the mean inelasticity and $\overline{\lambda}(E_p)$ is the mean path length for interaction. For the catastrophic loss processes, one can directly calculate the mean time scale on which the loss process occurs. To reduce the dynamic range when plotting the energy loss rates, one can instead plot the mean loss rate, $T^{-1}(E_p) = -{E_p}^{-1} dE_p/dt$. Each of the loss processes have been examined in detail and are described below.

6.5.1 Proton–Proton Losses

For proton–proton interactions the mean path length is given by $\overline{\lambda}_{pp}^{-1}(E_p) = n_p \sigma_{pp}(E_p)$, where n_p is the number density of protons within the central region of the AGN, and $\sigma_{pp}(E_p)$ is the inelastic cross section for proton–proton interactions. For a strong shock, the number density immediately downstream of the shock front is four times the number density immediately upstream, and so I have assumed that $n_p \simeq 4n(R_1)$. For $\sigma_{pp}(E_p)$, the following fit to the data (see Figure 4.24) of Alner *et al.* (1986),

$$\sigma_{pp}(E_p) \simeq 0.12 \log^2 \left(1.88 \times 10^{-9} \left(\frac{E_p}{\mathrm{eV}} \right) \right) + 27.25 \quad \mathrm{mb}. \tag{6.14}$$

has been used. The mean inelasticity for pp interactions is $\langle K_{pp}(E_p) \rangle \simeq 0.5$ (see e.g Gaisser 1990), and the mean energy loss rate is

$$\begin{aligned} \left. \frac{dE_p}{dt} \right|_{pp} &= -0.5 E_p n_p \sigma_{pp}(E_p) c \\ &\simeq -4.9 \times 10^{67} \frac{x_1^{-2.5}}{Q(x_1)} \left(\frac{L_c}{\mathrm{erg\ s^{-1}}} \right)^{-1} \left(\frac{\sigma_{pp}(E_p)}{\mathrm{cm}^2} \right) \left(\frac{E_p}{\mathrm{eV}} \right) \quad \mathrm{eV\ s^{-1}}, \end{aligned} \tag{6.15}$$

using Equation 6.5 to find the proton number density at the shock. Thus, the mean loss rate is given by

$$(U_{rad} T_{pp}(E_p))^{-1} \simeq 6.4 \times 10^1 \frac{x_1^{1.5}}{Q(x_1)} \left(\frac{\sigma_{pp}(E_p)}{\mathrm{cm}^2} \right) \quad \mathrm{s^{-1}\ (eV\ cm^{-3})^{-1}}. \tag{6.16}$$

[1] In the following discussion, I refer to the quantity dE_p/dt as the *energy loss rate* and the quantity $T^{-1}(E_p) = E_p^{-1} dE_p/dt$ as the *loss rate* for a given process.

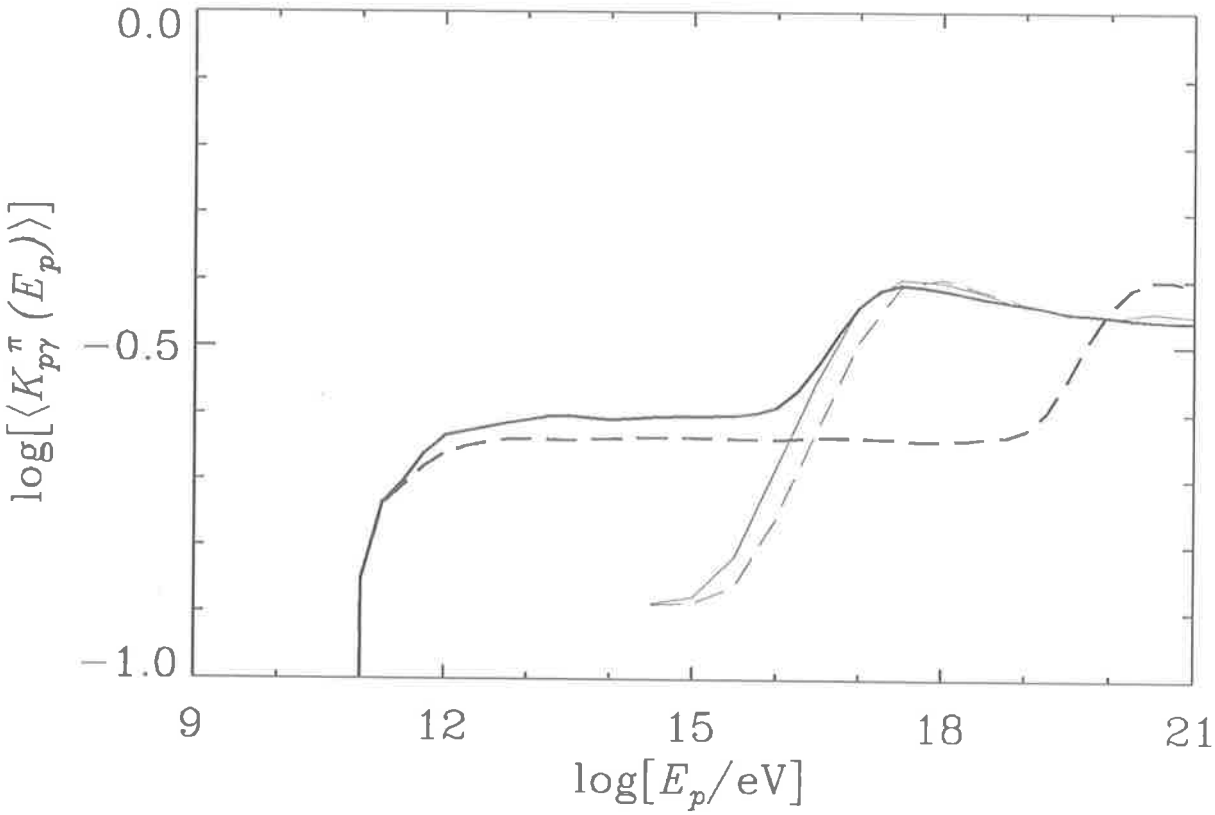

Figure 6.6: A plot of the mean inelasticity for pion photoproduction, $\langle K_{p\gamma}^{\pi}(E_p)\rangle$, calculated using spectrum (a) (solid curves) and spectrum (b) (dashed curves). In each case, the thin curves represent the results from interactions on blackbody photons, and the thick curves represent the results from interactions on power law photons.

The mean loss rate has been scaled by the radiation energy density in the central region (given by Equation 6.6) to aid comparison with the loss rates due to proton–photon interactions calculated below. I have calculated $(U_{rad}T_{pp}(E_p))^{-1}$ for $10 \leq x_1 \leq 100$ and the results are shown in Figure 6.5.

6.5.2 Pion Photoproduction Losses

For pion photoproduction the mean inelasticity, $\langle K^{\pi}_{p\gamma}(E_p)\rangle$, is energy dependent, and because of the form of the radiation field, it is not trivial to calculate the mean inelasticity as a function of primary proton energy. Hence, I have used a Monte Carlo simulation to model pion photoproduction interactions with both power law and black body photons, to calculate the mean energy lost per interaction. The results are shown in Figure 6.6 for both spectrum (a) and (b). One can see that while most of the interactions occur near threshold $\langle K^{\pi}_{p\gamma}(E_p)\rangle$ is approximately constant. However, once all of the photon spectrum is available for interactions with the proton the mean total energy of the interacting particles begins to increase, the mean inelasticity also increases until it reaches a constant value of $\langle K^{\pi}_{p\gamma}(E_p)\rangle \simeq 0.3$.

I have calculated the mean path length for pion photoproduction, $\overline{\lambda}^{\pi}_{\gamma p}(E_p)$, using Equation 4.3 for both spectrum (a) and (b). The results are shown in Figure 6.7, where the contributions from interactions on blackbody and power law photons are shown separately. In each case, $\overline{\lambda}^{\pi}_{\gamma p}(E_p)$ has been scaled by the radiation density within the central region so that the mean path length for interaction may be easily scaled for an arbitrary radiation energy density. See the discussion in Section 4.2 for a detailed description of the mean path length for interaction on power law and thermal photon distributions.

One now has all of the ingredients required to calculate the mean loss rate for pion photoproduction, $(T_{p\gamma\rightarrow\pi}(E_p))^{-1}$, and the results for interactions on power law and blackbody photons are shown separately in Figure 6.8. Once again, the mean loss rate has been scaled by U_{rad} to simplify calculating $(T_{p\gamma\rightarrow\pi}(E_p))^{-1}$ for an arbitrary photon energy density. From Figure 6.8, one can see that interactions on blackbody photons dominate for energies above $\sim 3 \times 10^{15}$ eV for spectrum (a). Similarly, for spectrum (b) protons with energies between $\sim 5 \times 10^{15}$ eV and $\sim 3 \times 10^{17}$ eV lose energy mainly through interactions with thermal photons. The sum of the loss rates on power law

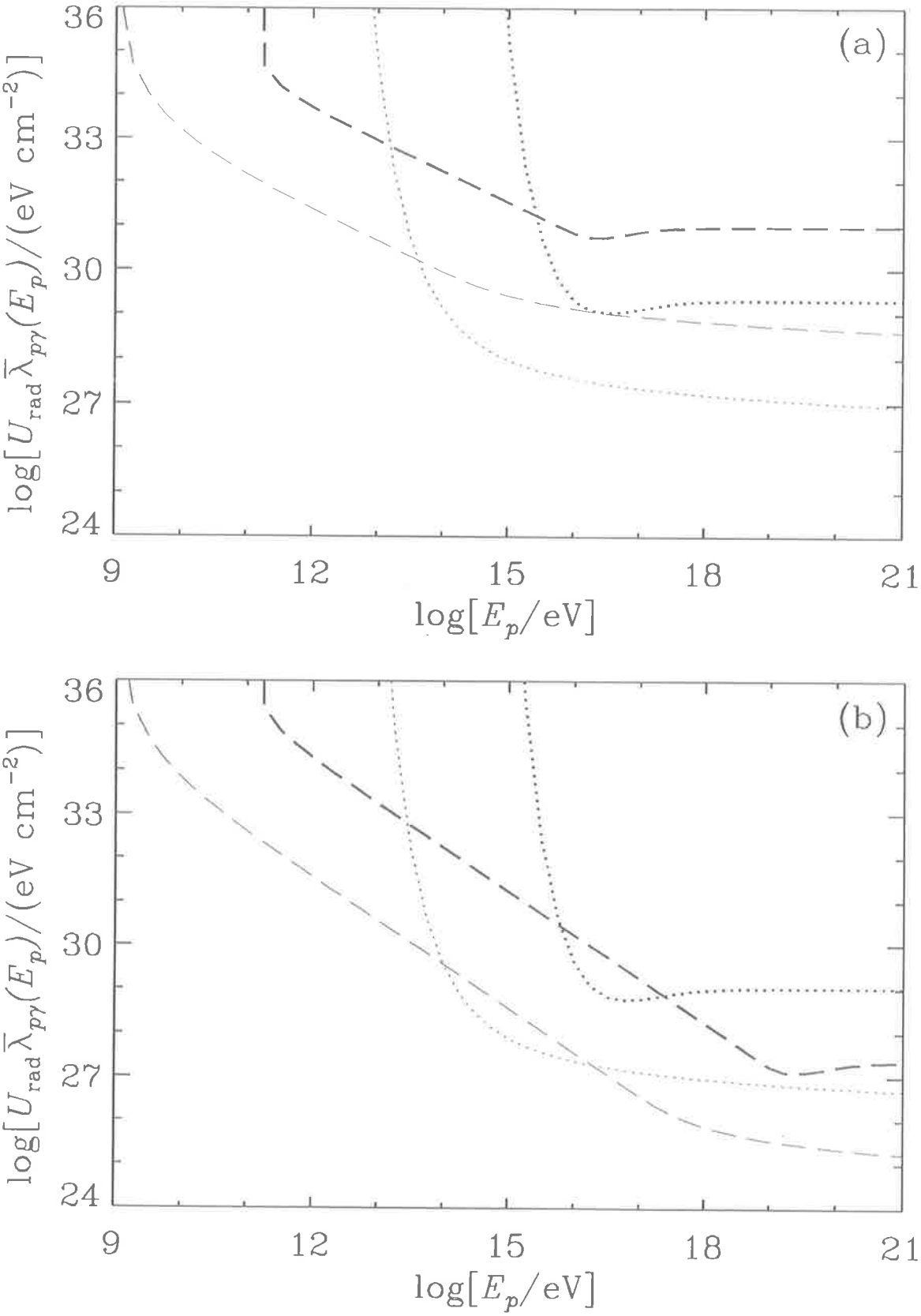

Figure 6.7: A plot of the mean path length for interaction (scaled by the radiation density U_{rad}) calculated using spectrum (a) (part (a)) and spectrum (b) (part(b)). The contributions from black body photons (dotted lines) and from power law photons (dashed lines) are shown separately. In each case, thick curves are the results for pion photoproduction, and thin curves are for pair production.

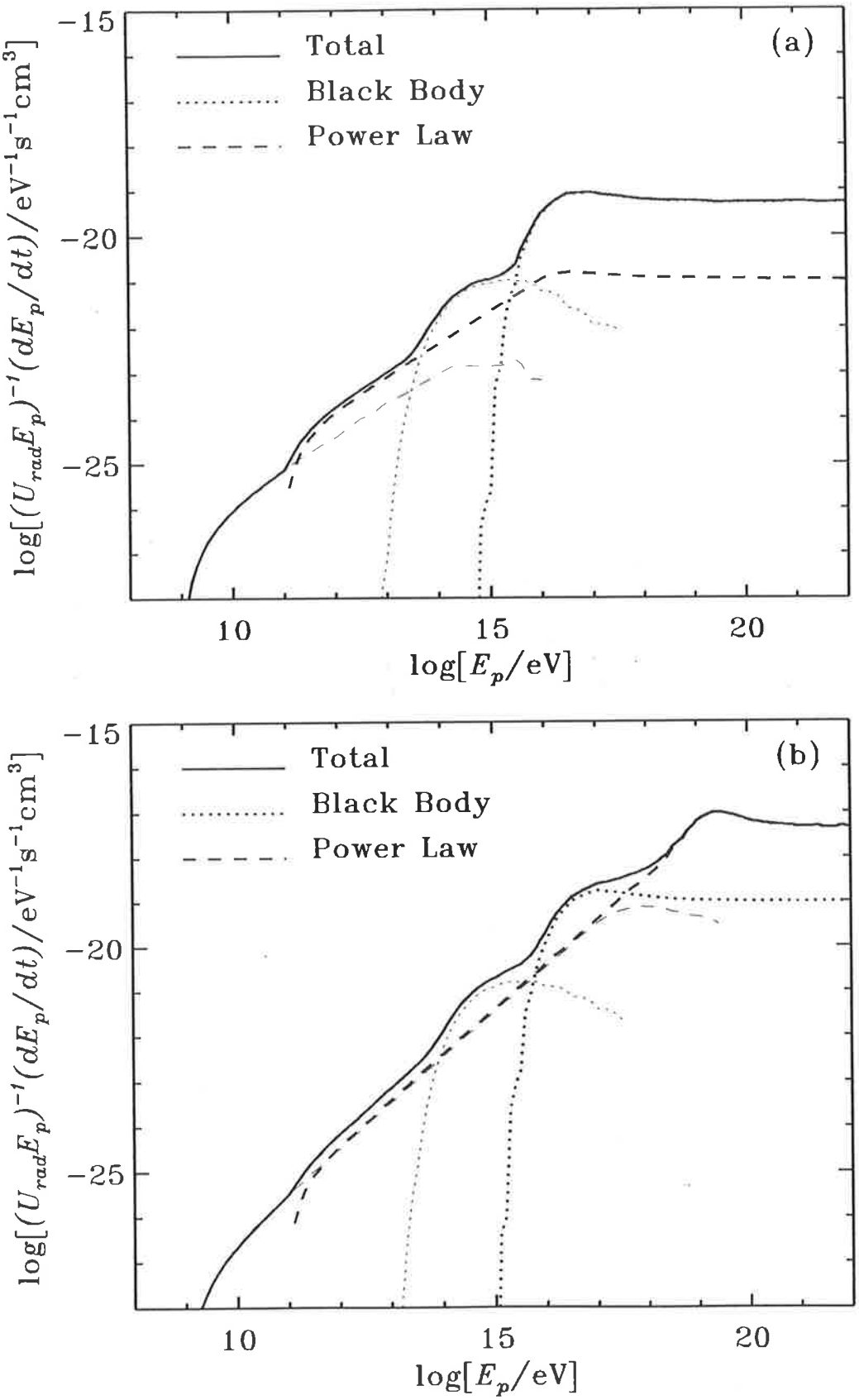

Figure 6.8: A plot of the mean loss rate (scaled by U_{rad}) due to pion photoproduction (thick curves) and pair production (thin curves), calculated using spectrum (a) (part (a)) and spectrum (b) (part (b)). In each case, the loss rate due to interactions on black body photons (dotted curves) and power law photons (dashed curves) are shown separately. The total loss rate due to pion photoproduction and pair production is shown by the solid curve.

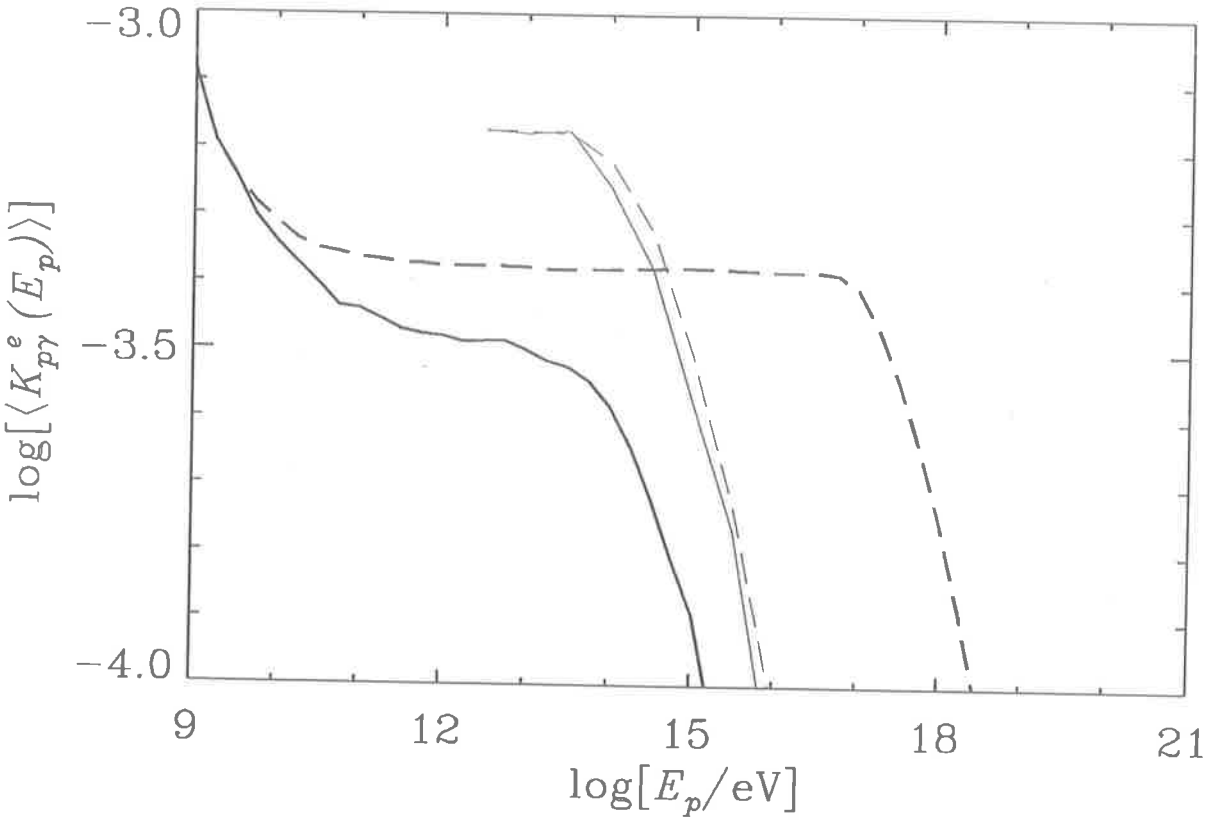

Figure 6.9: A plot of the mean inelasticity for pair production, $\langle K^e_{p\gamma}(E_p)\rangle$, calculated using spectrum (a) (solid curves) and spectrum (b) (dashed curves). In each case, thin curves represent the results from interactions on blackbody photons, whereas, thick curves represent the results from interactions on power law photons.

and thermal photon fields, has been added to Figure 6.5 where it is compared with the other loss rates. Notice that the total loss rate will be insensitive to the energy of the high energy cut off in the photon spectrum because for proton energies less than $\sim 10^{14}$ eV proton–proton losses dominate over pion photoproduction losses.

6.5.3 Pair Production Losses

As for pion photoproduction, I have used a Monte Carlo simulation to calculate the mean inelasticity for pair production, $\langle K^e_{p\gamma}(E_p)\rangle$. The results are shown in Figure 6.9 for both spectrum (a) and (b), and one can see that for the power law photon spectra $\langle K^e_{p\gamma}(E_p)\rangle$ falls rapidly just above threshold and then becomes approximately constant. The mean inelasticity becomes constant because most of the interactions occur near threshold, and the mean total energy of the interacting particles is approximately constant. For higher proton energies where all of photon spectrum is available to the proton and the mean total energy of the interacting particles begins to increase, and $\langle K^e_{p\gamma}(E_p)\rangle$ falls off rapidly. Similar behaviour is observed for interactions on blackbody photons.

I have calculated the mean path length for pair production, $\overline{\lambda}^e_{\gamma p}(E_p)$, using Equation 4.27 and the results have been added to Figure 6.7. The resulting mean loss rate, $(T_{p\gamma\to e}(E_p))^{-1}$, has been added to Figure 6.8, for comparison with the pion photoproduction loss rate calculated in Section 6.5.2. Again the contributions from interactions on power law and thermal photons have been shown explicitly. One can see that interactions on blackbody photons dominate for energies above $\sim 3\times 10^{13}$ eV for spectrum (a), and for energies between $\sim 10^{14}$ eV and $\sim 5\times 10^{15}$ eV for spectrum (b). For spectrum (a) pion photoproduction losses dominate over pair production losses on power law photons. For spectrum (b) both pion photoproduction and pair production losses are approximately equal. This situation arises for spectrum (b) because while $\langle K^\pi_{p\gamma}(E_p)\rangle \simeq 500\langle K^e_{p\gamma}(E_p)\rangle$, pair production interactions occur ~ 500 times more often. A curve representing the total loss rate due to pair production has been added to Figure 6.5, where it may be compared with the other loss rates. Again, proton–proton losses dominate over pair production losses at low energies, and hence the total loss rate will be insensitive to the high energy cut off in the photon spectrum.

6.5.4 Proton Diffusion and Escape from the Central Region

For a diffusion coefficient, D, protons will take a time $T_{\rm diff}(E_p) \simeq R_1^2/2D$ to diffuse out of the central region of AGN. Using Equation 6.8 for the diffusion coefficient, the loss rate due to diffusion is given by

$$(U_{rad}T_{\rm diff}(E_p))^{-1} \simeq 1.8 \times 10^{-21} b x_1^2 \left(\frac{E_p}{\rm eV}\right) \left(\frac{L_{\rm c}}{\rm erg\ s^{-1}}\right)^{-0.5} \quad {\rm s^{-1}\ (eV\ cm^{-3})^{-1}}, \quad (6.17)$$

where Equation 6.2 has been used for R_s. However, when the mean path length for scattering on the magnetic field becomes larger than the central region, i.e. $br_g > R_1$, then diffusion is no longer appropriate. In this case, the time scale for proton escape from the central region is approximately, $T_{\rm esc} \simeq R_1/c \simeq 9.83 \times 10^{-44} x_1^2 (L_{\rm c}/{\rm erg\ s^{-1}})$ s. Thus, for energies greater than,

$$E_{\rm esc} \simeq 7.4 \times 10^{-3} b^{-1} \left(\frac{L_{\rm c}}{\rm erg\ s^{-1}}\right)^{0.5} \quad {\rm eV}, \quad (6.18)$$

the mean loss rate due to escape from the central region of AGN is

$$(U_{rad}T_{\rm esc})^{-1} \simeq 1.3 \times 10^{-23} x_1^2 \quad {\rm s^{-1}\ (eV\ cm^{-3})^{-1}}. \quad (6.19)$$

I have calculated the mean loss rate due to diffusion and escape from the central region for $b^{-1}{L_{\rm c}}^{0.5} = 10^{19}$, 10^{20},...10^{24} $({\rm erg\ s^{-1}})^{0.5}$. A shaded band representing results for shock radii in the range $10 \leq x_1 \leq 100$ with $b^{-1}L_c^{0.5} = 10^{21}$ $({\rm erg\ s^{-1}})^{0.5}$ has been added to Figure 6.5. Results for all of the other values of $b^{-1}L_c^{-0.5}$ can be found in Appendix D.

6.5.5 Proton Advection onto the Black Hole

If one assumes that the protons are tied to the accreting plasma, and that within the central region the plasma has velocity, $u = u_1/4$, then the time scale on which protons fall onto the black hole from a radius R_1 is $T_{\rm infall} \simeq 4R_1/u_1 \simeq 3.93{\times}10^{-43} x_1^{2.5} (L_{\rm c}/{\rm erg\ s^{-1}})$ s. However, in reality protons will diffuse as they advect onto the black hole. During the time $T_{\rm infall}$ protons will have diffused a mean distance $R_{\rm diff} \simeq (2DT_{\rm infall})^{0.5}$, where D is the diffusion coefficient within the central region of the AGN given by Equation 6.8. Thus, the fraction of the accreting protons which are advected onto the black hole is approximately

$$f_{\rm infall}(E_p) \simeq \frac{\pi R_s^2}{\pi R_{\rm diff}^2}$$

$$\simeq 1.8 \times 10^{-3} b^{-1} x_1^{-2.5} \left(\frac{E_p}{\mathrm{eV}}\right)^{-1} \left(\frac{L_c}{\mathrm{erg\ s^{-1}}}\right)^{0.5}. \quad (6.20)$$

Diffusion will only affect the time scale for advection onto the black hole, if $R_{\mathrm{diff}} > R_s$. This will occur for protons with energy greater than

$$E_{\mathrm{advec}} \simeq 1.8 \times 10^{-3} b^{-1} x_1^{-2.5} \left(\frac{L_c}{\mathrm{erg\ s^{-1}}}\right)^{0.5} \quad \mathrm{eV}. \quad (6.21)$$

Hence, the time scale for advection is

$$T_{\mathrm{advec}}(E_p) \simeq \begin{cases} T_{\mathrm{infall}} & \text{for } E_p \leq E_{\mathrm{advec}} \\ f_{\mathrm{infall}}^{-1}(E_p) T_{\mathrm{infall}} & \text{for } E_p > E_{\mathrm{advec}} \end{cases}, \quad (6.22)$$

and the mean loss rate is given by

$$(U_{rad} T_{\mathrm{advec}}(E_p))^{-1} \simeq \begin{cases} 3.3 \times 10^{-24} x_1^{1.5} & \text{for } E_p \leq E_{\mathrm{advec}} \\ 6.1 \times 10^{-27} b^{-1} x_1^{-1} \left(\frac{E_p}{\mathrm{eV}}\right)^{-1} \left(\frac{L_c}{\mathrm{erg\ s^{-1}}}\right)^{0.5} & \text{for } E_p > E_{\mathrm{advec}} \end{cases}$$
$$\mathrm{s^{-1}(eV\ cm^{-3})^{-1}}. \quad (6.23)$$

As for diffusion and escape from the central region, I have calculated the advection loss rate for $b^{-1} L_c^{0.5} = 10^{19}$, 10^{20},...10^{24} $(\mathrm{erg\ s^{-1}})^{-1}$. Again, a shaded band representing results for shock radii in the range $10 \leq x_1 \leq 100$ with $b^{-1} L_c^{0.5} = 10^{21}$ $(\mathrm{erg\ s^{-1}})^{0.5}$ has been added to Figure 6.5. Results for the other values of $b^{-1} L_c^{0.5}$ can be found in Appendix D.

6.5.6 Compton Losses

Compton interactions between low energy photons of energy ε and protons of energy E_p will be in the Thomson energy regime if the energy of the photon in the proton rest frame, $\varepsilon' \simeq \gamma\varepsilon$, is much less than $m_p c^2$, where $\gamma = E_p / m_p c^2$. For spectrum (a) (see Figure 6.2) most of the photons have an energy of $\sim kT = 4.3$ eV, and hence Compton interactions will be in the Thomson energy regime for $E_p \ll 2 \times 10^{17}$ eV. Similarly for spectrum (b), most of the photons have an energy of $\sim 10^{-2}$ eV and so protons need to have energy $E_p \ll 8.8 \times 10^{19}$ eV for the interactions to be in the Thomson energy regime. For the proton energies above about 10^{17} eV for spectrum (a) and 10^{19} eV for spectrum (b) the interactions are in the Klein–Nishina energy regime, and the energy loss rate is given by (see e.g. Blumenthal and Gould 1970)

$$\left.\frac{dE_p}{dt}\right|_{\mathrm{compt}} = -\int_0^\infty \int_\varepsilon^{\varepsilon_1^{\max}} (\varepsilon_1 - \varepsilon) \frac{dN}{dt\, d\varepsilon_1} d\varepsilon_1 d\varepsilon, \quad (6.24)$$

where ε_1 is the final energy of the photon measured in the LAB frame, and $\varepsilon_1^{\max} = 4\gamma\varepsilon E_p/(m_p c^2 + 4\varepsilon\gamma)$ is given by the kinematics of the interaction. Here,

$$\begin{aligned}
\frac{dN}{dt d\varepsilon_1} &= \frac{2\pi r_o^2 c n(\varepsilon)}{\gamma^2 \varepsilon}\left[2q\ln q + (1+2q)(1-q) + \frac{(\Gamma q)^2}{2(1+\Gamma q)}(1-q)\right], \\
q &= \frac{\varepsilon_1}{\Gamma(E_p - \varepsilon_1)}, \\
\Gamma &= \frac{4\varepsilon\gamma}{m_p c^2},
\end{aligned}$$

$r_o = e^2/m_p c^2 \simeq 1.53 \times 10^{-16}$ cm, and $n(\varepsilon)$ is the differential number density of the photon field. I have calculated the energy loss rates for Compton scattering of protons in spectrum (a) and (b) numerically, and the Compton loss rate $T_{\rm compt}{}^{-1}(E_p)$ scaled by U_{rad} have been added to Figure 6.5, where it is compared to the other loss rates.

6.5.7 Synchrotron Losses

A proton with energy E_p traversing a magnetic field of strength B will suffer energy losses due to synchrotron radiation. Synchrotron radiation can be thought of as scattering of the virtual photons in the magnetic field, and hence is directly analogous to Compton scattering. In the Thomson energy regime photons are typically produced with an energy of $\varepsilon_1 = \gamma^2 heB/2\pi m_p c$, where $\gamma = E_p/m_p c^2$, h is the Planck constant and e is the proton's charge (see e.g. Rybicki and Lightman 1979). This corresponds to a virtual photon energy of $\varepsilon' = \varepsilon_1' = E_1/\gamma$ in the proton rest frame. Hence, for protons with energy $E_p \ll E_{\rm crit} = 2\pi m_p^3 c^5/heB \simeq 25 x_1^2 (L_{\rm c}/{\rm erg\ s^{-1}})^{0.5}$ eV (using Equation 6.7) synchrotron radiation will be in the Thomson energy regime. Even for a luminosity of $L_{\rm c} = 10^{37}$ erg s^{-1} and $x_1 = 10$ the critical energy is $E_{\rm crit} \simeq 8 \times 10^{21}$ eV. Hence, the energy loss rate is (see e.g. Rybicki and Lightman, 1979),

$$\left.\frac{dE_p}{dt}\right|_{\rm synch} = -\frac{4}{9}\frac{e^4 E_p^2 B^2 \beta^2}{m_p^4 c^7}, \tag{6.25}$$

where all of the quantities are in cgs units, and βc is the velocity of the proton. For a discussion of synchrotron radiation in which quantum effects are important, i.e. for synchrotron radiation from ultra relativistic particles in strong magnetic fields, see Brainerd (1987), Brainerd and Petrosian (1987) and Harding and Preece (1987).

If one assumes that the magnitude of the magnetic field within the central region is uniform, and the same as the magnetic field in the vicinity of the shock, then the

synchrotron loss rate for ultra–relativistic protons ($\beta \simeq 1$) is given by

$$(U_{rad}T_{\rm synch}(E_p))^{-1} \simeq 9.0 \times 10^{-39} \left(\frac{E_p}{\rm eV}\right) \quad {\rm s}^{-1}\ ({\rm eV\ cm}^{-3})^{-1}, \tag{6.26}$$

which has been added to Figure 6.5.

6.6 The Maximum Proton Energy in AGN

The maximum proton energy achievable by shock acceleration in AGN, $E_{\rm max}$, may be estimated by equating the acceleration rate with the total loss rate. Notice that only the acceleration rate, the advection loss rate and the diffusion loss rate depend on b and $L_{\rm c}$, via a factor $b^{-1}L_c^{0.5}$. Hence, the quantity $b^{-1}L_c^{0.5}$ is a logical parameter for analysing the way in which the loss rate varies with b and $L_{\rm c}$. A shaded band representing the acceleration rate (see Equation 6.9) for the range $10 \leq x_1 \leq 100$ with $b^{-1}L_{\rm c} = 10^{21}$ erg$^{0.5}$ s$^{-0.5}$ has been added to Figure 6.5 for comparison with the loss rates. Similar plots for $b^{-1}L_c^{0.5} = 10^{19}$, 10^{20},...,10^{24} (erg s^{-1})$^{0.5}$ can be found in Appendix D. From these plots it can be seen that for $b^{-1}L_c^{0.5} > 10^{20}$ (erg s^{-1})$^{-1}$ the maximum proton energy is determined by pion photoproduction, pair production and synchrotron radiation. However, for reasonable values of $b \leq 100$ and $L_{\rm c} \leq 10^{48}$ erg s^{-1} synchrotron radiation is only important for the PG continuum, and the maximum proton energy is dominated by pion photoproduction losses. This is consistent with earlier work by Biermann and Strittmatter (1987) and Sikora *et al.* (1987) who found that the maximum proton energy in AGN was governed by pion photoproduction losses. For $b^{-1}L_c^{0.5} < 10^{20}$ (erg s^{-1})$^{0.5}$, it is primarily proton–proton interactions which determine $E_{\rm max}$. The maximum proton energy is given by solving the equation

$$\begin{aligned}\left.\frac{dE_p}{dt}\right|_{\rm acc}(E_{\rm max}, b, L_{\rm c}) &= \left.\frac{dE_p}{dt}\right|_{pp}(E_{\rm max}) + \left.\frac{dE_p}{dt}\right|_{p\gamma\rightarrow\pi}(E_{\rm max}) \\ &+ \left.\frac{dE_p}{dt}\right|_{p\gamma\rightarrow e}(E_{\rm max}) + \left.\frac{dE_p}{dt}\right|_{\rm advec}(E_{\rm max}, b, L_{\rm c}) \\ &+ \left.\frac{dE_p}{dt}\right|_{\rm synch}(E_{\rm max}) + \left.\frac{dE_p}{dt}\right|_{\rm diff}(E_{\rm max}, b, L_{\rm c})\end{aligned} \tag{6.27}$$

where the energy loss rate due to Compton scattering has been omitted because it is negligible compared to the other energy loss rates. I have solved Equation 6.27 numerically for $E_{\rm max}$ as a function of $L_{\rm c}$ with $b = 1$ and $b = 10$, and the results are

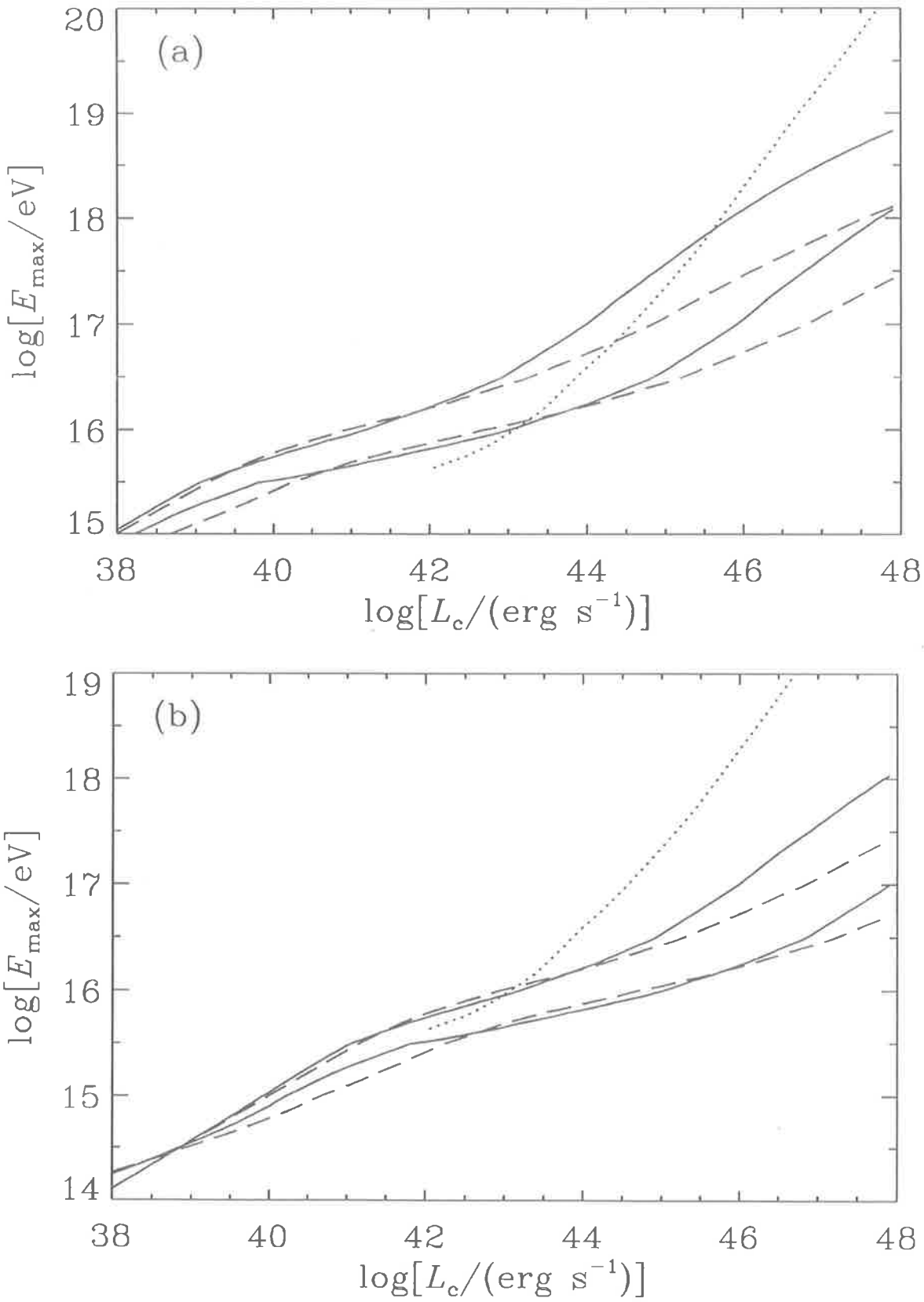

Figure 6.10: A plot of the maximum proton energy achievable in AGN, $E_{\rm max}$, as a function of the continuum luminosity of the AGN, $L_{\rm c}$. Curves are shown for spectrum(a) (solid curves) and for spectrum (b) (dashed curves). In each case, the upper curve corresponds to $x_1 = 100$ and the lower curve to $x_1 = 10$. Results are shown for (a) $b = 1$, and (b) $b = 10$. Results from Stecker *et al.* (1991b) (dotted curve) are also shown for comparison.

shown in Figure 6.10. The results from a calculation by Stecker *et al.* (1991a,b, 1992) in which only pion photoproduction losses are included has been added to the plot for comparison. For $L_c > 10^{46}$ erg s^{-1} (see Figure 6.10(a)) the effect of the synchrotron and pair production losses can be clearly seen, as the results of Stecker *et al.* predict higher $E_{\rm max}$ values. From Figure 6.10 it can also be seen that for $10^{38} \leq L_c \leq 10^{40}$ erg s^{-1} the maximum proton energy produced in AGN is in the range $10^{15} \leq E_{\rm max} \leq 10^{19}$ eV for b=1, and in the range $10^{14} \leq E_{\rm max} \leq 10^{18}$ eV for b=10.

For the calculation of the neutrino spectra from AGN, I have adopted the maximum proton energy as a parameter. This is quite useful as it effectively reduces the calculation to one dependent on only three parameters, the dimensionless shock radius, x_1, the ratio of the proton's diffusion coefficient to the minimum diffusion coefficient, b, and maximum proton energy $E_{\rm max}$. Once these quantities have been set then the model is completely defined. For example, if x_1, b and $E_{\rm max}$ are given then the continuum luminosity of the AGN can simply be read off Figure 6.10, and this in turn defines the radiation and matter densities within the central region and hence the loss rates. The use of the maximum proton energy as a parameter for the calculation also has the advantage that the loss rates (scaled by U_{rad}) are uniquely defined by $E_{\rm max}$ for a given value of x_1. This arises because $U_{rad}T_{\rm advec}$ and $U_{rad}T_{\rm diff}$ depend on a factor $b^{-1}L_c^{0.5}$, as does $U_{rad}T_{\rm acc}$. Hence, if b increases by a factor of 10 then L_c increases by a factor of 100 (see Figure 6.10) and the loss rates scaled by the radiation energy density stays the same. Notice that the individual loss rates will not *be* the same, but that everything scales with the radiation density so that the loss rates relative to the total loss rate will be the same.

6.7 Will Neutrons Escape from the Central Region?

Neutrons are not coupled to the accreting plasma via the magnetic field and so they may escape from the central region of the AGN. Neutron escape is an important means of transporting particles away from the central region. Outside of the central region the neutrons may decay and have observable consequences such as the production of boron (Kirk and Mastichiadis 1987), γ–rays (Mastichiadis and Protheroe 1990, Atoyan

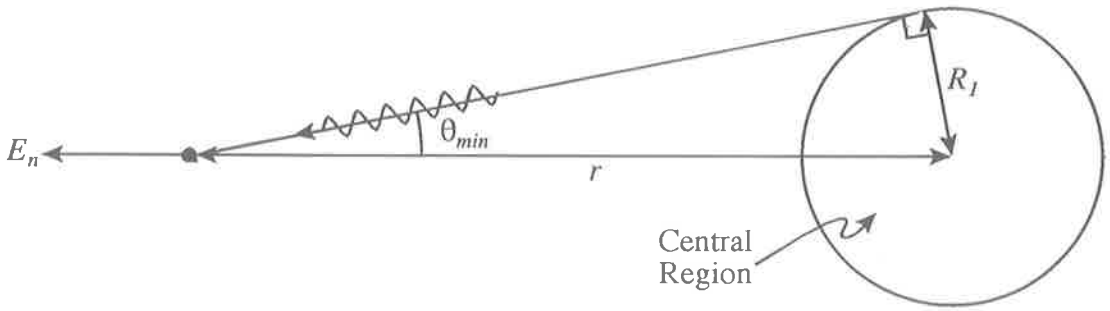

Figure 6.11: A schematic diagram illustrating the minimum interaction angle, θ_{min}, between a neutron and a photon from the central region of the AGN.

1992) or may drive a wind in the broad line emission region of quasars (Begelman, Rudak and Sikora 1990).

Neutrons can interact with matter in the accretion flow or with the photon field. Inside the central region, the mean free path length for np interactions is given by $\overline{\lambda}_{np}^{-1}(E_n) \simeq n_p \sigma_{np}(E_n)$, where $n_p \simeq 4n(R_1)$ is the matter number density inside the central region and $\sigma_{np} \simeq \sigma_{pp} \simeq 30$ mb. Hence, the optical depth of the central region is $\tau_{pp}^{\rm in} = R_1/\overline{\lambda}_{np}(E_n) \simeq 2.9 \times 10^{-1} x_1^{-0.5} (Q(x_1))^{-1}$. Outside of the central region the number density is $\propto r^{-1.5}$ (see Equation 6.5) and the optical depth is given by $\tau_{pp}^{\rm out} \simeq \int_{R_1}^{\infty} n(r)\sigma_{np}(E_n)dr \simeq 1.4 \times 10^{-1} x_1^{-0.5} (Q(x_1))^{-1}$. Hence, for $10 \leq x_1 \leq 100$ AGN are optically thin for np interactions.

Similarly, the optical depth of the central region to neutron induced pion photoproduction is given by $\tau_{p\gamma}^{\rm in}(E_n) = R_1/\overline{\lambda}_{\gamma n}^{\pi}(E_n)$, where $\overline{\lambda}_{\gamma n}^{\pi}(E_n)$ is the mean free path length for neutron–photon interactions. If the total cross sections for $\gamma n \rightarrow \pi X$ and for $\gamma p \rightarrow \pi X$ are assumed to be the same then $\overline{\lambda}_{\gamma n}^{\pi} = \overline{\lambda}_{\gamma p}^{\pi}$, where $\overline{\lambda}_{\gamma p}^{\pi}(E_p)$ is given by Equation 4.3. Outside of the central region, the situation is quite different. Most of the photons come from the central region and so the radiation field is highly anisotropic. The optical depth a neutron traveling radially outward from the shock 'sees' is

$$\tau_{p\gamma}^{\rm out}(E_n) = \int_{R_1}^{\infty} \frac{dr}{\overline{\lambda}_{\gamma n}^{\pi}(E_n, r)}, \tag{6.28}$$

where the mean path length for interaction, $\overline{\lambda}_{\gamma n}^{\pi}(E_n, r)$ is now dependent on r as the number density of photons decreases as the neutron moves away from the central region. I have calculated $\overline{\lambda}_{\gamma n}^{\pi}(E_n, r)$ by assuming an isotropic photon field and only integrating over contributions from photons which come from the central region. From Figure 6.11, one can see that the minimum interaction angle possible, if the photon is to originate from the central region is,

$$\cos\theta_{min} = \sqrt{1 - \frac{R_1^2}{r^2}}. \tag{6.29}$$

Hence,

$$[\overline{\lambda}_{\gamma n}^{\pi}(E_n, r)]^{-1} = \int_{\varepsilon_{th}^{\pi}}^{\infty} n(\varepsilon) \int_{(1-R_1^2/r^2)^{1/2}}^{\cos\theta_{\rm max}} \frac{\sigma_{\gamma n}^{\pi}(s)(1 - \beta\cos\theta)}{2} d\cos\theta d\varepsilon, \tag{6.30}$$

where $\cos\theta_{max}$ and ε_{th}^{π} are given by the Equations 4.4 and 4.2 respectively, substituting E_n for E_p. Both $\tau_{p\gamma}^{\rm in}$ and $\tau_{p\gamma}^{\rm out}$ are shown in Figure 6.12. Here the optical depths have

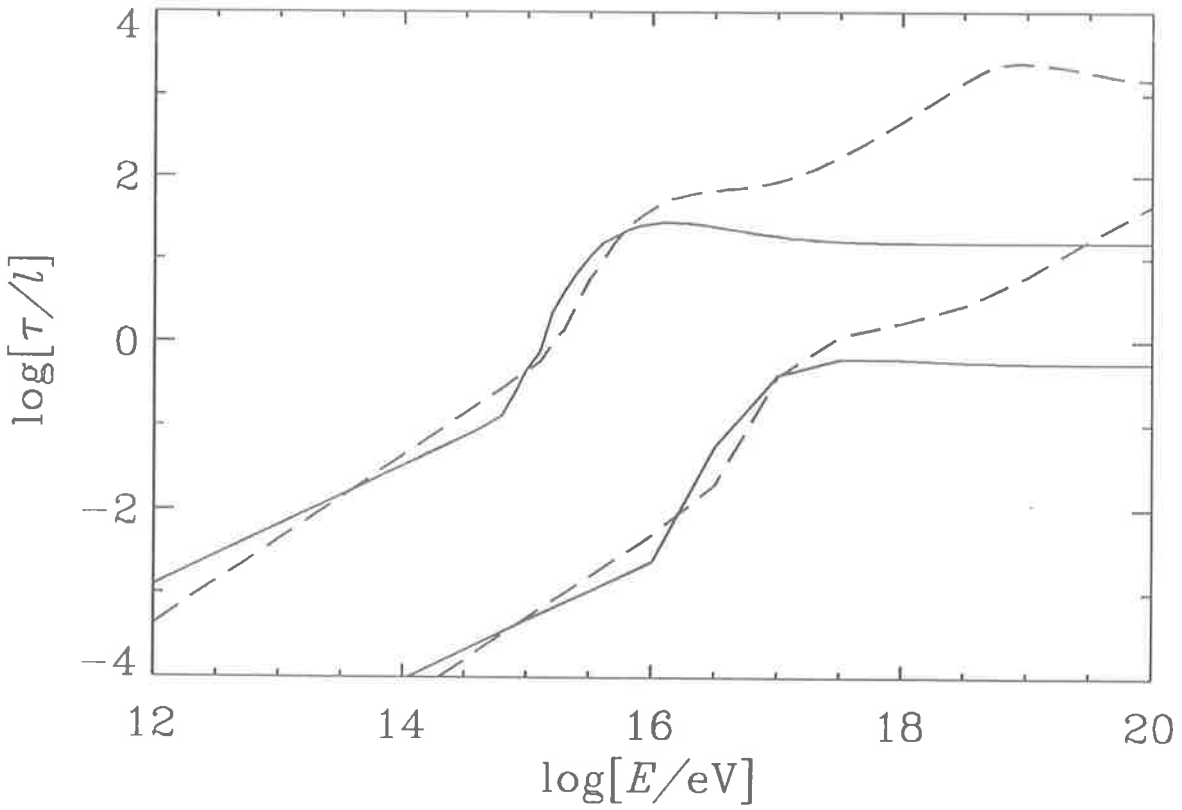

Figure 6.12: A plot of the optical depth of the AGN divided by the compactness, l, as a function of neutron energy, E. The upper curves show the optical depth of the central region, $\tau_{p\gamma}^{\rm in}$, to pion photoproduction. The lower curves show the optical depth outside the central region of the AGN, $\tau_{p\gamma}^{\rm out}$. Solid curves are for spectrum (a) and dashed curves are for spectrum (b).

been scaled by the compactness parameter of the AGN,

$$l = \frac{L_c \sigma_T}{4\pi m_e c^3 R_1} \simeq 730 x_1^{-2}, \quad (6.31)$$

to remove the dependence on the radiation energy density, and Equation 6.2 has been used to simplify the expression for l.

Clearly, the optical depth for pion photoproduction seen by a neutron within the central region will depend on its position and direction. However, the optical depth will have a lower bound given by, $\tau_{p\gamma}^{\rm out}$, corresponding to a neutron moving radially outward from the edge of the central region, and an upper bound $(2\tau_{p\gamma}^{\rm in} + \tau_{p\gamma}^{\rm out})$, corresponding to a neutron crossing the diameter of the central region and then moving outwards. From Figure 6.12, one can see that for $10 \leq x_1 \leq 100$ all neutrons with energy below $\sim 10^{15}$ eV escape from the central region of AGN. However, above 10^{15} eV the probability of escape depends strongly on where the neutron was produced and which photon spectrum is used. For example, for spectrum(a) all neutrons produced at the shock traveling radially outwards will escape from the central region, assuming $x_1 = 100$. Whereas for spectrum (b) no neutrons with energy greater than $\sim 10^{17}$ eV will escape. For simplicity, in the present calculation I have assumed that all neutrons produced within the central region of the AGN will escape. The question of neutron escape has been examined in more detail by Protheroe and Szabo (1992), who have shown that the escaping neutrons may result in a flux of high energy cosmic rays from AGN.

6.8 The Spectrum of Particles Produced per Injected Proton

In order to see how the calculation shall proceed, it is instructive to obtain a qualitative feel for what will happen when protons are accelerated in AGN. Accreting protons are injected into the accelerator and gain energy at a constant rate given by Equation 6.10. For $10^{20} < b^{-1} L_c^{0.5} < 10^{24}$ (erg s^{-1})$^{0.5}$ the acceleration rate is much higher than all of the loss rates for energies below $\sim 10^{15}$ eV. However, at energies greater than $\sim 10^{15}$ eV the acceleration rate becomes comparable with the total loss rate which is dominated by contributions from pion photoproduction, pair production and synchrotron radiation.

Therefore, in the absence of catastrophic losses protons would accumulate near $E_{\rm max}$ producing high energy pions and electrons from interactions with photons. However, protons are catastrophically lost as they may escape from the accelerator, or they may experience a charge exchange interaction such as $\gamma p \rightarrow nX$.

Once protons have escaped from the accelerator they will diffuse within the central region until they interact or are catastrophically lost. From Figure 6.5 it can be seen that while the proton's energy is above $\sim 10^{14}$ eV for $x_1 = 10$, and above $\sim 5 \times 10^{15}$ eV for $x_1 = 100$, pion photoproduction, pair production and synchrotron radiation are the dominant loss mechanisms. Below these energies, the losses are dominated by proton–proton interactions and advection onto the black hole. For low values of $b^{-1}L_c^{0.5}$, proton diffusion out of the central region of the AGN may also be an important loss process. The protons will cascade in the central region until they have lost all of their kinetic energy, or they are catastrophically lost due to charge exchange, advection onto the black hole or diffusion out of the central region.

As discussed in Section 6.7, the neutrons produced during and after acceleration are all assumed to escape from the central region. However, a relativistic neutron has a mean life time of $\sim 9.5 \times 10^{-7} \left(\frac{E_p}{\rm eV}\right)$ s, after which it beta decays. In this time the neutron will have travelled a distance $\sim 2.9 \times 10^{4} \left(\frac{E_p}{\rm eV}\right)$ cm, and therefore neutrons with energy greater than $\sim 10^{-27} x_1^2 \left(\frac{L_c}{\rm erg\ s^{-1}}\right)$ eV will decay outside the central region of the AGN. For example, for a continuum luminosity of 10^{45} erg s^{-1} and $x_1 = 100$, all neutrons with energy greater than $\sim 10^{12}$ eV decay outside of the central region of AGN. Hence, I have made the approximation that all neutrons decay outside the central region. The protons produced by neutron decay are coupled to the accreting plasma via the magnetic field, and so protons will diffuse in the accretion flow until they interact or they diffuse out of the AGN. The photon number density outside of the central region is $\propto r^{-2}$ as most of the photons are produced in the central region, whereas the number density of protons in the accretion flow is $\propto r^{-1.5}$ (see Equation 6.5). Thus, proton–proton interactions will become more important relative to proton–photon interactions as one moves away from the central region of the AGN. Here I have made the approximation that all of the protons interact with the matter in the accretion flow.

From the above discussion it can be seen that there are three distinct parts to the

calculation of the spectra of particles produced per proton injected into the accelerator. They are the calculation of the spectrum of particles produced (i) *during* acceleration, (ii) by protons as they cascade in the accreting matter and the radiation field within the central region, and (iii) by proton–proton interactions outside the central region. For the calculation of the spectrum of particles produced during acceleration, I have made the approximation that pion photoproduction and pair production interactions are the dominant loss processes. The effect of synchrotron losses on the spectra has been included in an approximate way by scaling the spectra. From Figure 6.7 it can be seen that pair production interactions on power law photons occur a factor of ~ 150 and ~ 460 times more often than pion photoproduction interactions for spectrum (a) and (b) respectively. Hence, to obtain good statistics for the spectra of particles produced by pion photoproduction several hundred more pair production interactions would have to be modelled. Modelling of pair production is quite computer intensive because the modelling algorithm becomes increasingly inefficient as the total CM frame energy of the interaction increases. As a result, the calculation has been separated into two parts, the calculation of the proton and $e^{\pm}$ spectra and the calculation of the pion spectra. The spectrum of protons escaping from the accelerator and the spectrum of $e^{\pm}$ produced, have been calculated using the straightforward approach of following each proton and modelling each interaction as it occurs using the Monte Carlo method. A system of weights has also been used to further reduce the computing time required for the simulation. For the calculation of the spectrum of particles produced by pion photoproduction, I have made the approximation that the pair production losses are continuous. In this case, the acceleration rate experienced by a proton is reduced because of pair production losses, and only the pion photoproduction interactions are modelled.

To simulate the protons which have escaped from the accelerator as they cascade in the accreting matter and the radiation field, the spectrum of interactions for the cascade has been calculated. This is the number of interactions which occur in a given energy bin during the cascade. The total spectrum of particles produced is then given by convolving the distribution of particles produced by protons in each energy bin with the spectrum of interactions. All of the relevant loss processes discussed in Section 6.5 have been included, except for Compton losses which are negligible in comparison to the

total proton loss rate. A similar approach has been used for calculating the spectrum of pions produced by neutrons which have escaped from the central region of the AGN. However, in this case protons and neutrons are treated identically, and only pp and np interaction have been considered. The total spectrum of pions produced outside of the central region of the AGN is given by convolving the spectrum of interactions with the pion distributions given by Hillas (1979).

In the following Sections each aspect of the simulation is described in detail and representative results for each stage of the calculation are presented. A compilation of all of the results may be found in Appendix D.

6.8.1 Particles Produced During Acceleration

The Proton and $e^{\pm}$ Spectra

The simple idealised picture of shock acceleration described in Section 2.3.3 has been used to calculate the spectrum of particles produced during acceleration. This simplifies the calculation as the spectrum of protons which escape from the accelerator is known. Rather than follow each proton until it escapes from the accelerator or it is catastrophically lost, a system of weights has been used. Protons are injected into the accelerator with weight $\mathcal{W} = 1.0$ and with an energy of $E_o = 1$ GeV. In the absence of losses the probability that a proton attains an energy E'_o without escaping from the accelerator is E_o/E'_o (see Section 2.3.3), and hence the weight of the is $\mathcal{W} = E_o/E'_o$. If the proton interacts with energy E'_o and has energy E_1 after the interaction, then after i interactions the weight of the proton will be

$$\mathcal{W} = \frac{E_o}{E'_o}\frac{E_1}{E'_1}\cdots\frac{E_i}{E'_i}. \tag{6.32}$$

The amount by which the weight of the proton decreases between interactions is due to protons escaping the accelerator. From Section 2.3.2 it can be seen that in the absence of losses, there is an E_p^{-2} spectrum of protons escaping from the accelerator. The contribution to the total spectrum from protons which have escaped from the accelerator after the i^{th} interaction is $E'_i E_p^{-2}/E_i$ for $E_i \leq E_p \leq E'_i$. Hence, to calculate the total spectrum of protons escaping the accelerator it is simply matter of sampling the energy of the proton when it interacts and adding the portion of the proton which has escaped from the accelerator to the total spectrum.

To decide how far the proton has travelled and therefore what energy it has when it interacts, a dimensionless path length , τ, is sampled for both pair production and pion photoproduction using a method similar to that described by Protheroe (1990). The path length for interaction is given by $\lambda^j_{p\gamma}(E_p) = \tau\overline{\lambda}^j_{p\gamma}(E_p)$, and hence

$$\frac{d\lambda^j_{p\gamma}}{d\tau} = \overline{\lambda}^j_{p\gamma}(E_p), \tag{6.33}$$

where $j = e$ or π for pair production and pion photoproduction respectively, which has the obvious boundary condition $\lambda^j_{p\gamma} = 0$ for $\tau = 0$. However, the proton is also being accelerated at a constant rate

$$\left.\frac{dE_p}{d\lambda^j_{p\gamma}}\right|_{\rm acc} = \frac{a(E_{\rm max}, b, L_c)}{c} = \frac{a}{c}, \tag{6.34}$$

and therefore to find the path length of the proton a pair of coupled differential equations must be solved. The solution of the Equation 6.34 is straightforward (using $E_p = 0$ for $\lambda^j_{p\gamma} = 0$), and the energy of the proton as a function of path length for interaction is $E_p(\lambda^j_{\gamma p}) = E_p(0) + a\lambda^j_{\gamma p}/c$. However, as the mean path length for the interactions is not a simple function of E_p, numerical methods are required to solve Equation 6.33. The $4^{\rm th}$ order Runge–Kutta technique described in Appendix C has been used to solve for $\lambda^j_{\gamma p}$. In this way values are sampled for $\lambda^e_{\gamma p}(E_p)$ and $\lambda^\pi_{\gamma p}(E_p)$ and whichever interaction has the shorter path length is assumed to occur. The interaction is then modelled as described in Sections 4.2 and 4.3, and the energy of the products are binned with weight $\mathcal{W}$. If the proton survives the interaction, then its progress is followed with the new value of energy after the interaction. However, if a charge exchange interaction occurs then the neutron's energy is binned and another proton is injected with energy E_o and weight $\mathcal{W} = 1$. Protons are injected and their progress is followed in this manner until the spectra of the escaping protons and the $e^\pm$ are smooth, and the statistical fluctuations between adjacent energy bins are small.

The Neutron, $\pi^\pm$ and π^o Spectra

To calculate the spectrum of particles produced by pion photoproduction during acceleration, the approximation that the pair production losses are continuous has been used. This approximation can be made because the mean inelasticity for pair production is much smaller than that for pion photoproduction. Again protons are injected

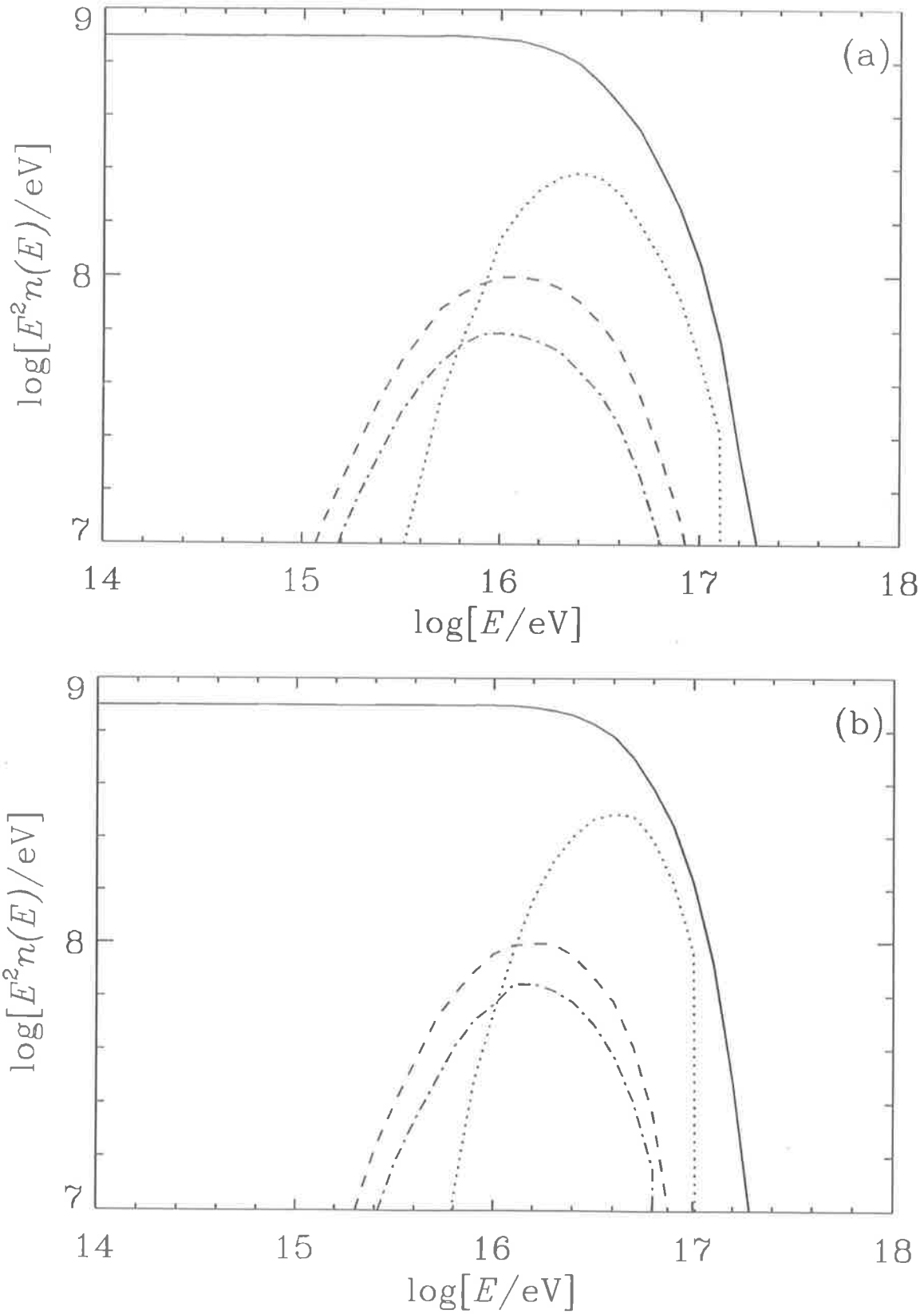

Figure 6.13: A plot of the differential spectrum of particles, $n(E) = dn/dE$, produced by the accelerator per injected proton for $E_{\max} = 10^{17}$ eV, multiplied by a factor of E^2. Plots are the spectra resulting using (a) the Palomar–Green continuum (spectrum a), and (b) the spectra resulting using flat AGN continuum (spectrum b). Shown are the spectrum of protons escaping the accelerator (solid curve), and the spectra of neutrons (dotted curve), $\pi^{\pm}$s (dashed curve) and π^os (dot dashed curve) produced during acceleration. In each case, $n(E)$ has been multiplied by E^2 to reduce the dynamic range of the plot.

into the accelerator with energy E_o. However, when the proton undergoes pion photoproduction with energy E'_o its weight will not simply be E_o/E'_o as the effective acceleration rate will be less than a due to pair production losses. The effective acceleration rate will be

$$\frac{dE_p}{dt} = a - b_e(E_p) = -b(E_p), \tag{6.35}$$

where $b_e(E_p) = \frac{dE_p}{dt}\Big|_{p\gamma\to e}(E_p)$ is the energy loss rate due to pair production (see Section 6.5.3). The weight of the proton when it interacts can be found by solving the transport equation (c.f. Equation 2.1)

$$\frac{\partial}{\partial E_p}\left[b(E_p)\mathcal{N}(E_p)\right] - \frac{\mathcal{N}(E_p)}{T_{\rm esc}} = 0, \tag{6.36}$$

for the case in which only energy losses and escape are included, where $\mathcal{N}(E_p)$ is the differential number density of protons of energy E_p, and $T_{\rm esc} = E_p/a$ is the time scale for escape from the accelerator. Re–arranging Equation 6.36 gives,

$$\frac{\partial \mathcal{N}}{\partial E_p} = \frac{\mathcal{N}(E_p)}{b(E_p)}\left[\frac{a}{E_p} - \frac{\partial b_e(E_p)}{\partial E_p}\right] \tag{6.37}$$

which I have solved numerically $\mathcal{N}(E_p)$ using the $4^{\rm th}$ order Runge–Kutta technique. If the boundary condition $\mathcal{N}(E_o) = 1$ is used then $\mathcal{N}(E'_o) = \mathcal{W}$, the weight of the proton when it has been accelerated to energy E'_o.

As before, a pair of coupled differential equations must be solved to sample the path length of the proton. However, the rate at which protons gain energy is no longer constant, and hence the energy of the proton as a function of the path length for pion photoproduction is given by solving the equation

$$\frac{dE_p}{d\lambda^{\pi}_{\gamma p}(E_p)} = \frac{(a - b_e(E_p))}{c}, \tag{6.38}$$

with the boundary condition $E_p = E_p(0)$ for $\lambda^{\pi}_{\gamma p}(E_p) = 0$. This has been done numerically using the $4^{\rm th}$ Runge–Kutta technique. Having sampled the energy of the proton when it interacts, the pion photoproduction interaction is modelled as described in Section 4.2. Once again, the energies of the produced particles are binned with weight $\mathcal{W}$ and if the proton survives its progress is followed. Otherwise, another proton with energy E_o is sampled and the process repeated until adequate statistics have been built up.

Results

I have calculated the differential spectra of particles, $n(E) = dn/dE$ (particles eV^{-1}), produced during acceleration per injected proton for $E_{\max} = 10^{15}$, 10^{16},...,10^{19} eV, for both spectrum (a) and (b). Representative results for $E_{\max} = 10^{17}$ eV are shown in Figure 6.13, from which it can be seen that the spectrum of protons which escape from the accelerator (solid curves) is $\propto E_p^{-2}$, for $E_p < 0.1E_{\max}$. For energies near $E_{\max}$, protons interact with the radiation field until they escape from the accelerator or they undergo charge exchange, giving rise to the smooth cut off in the spectrum near $E_{\max}$. These interactions, all with $E_p \sim E_{\max}$, produce the peaked neutron and pion spectra shown in Figure 6.13. To illustrate the form of the $e^{\pm}$ spectra produced during acceleration, results for $E_{\max} = 10^{15}$ eV are shown in Figure 6.14. From Figure 6.8 it can be seen that for $E_p \sim 10^{15}$ eV pair production interactions occur primarily with thermal photons, and this is reflected in the shape of the $e^{\pm}$ spectra. For $E_{\max} = 10^{18}$ and 10^{19}, it can be seen from Figure 6.5 that synchrotron losses are important for spectrum (a). I have approximated the effect on the results, by scaling the neutron, $\pi^{\pm}$ and π^o spectra by a factor of $(dE_p/dt|_{p\gamma\to\pi}(E_{\max}))/(dE_p/dt(E_{\max}))$ for these $E_{\max}$ values, where dE_p/dt is the total energy loss rate given by the RHS of Equation 6.27. Results for $E_{\max} = 10^{15}$, 10^{16},...,10^{19} eV may be found in Appendix D.

6.8.2 Particles Produced After Acceleration

The Spectrum of Particles Produced within the Central Region

Protons which have escaped from the accelerator cascade in the accreting matter and the radiation field in the central region of the AGN until they have lost all of their energy or they are catastrophically lost. Catastrophic losses take the form of charge exchange interaction, advection onto the black hole or diffusion out of the central region. The techniques described in the Section 6.8.1 are very computer intensive and difficult to modify to calculate the spectra of particles produced within the central region after acceleration, and hence an alternative technique has been developed. The new technique is based on a calculation of the spectrum of interactions during the cascade, n_i^{int}, i.e. the number of interactions which occur in a given energy bin during the entire cascade. The spectrum of interactions is calculated using an iterative method.

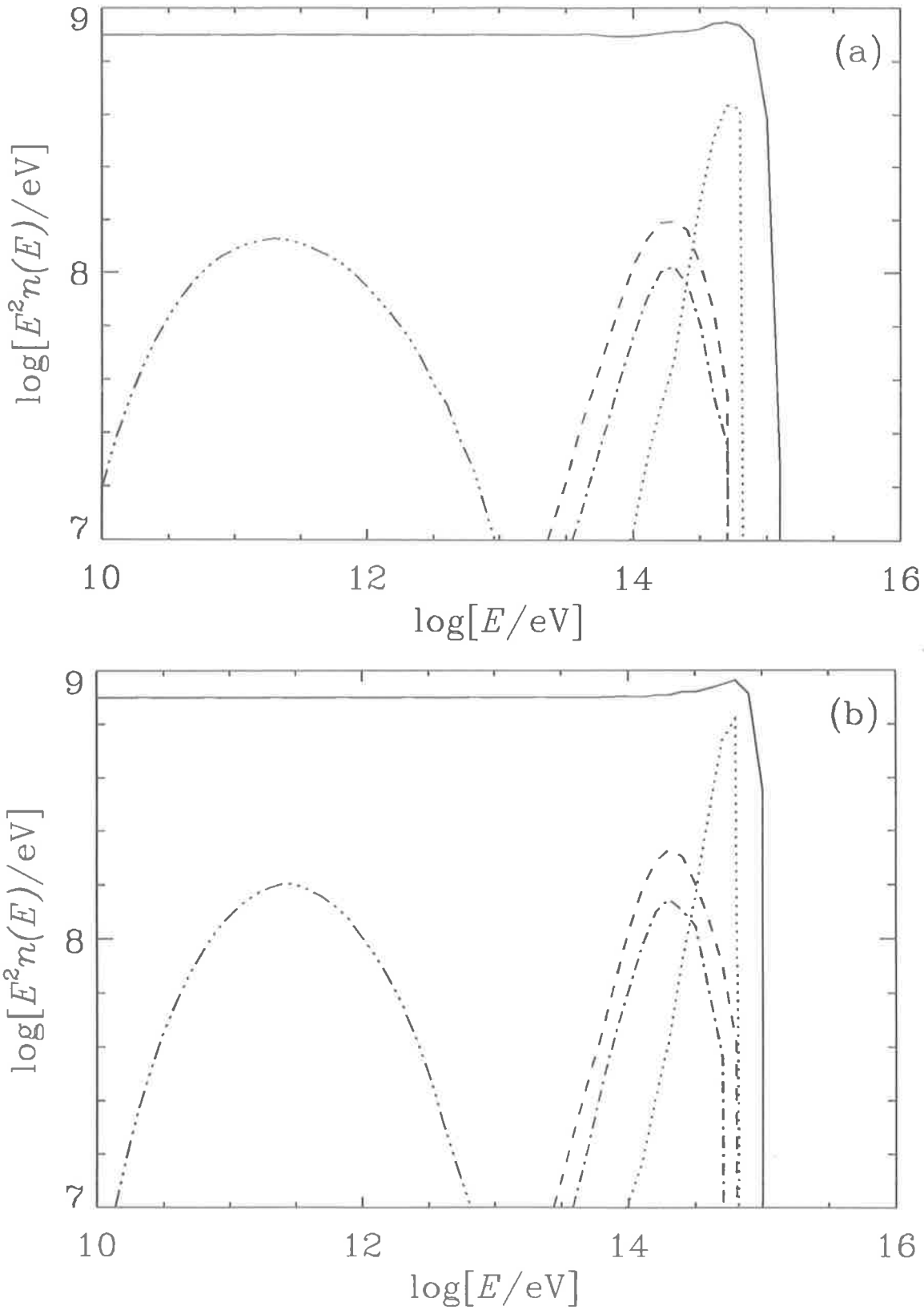

Figure 6.14: A plot of the differential spectrum of particles (multiplied by E^2) produced by the accelerator per injected proton for $E_{\max} = 10^{15}$ eV. Plots are the spectra resulting using (a) the Palomar–Green continuum (spectrum a), and (b) the flat AGN continuum (spectrum b). Curves are defined as in Figure 6.13 except that the $e^{\pm}$ spectra (dot dot dot dash curve) are also shown.

The highest energy protons are considered first and are cascaded down in energy summing the contributions from the lower energy protons as the cascade is followed. Once the spectrum of interactions has been calculated, it is straightforward to convolve $n_i^{\rm int}$ with the distribution of particles produced by the protons when they interact in the accreting matter or the radiation field.

Consider the $i^{\rm th}$ energy bin of width, ΔE_i, which has a midpoint energy E_i and which contains n_i protons. The total energy loss rate experienced by protons in this bin is

$$\begin{aligned}\frac{dE_p}{dt}(E_i) \simeq & \left.\frac{dE_p}{dt}\right|_{pp}(E_i) + \left.\frac{dE_p}{dt}\right|_{p\gamma\rightarrow\pi}(E_i) + \left.\frac{dE_p}{dt}\right|_{p\gamma\rightarrow e}(E_i) \\ & + \left.\frac{dE_p}{dt}\right|_{\rm advec}(E_i) + \left.\frac{dE_p}{dt}\right|_{\rm synch}(E_i) + \left.\frac{dE_p}{dt}\right|_{\rm diff}(E_i), \end{aligned} \tag{6.39}$$

where only the dependence on the proton energy has been shown explicitly. On average the time take for the energy contained by the protons in the bin to be lost is $\Delta t = \Delta E_i/(dE_p(E_i)/dt)$. Protons interact via pion photoproduction, pair production and proton–proton interactions, and therefore the mean path length for interaction is

$$\overline{\lambda}(E_i) = [(\overline{\lambda}^{\pi}_{\gamma p}(E_i))^{-1} + (\overline{\lambda}^{e}_{\gamma p}(E_i))^{-1})^{-1} + (\overline{\lambda}_{pp}(E_i))^{-1}]^{-1}. \tag{6.40}$$

Interactions occur at a rate $c/\overline{\lambda}(E_i)$, and on average the number of interactions which occur in this bin is approximately given by,

$$n_i^{\rm int} \simeq n_i \frac{c}{\overline{\lambda}(E_i)} \frac{\Delta E_i}{\frac{dE_p}{dt}(E_i)}. \tag{6.41}$$

If the energy losses were continuous then after time Δt had elapsed, all of the protons would have moved into the $(i-1)^{\rm th}$ energy bin. For pair production interactions the mean energy lost per interaction is much smaller than ΔE_i, and so if pair production were the only loss process the approximation that all of the protons to move into the $(i-1)^{\rm th}$ energy bin could be used. However, for pion photoproduction and proton–proton interactions a large fraction of the proton's energy is lost per interaction, and this approximation is not appropriate for these processes. Protons which interact via pion photoproduction or proton–proton interactions produce a spectrum of secondary protons which can be defined in terms of a transfer matrices $T_{ij}^{pp\rightarrow p}$ and $T_{ij}^{p\gamma\rightarrow p}$. The transfer matrix $T_{ij}^{pp\rightarrow p}$ gives the probability that a proton in energy bin i produces a

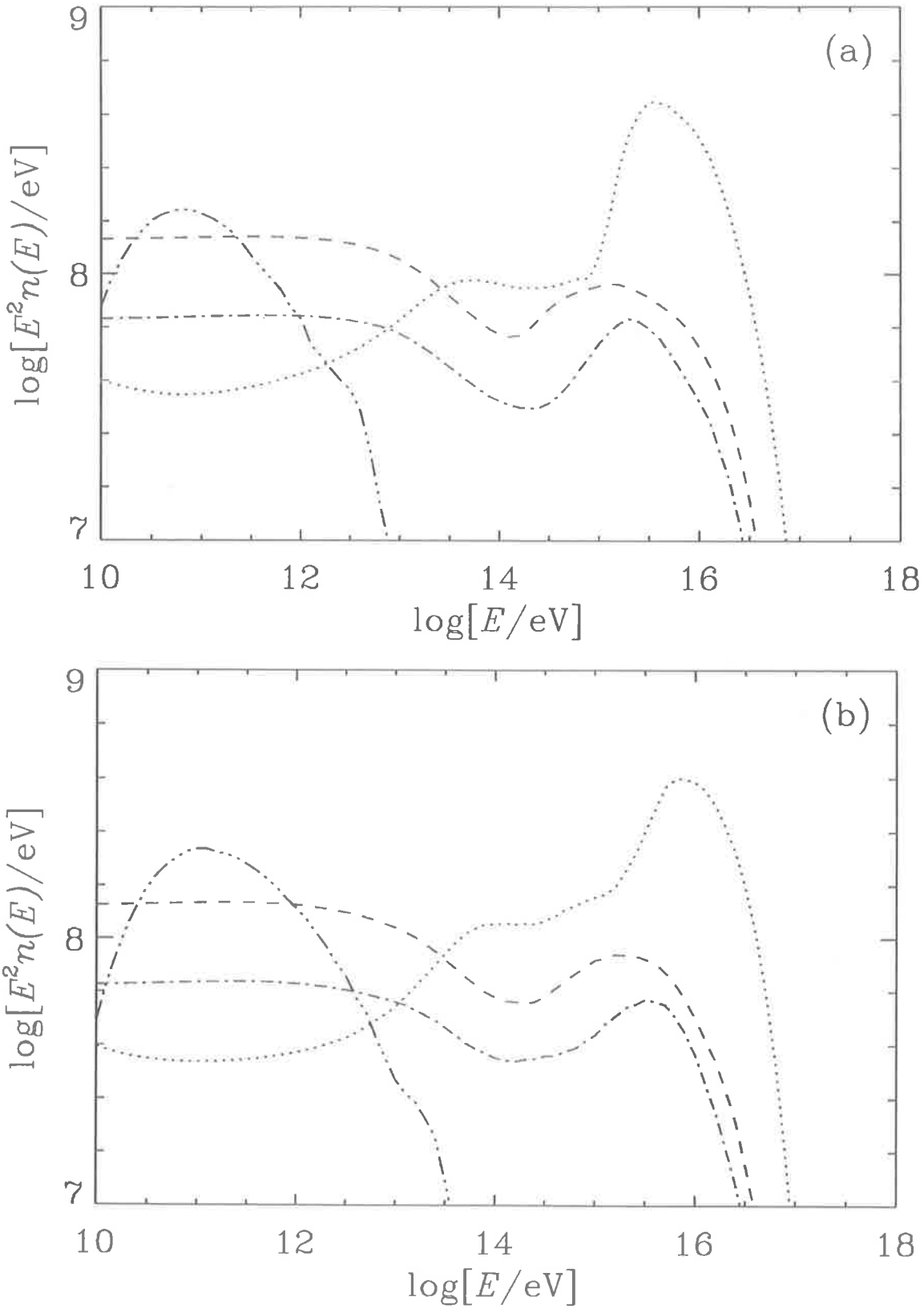

Figure 6.15: A plot of the differential spectrum of particles (multiplied by E^2) produced within the central region of AGN by protons which have escaped the accelerator, per proton injected into the accelerator for $E_{\max} = 10^{17}$ eV. Plots are the spectra resulting for $x_1 = 10$ using (a) the Palomar–Green continuum (spectrum a), and (b) flat AGN continuum (spectrum b). Curves are defined as in Figures 6.13 and 6.14.

proton in bin j when it undergoes a proton–proton interaction. Therefore, the number of protons produced in the $j^{\rm th}$ bin ($j < i$) due to interactions in the $i^{\rm th}$ bin is

$$n_{ij} = n_i^{\rm int}\left(\frac{\overline{\lambda}(E_i)}{\overline{\lambda}_{pp}(E_i)}T_{ij}^{pp\rightarrow p} + \frac{\overline{\lambda}(E_i)}{\overline{\lambda}_{\gamma p}^{\pi}(E_i)}T_{ij}^{p\gamma\rightarrow p}\right). \tag{6.42}$$

In addition, protons may be catastrophically lost from the $i^{\rm th}$ energy bin due to advection onto the black hole and diffusion out of the central region. Hence, the total number of protons which move into the $(i-1)^{\rm th}$ energy bin is given by

$$\begin{aligned} n'_{i-1} = n_i \;&-\; n_i^{\rm int}\left(\frac{\overline{\lambda}(E_i)}{\overline{\lambda}_{pp}(E_i)} + \frac{\overline{\lambda}(E_i)}{\overline{\lambda}_{pp}(E_i)}\right) \\ &-\; n_i\frac{\Delta E_i}{\frac{dE_p}{dt}(E_i)}\left(\left.\frac{dE_p}{dt}\right|_{\rm advec}(E_i) + \left.\frac{dE_p}{dt}\right|_{\rm diff}(E_i)\right) + n_{i(i-1)} \end{aligned} \tag{6.43}$$

where the second term on the RHS gives the number of proton–proton and pion photoproduction interactions which occur in the $i^{\rm th}$ bin. The third term gives the number of protons lost from the $i^{\rm th}$ bin due to advection and diffusion, and the last term gives the number protons which are produced in the $(i-1)^{\rm th}$ bin due to interactions (using Equation 6.42).

An iterative procedure using the ideas outlined above has been used to calculate the spectra of particles produced within the source region by protons which have escaped from the accelerator. The highest energy bin (the $i^{\rm th}$) is considered first, and the number of interactions in this bin is calculated using Equation 6.41. The number of protons in the next highest energy bin is then incremented according to the relation

$$n_{i-1} = n_{i-1} + n'_{i-1}. \tag{6.44}$$

For energy bins $j < (i-1)$ the number of protons in each bin is incremented according to the relation $n_j = n_j + n_{ij}$, where Equation 6.42 is used for n_{ij}. The $(i-1)^{\rm th}$ bin is considered next, and the process continued until all of the protons have lost all of their kinetic energy. The spectrum of n, $\pi^{\pm}$, π^{o} and $e^{\pm}$ produced during the entire cascade is then calculated by convolving the spectrum of interactions with the distribution of particles produced by protons in each energy bin. Hence, the number of neutrons, $\pi^{\pm}$s, π^{o}s and $e^{\pm}$s in the $j^{\rm th}$ energy bin after the cascade is

$$n_j^n = \sum_{i>j} n_i^{\rm int}\left(T_{ij}^{p\gamma\rightarrow n}\frac{\overline{\lambda}(E_i)}{\overline{\lambda}_{\gamma p}^{\pi}(E_i)} + T_{ij}^{pp\rightarrow n}\frac{\overline{\lambda}(E_i)}{\overline{\lambda}_{pp}(E_i)}\right) \tag{6.45}$$

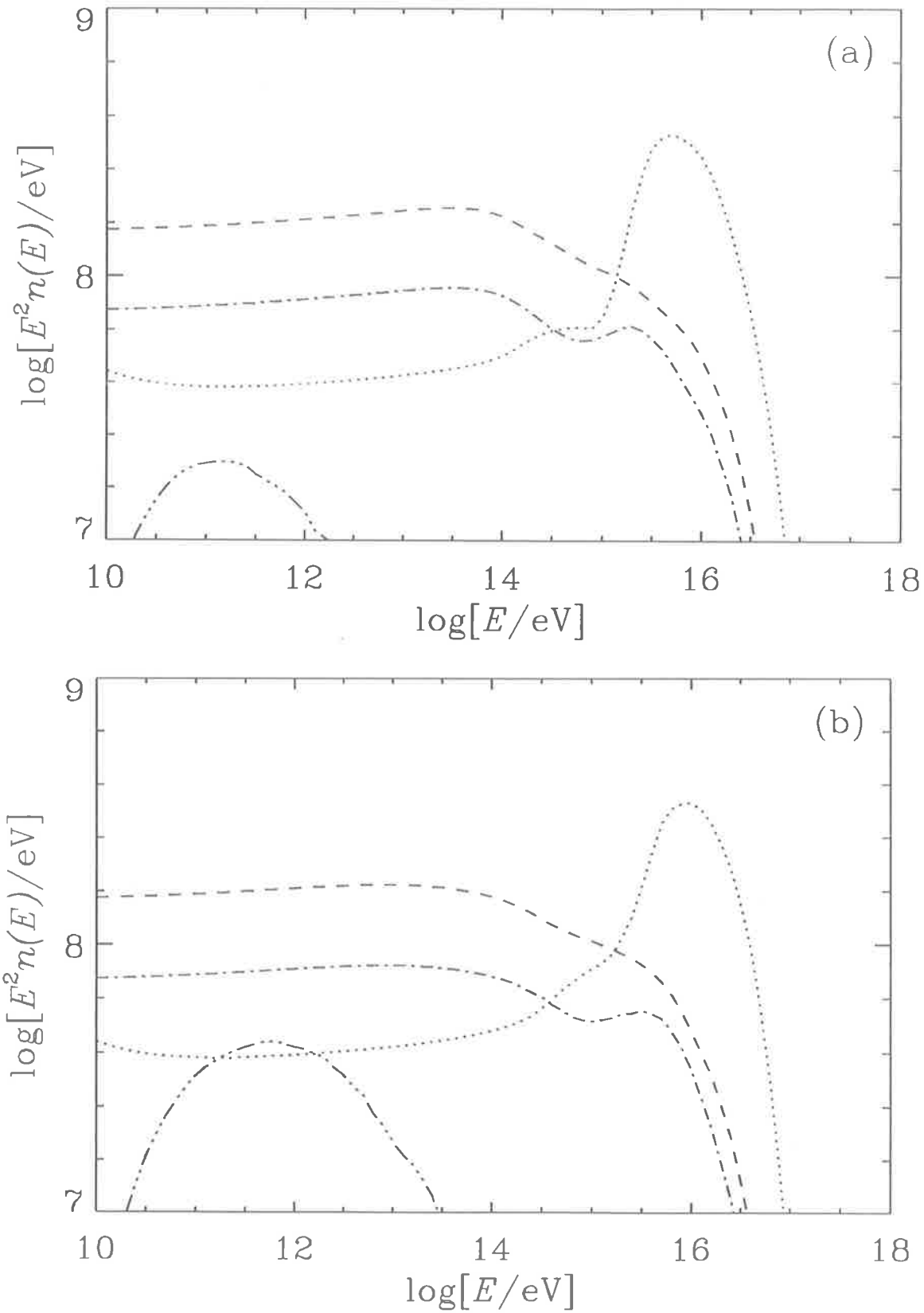

Figure 6.16: A plot of the differential spectrum of particles (multiplied by E^2)produced within the central region of AGN by protons which have escaped the accelerator, per proton injected into the accelerator for $E_{\max} = 10^{17}$ eV. Plots are the spectra resulting for $x_1 = 100$ using (a) the Palomar–Green continuum (spectrum a), and (b) flat AGN continuum (spectrum b). Curves are defined as in Figures 6.13 and 6.14.

$$n_j^{\pi^\pm} = \sum_{i>j} n_i^{\rm int} \left(T_{ij}^{p\gamma\to\pi^\pm} \frac{\overline{\lambda}(E_i)}{\overline{\lambda}_{\gamma p}^{\pi}(E_i)} + T_{ij}^{pp\to\pi^\pm} \frac{\overline{\lambda}(E_i)}{\overline{\lambda}_{pp}(E_i)} \right) \tag{6.46}$$

$$n_j^{\pi^o} = \sum_{i>j} n_i^{\rm int} \left(T_{ij}^{p\gamma\to\pi^o} \frac{\overline{\lambda}(E_i)}{\overline{\lambda}_{\gamma p}^{\pi}(E_i)} + T_{ij}^{pp\to\pi^o} \frac{\overline{\lambda}(E_i)}{\overline{\lambda}_{pp}(E_i)} \right) \tag{6.47}$$

$$n_j^{e^\pm} = \sum_{i>j} n_i^{\rm int} T_{ij}^{p\gamma\to e^\pm} \frac{\overline{\lambda}(E_i)}{\overline{\lambda}_{\gamma p}^{e}(E_i)}. \tag{6.48}$$

Here the transfer matrix $T_{ij}^{p\gamma\to n}$ gives the number of neutrons in energy bin j produced by via pion photoproduction per proton in bin $i^{\rm th}$, with the other transfer matrices defined similarly. For proton–proton interactions the particle distributions of Hillas (1979) have been used to calculate the transfer matrices. In the cases of pion photoproduction and pair production, Monte Carlo calculations have been used to calculate the transfer matrices. This has been done by sampling a large number of protons from the each energy bin and modelling their interaction with the radiation field as described in Sections 4.2 and 4.3. The products are binned in energy, and the spectra normalised to the mean multiplicity for each particle type.

Using the procedure described above, I have calculated the differential spectra of particles produced by protons which have escaped from the accelerator, per proton injected into the accelerator. Representative results for $E_{\rm max} = 10^{17}$ eV are shown in Figures 6.15 ($x_1 = 10$) and 6.16 ($x_1 = 100$). Results for $E_{\rm max} = 10^{15}$, 10^{16},..., 10^{20} eV with $x_1 = 10$ and $x_1 = 100$ may be found in Appendix D. The general shape of the neutron, $\pi^\pm$ and π^o spectra reflects the E_p^{-2} nature of the spectrum of protons which have escaped from the accelerator (see e.g. Figure 6.13). The peaks and troughs seen in Figures 6.15 and 6.16 are caused be the changing dominance of the loss processes with energy. For example, consider the neutron spectrum (dotted curve) shown in Figure 6.15(a). For $E_p \sim E_{\rm max}$ protons interact primarily via pion photoproduction on thermal photons (see Figure 6.8), and this gives rise to the peak in the neutron spectrum for energies $10^{15} \leq E \leq 10^{16}$ eV. Below $E \sim 10^{15}$ eV the neutron spectrum decreases because pair production becomes the dominant loss mechanism (see Figure 6.5). At even lower energies, below $\sim 3 \times 10^{13}$, proton–proton interactions and advection onto the black hole are the dominant loss mechanisms. However, the catastrophic advection losses are comparable in magnitude to the proton–proton losses, and this leads to the decrease in $E^2 n(E)$ below $E \sim 3 \times 10^{13}$ eV. The behaviour of the $\pi^\pm$ and π^o spectra may be rationalised in a similar way. Again pair production losses occur primarily on

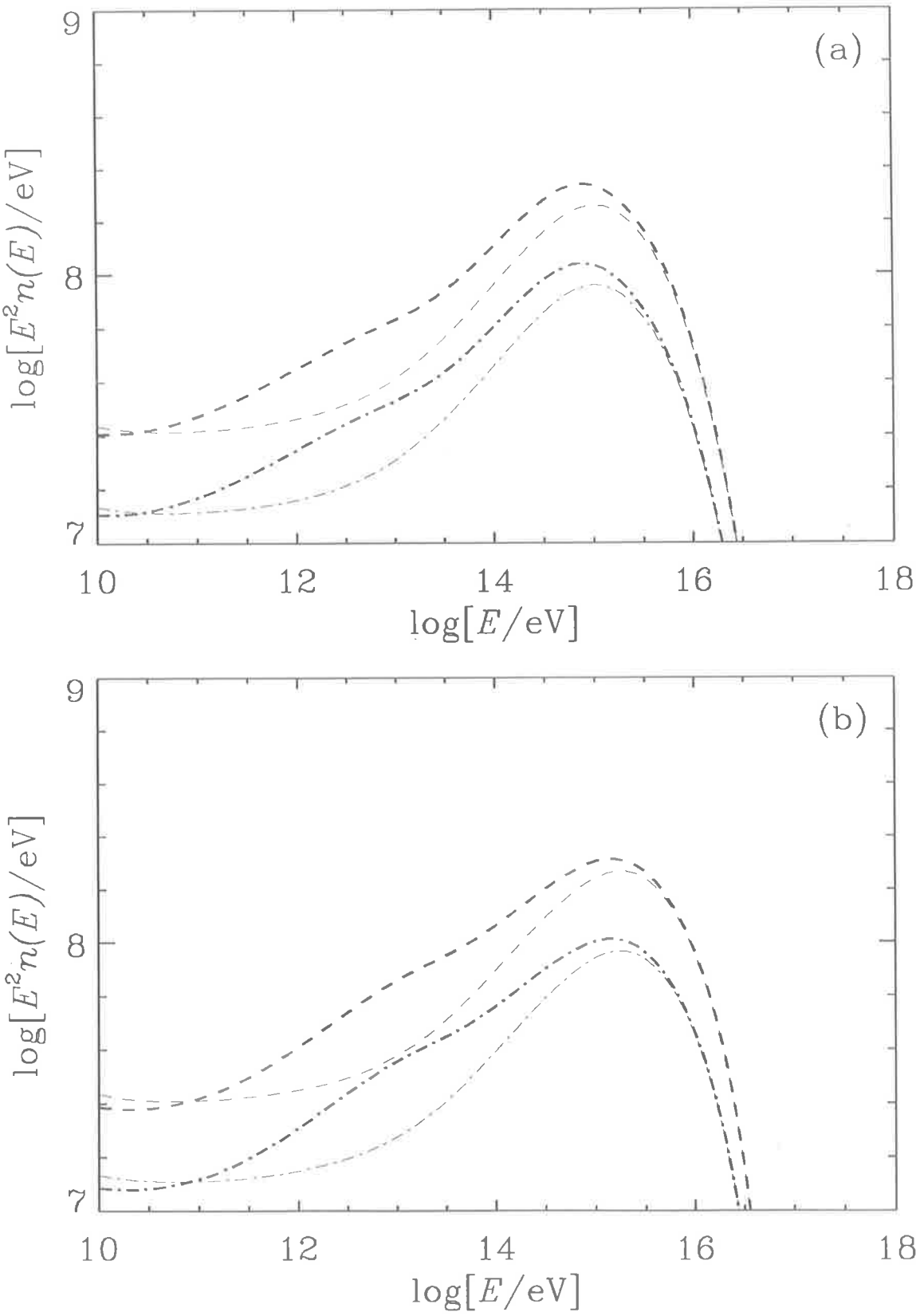

Figure 6.17: A plot of the differential spectrum of pions (multiplied by E^2) produced by neutrons which have escaped from the central region of AGN, for $E_{\max} = 10^{17}$ eV. Plots are the spectra which result for $x1 = 10$ (thick curves) and $x_1 = 100$ (thin curves) using (a) the Palomar–Green continuum (spectrum a), and (b) the flat AGN continuum (spectrum b). Shown are the $\pi^{\pm}$ (dashed curves) and the π^o (dash dot curves) spectra.

thermal photons giving rise to the peaked $e^{\pm}$ spectra.

An alternative method of calculation based on the approach of following each proton as it interacts in the cascade, has been used for the special case in which only pair production and pion photoproduction losses are included. This calculation served as a check of the method described above (when only the pair production and pion photoproduction losses are included), and the results where in good agreement.

The Spectrum of Particles Produce Outside the Central Region

An iterative method similar to the one described above has been used to calculate the spectrum of particles produced outside the central region of the AGN. Once again, the spectrum of interactions during the cascade has been calculated. However, only *pp* and *np* interaction are considered, and hence *all* of the nucleons in a given energy bin interact. The highest energy bin (the i^{th}) of the total neutron spectrum, n_i^n, now defined as the sum of the spectra of neutrons produced during and after acceleration, is considered first. The number of interactions in this bin is $n_i^{\text{int}} = n_i^n$, and number of nucleons in the lower energy bins are incremented according to the relation $n_j^n = n_j^n + n_i^{\text{int}}(T_{ij}^{pp\to p} + T_{ij}^{pp\to n})$ due to the secondary protons and neutrons produced by interactions in the i^{th} bin. The $(i-1)^{\text{th}}$ bin is considered next and the process continued in this fashion until all of the protons have lost all of their kinetic energy. The spectra of pions produced during the cascade are given by

$$n_j^{\pi^{\pm}} = \sum_{i>j} n_i^{\text{int}} T_{ij}^{pp\to\pi^{\pm}} \tag{6.49}$$

$$n_j^{\pi^o} = \sum_{i>j} n_i^{\text{int}} T_{ij}^{pp\to\pi^o}. \tag{6.50}$$

I have calculated the differential spectra of $\pi^{\pm}$s and π^os produced by neutrons which have escaped from the central region of AGN, for $E_{\text{max}} = 10^{15}$, 10^{16},..., 10^{19} eV and plots of all of the results may be found in Appendix D. Representative results for $E_{\text{max}} = 10^{17}$ eV are shown in Figure 6.17. The features of the spectra reflect the shape of the total spectrum of neutrons escaping from the central region of AGN.

6.8.3 The Total Neutrino Spectrum per Injected Proton

Having calculated the spectra of pions produced during and after acceleration, it is straightforward to decay them using the procedure described in Sections 4.5 and 4.6 to

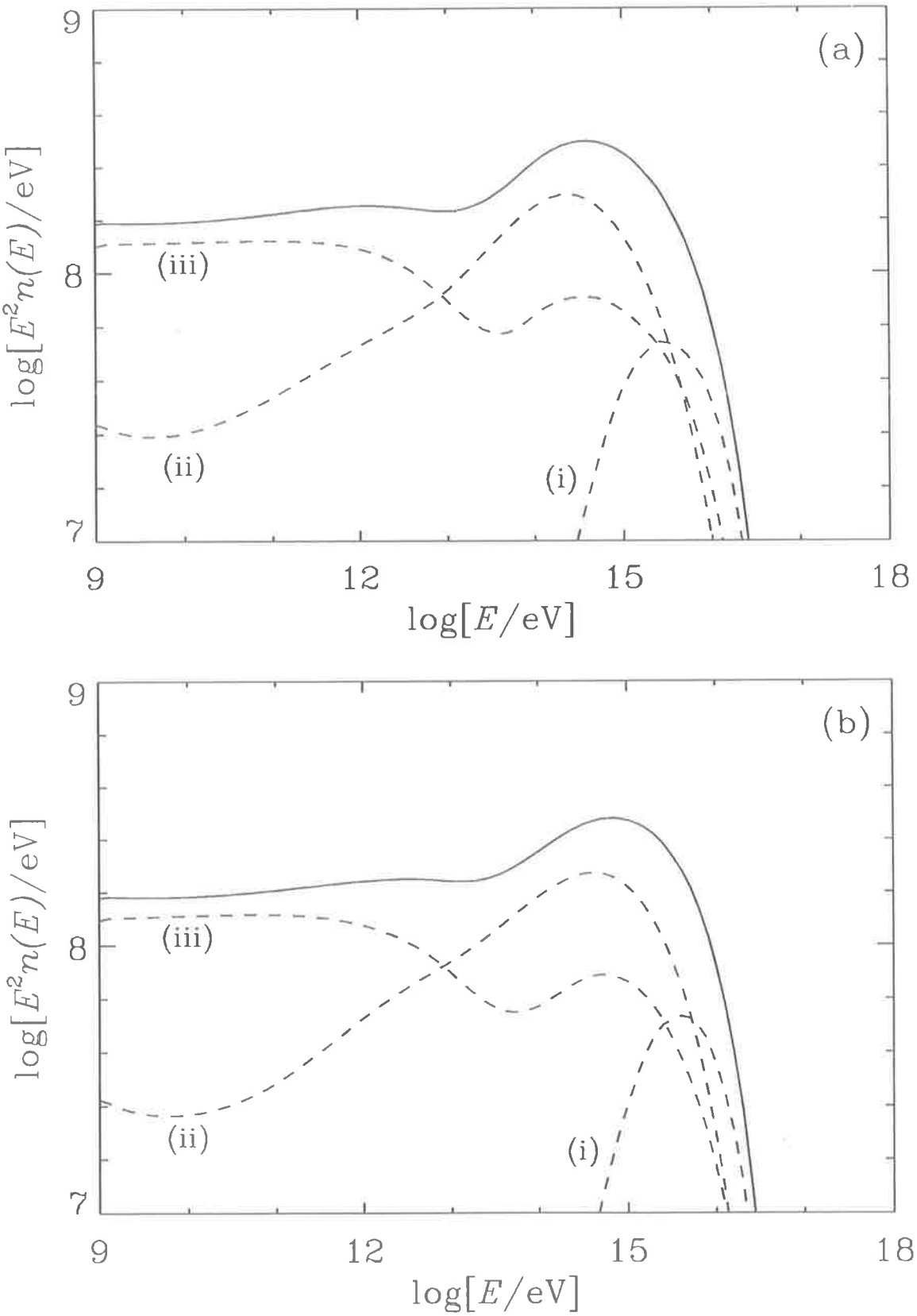

Figure 6.18: A plot of the total differential neutrino spectrum per proton injected into the accelerator multiplied by E^2 (solid curve), for $E_{\max} = 10^{17}$ eV. The dashed curves show the contributions from pions produced (i) during acceleration, (ii) after acceleration within the central region, and (iii) outside of the central region. Part (a) show the results using the PG continuum (spectrum (a)), and part (b) the results using the flat AGN continuum (spectrum (b)).

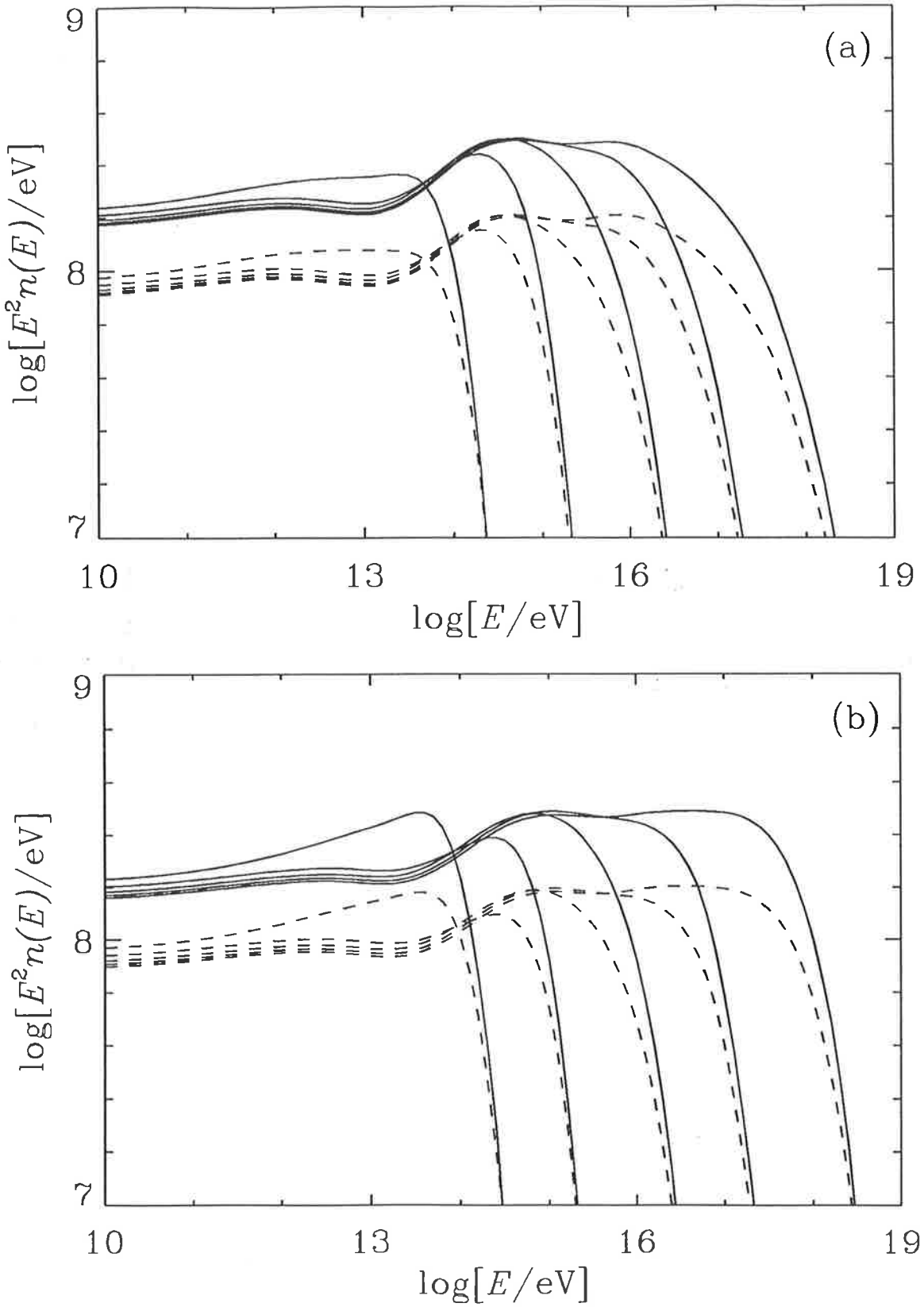

Figure 6.19: A plot of the total differential neutrino spectrum (multiplied by E^2) per proton injected into the accelerator, for (left to right) $E_{\max} = 10^{15}$, 10^{16},...,10^{19} eV and using $x_1 = 10$. Part (a) shows the results using the PG continuum (spectrum (a)), and part (b) the results using the flat AGN continuum (spectrum (b)). Also shown is the sum of the electron neutrino and antineutrino spectra (dashed curves).

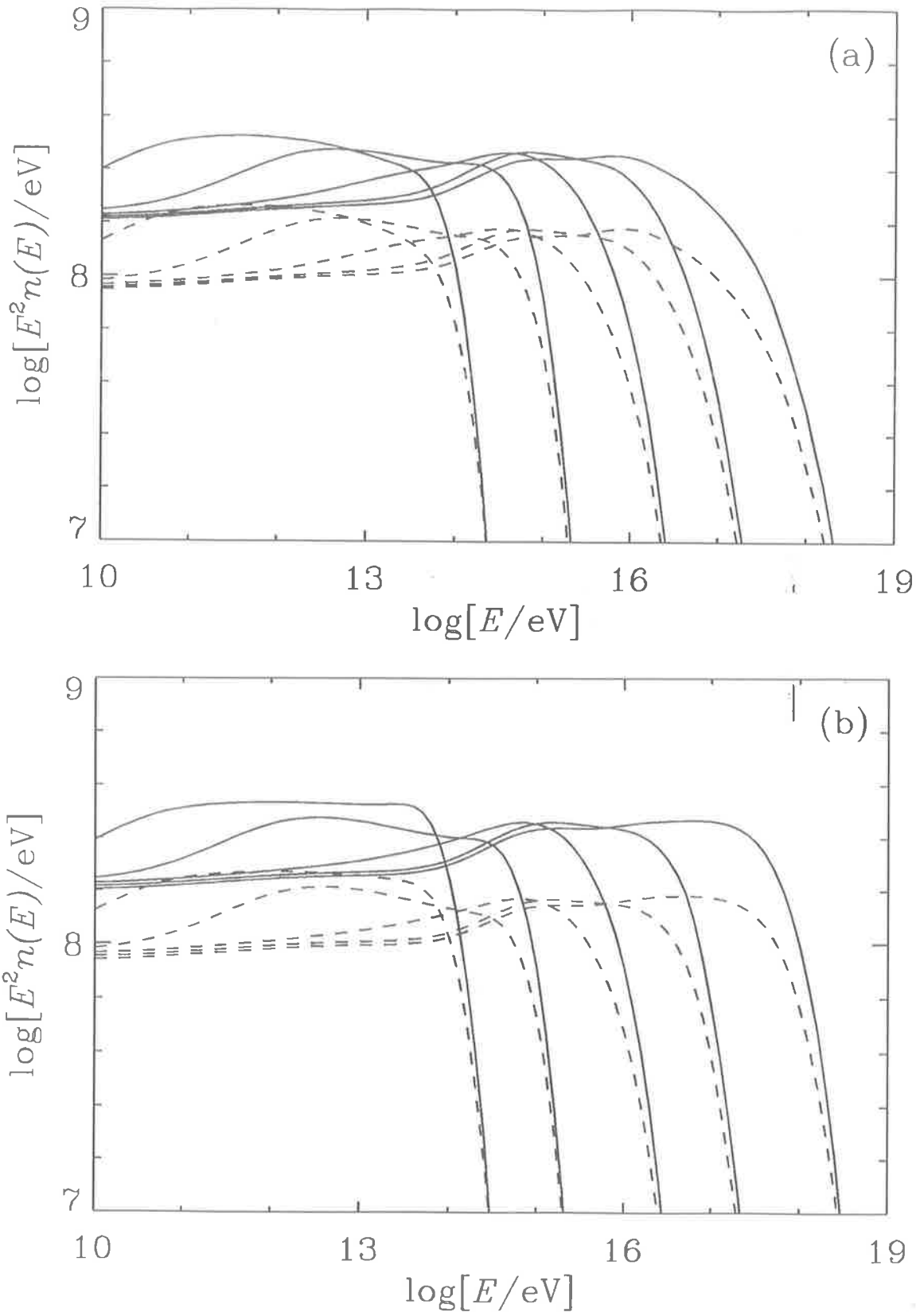

Figure 6.20: A plot of the total differential neutrino spectrum (multiplied by E^2)per proton injected into the accelerator, for (left to right) $E_{\max} = 10^{15}$, 10^{16},...,10^{19} eV and using $x_1 = 100$. Part (a) shows the results using the PG continuum (spectrum (a)), and part (b) the results using the flat AGN continuum (spectrum (b)). Also shown is the sum of the electron neutrino and antineutrino spectra (dashed curves).

obtain the differential neutrino spectra [2], $n_\nu(E_\nu) = \frac{dn_\nu}{dE_\nu}$. In Figure 6.18 the differential neutrino spectra produced by the various components of the total $\pi^\pm$ spectra (dashed curves) are shown for $E_{\max} = 10^{17}$ eV. Also shown is the total neutrino spectra produced per proton injected into the accelerator (solid curve). The total neutrino spectra per injected proton for $E_{\max} = 10^{15}$, 10^{16},..., 10^{19} eV are shown in Figures 6.19 ($x_1 = 10$) and 6.20 ($x_1 = 100$) for both spectrum (a) and spectrum (b). The sum of the ν_e and the $\overline{\nu}_e$ spectra have also been shown (dashed curves), and it can be seen that they follow the $\nu_\mu + \overline{\nu}_\mu$ spectra closely except that they are a factor of ~ 1.8 lower. From Figures 6.19 and 6.20 it can be seen that the differences between the two photon spectra used (spectrum (a) and (b)) have little effect on the total spectrum of neutrinos produced per injected proton. The main difference is at energies greater than $\sim 10^{16}$ eV, where the effect of synchrotron losses on the results for spectrum (a) can be seen.

6.9 The Neutrino Flux from Individual AGN

The neutrino flux from individual AGN is thought to be unobservable with the proposed neutrino telescopes (see e.g. Stecker *et al.* 1991a,b, 1992). However, the method of scaling the neutrino spectrum per proton injected into the accelerator for an arbitrary AGN is described here, as it will be used in Section 6.10 to calculate the diffuse AGN flux.

Consider a source at redshift z with differential neutrino luminosity dL_ν/dE'_ν (eV s^{-1} eV^{-1}). Neutrinos emitted by the source with energy E'_ν, will have energy $E_\nu = E'_\nu/(1+z)$ when they reach the Earth due to redshifting. The energy flux received at Earth in the energy range $E_\nu \rightarrow E_\nu + dE_\nu$ is (see e.g. Rowan–Robinson 1985)

$$E_\nu \frac{dF_\nu}{dE_\nu}(E_\nu, z)dE_\nu = \frac{1}{4\pi d_L^2}\frac{dL_\nu}{dE'_\nu}(E'_\nu)dE'_\nu, \tag{6.51}$$

where $d_L = R_o^2 r^2 (1+z)^2 = \frac{c}{H_o q_o^2}\{zq_o + (q_o - 1)(\sqrt{2q_o z + 1} - 1)\}$ is the luminosity distance to the AGN (see e.g. Weinberg 1972), R_o is the scale factor of the Universe at the present epoch, H_o is the Hubble constant, q_o is the deceleration parameter and r is a co–moving radial coordinate. Hence, the differential neutrino flux at Earth, dF_ν/dE_ν

[2] In the following " neutrino spectra" should be taken to mean the sum of the muon neutrino and anti–neutrino spectra

$E_{\max}$ [eV]	$W_{e\gamma}$ [GeV]			
	Spectrum (a)		Spectrum (b)	
	$x_1 = 10$	$x_1 = 100$	$x_1 = 10$	$x_1 = 100$
10^{15}	4.83	5.10	4.89	5.44
10^{16}	4.40	4.38	4.84	4.68
10^{17}	4.74	4.24	5.19	4.41
10^{18}	5.16	4.50	5.70	4.74
10^{19}	5.54	4.79	6.16	5.16

Table 6.1: A table of the energy going into $e^{\pm}$s and γ-rays within the central region of AGN per proton injected into the accelerator, $W_{e\gamma}$, as a function of the maximum proton energy, $E_{\max}$.

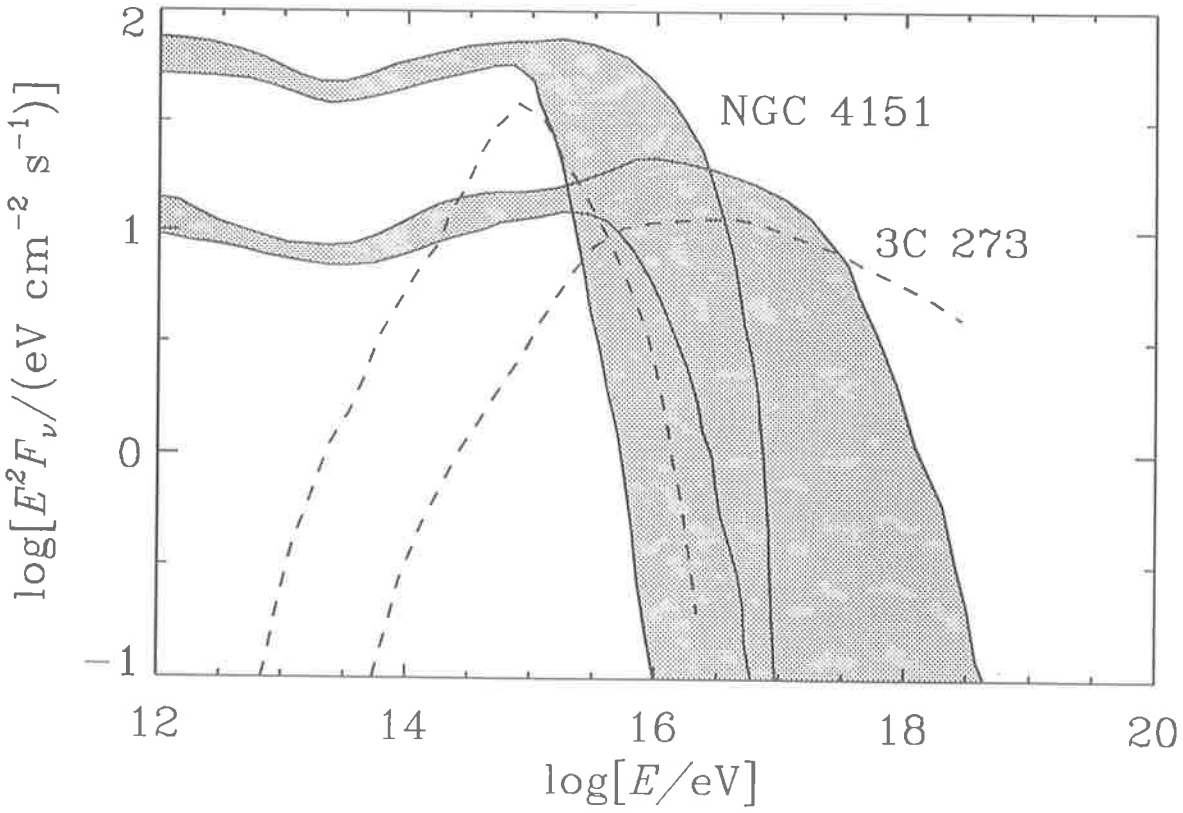

Figure 6.21: A plot of the differential neutrino flux, $F_\nu = dF_\nu/dE_\nu$, multiplied by the square of the neutrino energy, for the quasar 3C 273 and the nearby AGN NGC 4151. The bands corresponding to the range $x_1 = 10$ (lower bound) to $x_1 = 100$ show the results from a preliminary calculation in which only proton–photon interactions within the central region of the AGN were considered, using spectrum (a) for the radiation field. Also shown (dashed curves) are the predictions for these sources made by Stecker *et al.* (1991a, 1991b, 1992). Adapted from Szabo and Protheroe (1992a).

(neutrinos $\mathrm{cm}^{-2}\ \mathrm{s}^{-1}\ \mathrm{eV}^{-1}$), is

$$\frac{dF_\nu}{dE_\nu}(E_\nu, z) = \frac{(1+z)}{4\pi E_\nu d_L^2}\frac{dL_\nu}{dE'_\nu}(E_\nu(1+z)). \tag{6.52}$$

The neutrino spectra given in Section 6.8.3 can be scaled to give the differential neutrino luminosity of an AGN by calculating the rate at which protons are injected into the accelerator. If one assumes that all of the energy channelled into $e^{\pm}$s and γ–rays within the central region of the AGN is ultimately responsible for the observed infrared to X–ray continuum emissions from AGN (see e.g. Zdziarski 1986 and Done and Fabian 1989), then the rate at which protons are injected into the accelerator is

$$R_p^{\mathrm{inj}}(E_{\mathrm{max}}) \simeq \frac{L_{\mathrm{c}}}{W_{e\gamma}(E_{\mathrm{max}})}. \tag{6.53}$$

Here, $W_{e\gamma}(E_{\mathrm{max}})$ is the energy per proton injected into the accelerator which goes into $e^{\pm}$ and γ–ray production within the central region, and $E_{\mathrm{max}} = E_{\mathrm{max}}(L_{\mathrm{c}})$ (see Figure 6.10). Table 6.1 shows the $W_{e\gamma}$ values which result from the calculation described in Section 6.8 for both spectrum (a) and (b). The differential neutrino luminosity of the AGN is given by,

$$\frac{dL_\nu}{dE'_\nu}(E'_\nu, L_{\mathrm{c}}) = R_p^{\mathrm{inj}}(E_{\mathrm{max}})E'_\nu\frac{dn_\nu}{dE'_\nu}(E'_\nu, E_{\mathrm{max}}), \tag{6.54}$$

where dn_ν/dE'_ν is the differential neutrino spectrum produced per injected proton calculated as described in Section 6.8.3, and the dependence on L_{c} enters via the maximum proton energy in the AGN, E_{max}.

Therefore, given the distance to an AGN and its observed continuum luminosity (or alternatively its X–ray luminosity which can be scaled to give L_{c}), it is straightforward to calculate the flux of neutrinos observed at Earth. For example, the neutrino flux from the nearby active galaxy NGC 4151 ($z = 0.0033$, L_{x}(2–10 keV) $= 1.04 \times 10^{43}$ erg s^{-1}, Piccinotti *et al.* 1982) and the quasar 3C 273 ($z = 0.158$, L_{x}(0.3–3.5 keV) $= 8.45 \times 10^{45}$ erg s^{-1}, Wilkes and Elvis 1987) have been calculated by Szabo and Protheroe (1992a) and are shown in Figure 6.21 (shaded bands). In each case, the results of Stecker *et al.* (1991a,b, 1992) have also been shown for comparison (dashed lines). For NGC 4151 our results are consistent with those of Stecker *et al.* for $E_\nu > 10^{15}$ eV. However, below $\sim 10^{15}$ eV we predict considerable higher fluxes of neutrinos than Stecker *et al.*. This is because they have only considered interactions with photons from the UV bump. In

our calculation protons may also interact with X–ray photons in the radiation field as well as with the accreting matter which results in an E_ν^{-2} neutrino spectrum following the accelerated proton spectrum. For 3C 273 our results are consistent with those of Stecker *et al.* for energies in the range $10^{16} < E_\nu < 3 \times 10^{17}$ eV, and for the reason discussed above we again predict higher fluxes below $E_\nu \sim 10^{16}$. Stecker *et al.* also predict a flux of neutrinos at higher energies from 3C 273 than we do, and this is because they only consider pion photoproduction interactions in determining, $E_{\rm max}$, resulting in a higher maximum proton energy. The prediction of an increased neutrino flux at energies below $\sim 10^{16}$ eV is important because, as discussed in Section 5.3, the main contribution to the muon signal in a neutrino telescope resulting from an $\sim E_\nu^{-2}$ neutrino spectrum comes from neutrinos with energies below $\sim 10^{12}$ eV.

6.10 The Diffuse Neutrino Background from AGN

The total neutrino spectrum per injected proton (see Section 6.8.3), and the method of scaling the results for arbitrary AGN (see Section 6.9) have been used by Szabo and Protheroe (1992a,b) to calculate the contribution from AGN to the diffuse neutrino background. To do this we require the differential number density of active galaxies, $dn_{\rm agn}/dL$ (number of AGN Mpc^{-3} erg^{-1} s), as a function of redshift and luminosity[3], L. This quantity is also called the luminosity function as it describes the luminosity distribution of AGN. We have used a luminosity function of the form

$$\frac{dn_{\rm agn}}{dL}(z,L) = \frac{g(z)}{f(z)}\rho_o\left(\frac{L}{f(z)}\right), \tag{6.55}$$

where $g(z)$ and $f(z)$ describe the density and luminosity evolution of the AGN respectively and $\rho_o\left(\frac{L}{f(0)}\right)$ is the local value of the differential number density of AGN. The total flux of neutrinos from AGN seen at Earth, is given by integrating over co–moving volume V and luminosity giving

$$\frac{dF_{\rm tot}}{dE_\nu}(E_\nu) = \int\int \frac{dn_{\rm agn}}{dL}(E_\nu,z,L)\frac{dF_\nu}{dE_\nu}(E_\nu,z,L)dVdL. \tag{6.56}$$

[3]In general the luminosity function can be defined in terms of any of the energy bands, and hence here I will use the general symbol L for the luminosity of the AGN

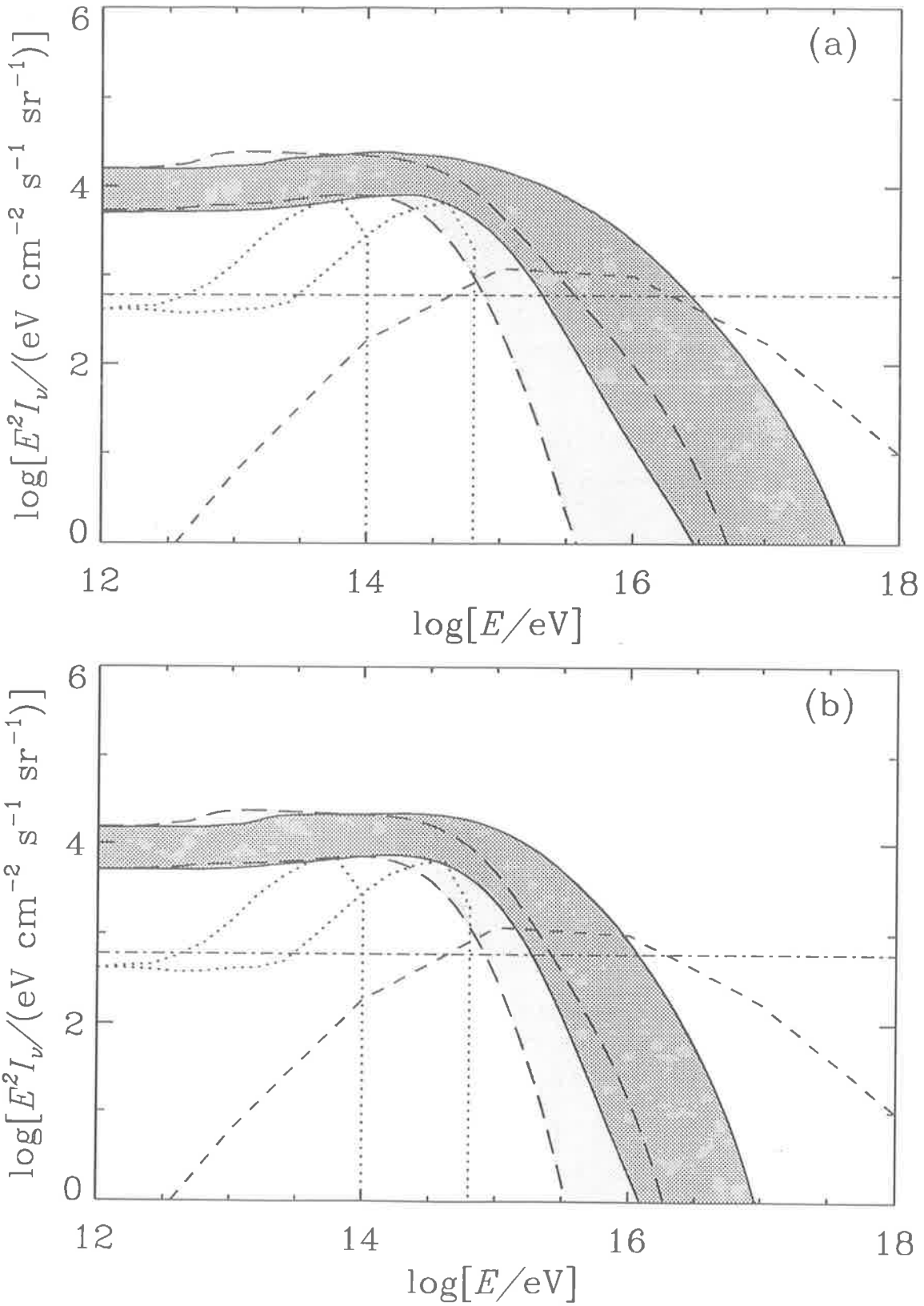

Figure 6.22: A plot of the differential intensity, $I_\nu = dI_\nu/dE_\nu$, of neutrinos from all AGN, multiplied by E^2. The shaded bands represents the range of results for $10 \leq x_1 \leq 100$ and the variations in the fits to the observed X–ray luminosity function used. The darker shaded band if for $b = 1$, and the lighter shaded band is for $b = 10$. Part (a) was calculated using for the PG continuum (spectrum (a)) and part (b) using the flat AGN continuum (spectrum (b)). Also shown for comparison are the results of Stecker *et al.* (1992) (dashed curve), Sikora and Begelman (1992) (dotted curves for $z = 0$ (peaks at higher energy) and $z = 5$) and Biermann (1992) (dot dash curve).

The integral can be expressed in terms of the redshift by using the relation (see e.g. Avni 1978)

$$\frac{dV}{dz} = \frac{4\pi d_L^2 c}{H_o} \frac{1}{(1+z)^3} \frac{1}{\sqrt{1+2q_o z}}, \tag{6.57}$$

giving

$$\frac{dF_{\rm tot}}{dE_\nu}(E_\nu) = \frac{c}{E_\nu H_o} \int\int \frac{g(z)}{f(z)} \rho_o \left(\frac{L}{f(z)}\right) \frac{dL_\nu}{dE_\nu}(E_\nu(1+z), kL) \frac{dz}{(1+z)^2\sqrt{1+2q_o z}} dL, \tag{6.58}$$

using Equations 6.52 and 6.55, where $k = L_c/L$. However, in neutrino astronomy it makes more sense to talk about numbers of particles, and so the differential neutrino intensity $dI_\nu/dE_\nu = (1/4\pi)(dF_{\rm tot}/dE_\nu)$ has been calculated.

We have used fits to the luminosity function based on X–ray observations of AGN given by Morisawa and Takahara (1989), Morisawa *et al.* (1990) and Maccacaro *et al.* (1991) to calculate the intensity of neutrinos expected from all AGN. In each case, the values of q_o, H_o and $z_{\rm max}$ given in each of the papers for the various fits have been used. The results are shown in Figure 6.22, where a band representing the range of neutrino intensities given by the various luminosity functions and dimensionless shock radii in the range $10 \leq x_1 \leq 100$, has been plotted for both spectrum (a) and (b) with $b = 1$ (darker band) and $b = 10$ (lighter band). The results for spectrum (a) and spectrum (b) are very similar, and the main difference is that neutrinos of slightly higher energies can be produced using spectrum (a). This is because for spectrum (b) protons can interact on infrared photons which reduced the maximum proton energy which can be achieved. Increasing the diffusion coefficient in the central region of the AGN has the effect of decreasing the energy of the neutrinos which can be produced in AGN. This is expected, as increasing b decreases the maximum energy of protons which can be produced in AGN (see Figure 6.10). The diffuse electron neutrino and antineutrino intensity from AGN can be found by reducing the neutrino intensity shown in Figure 6.22 by a factor of ~ 1.8. It should be noted that the published fits of Morisawa and Takahara (1989) contain a typographical error (see e.g. Szabo and Protheroe 1992a,b), and the results shown here have been obtained using the corrected version.

The diffuse flux of neutrinos from AGN was first calculated by Stecker *et al.* (1991a,b), using the incorrect luminosity functions published by Morisawa and Takahara (1989). The diffuse flux has been recalculated by Stecker *et al.* (1992) using the fits to the luminosity function of Della Ceca and Maccacaro (1991), and their revised results

have been added to Figure 6.22 (dashed curves) for comparison with our results. For both spectrum (a) and (b), we predict higher fluxes of neutrinos below $\sim 10^{15}$ eV, and as discussed in Section 6.9 this is because Stecker *et al.* only consider interactions with UV bump photons. They also predict a higher flux of neutrinos at high energies ($E_\nu > 5 \times 10^{16}$ eV for spectrum (a), and $E_\nu > 10^{16}$ eV for spectrum (b)) than we do, reflecting the different $E_{\rm max}$ versus $L_{\rm c}$ relationship we have used which takes into account all loss processes (see Figure 6.10).

Biermann (1992) and Sikora and Begelman (1992) have made independent calculations of the diffuse neutrino background from AGN by scaling the neutrino flux to the observed X–ray background, and their results have also been added to Figure 6.22. The results of Biermann have an uncertain high energy cut off which depends on details of the model used, and hence only the level of the predicted neutrino flux is shown (dot dashed curve). Our results predict a higher flux of neutrinos for $E_\nu < 2 \times 10^{15}$ eV compared to those of Biermann. Sikora and Begelman have calculated the diffuse neutrino flux from AGN by considering two extremes, that all AGN are local ($z = 0$, dotted curve which peaks at higher energy) and that all AGN are at a redshift $z = 5$. They have also assumed that all AGN produce the same neutrino spectrum. Our results are consistent with the peak flux predicted by Sikora and Begelman.

6.11 The Prospects for Observing Neutrinos from AGN

The muon signal in a neutrino telescope can be estimated from the predicted intensity of diffuse neutrinos from AGN (see Figure 6.22), using the method described in Section 5.3. I have calculated the signal for a muon threshold energy of 2 GeV, and obtain $S_\mu(E_\mu > 2$ GeV$) = 0.17$–0.56 muons m^{-2} yr^{-1} using spectrum (a), and $S_\mu(E_\mu > 2$ GeV$) = 0.16$–0.54 muons m^{-2} yr^{-1} using spectrum (b), for both $b = 1$ and $b = 10$. This is because for $E_\nu < 10^{12}$ eV the intensities are the essentially the same for $b = 1$ and $b = 10$. Using these results, DUMAND II with its area of $\sim 20,000$ m^2 would see 3,200–11,200 events per year. However, it must be pointed out that the above event rates are upper limits as DUMAND II will have a higher energy threshold (~ 25 GeV). Also a 100% duty cycle has been assumed (e.g. in a surface neutrinos detector the flux

would be reduced by a factor of ~ 0.5), and the angular dependence of the flux due to attenuation of neutrinos by the Earth has been ignored. These effects will be offset somewhat at high energies because the effective area of the telescope can exceed its physical area. For example the effective area of DUMAND II is twice its physical area at energies above $\sim 10^5$ GeV (Stenger 1992).

Using the preliminary results of Szabo and Protheroe (1992a,b), Stenger (1992) has calculated the neutrino induced muon signal in DUMAND II. Stenger obtained signals of 109 ($E_\mu > 100$ GeV) and 23 ($E_\mu > 10$ TeV) muons per year, compared with an atmospheric background of 2950 and 22.8 respectively. Clearly, the estimation I have made of the muon signal above is not consistent with these results. However, Stenger obtained signals of 897 ($E_\mu > 100$ GeV) and 148 ($E_\mu > 10$ TeV) muons per year for the neutrino flux calculated by Sikora and Begelman (1992), and 366 ($E_\mu > 100$ GeV) and 23 ($E_\mu > 10$ TeV) for the neutrino flux calculated by Biermann (1992), both of whom predict lower neutrino fluxes than we do. Based on this we conjecture that Stenger may have made an error in calculating the muon signal using our flux predictions.

Stanev (1992) has used our preliminary results to obtain a signal of 1350–5000 muons per year with energies above 1 TeV in a 10^5 m^2 detector, with an atmospheric background of 900. Even using the incorrect results of Stecker *et al.* (1991a,b), Stanev only obtained a muon signal of 630 muons per year in a detector of the same area (this reduces by a factor of ~ 40 for Stecker *et al.*'s revised calculation), and this highlights the important contribution made by neutrinos with energies less than $\sim 10^{15}$ eV.

From Figure 6.21, it can be seen that the neutrino flux from NGC 4151 is approximately two thousand times less than the diffuse neutrino flux from AGN at $E_\nu = 10^{12}$ eV. This means that the signal from NGC 4151 would be approximately 2–6 muons per year above 2 GeV in DUMAND II, using my estimation for the signal due to the neutrino background from AGN. This is too low to be observable, although the situation is not as bad as it first seems as all of the events come from a given direction, and hence the background is greatly reduced.

From these calculation one can conclude that if this model of AGN is correct, then the diffuse neutrino flux from AGN should be observable with the proposed neutrino telescopes.

Chapter 7

Summary and Further Work

The main result presented in this thesis was the spectrum of neutrinos produced in AGN, per proton injected into the accelerator. An accreting supermassive black hole model for AGN was used to calculate the contribution to the neutrino spectrum from pions produced both during and after proton acceleration. The contribution to the neutrino spectrum from neutrons which have escaped from the central region of AGN has also been included. Protons were assumed to be accelerated by the first order Fermi mechanism at a shock in the accretion flow. A simple leaky box picture of shock acceleration was used to model proton acceleration. All relevant loss process were considered. Proton–proton, pion photoproduction and pair production were found to be the most important interactions, and advection onto the black hole, diffusion out of the central region and synchrotron radiation were found to be important loss mechanisms. The neutrino spectrum produced per proton injected into the accelerator has been used to calculate the flux of neutrinos expected from the active galaxies NGC 4151 and 3C 273, and to calculate the contribution to the diffuse neutrino background from AGN. The resulting neutrino background was compared to recent calculations of Stecker *et al.* (1992), Biermann (1992) and Sikora and Begelman (1992). The effect of the photon spectrum on the results was examined, and it was found that if the infrared emissions in AGN are produced at small radii with a power law spectrum, then this has the effect of reducing the flux of high energy neutrinos produced in AGN. The effect of increasing the diffusion coefficient in the central region of the AGN was also examined, and this also was found to decrease the flux of high energy neutrino from AGN. The signals expected in a neutrino telescope both from individual AGN and from the sum

of all AGN were estimated. It was found that, using this model, the diffuse neutrino background is a good candidate for observation with the proposed neutrino telescopes, which were reviewed in Chapter 5.

Accurate modelling of the interactions a proton experiences in an AGN formed a fundamental part of the calculation of the neutrino spectrum from AGN. Pion photoproduction and pair production interactions were modelled exactly using the Monte Carlo method. For pion photoproduction, the fits to the exclusive data given by Genzel, Joos and Pfeil (1973) were used near threshold, and the inclusive data of Moffeit *et al.* (1972) were used for interactions which occurred at energies above the resonance region. Pair production was modelled using the compilation of differential cross sections given by Motz, Olsen and Koch (1969). Proton–proton interactions were modelled using the fits to the inclusive data given by Hillas (1979). The accurate modelling of all of the interactions represents a significant improvement on the other calculations made recently, which use simple δ–function distributions for the spectrum of particles produced in each interaction.

Further work can take two forms, development of the model and/or detailed examination of the consequences of the model. For example, a more detailed analysis of neutron escape from the central region of AGN, including the effect of increasing the size of the region from which the UV emissions come from has already been completed (see Protheroe and Szabo 1992 for preliminary results). The flux of neutrons which escape from the central region has been used to calculate the flux of protons which diffuse out of active galaxies. Integrating over the contributions from all active galaxies, has shown that protons from AGN may contribute to the observed cosmic ray spectrum at energies above the "knee". If this is the case, and AGN form the main component of the cosmic ray spectrum above the "knee', then a direct observational consequence is that cosmic rays above $\sim 10^{15}$ eV will be almost entirely protons. Work on other consequences of the model is in progress.

Finally, the model for AGN can be applied to other astrophysical source, in particular accreting black holes within our galaxy. The model scales with the mass of the black hole, and so it is possible to estimate the spectrum of neutrinos produced by a galactic black hole. For a one solar mass black hole, Equation 6.1 gives the luminosity of the black hole as $L_c \sim 10^{36}$–10^{37} erg s^{-1} for $10 \leq x_1 \leq 100$, and hence $E_{max} \sim 10^{14}$–

10^{15} eV. Therefore, if the photon spectrum near the galactic black hole is the same as for AGN, then the spectrum of neutrinos produced by a galactic black hole will be approximately be given by the $E_{\max} = 10^{15}$ eV curve in Figure 6.19. However, a more detailed analysis of the problem is required, to make predictions of the flux of neutrinos expected from galactic black hole candidates.

References

Achar, C.V., Menon, M.G.K., Narasimham, V.S., Ramana–Murthy, P.V., Sreekantan, B.V., Hinotani, K., Miyake, S., Creed, D.R., Osborne, J.L., Pattison, J.B.M and Wolfendale, A.W., 1965: *Phys. Lett.*, 18, 196.

Alner, G.J., Ansorge, R.E., Asman, B., Booth, C.N., Buruw, L., Carlson, P., DeClercq, C., DeWolf, R.S., Drees, A., Eckart, B., Ekspong, G., Evangelou, I., Eyring, A., Fabre, J.–P., Frobel, L., Fuglesang, C., Gaudaen, J., Geich–Gimbel, C., Holl, B., von Holtey, G., Hospes, R., Jon–And, K., Kokott, Th., Lotse, F., Manthos, N., Meinke, R., Munday, D.J., Ovens, J.E.V., Pelzer, W., Reidy, J.J., Rushbrooke, J.G., Schmickler, H., Triantis, F., Van hamme, L., Walck, Ch., Ward, C.P., Ward, D.R., Webber, C.J.S., White, T.O., Wilquet, G. and Yamdagni, N., 1986: *Zeit. Phys. C - Particles and Fields*, 32, 153.

Arnett, W.D., Bahcall, J.N., Kirshner, R.P. and Woosley, S.E., 1989: *Ann. Rev. Astron. Ap.*, 27, 629.

Atoyan, A.M., 1992: *Astron. Ap.*, 257, 476.

Auriemma, G., 1991: *"Proceedings of the 22nd International Cosmic Ray Conference"*, Dublin, The Dublin Institute for Advanced Studies (Dublin) 4, 682.

Avni, Y., 1978: *Astron. Astrophys.*, 63, L13.

Axford, W.I., Leer, E. and Skadron, G., 1977: *"Proceedings of the 15th International Cosmic Ray Conference"*, Plovdiv, Bulgarian Academy of Sciences (Plovdiv), 11, 132.

Barwick, S.W., Halzen, F., Lowder, D.M., Lynch, J., Miller, T., Morse, R., Price, P.B., Westphal, A. and Yodh, G.B., 1991a: *"Proceedings of the 22nd International Cosmic Ray Conference*, Dublin, The Dublin Institute for Advanced Studies (Dublin), 4, 658.

Barwick, S.W., Halzen, F., Lowder, D.M., Miller, T., Morse, R., Price, P.B. and Westphal, A., 1991b: *"Third International Workshop on Neutrino Telescopes"*, Venice, edited by M. Baldo–Ceolin, 437.

Barwick, S.W., Halzen, F., Lowder, D.M., Miller, T., Morse, R., Price, P.B. and Westphal, A., 1992: *J. Phys. G: Nucl. Part. Phys.*, 18, 225.

Begelman, M.C., Blandford, R.D. and Rees, M.J., 1984: *Rev. Mod. Phys.*, 56, 255.

Begelman, M.C., Rudak, B. and Sikora, M., 1990: *Ap. J.*, 362, 38.

Bell, A.R., 1978a: *Mon. Not. R. Astron. Soc.*, 182, 147.

Bell, A.R., 1978b: *Mon. Not. R. Astron. Soc.*, 182, 443.

Belolaptikov, I.A., Bezrukov, L.B., Borisovets, B.A., Bugaev, E.V., Domogatsky, G.V., Doroshenko, A.A., Galperin, M.D., Golikov, A.V., Jilkibaev, Zh.–A.M., Klabukov, A.M., Klimushin, S.I., Lubsandorzhiev, B.K., Panfilov, A.I., Sokal'sky, I.A., Stepanov, L.N., Trofimenko, I.I., Budnev, N.M., Chensky, A.G., Dobrynin, V.I., Fomin, A.D., Koshechkin, A.P., Lanin, J.B., Litunenko, G.A., Lopin, A.V., Naumov, V.A., Nemchenko, M.I., Parfenov, Yu.A., Pavlov, A.A., Poleschuk, V.A., Primin, V.A., Schestakov, A.A., Taraschansky, V.A., Yakup, A.V., Zurbanov, V.L., Golikov, A.V., Saslavskaya, E.S., Kabikov, V.B., Kuzmichev, L.A., Kusner, Yu.S., Scherstyankin, P.P., Dudkin, G.N., Ovcharov, A.M., Padalko, V.M., Krabi, J., Spiering, Ch., Weinert, T., Wischnewski, R., Kakas, P., Kiss, D. and Tankó, L., 1990: *Nucl. Phys. B (Proc. Suppl.)*, 14B, 51.

Belolaptikov, I.A., Bezrukov, L.B., Borisovets, B.A., Bugaev, E.V., Domogatsky, G.V.,

Donskich, L.A., Doroshenko, A.A., Djilkibaev, Zh.A.M., Galperin, M.D., Gushtan, M.N., Klabukov, A.M., Klimushin, S.I., Lanin, O.J., Lubsandorzhiev,B.K., Ogievietzky, N.V., Panfilov, A.I., Sokalsky, I.A., Trofimenko, I.I., Budnev, N.M., Chensky, A.G., Dobrynin, V.I., Gress, O.A., Koshechkin, A.P., Lanin, J.B., Litunenko, G.A., Lopin, A.V., Naumov, V.A., Nemchenko, M.I., Parfenov, Yu.A., Pavlov, A.A., Pokalev, O.P., Primin, V.A., Sumanov, A.A., Tarashansky, V.A., Zurbanov, V.L., Golikov, A.V., Zaslavskaya, E.S., Kabikov, V.B., Kuzmichov, L.A., Osipova, E.A., Dudkin, G.N., Egorov, V.Yu., Lukanin, A.A., Ovcharov, A.M., Padalko, V.M., Padusenko, A.H., Alatin, S.D., Fialkovsky, S.V., Kulepov, V.F., Milenin, M.B., Levin, A.A., Nikiforov, A.I., Rosanov, M.I., Heukenkamp, H., Krabi, J., Mikolajski, T., Spiering, Ch., Wischnewski, R., Jenek, L., Kiss, D., Tankó, L., Kusner, Yu.S., Poleschuk, V.A. and Sherstyankin, P.P., 1991a: *"Third International Workshop on Neutrino Telescopes"*, Venice, edited by M. Baldo–Ceolin, 365.

Belolaptikov, I.A., Bezrukov, L.B., Borisovets, B.A., Bugaev, E.V., Domogatsky, G.V., Donskich, L.A., Doroshenko, A.A., Galperin, M.D., Djilkibaev, Zh.A.M., Klabukov, A.M., Klimushin, S.I., Lanin, O.J., Lubsandorzhiev,B.K., Panfilov, A.I., Sokalsky, I.A., Trofimenko, I.I., Budnev, N.M., Chensky, A.G., Dobrynin, V.I., Gress, O.A., Koshechkin, A.P., Lanin, J.B., Litunenko, G.A., Lopin, A.V., Naumov, V.A., Nemchenko, M.I., Parfenov, Yu.A., Pavlov, A.A., Pokalev, O.P., Primin, V.A., Sumanov, A.A., Tarashansky, V.A., Zurbanov, V.L., Golikov, A.V., Zaslavskaya, E.S., Kabikov, V.B., Kuzmichov, L.A., Osipova, E.A., Dudkin, G.N., Egorov, V.Yu., Gushtan, M.N., Lukanin, A.A., Ovcharov, A.M., Padalko, V.M., Padusenko, A.H., Krabi, J., Mikolajski, T., Spiering, Ch., Wischnewski, R., Jenek, L., Kiss, D., Tankó, L., Kusner, Yu.S., Poleschuk, V.A. and Sherstyankin, P.P., 1991b: *Nucl. Phys. B (Proc. Suppl.)*, 19, 388.

Berezinsky, V.S., 1991: *"Third International Workshop on Neutrino Telescopes"*, Venice, edited by M. Baldo–Ceolin, 125.

Berezinsky, V.S., 1992: *Nucl. Phys. B (Proc. Suppl.)*, 28A, 352.

Berezinskiĭ, V.S. and Zatsepin, G.T., 1977: *Sov. Phys. Usp.*, 20, 361.

Berezinsky, V.S. and Ginzburg, V.L., 1981: *Mon. Not. R. Astron. Soc.*, 194, 3.

Berezinskiĭ, V.S., Bulanov, S.V., Dogiel, V.A., Ginzburg, V.L. and Ptuskin, V.S., 1990: *"Astrophysics of Cosmic Rays"*, translated by L.J. Reinders, North–Holland (Amsterdam).

Berezinsky, V.S. and Learned, J.G., 1992: *"Proceedings of the High Energy Neutrino Astrophysics Workshop"*, edited by V.J. Stenger, J.G. Learned, S. Pakvasa and X. Tata, World Scientific (Singapore), in press.

Biermann, P.L., 1992: *"Proceedings of the High Energy Neutrino Astrophysics Workshop"*, edited by V.J. Stenger, J.G. Learned, S. Pakvasa and X. Tata, World Scientific (Singapore), in press.

Biermann, P.L. and Strittmatter, P.A., 1987: *Ap. J.*, 322, 643.

Blandford, R.D. and Ostriker, J.P., 1978: *Ap. J.*, 221, L29.

Blandford, R. and Eichler, D., 1987: *Phys. Rep.*, 154, 1.

Blandford, R.D., Netzer, H. and Woltjer, L., 1990: *"Active Galactic Nuclei"*, Springer–Verlag (Heidelberg).

Blumenthal, G.R.. and Gould, R.J., 1970: *Rev. Mod. Phys.*, 42, 237.

Bøggild, H. and Ferbel, T., 1974: *Ann. Rev. Nucl. Sc.*, 24, 451.

Boldyrev, I.N., Gogin, A.A., Gusev, G.A., Markov, M.A., Pozovnoy, V.O., Provorov,

A.L., Zheleznykh, I.M., Bukhteev, A.N., Eremeev, V.I., Nazarkin, V.A., Bojarsky, V.I., Poznjak, V.I. and Sheremetjev, A.N., 1991: *"Third International Workshop on Neutrino Telescopes"*, Venice, edited by M. Baldo-Ceolin, 337.

Bowen, T., 1979: *"Proceedings of the 16th International Cosmic Ray Conference"*, Kyoto, Institute for Cosmic Ray Research (Tokyo), 11, 184.

Bowler, M.G., 1986: *"Lectures on Special Relativity"*, Pergamon Press (Oxford, New York, Beijing, Frankfurt, Sao Paulo, Sydney, Tokyo, Toronto).

Boyer, J., 1991: *"Proceedings of the 22nd International Cosmic Ray Conference"*, Dublin, The Dublin Institute for Advanced Studies (Dublin), 4, 634.

Brainerd, J.J, 1987: *Ap. J.*, 320, 714.

Brainerd, J.J. and Petrosian, V., 1987: *Ap. J.* 320, 703.

Carleton, N.P., Elvis, M., Fabbiano, G., Willner, S.P., Lawrence, A. and Ward, M., 1987: *Ap. J.*, 318, 595.

Cassiday, G.L., Cooper, R., Dawson, B.R., Elbert, J.W., Fick, B.E., Green, K.D., Ko, S., Loh, E.C., Salamon, M.H., Smith, J.D., Sokolsky, P., Sommers, P. and Thomas, S.B., 1989: *"Proceedings of the Workshop on Particle Astrophysics: Forefront Experimental Issues"*, Berkley, edited by E. B. Norman, World Scientific (Singapore, New Jersey, London, Hong Kong), 259.

Chini, R., Kreysa, E. and Biermann, P.L., 1989: *Astron. Ap.*, 219, 87.

Chodorowski, M. and Zdziarski, A.A., 1990: in preparation.

Collins, P.D.B. and Martin, A.D., 1984: *"Hadron Interactions"*, Adam Hilger Ltd. (Bristol).

De Palma, M., Iaselli, G., Maggi, C., Natali, S., Nuzzo, S., Ranieri, A., Raso, C., Romano, F., Ruggeri, F., Selvaggi, G., Tempesta, P., Zito, G., Rossi, A., Susinno, G., Grillo, A., Ronga, F., Valente, V., Bernardini, P., Pistilli, P., Watson, A., Reid, R., Lawrence, M., Ambrosio, M., Barbarino, G., Bartoli, B., Silverstrini, V., Buccheri, R., Carollo, M., Catalano, O., Linsley, J., Scarsi, L., Bressi, G., Lanza, A., Cambiaghi, M., Ratti, S., Bonori, M., D'Agostini, G., De Vincenzi, M., Lamanna, E., Lipari, P., Martellotti, G., Massa, F., Mattioli, M., Nigro, A., Petrera, S., Cardarelli, R., Rossi, F., Santonico, R., De Cesare, L., Grella, G., Guida, M., Mancini, F., Marini, G., Romano, G., Vitiello, G., Cappa, C., D'Ettorre Piazzoli, B., Ghia, P., Gomez, G. and Trivero, P., 1990: *Nucl. Phys. B (Proc. Suppl.)*, 14B, 69.

Della Ceca, R. and Maccacaro, T., 1991: *"Proceedings of the Workshop on the Space Distribution of Quasars"*, in press.

Done, C. and Fabian, A.C., 1989: *Mon. Not. R. Astron. Soc.*, 240, 81.

Drechsel, D. and Tiator, L., 1992: *J. Phys. G: Nucl. Part. Phys.*, 18, 449.

Drees, M. and Halzen, F., 1988: *Phys. Rev. Lett.*, 61, 275.

Drury, L.O'C., 1983: *Rep. Prog. Phys.*, 46, 973.

Edelson, R.A. and Malkan, M.A., 1986: *Ap. J.*, 308, 59.

Eichler, D., 1979: *Ap. J.*, 232, 106.

Eichler, D., 1984: *Ap. J.*, 277, 429.

Ellison, D.C. and Eichler, D., 1984: *Ap. J.*, 286, 691.

Everett, C.J. and Cashwell, E.D., 1983: *"A Third Monte Carlo Sampler"*, Los Alamos National Laboratory (New Mexico), LA-9721-MS.

Fermi, E., 1949: *Phys. Rev.*, 75, 1169.

Feynman, R.P., 1969: *Phys. Rev. Lett.*, 23, 1415.

Frazer, W.R., Ingber, L., Mehta, C.H., Poon, C.H., Silverman, D., Stowe, K., Ting, P.D. and Yesian, H.J., 1972: *Rev. Mod. Phys.*, 44, 284.
French, A.P., 1968: *"Special Relativity"*, W.W. Norton and Company Inc. (New York).
Gaisser, T.K., 1974: *J. Franklin Inst.*, 298, 271.
Gaisser, T.K. and Grillo, A.F., 1987: *Phys. Rev. D*, 36, 2752.
Gaisser, T.K. and Stanev, T., 1984: *Phys. Rev. D*, 30, 985.
Gaisser, T.K. and Stanev, T., 1985: *Phys. Rev. D*, 31, 2770.
Gaisser, T.K., 1990: *"Cosmic Rays and Particle Physics"*, Cambridge University Press (Cambridge).
Genzel, H., Joos, P., and Pfeil, W., 1973: *"Landolt–Börnstein: Photoproduction of Elementary Particles"*, 8, edited by H. Schopper, Springer Verlag (Berlin, Heidelberg, New York).
Ginzburg, V.L. and Syrovatskii, S.I., 1964: *"The Origin of Cosmic Rays"*, Pergamon Press (Oxford).
Gould, R.J., 1971: *Amer. J. Phys.*, 39, 911.
Gould, R.J and Schréder, G.P., 1967: *Phys. Rev.*, 155, 1404.
Grieder, P.K.F., 1986: *Il Nuovo Cimento*, 9C, 222.
Haines, T.J., 1989: *Annals of the New York Acad. of Sci.*, 571, 631.
Halzen, F., 1990: *"Proceedings of the 21st International Cosmic Ray Conference"*, Adelaide, edited by R.J. Protheroe, The University of Adelaide (Adelaide), 12, 101.
Halzen, F., Learned, J. and Stanev, T., 1989: *"Astrophysics in Antarctica"*, edited by D.J. Mullian, M.A. Pomerantz and T. Stanev, American Institute of Physics (New York), 39.
Harding, A.K. and Preece, R., 1987: *Ap. J.*, 319, 939.
Harding, A.K., Mastichiadis, A. and Protheroe, R.J., 1990: *"Proceedings of the 21st International Cosmic Ray Conference"*, Adelaide, edited by R.J. Protheroe, The University of Adelaide (Adelaide), 2, 226.
Harding, A.K., Mastichiadis, A., Szabo, A.P. and Protheroe, R.J., 1991: *Ap. J.*, 378, 163.
Hazard, C. and Mitton, S., 1979: *"Active Galactic Nuclei"*, Cambridge University Press (Cambridge, London, New York, Melbourne).
Hillas, A.M., 1975: *Phys. Rep.*, 20, 59.
Hillas, A.M., 1979: *"Proceedings of the 16th International Cosmic Ray Conference"*, Kyoto, Institute for Cosmic Ray Research (Tokyo), 6, 13.
Hillas, A.M., 1984: *Ann. Rev. Astron. Ap.*, 22, 425.
Hillier, R., 1984: *"Gamma Ray Astronomy"*, Clarendon Press (Oxford).
Ip, W.–H. and Axford, W.I., 1991: *"Astrophysics of the Most Energetic Cosmic Rays"*, edited by M. Nagano and F. Takahara, World Scientific (Singapore), 273.
Jones, F.C. and Ellison, D.C., 1991: *Space Science Reviews*, 58, 259.
Kazanas, D. and Ellison, D.C., 1986: *Ap.J.*, 304, 178.
Kirk, J.G. and Mastichiadis, A., 1989: *Astron. Ap.*, 213, 75.
Krymsky, G.F., 1977: *Sov. Phys.–Dokl*, 23, 327.
Learned, J.G. and Stanev, T., 1991: *"Proceedings of the Third International Workshop on Neutrino Telescopes*, Venice, edited by M. Baldo–Ceolin, 473.
Longair, M.S., 1981: *"High Energy Astrophysics"*, Cambridge University Press (Cambridge, London, New York, New Rochelle, Melbourne, Sydney).

Lowder, D.M., Miller, T., Price, P.B., Westphal, A., Barwick, S.W., Halzen, F. and Morse, R., 1991: *"Proceedings of the 22nd International Cosmic Ray Conference"*, Dublin, The Dublin Institute for Advanced Studies (Dublin), 4, 654.

Maccacaro, T., Della Ceca, R., Gioia, I.M., Morris, S,L., Stoke, J.T. and Wolter, A., 1991: *Ap. J.*, 374, 117.

MacDonald, J., Stanev, T., and Biermann, P.L., 1991: *Ap. J.*, 378, 30.

Malkan, M.A. and Sargent, W.L., 1982: *Ap. J.*, 254, 22.

Mannheim, K. and Biermann, P.L., 1989: *Astron. Ap.*, 221, 211.

Mastichiadis, A. and Protheroe, R.J., 1989: *Mon. Not. R. Astron. Soc.*, 246, 279.

Maximon, L.C., 1968: *J. Res. Natl. Bur. Std.*, 72B, 79.

Moffeit, K.C., Ballam, J., Chadwick, G.B., Della–Negra, M., Gearhart, R., Murray, J.J., Seyboth, P., Sinclair, C.K., Skillicorn, I.O., Spitzer, H., Wolf, G., Bingham, H.H., Fretter, W.B., Podolsky, W.J., Rabin, M.S., Rosenfeld, A.H., Windmolders, R., Yost, G.P. and Milburn, R.H., 1972: *Phys. Rev. D*, 5, 1603.

Morisawa, K. and Takahara, F., 1989: *Publ. Astron. Soc. Japan*, 41, 873.

Morisawa, K., Matsuoka, M., Takahara, F. and Piro, L., 1990: *Astron. Ap.*, 236, 299.

Motz, J.W., Olsen, H.A. and Koch, H.W., 1969: *Rev. Mod. Phys.*, 41, 581.

Particle Data Group, 1988: *Phys. Lett. B*, 204B, 1.

Particle Data Group, 1990: *Phys. Lett. B*, 239, 1.

Piccinotti. G., Mushotsky, R.F., Boldt, A., Holt, S.S, Marshall, P.J., Serlemitsos, P.J. and Shafer, R.A., 1982: *Ap. J.*, 253, 485.

Pistilli, P., 1991: *"Proceedings of the Third International Workshop on Neutrino Telescopes*, Venice, edited by M. Baldo–Ceolin, 379.

Press, W.H., Flannery, B.P., Teukolsky, S.A. and Vetterling, W.T., 1986: *"Numerical Recipes: The Art of Scientific Computing"*, Cambridge University Press (Cambridge, New York, New Rochelle, Melbourne, Sydney).

Protheroe, R.J., 1986: *Mon. Not. R. Astron. Soc.*, 221, 769.

Protheroe, R.J., 1990: *Mon. Not. R. Astron. Soc.*, 246, 628.

Protheroe, R.J. and Kazanas, D., 1983: *Ap. J.*, 265, 620.

Protheroe, R.J. and Szabo A.P., 1992: *"Proceedings of the IVth Rencontre de Blois"*, edited by J. Tran Than Van, Editions Frontieres (Gif sur Yvette), in press.

Quigg, C., Reno, M.H. and Walker, T.P., 1986: *Phys. Rev. Lett.*, 57, 774.

Rachen, J. and Biermann, P.L., 1992: *"Particle Acceleration in Cosmic Plasmas"*, edited by G.P. Zank and T.K. Gaisser, American Institute of Physics (New York), in press.

Rees, M.J., 1984: *Ann. Rev. Astron. Ap.*, 22, 471.

Reines, F., Crouch, M.F., Jenkins, T.L., Kropp, W.R., Gurr, H.S. and Smith, G.R., 1965: *Phys. Rev. Lett.*, 15, 429.

Reno, M.H. and Quigg, C., 1988: *Phys. Rev. D*, 37, 657.

Rothschild, R.E., Mushotsky, R.F., Baity, W.A., Gruber, D.E., Matteson, J.L and Peterson, L.E., 1983: *Ap. J.*, 269, 423.

Rowan–Robinson, M., 1985: *"The Cosmological Distance Ladder"*, W.H. Freeman and Company (New York).

Rybicki, G.B and Lightman, A.P., 1979: *"Radiative Processes in Astrophysics"*, John Wiley and Sons (New York).

Saunders, D.B., Phinney, E.S., Neugebauer, G., Soifer, B.T. and Matthews, K., 1989: *Ap. J.*, 347, 29.

Sikora, M., Begelman, M.C. and Rudak, B., 1989: *Ap. J.*, 341, L33.

Sikora, M., Kirk, J.G., Begelman, M.C. and Schneider, P., 1987: *Ap.J.*, 320, L81.
Sikora, M. and Begelman M.C., 1992: *"Proceedings of the High Energy Neutrino Astrophysics Workshop"*, edited by V.J. Stenger, J.G. Learned, S. Pakvasa and X. Tata, World Scientific (Singapore), in press.
Silberberg, R. and Shapiro, M.M., 1983: *"Composition and Origin of Cosmic Rays"* edited by M.M. Shapiro, D. Reidel Publishing Comp. (Dohrdrecht), 231.
Shapiro, M.M. and Silberberg, R., 1983: *Space Science Rev.*, 36, 512.
Sobel, H., 1990: *Nucl. Phys. B (Proc. Suppl.)*, 14A, 125.
Sobel, H.W., 1991: *Nucl. Phys. B (Proc. Suppl.)*, 19, 444.
Stanev, T., 1992: *"Proceedings of the High Energy Neutrino Astrophysics Workshop"* edited by V.J. Stenger, J.G. Learned, S. Pakvasa and X. Tata, World Scientific (Singapore), in press.
Stecker, F.W., 1968: *Phys. Rev. Lett.*, 21, 1016.
Stecker, F.W., 1971: *"Cosmic Gamma Rays"*, National Aeronautics and Space Administration (Washington DC), NASA SP–249.
Stecker, F.W., Done, C., Salamon, M.H. and Sommers, P., 1991a: *Phys. Rev. Lett.*, 66, 2697.
Stecker, F.W., Done, C., Salamon, M.H. and Sommers, P., 1991b: *"Proceedings of the UCLA International Conference on Trends in Astrophysics"*, in press.
Stecker, F.W., Done, C., Salamon, M.H. and Sommers, P., 1992: *"Proceedings of the High Energy Neutrino Astrophysics Workshop"*, edited by V.J. Stenger, J.G. Learned, S. Pakvasa and X. Tata, World Scientific (Singapore), in press.
Stenger, V.J., 1990: *Nucl. Phys. B (Proc. Suppl.)*, 14A, 153.
Stenger, V.J., 1992: *"Proceedings of the IVth Rencontre de Blois"*, edited by J. Tran Than Van, Editions Frontieres (Gif sur Yvette), in press.
Szabo, A.P. and Protheroe, R.J., 1991: *Proceedings of the 22nd International Cosmic Ray Conference"*, Dublin, The Dublin Institute for Advanced Studies, 2, 380.
Szabo, A.P. and Protheroe, R.J., 1992a: *"Proceedings of the High Energy Neutrino Astrophysics Workshop"*, edited by V.J. Stenger, J.G. Learned, S. Pakvasa and X. Tata, World Scientific (Singapore), in press.
Szabo, A.P. and Protheroe, R.J., 1992b: *"Particle Acceleration in Cosmic Plasmas"* edited by G.P. Zank and T.K. Gaisser, American Institute of Physics (New York), in press.
Trombka, J.I. and Fichtel, C.E., 1983: *Phys. Rep.*, 97, 173.
Turner, T.J. and Pounds, K.A., 1989: *Mon. Not. R. Astron. Soc.*, 240, 833.
Ward, M., Elvis, M., Fabbiano, G., Carleton, N.P., Willner, S.P. and Lawrence, A., 1987: *Ap. J.*, 315, 74.
Weekes, T.C., 1988: *Phys. Rep.*, 160, 1.
Weinberg, S., 1972: *"Gravitation and Cosmology: Principles and Applications of the General Theory of Relativity"*, John Wiley and Sons Inc. (New York).
Wiita, P.J., 1985: *Phys. Rep.*, 123, 117.
Wilkes, B.J. and Elvis, M., 1987: *Ap. J.*, 323, 243.
Zatsepin, G.T. and Kuz'min, V.A., 1962: *Sov. Phys. JETP*, 14, 1294.
Zdziarski, A.A., 1986: *Ap. J.*, 305, 45.

Appendix A

Monte Carlo Techniques

The Monte Carlo method is a statistical technique which is used to model a wide variety of phenomena. A simple example serves to illustrate the fundamental ideas behind the technique. Consider variables x and y which have distributions $p(x)$ and $q(y)$, i.e. $p(x)dx$ gives the probability of finding x in the range x to $x+dx$. If one wants to find the distribution of values formed by the product xy, then one could work out the answer analytically. Alternatively, one could sample a value of x from $p(x)$, and a value of y from $q(y)$, calculate the product and bin the result. After a large number of sampled values, the distribution formed by the binned results would approach the required distribution. This method is a powerful tool where analytical calculations are not possible, due to the complexity of the distributions and the relationship between variables. The ever increasing speed of computers also means that good statistics can be achieved on reasonable time scales.

Clearly, a fundamental aspect of the Monte Carlo method is the ability to sample from distributions quickly and accurately. Below two general methods for sampling from distributions are described. For a useful collection of sampling routines see Everett and Cashwell (1983).

A.1 Inverse Function Method

This method is based on mapping the distribution to be sampled, onto a uniform distribution in a variable ξ on the range $[0,1]$. Consider an arbitrary distribution $f(x)$ defined on $[x_1, x_2]$. The simplest way of mapping $f(x)$ to a uniform distribution is to integrate, i.e.

$$\xi = \frac{\int_{x_1}^{x} f(x)dx}{\int_{x_1}^{x_2} f(x)dx}. \tag{A.1}$$

To sample a value of x, one then samples a random deviate ξ and solves Equation A.1. Clearly, to be able to use this method the function $f(x)$ must be integrable, and one must be able to solve Equation A.1 for x. For example, consider the uniform distribution $f(x) = 1/2$ defined on $-1 \leq x \leq 1$. Equation A.1 becomes

$$\begin{aligned} \xi &= \frac{\int_{-1}^{x} \frac{dx}{2}}{\int_{-1}^{1} \frac{dx}{2}} \\ &= \frac{(x+1)}{2}, \end{aligned} \tag{A.2}$$

which can be rearranged to give $x = 2\xi - 1$. Some other useful sampling algorithms are given in the table below.

Distribution	Algorithm
$f(x) = A$, for $x_1 \leq x \leq x_2$	$x = (x_2 - x_1)\xi + x_1$
$f(x) = Ae^{-ax}$, for $a > 0$ and $x > 0$	$x = -\ln(\xi)/a$
$f(x) = Ax^{-a}$, for $a > 1$ and $x_1 \leq x \leq x_2$	$x = [(x_2^{(1-a)} - x_1^{(1-a)})\xi + x_1^{(1-a)}]^{1/(1-a)}$
$f(x) = Ax^{-1}$, for $x_1 \leq x \leq x_2$	$x = x_1(x_2/x_1)^{\xi}$

A.2 Rejection Method

For distributions which cannot be sampled by the inverse function method described above, one uses the rejection method. Consider a distribution $f(x)$ defined for $x_1 \leq x \leq x_2$ which cannot be sampled using the inverse function method. Also consider a second distribution $f'(x)$ defined on $x_1 \leq x \leq x_2$ for which a sampling routine exists and which satisfies $f'(x) > f(x)$ for all x. In this case, one samples a value of x from $f'(x)$ and then accepts this value of x if $\xi < f(x)/f'(x)$. Otherwise, a new value of x is sampled from $f'(x)$ and the condition tested again. The process is repeated until a value of x is accepted. Clearly, this process will be highly inefficient if $f'(x) \gg f(x)$. Thus, the distribution $f'(x)$ must be chosen carefully to ensure and efficient sampling routine. The rejection method is very powerful in that any distribution can be sampled in this way.

For example, consider the distribution $f(x) = e^{-x}$, defined on $0 \leq x \leq 1$. This distribution can be modeled using the inverse function method however, for the purpose of this example we will assume it cannot. Consider also the distribution $f'(x) = 1$, defined on $0 \leq x \leq 1$. Clearly, $f'(x)$ satisfies the conditions $f'(x) > f(x)$ for all x, and may easily be sampled. Thus, to sample a value from $f(x)$ one would firstly sample a value of x from $f'(x)$, i.e. $x = \xi_1$, and then test the condition $\xi_2 < f(x)/f'(x)$, where ξ_1 and ξ_2 are random deviates. If this condition is true the value of x is accepted, else another value of x is sample from $f'(x)$, and the process repeated until a value of x is chosen which is accepted.

Appendix B

Tables

The table below gives the coefficients used to fit the differential cross section for the reaction $p\gamma \rightarrow \pi^+ n$, from Genzel, Joos and Pfeil (1973). Fits are of the form

$$\frac{d\sigma_{\pi+}}{d\Omega^\star}(\varepsilon', \cos\theta^\star_{\pi r}) = \frac{1}{(1-\beta^\star_\pi \cos\theta^\star_{\pi r})^2} \sum_{n=0}^{8} a_n(\varepsilon') \cos^n \theta^\star_{\pi r}. \qquad \text{(B.1)}$$

ε' [GeV]	a_0	a_1	a_2	a_3	a_4	a_5	a_6	a_7	a_8
0.170	6.554	-6.506	1.965	0.000	0.000	0.000	0.000	0.000	0.000
0.180	7.508	-8.632	3.150	0.000	0.000	0.000	0.000	0.000	0.000
0.190	8.535	-11.167	4.160	0.000	0.000	0.000	0.000	0.000	0.000
0.200	9.239	-13.272	5.278	0.000	0.000	0.000	0.000	0.000	0.000
0.210	10.261	-15.676	6.195	0.000	0.000	0.000	0.000	0.000	0.000
0.220	10.596	-17.126	7.064	0.000	0.000	0.000	0.000	0.000	0.000
0.230	13.046	-22.624	6.997	6.609	-3.497	0.000	0.000	0.000	0.000
0.240	13.852	-24.603	8.021	5.576	-2.410	0.000	0.000	0.000	0.000
0.250	16.510	-29.870	9.275	8.466	-4.020	0.000	0.000	0.000	0.000
0.260	16.692	-30.219	9.221	7.465	-2.840	0.000	0.000	0.000	0.000
0.280	19.999	-36.512	10.858	8.981	-3.011	0.000	0.000	0.000	0.000
0.290	20.635	-36.976	9.329	10.435	-3.120	0.000	0.000	0.000	0.000
0.300	22.915	-42.670	11.511	15.951	-7.426	0.000	0.000	0.000	0.000
0.310	21.237	-38.009	10.127	11.171	-4.198	0.000	0.000	0.000	0.000
0.320	21.730	-39.077	9.178	14.815	-6.284	0.000	0.000	0.000	0.000
0.340	18.798	-32.475	6.685	12.418	-5.076	0.000	0.000	0.000	0.000
0.350	16.440	-25.974	2.584	10.244	-2.929	0.000	0.000	0.000	0.000
0.360	15.168	-24.574	3.570	9.230	-3.045	0.000	0.000	0.000	0.000
0.370	12.389	-18.365	1.415	5.192	-0.267	0.000	0.000	0.000	0.000
0.380	12.232	-17.959	0.672	6.556	-1.207	0.000	0.000	0.000	0.000
0.400	9.769	-13.232	-0.516	4.138	0.116	0.000	0.000	0.000	0.000
0.420	8.454	-10.426	-1.731	2.600	1.371	0.000	0.000	0.000	0.000
0.450	6.904	-7.675	-2.066	0.804	2.203	0.000	0.000	0.000	0.000
0.500	6.254	-6.338	-3.786	1.646	3.522	-1.181	0.000	0.000	0.000
0.510	6.219	-5.164	-4.223	-1.365	4.646	0.000	0.000	0.000	0.000
0.530	6.037	-5.456	-3.665	-0.334	3.529	0.000	0.000	0.000	0.000
0.540	5.991	-4.892	-5.436	0.589	6.138	-2.294	0.000	0.000	0.000
0.550	6.090	-6.193	-4.415	5.219	1.215	-5.171	3.358	0.000	0.000

ε' [GeV]	a_0	a_1	a_2	a_3	a_4	a_5	a_6	a_7	a_8
0.570	6.167	-6.160	-3.953	3.091	2.473	-3.234	1.697	0.000	0.000
0.580	5.978	-4.399	-5.896	0.120	6.159	-1.873	0.000	0.000	0.000
0.590	6.463	-5.717	-6.418	4.544	3.857	-4.730	2.080	0.000	0.000
0.600	6.245	-5.358	-5.135	0.794	5.091	-1.547	0.000	0.000	0.000
0.620	6.491	-5.186	-5.477	-0.826	6.065	0.292	-1.285	0.000	0.000
0.630	6.631	-5.196	-6.178	-0.460	6.755	-0.075	-1.412	0.000	0.000
0.650	7.035	-5.290	-6.573	-2.275	8.117	2.350	-3.302	0.000	0.000
0.660	7.440	-6.750	-5.434	-0.729	6.027	2.050	-2.543	0.000	0.000
0.670	7.656	-7.468	-5.784	3.060	3.726	-1.131	0.000	0.000	0.000
0.680	7.740	-5.999	-8.550	0.464	8.788	-0.123	-2.265	0.000	0.000
0.690	8.098	-10.045	-1.148	7.874	-10.483	-3.588	9.392	0.000	0.000
0.700	8.152	-7.690	-5.116	-3.242	7.657	5.483	-5.189	0.000	0.000
0.710	7.834	-6.388	-5.348	-6.755	10.300	7.139	-6.739	0.000	0.000
0.720	8.165	-10.534	-2.870	5.321	-0.037	0.000	0.000	0.000	0.000
0.730	7.893	-8.326	-3.990	-2.338	6.304	5.665	-5.173	0.000	0.000
0.750	7.043	-9.210	-1.583	2.541	0.541	2.155	-1.454	0.000	0.000
0.770	6.339	-8.384	-1.798	3.958	-0.083	0.000	0.000	0.000	0.000
0.790	4.850	-7.085	0.021	4.644	-2.563	-2.006	2.169	0.000	0.000
0.800	4.994	-8.048	0.807	6.790	-4.966	-2.987	3.442	0.000	0.000
0.810	3.986	-6.946	4.811	1.961	-10.405	3.977	5.794	-3.150	0.000
0.820	3.542	-6.772	7.831	1.152	-18.840	8.700	11.956	-7.541	0.000
0.830	3.408	-6.514	6.129	2.785	-15.070	4.628	9.902	-5.243	0.000
0.840	2.940	-5.214	7.146	-1.317	-15.184	8.320	9.744	-6.410	0.000
0.850	2.817	-5.005	6.420	-1.031	-12.607	6.461	7.847	-4.880	0.000
0.860	2.520	-5.099	9.579	-2.932	-19.073	11.508	11.685	-8.166	0.000
0.880	2.311	-4.011	8.675	-6.251	-12.653	11.054	5.966	-5.072	0.000
0.900	2.111	-4.089	10.984	-6.816	-17.850	13.243	9.635	-7.199	0.000
0.920	2.037	-3.778	12.647	-9.373	-22.076	18.546	12.316	-10.303	0.000
0.930	2.027	-3.547	12.576	-10.565	-21.060	19.477	11.306	-10.201	0.000
0.950	2.265	-3.805	11.335	-8.358	-19.837	16.190	11.281	-9.058	0.000
0.960	1.988	-3.433	13.495	-11.675	-22.489	21.126	11.627	-10.629	0.000
0.970	2.110	-2.884	14.093	-14.129	-24.017	24.393	12.265	-11.819	0.000
0.980	2.234	-3.899	15.981	-12.982	-29.268	26.227	15.601	-13.884	0.000
1.000	2.218	-2.886	13.285	-14.117	-21.241	22.910	10.003	-10.161	0.000
1.010	2.130	-1.929	11.493	-16.012	-14.966	21.584	5.215	-7.504	0.000
1.020	2.061	-2.183	12.776	-15.963	-18.714	23.712	7.637	-9.318	0.000
1.030	2.006	-1.560	11.555	-16.998	-14.897	22.860	4.775	-7.733	0.000
1.050	1.830	-1.061	9.133	-15.539	-9.555	18.702	1.430	-4.933	0.000
1.060	1.817	-0.825	8.037	-13.573	-10.410	17.138	3.422	-5.598	0.000
1.070	1.528	-0.735	8.789	-14.531	-9.752	17.790	1.718	-4.800	0.000
1.080	1.384	0.428	6.727	-15.762	-4.591	16.188	-1.287	-3.080	0.000
1.090	1.108	0.165	4.675	-10.511	-4.088	11.069	0.270	-2.681	0.000
1.100	1.154	0.146	4.783	-9.588	-6.469	11.267	2.530	-3.817	0.000
1.130	1.161	-0.243	0.115	0.373	1.135	-13.415	6.894	11.979	-7.993
1.140	1.173	-0.361	0.316	0.766	-0.107	-12.838	7.661	11.237	-7.844
1.160	0.887	-0.227	0.796	-2.374	4.444	-9.450	0.601	11.047	-5.721
1.170	0.806	0.345	-0.951	-0.245	4.975	-12.796	2.458	11.733	-6.322
1.180	0.665	0.132	-0.430	1.173	3.994	-16.210	4.571	14.100	-7.989

ε' [GeV]	a_0	a_1	a_2	a_3	a_4	a_5	a_6	a_7	a_8
1.190	0.696	-1.151	0.161	6.062	-0.283	-19.905	8.929	14.298	-8.802
1.200	0.722	-0.992	0.062	5.252	-0.090	-18.250	8.245	13.276	-8.220
1.210	0.716	0.032	-1.337	1.342	5.449	-13.950	1.952	11.609	-5.809
1.230	0.545	-0.024	-0.718	0.400	7.082	-14.274	-0.341	13.306	-5.974
1.240	0.553	-0.323	0.200	0.743	3.898	-12.471	1.678	11.459	-5.732
1.260	0.579	-0.263	-1.420	2.950	6.404	-16.938	1.202	13.759	-6.270
1.270	0.575	-0.481	-0.038	1.064	4.557	-11.862	0.103	10.815	-4.728

The table below gives the coefficients used to fit the differential cross section for the reaction $p\gamma \rightarrow \pi^o p$, from Genzel, Joos and Pfeil (1973). Fits are of the form

$$\frac{d\sigma_{\pi^o}}{d\Omega^\star}(\varepsilon', \cos\theta^\star_{\pi r}) = \sum_{n=0}^{8} a_n(\varepsilon') \cos^n \theta^\star_{\pi r}. \tag{B.2}$$

ε' [GeV]	a_0	a_1	a_2	a_3	a_4	a_5	a_6	a_7	a_8
0.160	0.331	-0.211	0.039	0.000	0.000	0.000	0.000	0.000	0.000
0.170	0.600	-0.234	-0.273	0.000	0.000	0.000	0.000	0.000	0.000
0.180	0.981	-0.339	-0.385	0.000	0.000	0.000	0.000	0.000	0.000
0.190	1.730	-0.323	-0.929	0.000	0.000	0.000	0.000	0.000	0.000
0.210	2.736	-0.739	-1.110	0.000	0.000	0.000	0.000	0.000	0.000
0.230	5.363	0.069	-0.933	0.000	0.000	0.000	0.000	0.000	0.000
0.240	7.100	-1.042	-3.484	0.000	0.000	0.000	0.000	0.000	0.000
0.250	9.172	-1.759	-4.724	0.000	0.000	0.000	0.000	0.000	0.000
0.260	12.386	-1.687	-7.457	0.000	0.000	0.000	0.000	0.000	0.270
0.280	19.929	-0.965	-12.098	0.000	0.000	0.000	0.000	0.000	0.000
0.290	23.458	-1.868	-14.987	0.000	0.000	0.000	0.000	0.000	0.000
0.300	26.888	-1.106	-17.567	0.000	0.000	0.000	0.000	0.000	0.000
0.310	28.720	-1.634	-19.367	0.000	0.000	0.000	0.000	0.000	0.000
0.320	30.860	0.464	-20.112	0.000	0.000	0.000	0.000	0.000	0.000
0.330	30.098	-0.972	-21.016	0.000	0.000	0.000	0.000	0.000	0.000
0.340	28.728	1.132	-19.382	0.000	0.000	0.000	0.000	0.000	0.000
0.350	26.525	0.304	-18.695	0.000	0.000	0.000	0.000	0.000	0.000
0.360	23.874	2.284	-15.497	0.000	0.000	0.000	0.000	0.000	0.000
0.370	21.332	1.071	-14.880	0.000	0.000	0.000	0.000	0.000	0.000
0.380	18.655	2.285	-11.920	0.000	0.000	0.000	0.000	0.000	0.000
0.400	14.870	1.877	-9.835	0.000	0.000	0.000	0.000	0.000	0.000
0.410	13.370	1.361	-10.319	0.000	0.000	0.000	0.000	0.000	0.000
0.420	12.294	1.531	-9.073	0.000	0.000	0.000	0.000	0.000	0.000
0.430	10.899	0.788	-8.977	0.000	0.000	0.000	0.000	0.000	0.000
0.440	9.734	1.402	-6.930	0.000	0.000	0.000	0.000	0.000	0.000
0.450	8.879	0.759	-6.984	0.000	0.000	0.000	0.000	0.000	0.000
0.460	8.036	1.531	-5.083	0.000	0.000	0.000	0.000	0.000	0.000
0.470	7.761	1.293	-5.907	0.000	0.000	0.000	0.000	0.000	0.000
0.480	5.772	0.662	-3.370	0.000	0.000	0.000	0.000	0.000	0.000
0.490	5.803	0.649	-4.728	0.000	0.000	0.000	0.000	0.000	0.000
0.510	4.673	0.374	-3.161	0.000	0.000	0.000	0.000	0.000	0.000
0.520	4.446	0.920	-2.799	0.000	0.000	0.000	0.000	0.000	0.000
0.540	3.947	0.988	-2.446	0.000	0.000	0.000	0.000	0.000	0.000
0.550	4.348	-0.928	-8.361	1.036	5.704	0.000	0.000	0.000	0.000

ε' [GeV]	a_0	a_1	a_2	a_3	a_4	a_5	a_6	a_7	a_8
0.570	4.016	0.021	-7.120	-0.030	4.917	0.000	0.000	0.000	0.000
0.580	3.564	0.455	-6.080	-0.603	4.550	0.000	0.000	0.000	0.000
0.590	3.133	-0.526	-4.606	1.137	2.471	0.000	0.000	0.000	0.000
0.600	3.619	0.084	-5.555	0.352	2.886	0.000	0.000	0.000	0.000
0.610	2.935	-0.724	-4.074	1.113	2.010	0.000	0.000	0.000	0.000
0.620	3.525	0.404	-5.093	-0.277	2.425	0.000	0.000	0.000	0.000
0.630	2.705	-0.606	-3.217	0.755	1.332	0.000	0.000	0.000	0.000
0.640	3.321	-0.472	-5.254	0.625	2.897	0.000	0.000	0.000	0.000
0.650	3.013	-0.980	-5.875	0.940	4.053	0.000	0.000	0.000	0.000
0.660	3.349	-0.561	-4.719	0.573	2.264	0.000	0.000	0.000	0.000
0.670	3.226	0.062	-6.057	-2.470	3.689	2.453	0.000	0.000	0.000
0.680	3.480	-0.708	-4.066	2.782	1.555	-2.143	0.000	0.000	0.000
0.690	3.615	0.337	-5.488	-2.488	2.724	2.005	0.000	0.000	0.000
0.700	4.164	0.441	-6.338	-1.983	3.111	1.315	0.000	0.000	0.000
0.710	3.896	0.155	-5.246	-0.548	2.543	0.000	0.000	0.000	0.000
0.720	4.450	0.281	-6.205	-2.576	4.302	3.551	0.000	0.000	0.000
0.730	4.057	0.981	-6.356	-3.996	5.114	4.242	0.000	0.000	0.000
0.740	4.518	0.721	-5.321	-3.014	1.911	2.022	0.000	0.000	0.000
0.750	4.116	0.872	-4.812	-3.706	2.019	2.444	0.000	0.000	0.000
0.760	4.748	0.327	-6.930	-0.228	6.868	-0.501	-3.673	0.000	0.000
0.770	4.975	-2.898	-6.011	7.319	2.164	-4.871	0.000	0.000	0.000
0.780	4.116	0.490	-6.877	-1.442	11.302	0.701	-7.632	0.000	0.000
0.800	3.683	0.328	-5.274	-2.571	6.385	1.612	-3.466	0.000	0.000
0.830	2.938	-0.943	-2.376	0.230	0.651	0.000	0.000	0.000	0.000
0.850	2.528	0.139	-5.316	-6.927	15.043	15.788	-11.120	-9.823	0.000
0.880	2.318	0.154	-6.194	-7.589	20.950	22.460	-15.922	-15.868	0.000
0.910	1.938	-1.018	-2.977	1.086	10.947	-0.536	-9.114	0.000	0.000
0.920	1.727	-0.538	-1.055	-0.350	5.478	0.391	-5.331	0.000	0.000
0.930	1.746	-2.180	3.083	1.741	-4.000	0.000	0.000	0.000	0.000
0.950	1.714	-0.713	-1.820	-0.021	9.933	0.237	-8.996	0.000	0.000
0.970	1.773	-0.773	-2.202	0.023	12.720	0.358	-11.676	0.000	0.000
1.000	1.516	-1.103	0.836	1.418	6.081	-0.815	-7.666	0.000	0.000
1.020	1.635	-0.929	0.536	4.565	9.886	-4.129	-11.296	0.000	0.000
1.040	1.552	-0.495	2.282	3.913	-1.612	-13.392	-1.558	9.576	0.000
1.050	1.468	0.177	4.206	-2.206	-4.837	1.498	0.000	0.000	0.000
1.060	1.508	-0.298	3.444	2.231	-3.118	-7.504	-1.020	5.026	0.000
1.070	1.263	-0.251	1.253	2.994	6.968	-3.160	-8.788	0.000	0.000
1.080	1.249	-0.044	3.950	-0.519	-4.358	0.000	0.000	0.000	0.000
1.090	1.088	0.552	4.180	-1.192	-4.434	0.000	0.000	0.000	0.000
1.100	1.170	0.737	3.153	-1.205	-3.560	0.000	0.000	0.000	0.000
1.110	1.201	-0.697	4.187	0.252	-4.662	0.000	0.000	0.000	0.000
1.120	0.930	0.704	2.398	-1.155	-2.591	0.000	0.000	0.000	0.000
1.130	0.861	0.703	2.891	-1.196	-2.974	0.000	0.000	0.000	0.000
1.140	0.807	0.240	3.176	-0.420	-3.108	0.000	0.000	0.000	0.000
1.150	0.885	0.890	1.732	-1.334	-1.890	0.000	0.000	0.000	0.000
1.170	0.860	0.716	-1.365	0.140	6.449	-1.323	-5.061	0.000	0.000
1.180	0.896	0.248	-0.630	0.897	4.943	-1.452	-4.496	0.000	0.000
1.200	0.893	-0.557	1.642	1.981	-1.663	-1.885	0.000	0.000	0.000

Appendix C

The 4^{th} Order Runge–Kutta Technique

The 4^{th} order Runge–Kutta technique is a numerical method used for solving differential equations of the form

$$\frac{dy}{dx} = f(x, y), \tag{C.1}$$

with the boundary condition $y = y_o$, for $x = x_o$. The iterative algorithm is (Press *et al.* 1986),

$$\begin{aligned} k_1 &= hf(x_n, y_n) \\ k_2 &= hf(x_n + h/2, y_n + k_1/2) \\ k_3 &= hf(x_n + h/2, y_n + k_2/2) \\ k_4 &= hf(x_n + h, y_n + k_3) \\ y_{n+1} &= y_n + \frac{k_1}{6} + \frac{k_2}{3} + \frac{k_3}{3} + \frac{k_4}{6} \\ x_{n+1} &= x_n + h, \end{aligned} \tag{C.2}$$

where h is the step size. One can also use a variation of the Runge–Kutta technique for definite integrals of the form

$$y = \int_{x_o}^{x_1} f(x)dx, \tag{C.3}$$

with $y_o = 0$. In this case, the algorithm becomes

$$\begin{aligned} k_1 &= hf(x_n) \\ k_2 &= hf(x_n + h/2) \\ k_3 &= hf(x_n + h) \\ y_{n+1} &= y_n + \frac{k_1}{6} + \frac{2k_2}{3} + \frac{k_3}{6} \\ x_{n+1} &= x_n + h. \end{aligned} \tag{C.4}$$

This algorithm is equivalent to Simpson's Rule.

Appendix D

Results

On the following pages many of the results from the calculations described in Chapter 6 have been compiled. The loss rates for $b^{-1}L_c^{0.5} = 10^{19}$, 10^{20},...,10^{24} (erg s^{-1})$^{0.5}$ for both spectrum (a) and (b) are plotted on pages D2–D7. On pages D8 and D9 the spectrum of particles produced by the accelerator, per proton injected into the accelerator are shown for $E_{\max} = 10^{15}$, 10^{16},..., 10^{19} eV. The spectra of particles produced within the central region of the AGN by protons which have escaped from the accelerator can be found on pages D10–D13 for $E_{\max} = 10^{15}$, 10^{16},..., 10^{19} eV. The spectra of pions produced by neutrons which have escaped from the central region of the AGN are shown on pages D14 and D15, for $E_{\max} = 10^{15}$, 10^{16},..., 10^{19} eV.

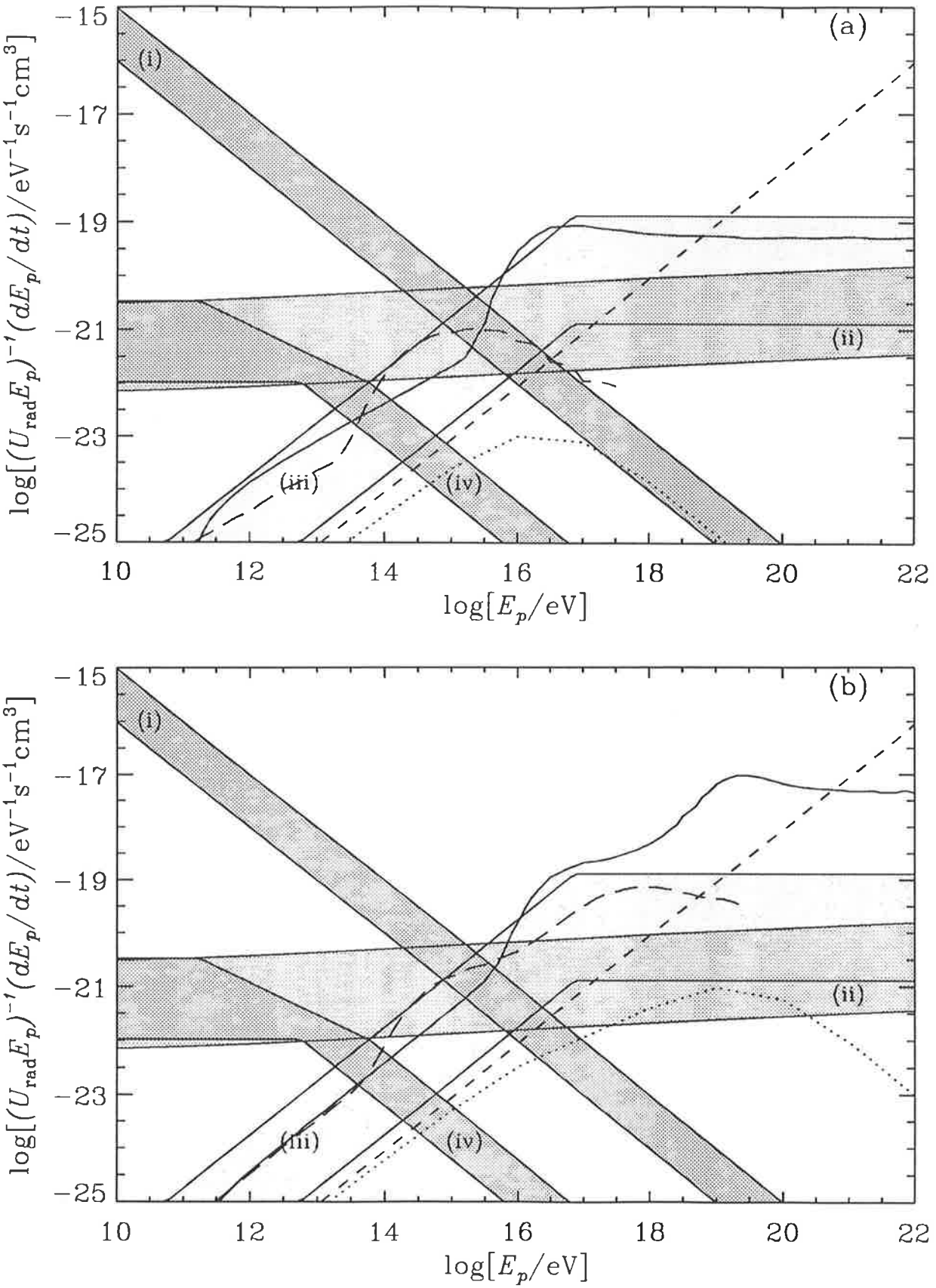

Figure D.1: The loss rates for $b^{-1}L_c^{0.5} = 10^{19}$ (erg s^{-1})$^{0.5}$, for (a) the PG continuum, and (b) the flat AGN continuum. See Figure 6.5 for a definition of the curves.

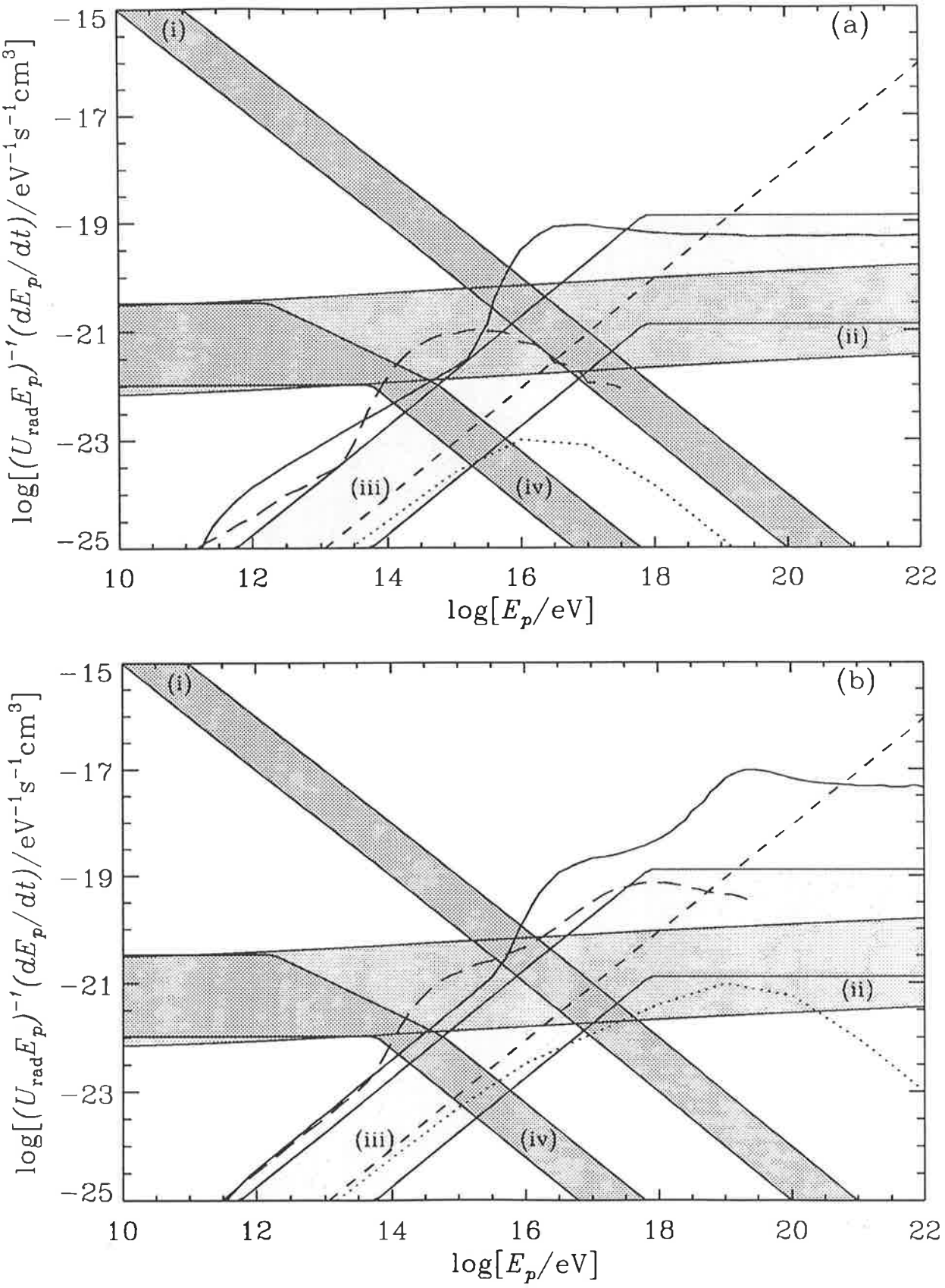

Figure D.2: The loss rates for $b^{-1}L_c^{0.5} = 10^{20}$ (erg s^{-1})$^{0.5}$, for (a) the PG continuum, and (b) the flat AGN continuum. See Figure 6.5 for a definition of the curves.

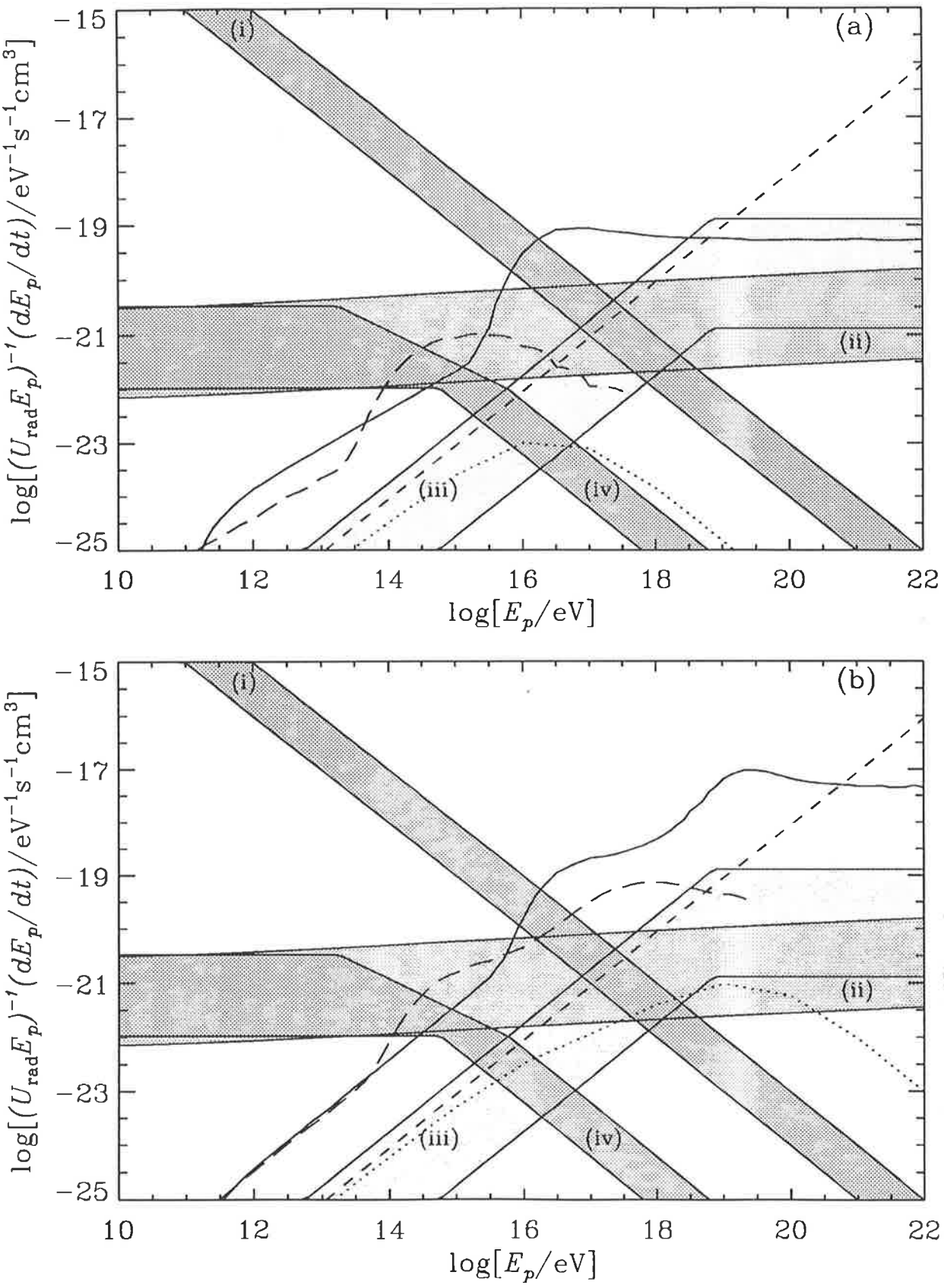

Figure D.3: The loss rates for $b^{-1}L_c^{0.5} = 10^{21}$ (erg s^{-1})$^{0.5}$, for (a) the PG continuum, and (b) the flat AGN continuum. See Figure 6.5 for a definition of the curves.

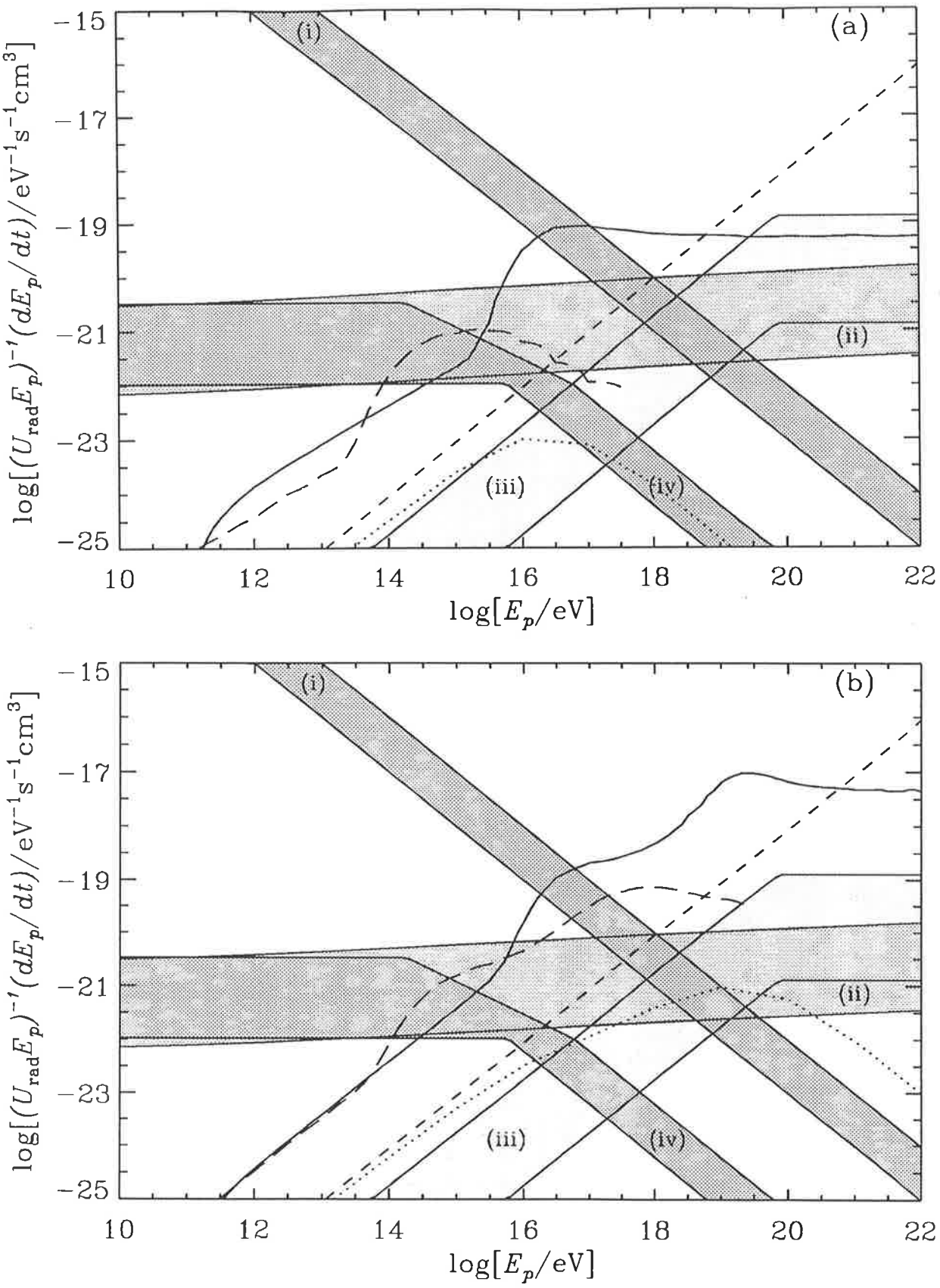

Figure D.4: The loss rates for $b^{-1}L_c^{0.5} = 10^{22}$ (erg s^{-1})$^{0.5}$, for (a) the PG continuum, and (b) the flat AGN continuum. See Figure 6.5 for a definition of the curves.

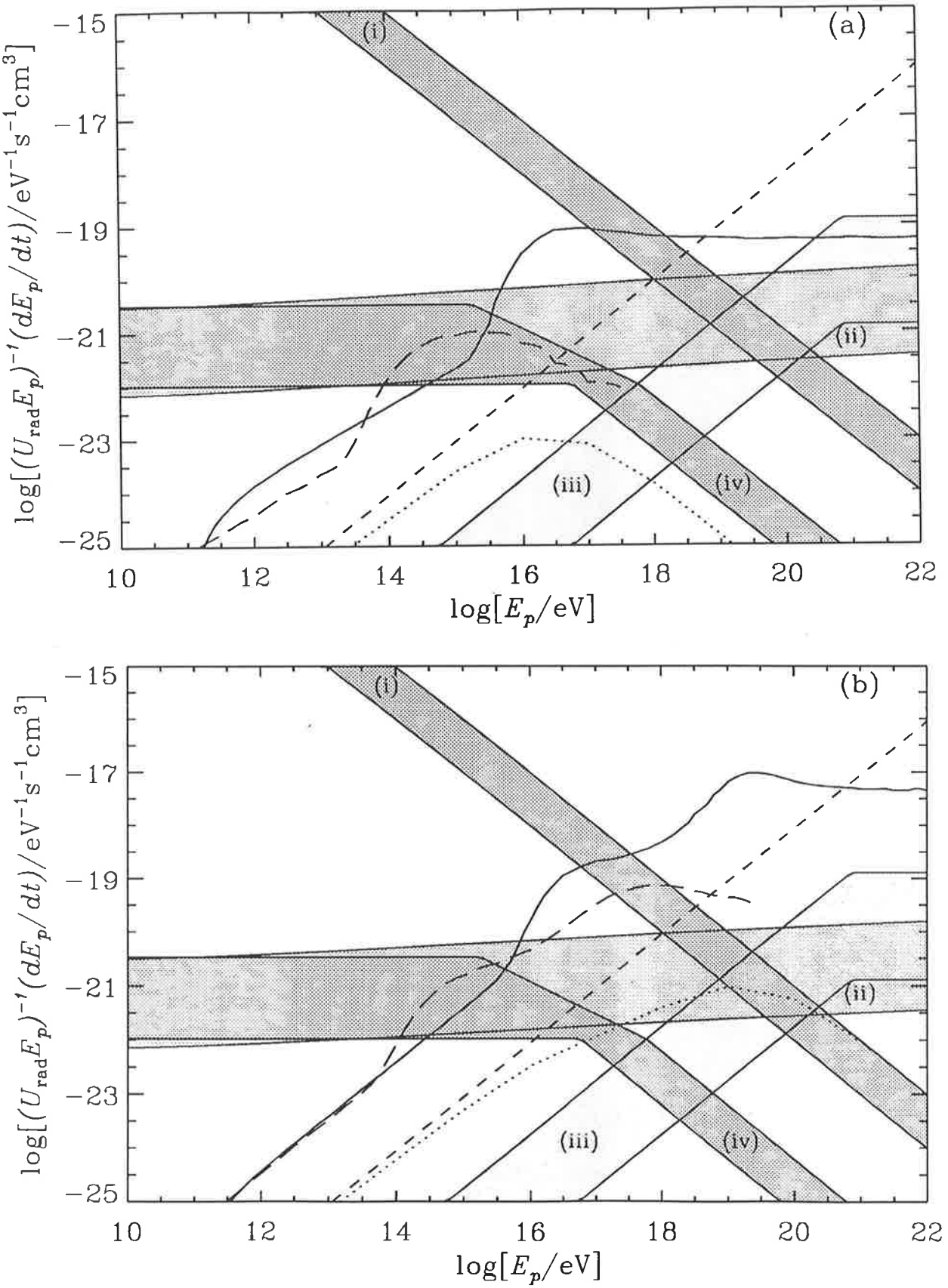

Figure D.5: The loss rates for $b^{-1}L_c^{0.5} = 10^{23}$ (erg s^{-1})$^{0.5}$, for (a) the PG continuum, and (b) the flat AGN continuum. See Figure 6.5 for a definition of the curves.

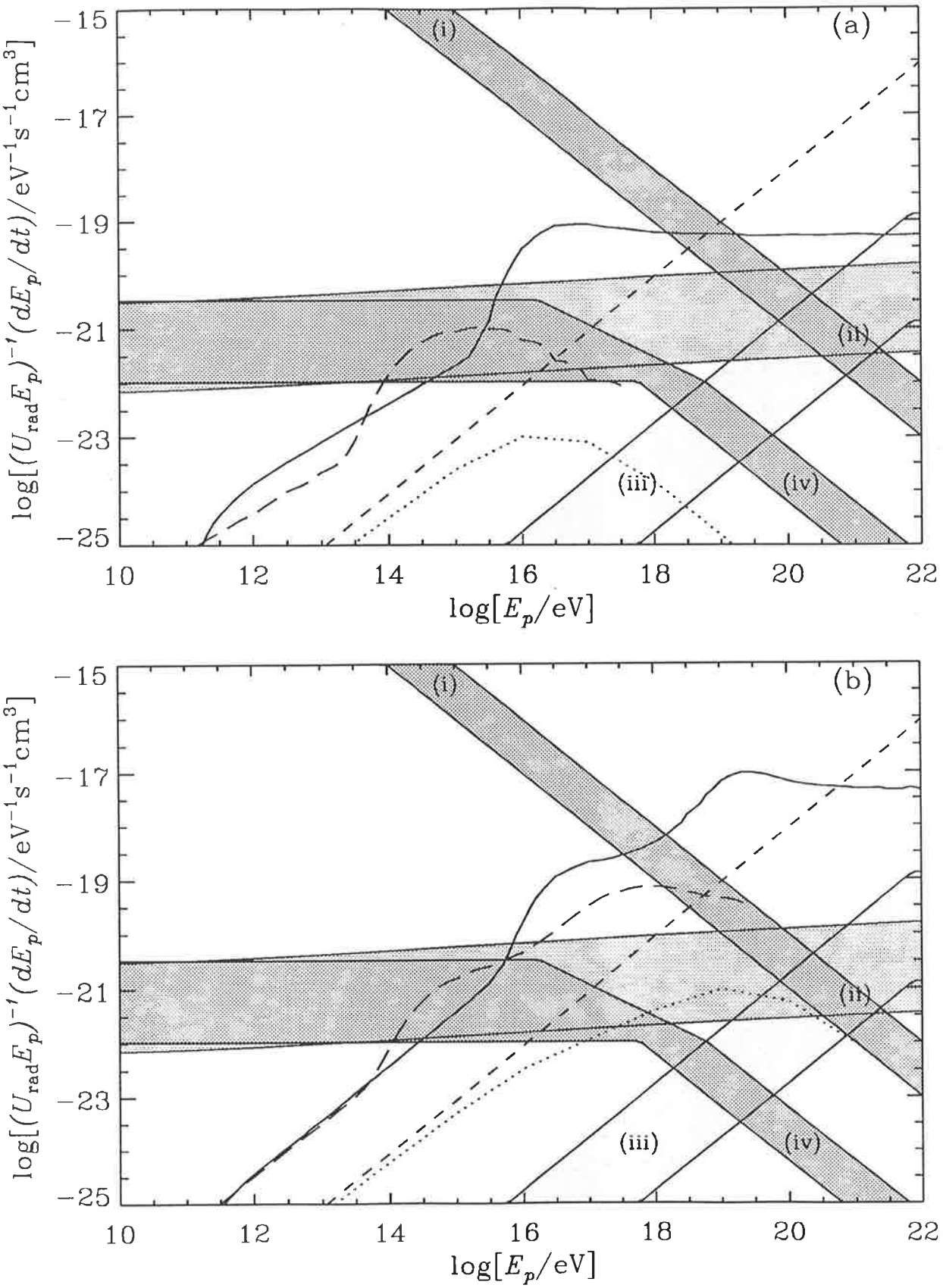

Figure D.6: The loss rates for $b^{-1}L_c^{0.5} = 10^{24}$ (erg s^{-1})$^{0.5}$, for (a) the PG continuum, and (b) the flat AGN continuum. See Figure 6.5 for a definition of the curves.

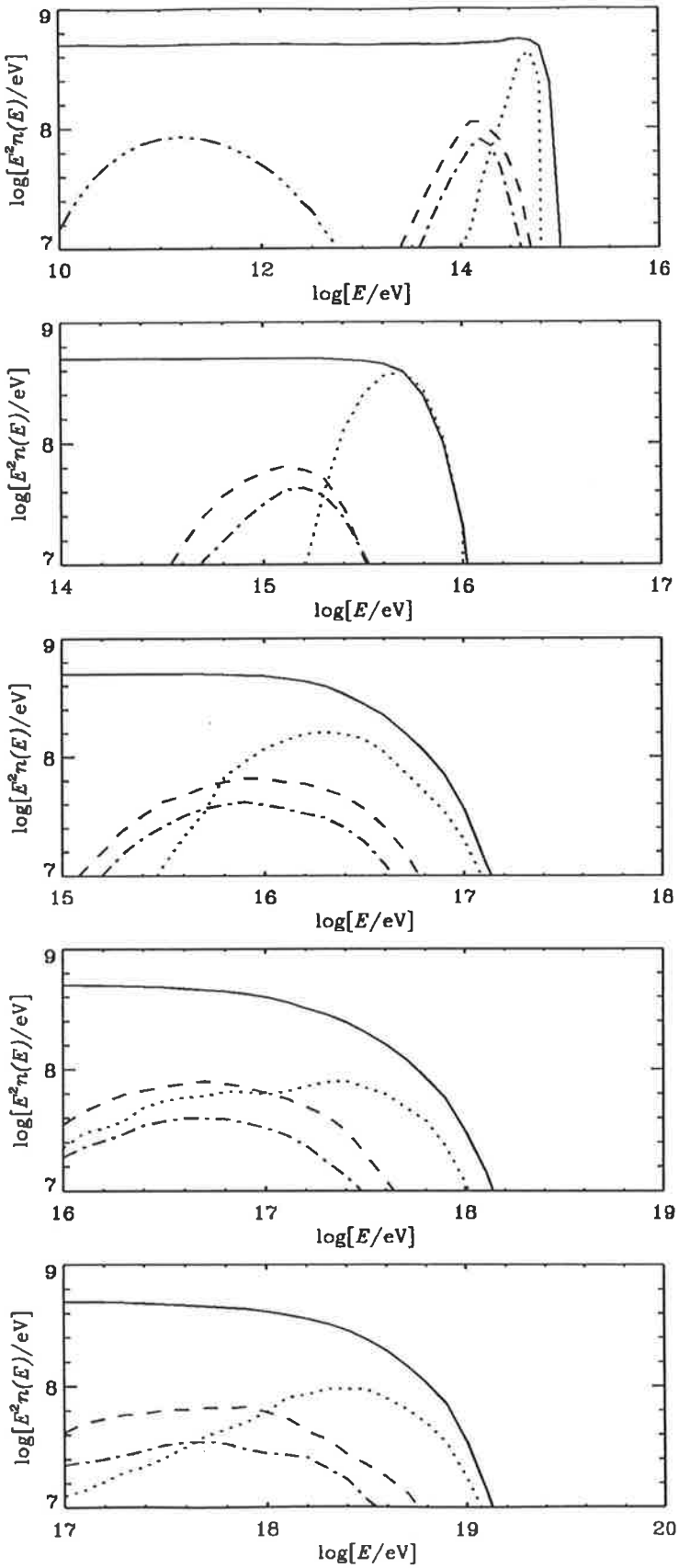

Figure D.7: The spectrum of particles produced by the accelerator calculated using the PG continuum (spectrum (a)). Plots are for $E_{\max} = 10^{15}$ (top plot), 10^{16},..., 10^{19} eV (bottom plot). Curves are defined as in Figure 6.13.

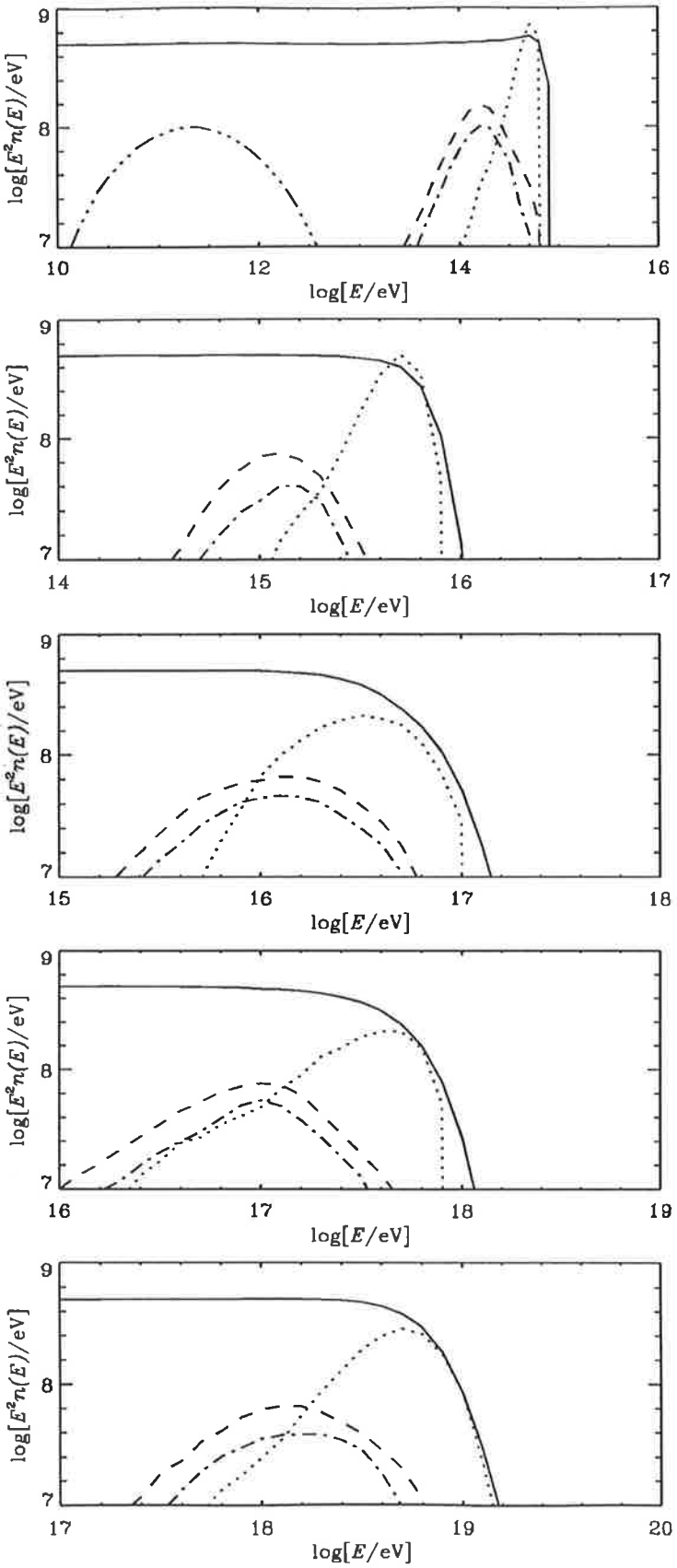

Figure D.8: The spectrum of particles produced by the accelerator calculated using the flat AGN continuum (spectrum (b)). Plots are for $E_{\max} = 10^{15}$ (top plot), 10^{16},..., 10^{19} eV (bottom plot). Curves are defined as in Figure 6.13.

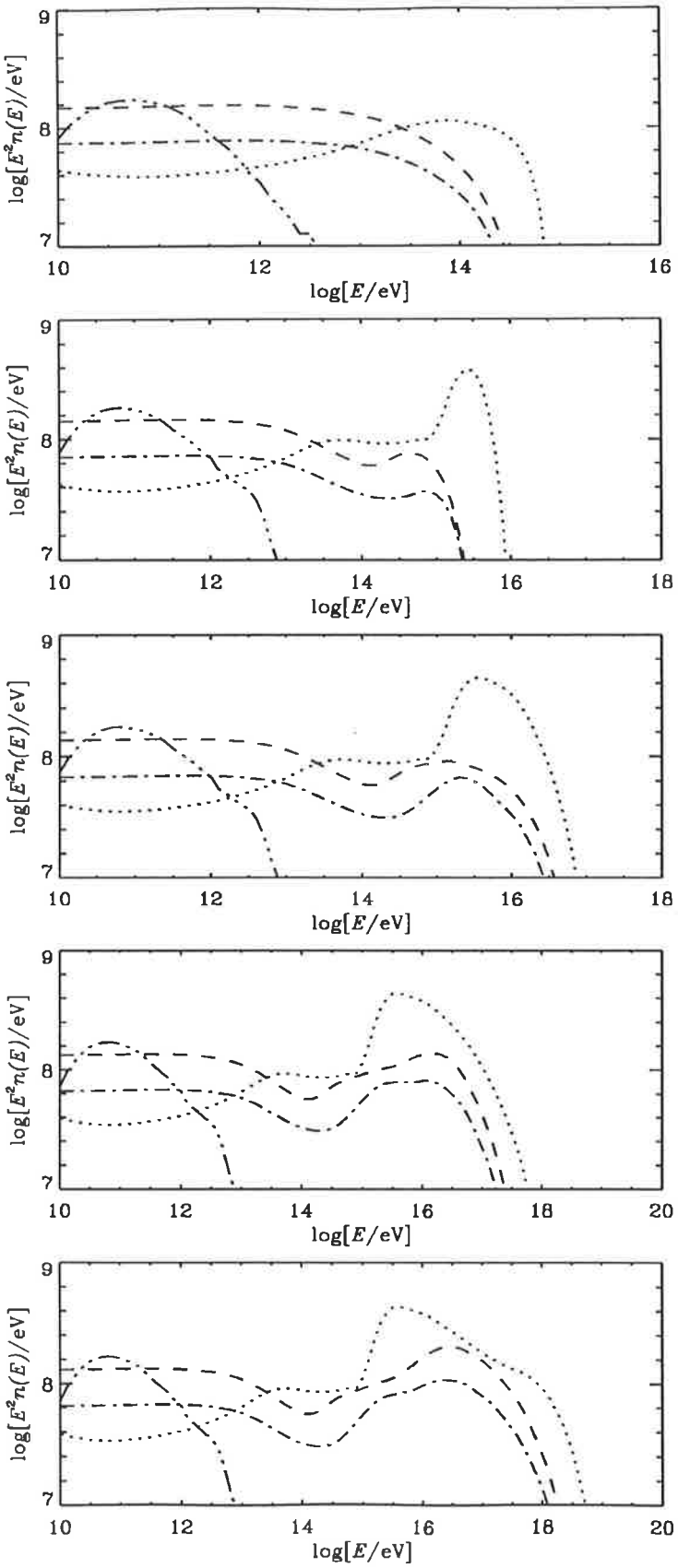

Figure D.9: The spectrum of particles produced within the central region of AGN by protons which have escaped from the accelerator, calculated using the PG continuum (spectrum (a)). Plots are for $E_{\max} = 10^{15}$ (top plot), 10^{16},..., 10^{19} eV (bottom plot), with $x_1 = 10$. Curves are defined as in Figure 6.15.

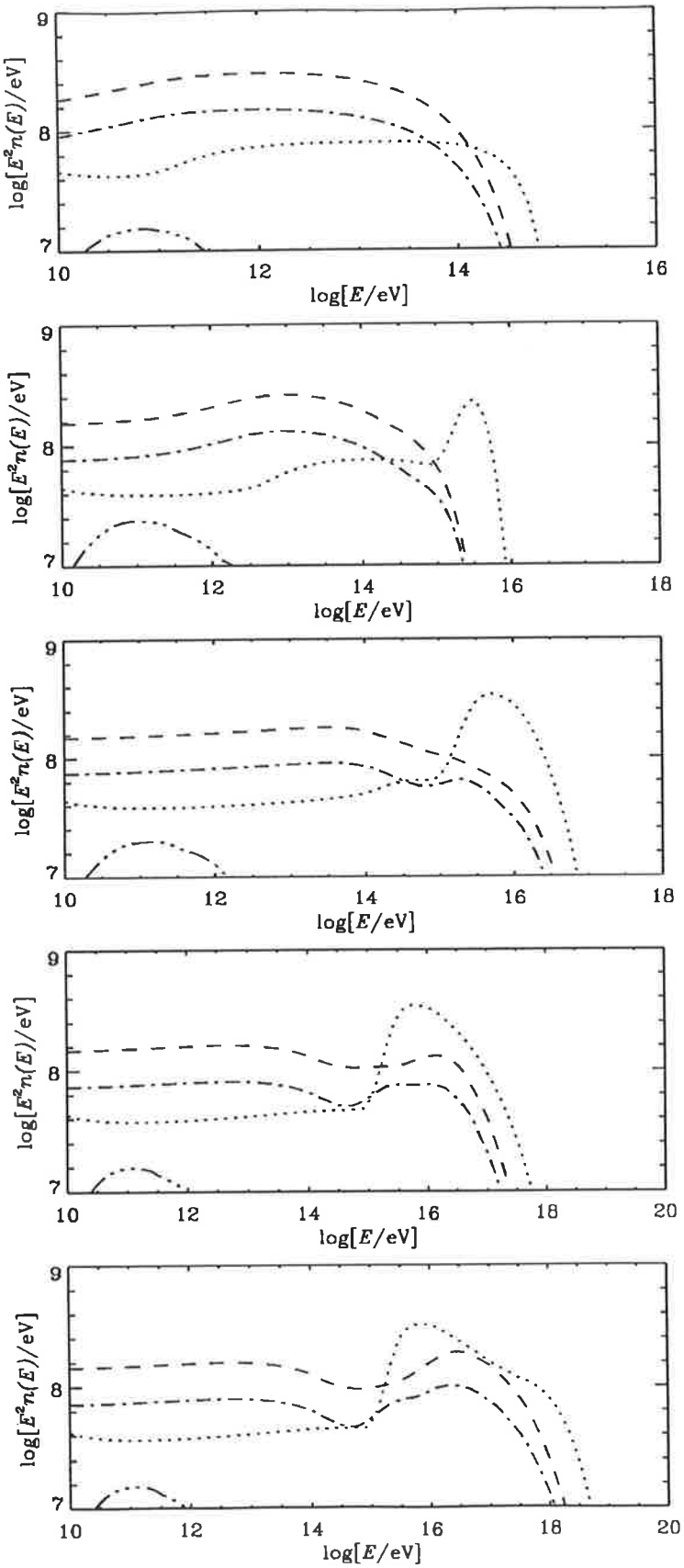

Figure D.10: The spectrum of particles produced within the central region of AGN by protons which have escaped from the accelerator, calculated using the PG continuum (spectrum (a)). Plots are for $E_{\max} = 10^{15}$ (top plot), 10^{16},..., 10^{19} eV (bottom plot), with $x_1 = 100$. Curves are defined as in Figure 6.15.

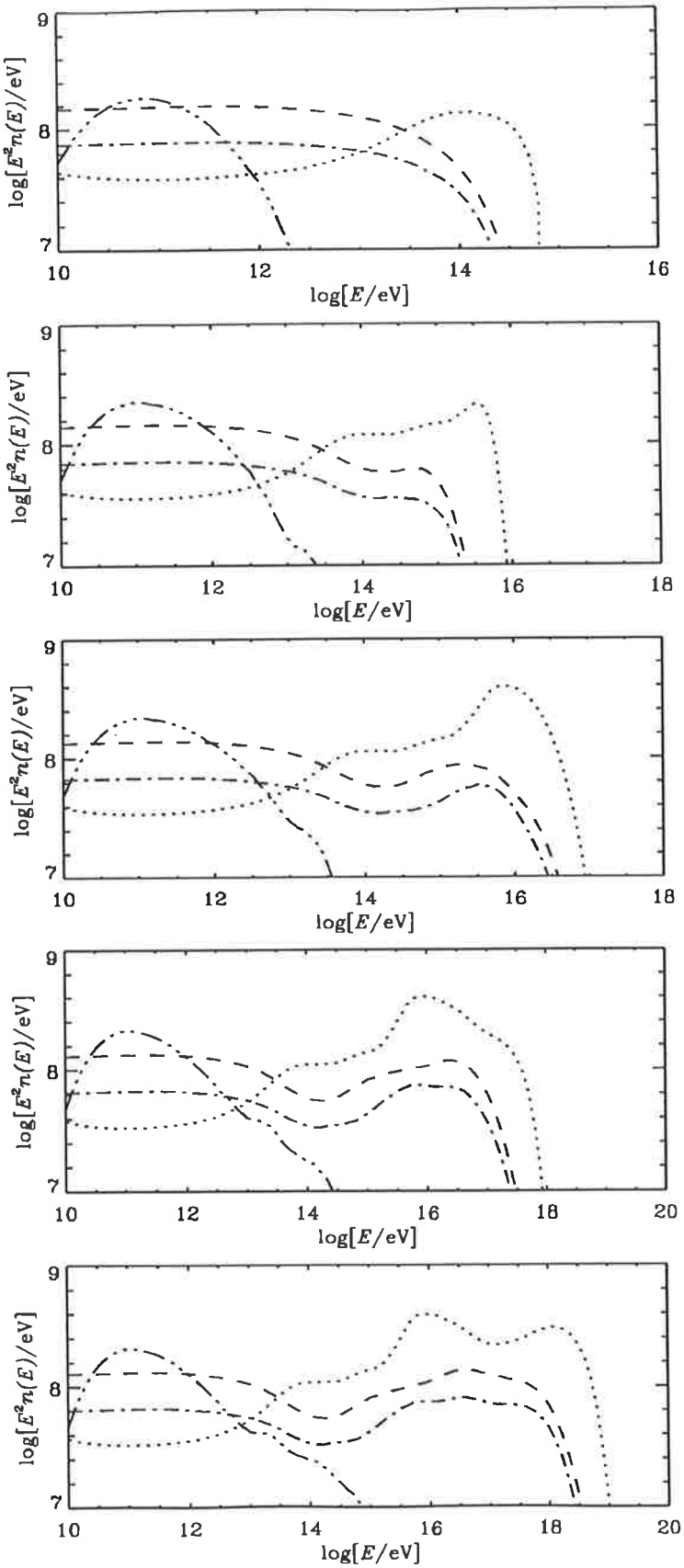

Figure D.11: The spectrum of particles produced within the central region of AGN by protons which have escaped from the accelerator, calculated using the flat AGN continuum (spectrum (b)). Plots are for $E_{\max} = 10^{15}$ (top plot), 10^{16},..., 10^{19} eV (bottom plot), with $x_1 = 10$. Curves are defined as in Figure 6.15.

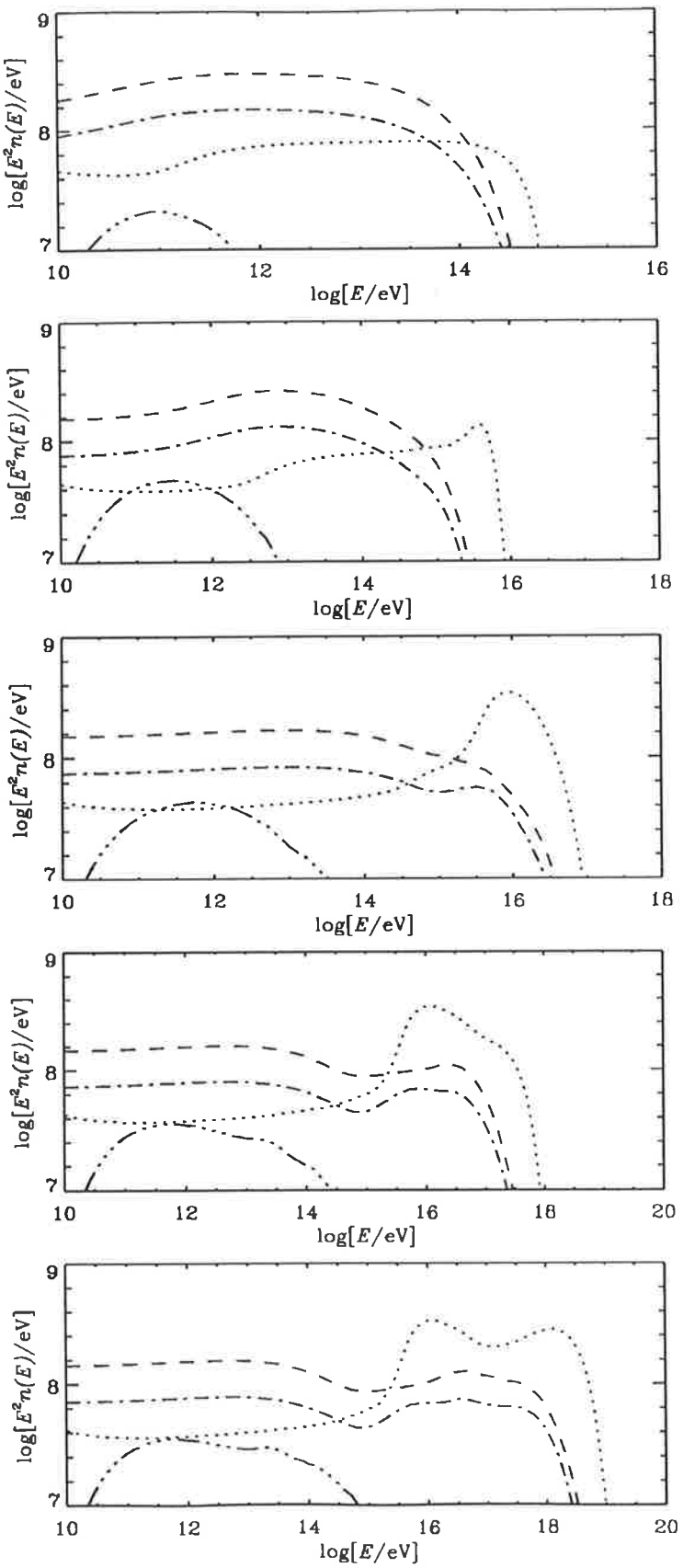

Figure D.12: The spectrum of particles produced within the central region of AGN by protons which have escaped from the accelerator, calculated using the flat AGN continuum (spectrum (b)). Plots are for $E_{\max} = 10^{15}$ (top plot), 10^{16},..., 10^{19} eV (bottom plot), with $x_1 = 100$. Curves are defined as in Figure 6.15.

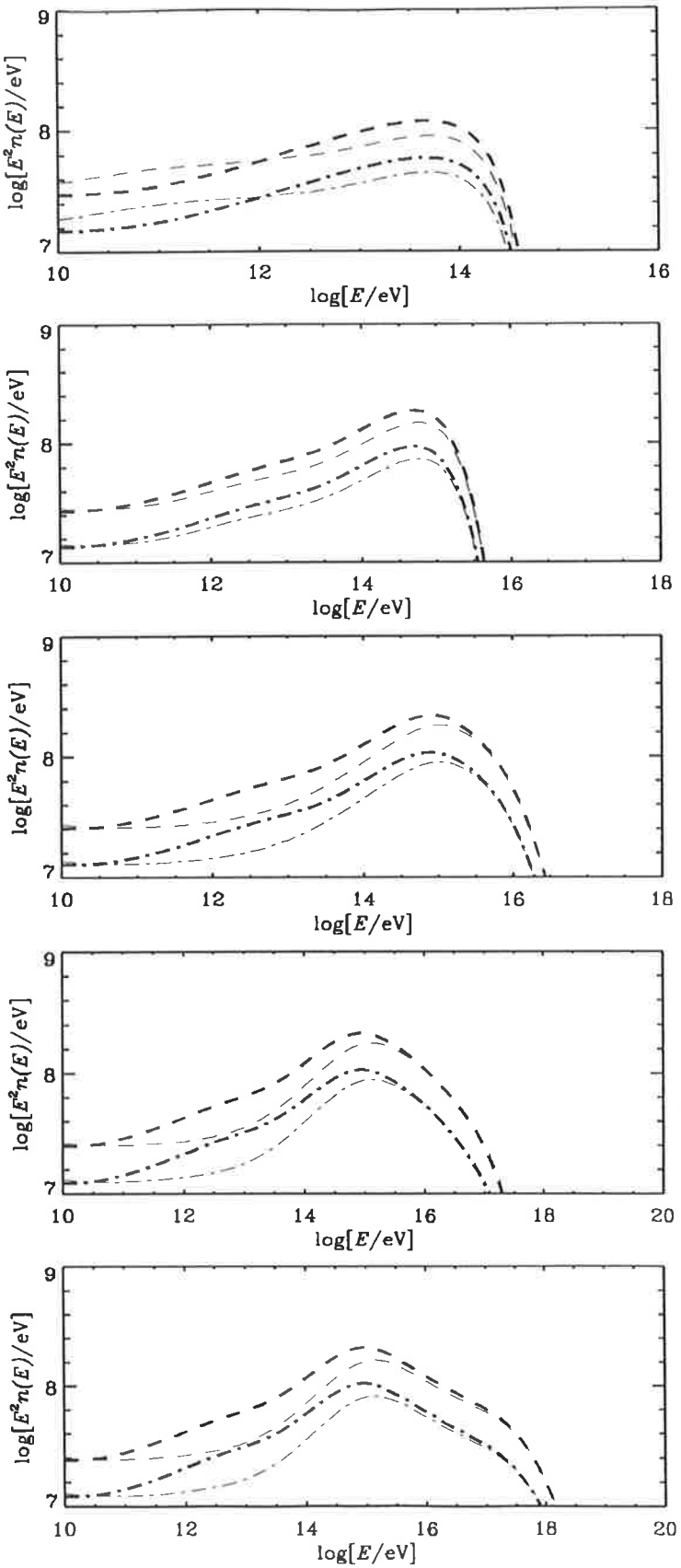

Figure D.13: The spectrum of pions produced by neutrons which have escaped from the central region of AGN, calculated using the PG continuum (spectrum (a)). Plots are for $E_{\max} = 10^{15}$ (top plot), 10^{16},..., 10^{19} eV (bottom plot). Curves are defined as in Figure 6.17.

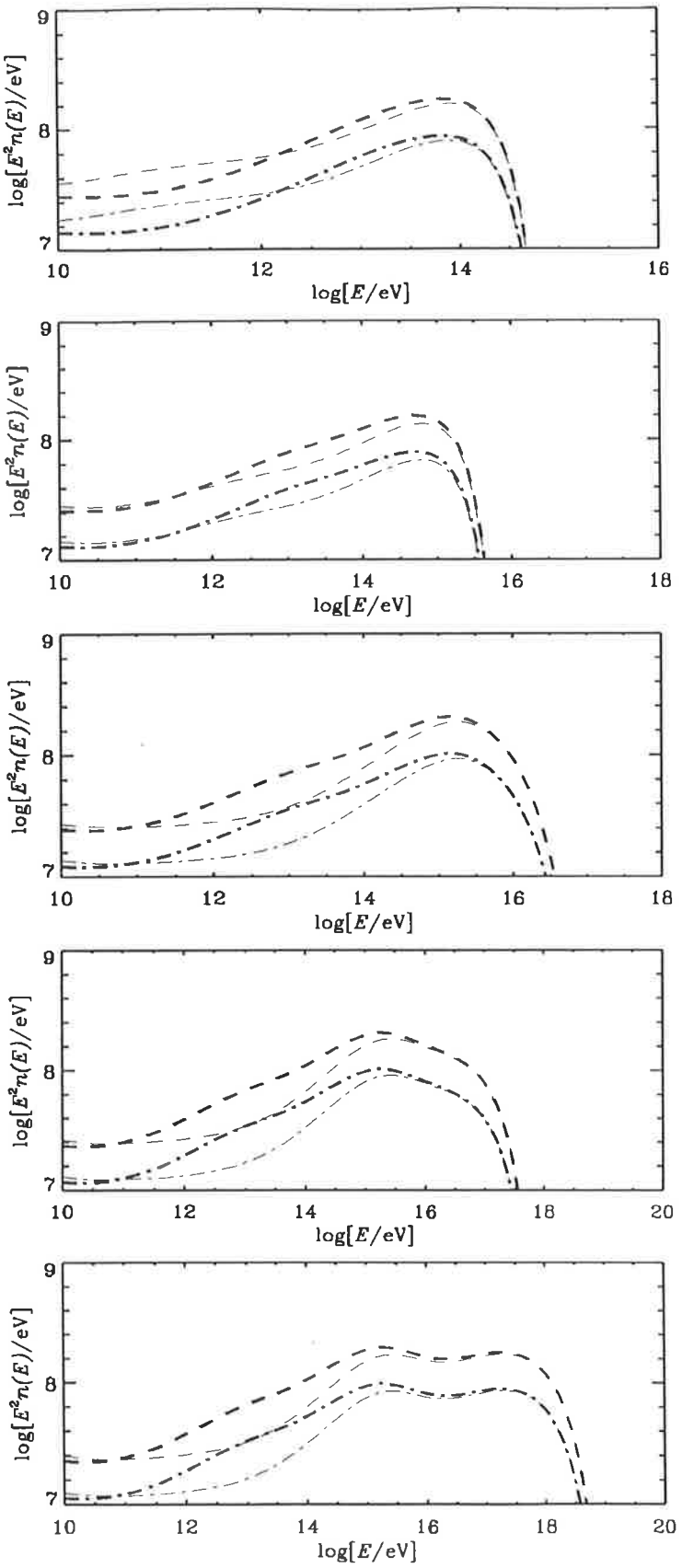

Figure D.14: The spectrum of pions produced by neutrons which have escaped from the central region of AGN, calculated using the flat AGN continuum (spectrum (b)). Plots are for $E_{\max} = 10^{15}$ (top plot), 10^{16},..., 10^{19} eV (bottom plot). Curves are defined as in Figure 6.17.